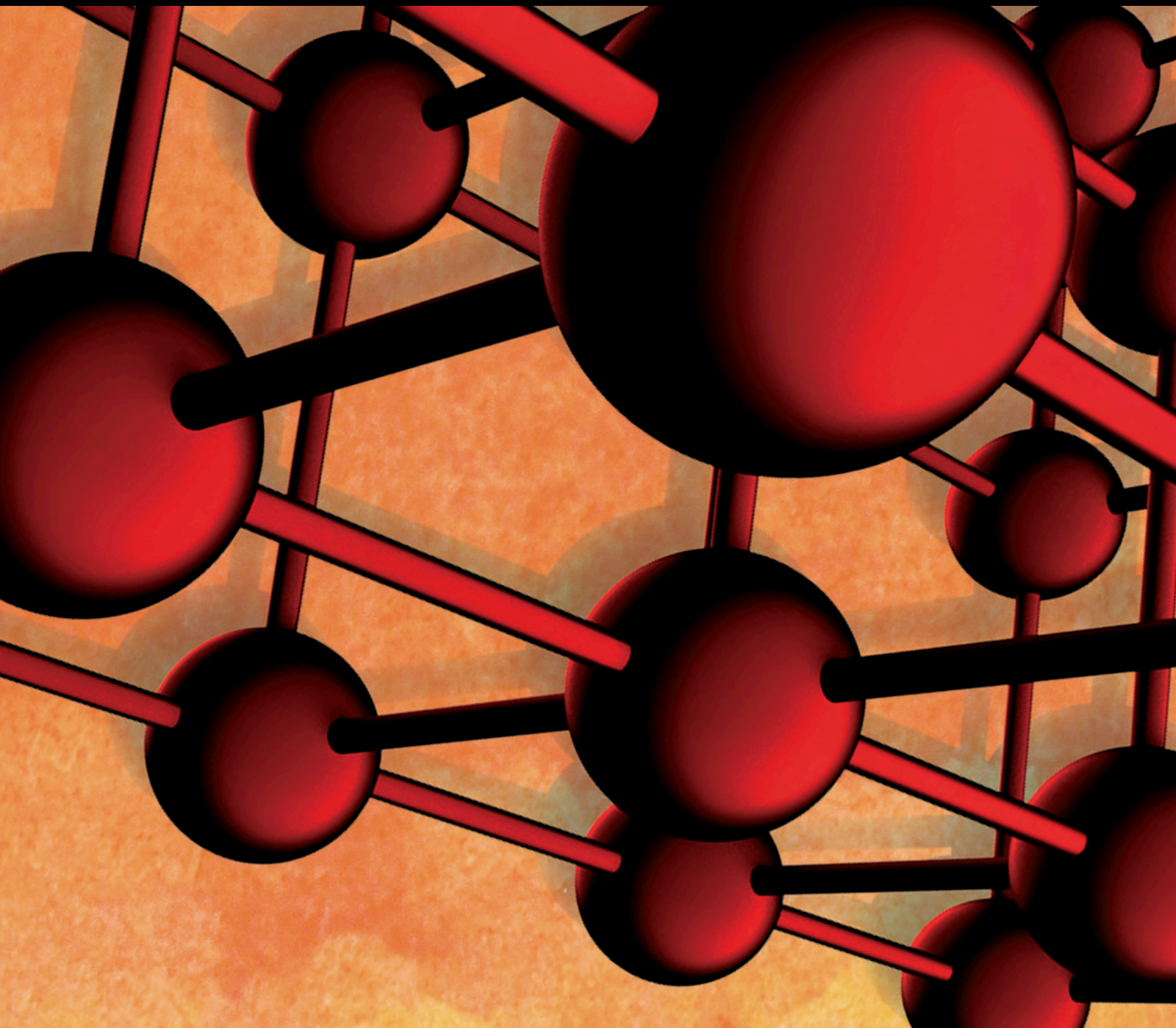


# Novel Bituminous Materials for Sustainable Pavements

Lead Guest Editor: Jose Norambuena-Contreras

Guest Editors: Lily Poulikakos, Hassan Baaj, and Quantao Liu





---

# **Novel Bituminous Materials for Sustainable Pavements**

Advances in Materials Science and Engineering

---

## **Novel Bituminous Materials for Sustainable Pavements**

Lead Guest Editor: Jose Norambuena-Contreras

Guest Editors: Lily Poulikakos, Hassan Baaj, and Quantao Liu



---

Copyright © 2020 Hindawi Limited. All rights reserved.

This is a special issue published in "Advances in Materials Science and Engineering." All articles are open access articles distributed under the Creative Commons Attribution License, which permits unrestricted use, distribution, and reproduction in any medium, provided the original work is properly cited.

# Chief Editor

Amit Bandyopadhyay, USA

## Editorial Board

Antonio Abate, Germany  
H.P.S Abdul Khalil, Malaysia  
Michael Aizenshtein, Israel  
Hamed Akhavan, Portugal  
Jarir Aktaa, Germany  
Amelia Almeida, Portugal  
Rajan Ambat, Denmark  
Konstantinos G. Anthymidis, Greece  
Santiago Aparicio, Spain  
Raul Arenal, Spain  
Alicia E. Ares, Argentina  
Farhad Aslani, Australia  
Apostolos Avgeropoulos, Greece  
Renal Backov, France  
Markus Bambach, Germany  
Massimiliano Barletta, Italy  
Stefano Bellucci, Italy  
Avi Bendavid, Australia  
Brahim Benmokrane, Canada  
Jamal Berakdar, Germany  
Jean-Michel Bergeau, France  
Guillaume Bernard-Granger, France  
Giovanni Berselli, Italy  
Patrice Berthod, France  
Michele Bianchi, Italy  
Hugo C. Biscaia, Portugal  
Antonio Boccaccio, Italy  
Susmita Bose, USA  
Heinz-Günter Brokmeier, Germany  
Steve Bull, United Kingdom  
Gianlorenzo Bussetti, Italy  
Jose M. Cabrera, Spain  
Antonio Caggiano, Germany  
Veronica Calado, Brazil  
Marco Cannas, Italy  
Gianfranco Carotenuto, Italy  
Paolo Andrea Carraro, Italy  
Victor M. Castaño, Mexico  
Michelina Catauro, Italy  
Robert Černý, Czech Republic  
Jose Cesar de Sa, Portugal  
Wensu Chen, Australia  
Daolun Chen, Canada  
Francisco Chinesta, France

Er-Yuan Chuang, Taiwan  
Gianluca Cicala, Italy  
Francesco Colangelo, Italy  
Marco Consales, Italy  
María Criado, Spain  
Gabriel Cuello, France  
Lucas da Silva, Portugal  
Narendra B. Dahotre, USA  
João P. Davim, Portugal  
Angela De Bonis, Italy  
Abílio De Jesus, Portugal  
José António Fonseca de Oliveira Correia, Portugal  
Luca De Stefano, Italy  
Francesco Delogu, Italy  
Luigi Di Benedetto, Italy  
Aldo Di Carlo, Italy  
Maria Laura Di Lorenzo, Italy  
Marisa Di Sabatino, Norway  
Luigi Di Sarno, Italy  
Ana María Díez-Pascual, Spain  
Guru P. Dinda, USA  
Nadka Tzankova Dintcheva, Italy  
Mingdong Dong, Denmark  
Hongbiao Dong, China  
Frederic Dumur, France  
Stanislaw Dymek, Poland  
Kaveh Edalati, Japan  
Philip Eisenlohr, USA  
Claude Estournès, France  
Luis Evangelista, Norway  
Michele Fedel, Italy  
Francisco Javier Fernández Fernández, Spain  
Isabel J. Ferrer, Spain  
Paolo Ferro, Italy  
Dora Foti, Italy  
Massimo Fresta, Italy  
Pasquale Gallo, Finland  
Germà Garcia-Belmonte, Spain  
Santiago Garcia-Granda, Spain  
Carlos Garcia-Mateo, Spain  
Georgios I. Giannopoulos, Greece  
Ivan Giorgio, Italy

Antonio Gloria, Italy  
Vincenzo Guarino, Italy  
Daniel Guay, Canada  
Gianluca Gubbiotti, Italy  
Jenő Gubicza, Hungary  
Xuchun Gui, China  
Benoit Guiffard, France  
Ivan Gutierrez-Urrutia, Japan  
Hiroki Habazaki, Japan  
Simo-Pekka Hannula, Finland  
Akbar Heidarzadeh, Iran  
David Holec, Austria  
Satoshi Horikoshi, Japan  
David Houivet, France  
Rui Huang, USA  
Yi Huang, United Kingdom  
Michele Iafisco, Italy  
Erdin Ibraim, United Kingdom  
Saliha Ilican, Turkey  
Md Mainul Islam, Australia  
Ilia Ivanov, USA  
Hom Kandel, USA  
kenji Kaneko, Japan  
Fuat Kara, Turkey  
Katsuyuki Kida, Japan  
Akihiko Kimura, Japan  
Soshu Kirihara, Japan  
Paweł Kłosowski, Poland  
Jan Koci, Czech Republic  
Ling B. Kong, Singapore  
Lingxue Kong, Australia  
Fantao Kong, China  
Pramod Koshy, Australia  
Hongchao Kou, China  
Alexander Kromka, Czech Republic  
Luciano Lamberti, Italy  
Andrea Lamberti, Italy  
Fulvio Lavecchia, Italy  
Marino Lavorgna, Italy  
Laurent Lebrun, France  
Joon-Hyung Lee, Republic of Korea  
Pavel Lejcek, Czech Republic  
Cristina Leonelli, Italy  
Ying Li, USA  
Yuanshi Li, Canada  
Yuning Li, Canada  
Guang-xing Liang, China

Barbara Liguori, Italy  
Shaomin Liu, Australia  
Yunqi Liu, China  
Jun Liu, China  
Meilin Liu, Georgia  
Zhiping Luo, USA  
Fernando Lusquiños, Spain  
Peter Majewski, Australia  
Georgios Maliaris, Greece  
Muhamamd A. Malik, United Kingdom  
Dimitrios E. Manolakos, Greece  
Necmettin Maraşlı, Turkey  
Enzo Martinelli, Italy  
Alessandro Martucci, Italy  
Yoshitake Masuda, Japan  
Bobby Kannan Mathan, Australia  
Roshan Mayadunne, Australia  
Mamoun Medraj, Canada  
Shazim A. Memon, Kazakhstan  
Philippe Miele, France  
Andrey E. Miroshnichenko, Australia  
Hossein Moayedi, Vietnam  
Sakar Mohan, India  
Jose M. Monzo, Spain  
Michele Muccini, Italy  
Alfonso Muñoz, Spain  
Roger Narayan, USA  
Rufino M. Navarro, Spain  
Miguel Navarro-Cia, United Kingdom  
Ali Nazari, Australia  
Behzad Nematollahi, Australia  
Luigi Nicolais, Italy  
Peter Niemz, Switzerland  
Hiroshi Noguchi, Japan  
Chérif Nouar, France  
Olanrewaju Ojo, Canada  
Dariusz Oleszak, Poland  
Laurent Orgéas, France  
Togay Ozbakkaloglu, United Kingdom  
Nezih Pala, USA  
Marián Palcut, Slovakia  
Davide Palumbo, Italy  
Gianfranco Palumbo, Italy  
Zbyšek Pavlík, Czech Republic  
Matthew Peel, United Kingdom  
Alessandro Pegoretti, Italy  
Gianluca Percoco, Italy

Claudio Pettinari, Italy  
Giorgio Pia, Italy  
Silvia M. Pietralunga, Italy  
Daniela Pilone, Italy  
Teresa M. Piqué, Argentina  
Candido Fabrizio Pirri, Italy  
Marinos Pitsikalis, Greece  
Alain Portavoce, France  
Simon C. Potter, Canada  
Ulrich Prah, Germany  
Viviana F. Rahhal, Argentina  
Carlos R. Rambo, Brazil  
Shahed Rasekh, Portugal  
Manijeh Razeghi, USA  
Paulo Reis, Portugal  
Yuri Ribakov, Israel  
Aniello Riccio, Italy  
Anna Richelli, Italy  
Antonio Riveiro, Spain  
Marco Rossi, Italy  
Sylvie Rossignol, France  
Pascal Roussel, France  
Fernando Rubio-Marcos, Spain  
Francesco Ruffino, Italy  
Mark H. Rummeli, China  
Pietro Russo, Italy  
Antti Salminen, Finland  
F.H. Samuel, Canada  
Maria Gabriella Santonicola, Italy  
Hélder A. Santos, Finland  
Carlo Santulli, Italy  
Fabrizio Sarasini, Italy  
Michael J. Schu#tze, Germany  
Raffaele Sepe, Italy  
Kenichi Shimizu, USA  
Fridon Shubitidze, USA  
Mercedes Solla, Spain  
Donato Sorgente, Italy  
Charles C. Sorrell, Australia  
Andres Sotelo, Spain  
Costas M. Soukoulis, USA  
Damien Soulat, France  
Adolfo Speghini, Italy  
Antonino Squillace, Italy  
Koichi Sugimoto, Japan  
Baozhong Sun, China  
Sam-Shajing Sun, USA

Youhong Tang, Australia  
Shengwen Tang, China  
Kohji Tashiro, Japan  
Miguel Angel Torres, Spain  
Laszlo Toth, France  
Achim Trampert, Germany  
Tomasz Trzepieciński, Poland  
Matjaz Valant, Slovenia  
Luca Valentini, Italy  
Ashkan Vaziri, USA  
Lijing Wang, Australia  
Zhongchang Wang, Portugal  
Rui Wang, China  
Lu Wei, China  
Jörg M. K. Wiezorek, USA  
Jiang Wu, China  
Guoqiang Xie, China  
Jinyang Xu, China  
Dongmin Yang, United Kingdom  
Zhonghua Yao, China  
Hemmige S. Yathirajan, India  
Yee-wen Yen, Taiwan  
Wenbin Yi, China  
Ling Yin, Australia  
Tetsu Yonezawa, Japan  
Hiroshi Yoshihara, Japan  
Belal F. Yousif, Australia  
Lenka Zaji#c#kova#, Czech Republic  
Zhigang Zang, China  
Michele Zappalorto, Italy  
Jinghuai Zhang, China  
Li Zhang, China  
Gang Zhang, Singapore  
Mikhail Zheludkevich, Germany  
Wei Zhou, China  
You Zhou, Japan  
Hongtao Zhu, Australia

# Contents

## **Novel Bituminous Materials for Sustainable Pavements**

José Norambuena-Contreras , Lily Poulikakos, Hassan Baaj , and Quantao Liu   
Editorial (2 pages), Article ID 3265052, Volume 2020 (2020)

## **Evaluating Fly Ash-Based Geopolymers as a Modifier for Asphalt Binders**

Abdulrahman Hamid , Hamed Alfaidi, Hassan Baaj , and Mohab El-Hakim   
Research Article (11 pages), Article ID 2398693, Volume 2020 (2020)

## **Antiaeging Performance Evaluation of Recycled Engine Oil Bottom Used in Asphalt Rejuvenation**

Miaozhang Yu , Jin Li , Xinzhuang Cui, Dedong Guo, and Xinjun Li  
Research Article (8 pages), Article ID 2947170, Volume 2019 (2019)

## **Effect of Blending Degree between Virgin and Aged Binder on Pavement Performance of Recycled Asphalt Mixture with High RAP Content**

Ying Xu , Zhijing Chou, Yunze Li, Jie Ji , and Shi-fa Xu  
Research Article (15 pages), Article ID 5741642, Volume 2019 (2019)

## **Properties and Components of Recycled Engine Oil Bottom Rejuvenated Asphalt and Its Grey Relationship Analysis**

Jin Li , Miaozhang Yu , Xinzhuang Cui, and Wentong Wang  
Research Article (11 pages), Article ID 2462487, Volume 2019 (2019)

## **Usage of Reclaimed Asphalt Material in Stone Mastic Asphalt**

Petr Hyzl, Ondrej Dasek , Iva Coufalikova, Michal Varaus, and Dusan Stehlik  
Research Article (8 pages), Article ID 3078708, Volume 2019 (2019)

## **Wetting Model of Asphalt on the Aggregate Surface and Its Effect Factors**

YuHui Pi, Yan Li , YingXing Pi, XiaoYong Tan, and MingMing He  
Research Article (7 pages), Article ID 4126464, Volume 2019 (2019)

## **Evaluation of the Effect of Fly Ash and Slag on the Properties of Cement Asphalt Mortar**

Tri H. M. Le , Dae-Wook Park , Jin-Yong Park, and Tam M. Phan   
Research Article (10 pages), Article ID 1829328, Volume 2019 (2019)

## **Investigating the Effects of Chopped Basalt Fiber on the Performance of Porous Asphalt Mixture**

Sheng Wang , Aihong Kang , Peng Xiao, Bo Li, and Weili Fu  
Research Article (12 pages), Article ID 2323761, Volume 2019 (2019)

## **Aesthetic and Mechanical Suitability of a Clear Synthetic Resin as a Unconventional Binder for Road Pavements**

Marco Pasetto , Andrea Baliello , Giovanni Giacomello , and Emiliano Pasquini   
Research Article (15 pages), Article ID 8643608, Volume 2019 (2019)

## **2S2P1D Model Calibration Error from User Panel for One Bitumen and One Bituminous Mixture**

S. Mangiafico , C. Sauzéat, and H. Di Benedetto  
Research Article (16 pages), Article ID 6547025, Volume 2019 (2019)

**Reuse of Zeolite By-Products Derived from Petroleum Refining for Sustainable Roads**

M. Sol-Sánchez, F. Moreno-Navarro , M. C. Rubio-Gómez , V. Pérez-Mena, and P. Cabanillas  
Research Article (10 pages), Article ID 4256989, Volume 2019 (2019)

**Induction Heating and Healing Behaviors of Asphalt Concretes Doped with Different Conductive Additives**

Hechuan Li, Jianying Yu, Quantao Liu , Yuanyuan Li, Yaqi Wu, and Haiqin Xu  
Research Article (10 pages), Article ID 2190627, Volume 2019 (2019)

**Assessment Model and Virtual Simulation for Fatigue Damage Evolution of Asphalt Mortar and Mixture**

Danhua Wang, Xunhao Ding , Linhao Gu, and Tao Ma   
Research Article (14 pages), Article ID 5904807, Volume 2018 (2018)

## Editorial

# Novel Bituminous Materials for Sustainable Pavements

José Norambuena-Contreras <sup>1</sup>, Lily Poulidakos,<sup>2</sup> Hassan Baaj <sup>3</sup>, and Quantao Liu <sup>4</sup>

<sup>1</sup>LabMAT, Department of Civil and Environmental Engineering, University of Bío-Bío, Concepción, Chile

<sup>2</sup>Empa-Swiss Federal Laboratories for Materials Science and Technology, Dübendorf, Switzerland

<sup>3</sup>Department of Civil and Environmental Engineering, University of Waterloo, Waterloo, Canada

<sup>4</sup>Wuhan University of Technology, State Key Laboratory of Silicate Materials for Architectures, Wuhan, China

Correspondence should be addressed to José Norambuena-Contreras; jnorambuena@ubiobio.cl

Received 20 December 2019; Accepted 17 January 2020; Published 19 February 2020

Copyright © 2020 José Norambuena-Contreras et al. This is an open access article distributed under the Creative Commons Attribution License, which permits unrestricted use, distribution, and reproduction in any medium, provided the original work is properly cited.

Bituminous materials are complex viscoelastic composites mainly used for road and airport pavement construction. Numerous advances on novel bituminous materials for sustainable pavements have been developed over the last years, turning this topic into an emerging field of study. The studies include several areas: characterization and modelling of bituminous materials, multiphase behaviour of bituminous materials, asphalt mixtures modified with phase change materials, self-healing of asphalt pavements, and valorisation of waste for roads.

This special issue presents a selection of thirteen recent research studies mainly focused on the multiscale characterization and numerical modelling of bituminous materials including modified asphalt mixtures, mastics and bituminous binders, recycling and valorisation of waste materials for asphalt pavements, as well as innovations in more sustainable bituminous materials development and on-site application. Scientific contributions from Canada, China, USA, Czech Republic, Republic of Korea, Italy, France, and Spain were received.

This special issue opens with the study conducted by A. Hamid et al. They have developed a laboratory study to investigate the effects of the fly ash-based geopolymer content on the rheological and microstructural properties of asphalt binders. The results indicate that geopolymers could be used as a sustainable and greener alternative to other asphalt modifiers due to their low carbon dioxide footprint and better recycling capacity, having minor effects on the performance and microstructure of the binder.

The paper by M. Yu et al. presents an experimental study that evaluates the antiageing performance of recycled engine oil bottom (REOB) as a rejuvenating agent for asphalt binders and dense-graded asphalt mixtures. The main results demonstrate that REOB can be used as an asphalt regenerative, complying with the antiageing requirements reported in the technical specifications.

The work by Y. Xu et al. studies the effect of the blending degree between virgin and aged binder on the pavement performance of hot-mix recycled asphalt mixtures (HMRAM) with a high RAP content. To do this, HMRAMs with different degrees of blending (DOBs) were prepared by changing the mixing temperature. The results prove that the content and physical properties of old aggregates in RAP materials have an important effect on the performance of HMRAMs with a high RAP content.

In the paper by J. Li et al., similar to M. Yu et al., several physical and rheological tests were carried out in addition to four-component and infrared spectroscopic analyses on aged asphalt binders containing three types of REOB from a recycling plant. The main results of the paper reveal that REOB is sensitive to the softening point, and the asphaltene content has a significant effect on the physical and rheological properties of REOB-rejuvenated asphalt.

The paper by P. Hyzl et al. presents the results of a 5-year research focused on the use of reclaimed asphalt (RA) in asphalt mixtures of the type stone mastic asphalt (SMA). The authors determine that it is possible to use RA in SMA-type mixtures without negative impacts on the functional properties or on the layer lifetime.

The paper by Y. Pi et al. analyses the general wetting process of asphalt on the aggregate surface based on the surface energy theory. As a main result, the authors establish a modified numerical wetting model to research the effects of initial temperature, cooling rate of asphalt, and aggregate surface texture sizes on the wetting process.

H. Li et al. study the effect of fly ash and slag on the properties of cement asphalt mortar (CAM). Experimental tests were conducted to determine the effect of these admixtures on the fresh and hardened characteristics of CAM. Based on the assessed properties, the CAM mixture with fly ash is suggested to be applied in further research as a cost-effective strategy.

The work by D. Wang et al. examines the effect of chopped basalt fibres with different lengths and contents of addition on the performance of porous asphalt mixtures. The results prove that the addition of chopped basalt fibres can improve the performance of porous asphalt mixtures because they form a three-dimensional network reinforcing structure inside the porous asphalt mixture.

The paper by M. Pasetto et al. carries out an experimental study aimed at analysing the chromatic and mechanical properties of a clear synthetic resin and its suitability as an unconventional bituminous binder for novel asphalt mixtures. The studied synthetic resin was a proprietary product composed by a thermoplastic bicomponent resin with bonding properties like those of traditional bitumen. The binder developed shows promising results in view of its effective use in more sustainable asphalt pavements.

S. Magniafico et al. in their work study the differences between experimental linear viscoelastic (LVE) properties of both straight-run bitumen and a bituminous mixture and simulations with analogical 2S2P1D model fitted by 14 different users. 2S2P1D (2 springs, 2 parabolic creep elements, and 1 dashpot) is a linear viscoelastic analogical model to simulate the behaviour of bituminous materials developed at the University of Lyon/ENTPE. The obtained results highlight the relevance of 2S2P1D model to perform multiscale modelling of LVE behaviour of bituminous materials, from bituminous binders to asphalt mixtures.

The paper by M. Sol-Sánchez et al. presents a research study that aims to analyse the reuse of zeolite waste derived from petroleum refining in the production of warm mix asphalts (WMA). Two different types of zeolite waste are analysed as additives for the manufacturing of two WMA, whose mechanical performance is compared with conventional WMA and hot-mix asphalt (HMA). The results indicate that zeolite waste with a content of 0.3% allows the production of WMA at temperatures around 145°C, with comparable workability and densification to conventional reference HMAs at 165°C, without reducing their mechanical properties.

The paper by H. Li et al. studies the induction heating efficiency and the healing capability of asphalt mixtures with different conductive additives. Steel fibre, steel grit, and steel slag are added to asphalt mixtures with induction heating purposes. The results show that the thermal properties of asphalt mixtures changed with the addition of different conductive additives. The modified asphalt mixture with

steel fibre showed the best induction heating performance. It was proven that the addition of conductive additives in asphalt is a potential solution in order to propose novel asphalt pavements with crack-healing properties.

Finally, this special issue closes with the paper by D. Wang et al. They conduct an experimental and numerical study to establish a fatigue damage evolution model for the asphalt mixtures. To achieve this, four-point bending fatigue tests and FEM simulations by ABAQUS on test specimens of asphalt mixtures are performed. Based on the combination of the damage model by fatigue bending tests and their virtual simulation, the factors influencing the fatigue resistance of the whole asphalt mixtures are evaluated.

## Conflicts of Interest

The editors declare that they have no conflicts of interest.

## Acknowledgments

We would like to express our gratitude to all authors who made this special issue possible. We hope this collection of papers will be useful to the scientific community focused on novel sustainable bituminous materials.

*José Norambuena-Contreras  
Lily Poulidakos  
Hassan Baaj  
Quantao Liu*

## Research Article

# Evaluating Fly Ash-Based Geopolymers as a Modifier for Asphalt Binders

Abdulrahman Hamid <sup>1</sup>, Hamed Alfaidi,<sup>1</sup> Hassan Baaj <sup>1</sup> and Mohab El-Hakim <sup>1,2</sup>

<sup>1</sup>Department of Civil and Environmental Engineering, University of Waterloo, Waterloo, Canada N2L 3G1

<sup>2</sup>Department of Civil and Environmental Engineering, Manhattan College, Bronx, NY, USA

Correspondence should be addressed to Hassan Baaj; [hassan.baaj@uwaterloo.ca](mailto:hassan.baaj@uwaterloo.ca)

Received 29 May 2019; Revised 3 September 2019; Accepted 16 September 2019; Published 19 February 2020

Academic Editor: María Criado

Copyright © 2020 Abdulrahman Hamid et al. This is an open access article distributed under the Creative Commons Attribution License, which permits unrestricted use, distribution, and reproduction in any medium, provided the original work is properly cited.

Severe Canadian winter conditions and growing traffic volumes are vital factors resulting in a reduction of the service life of flexible pavements. Researchers and engineers strived to develop several additives to develop balanced asphalt mixers capable of resisting distresses that caused deterioration of flexible pavements in Canada. In this study, a critical literature review regarding the use of geopolymers and their application in construction materials is provided. Moreover, an experimental matrix of laboratory testing was conducted to study the rheological and microstructural properties of the PG 58-28 asphalt binder, with different percentages (0%, 3%, 6%, and 9%) of geopolymer. The effect of geopolymer-curing time on rheological properties was investigated. Rotational viscometer, dynamic shear rheometer (DSR), and environmental scanning electron microscopy (ESEM) imaging devices were used to compare the performance of control binder with a binder with different percentages of geopolymers. Results indicated that the increase in the geopolymer content and the curing time affect the rheological behavior of the asphalt binder by increasing its viscosity, complex shear modulus, and failure temperature. Samples with higher geopolymer percentage exhibited better performance in terms of rutting resistance. Moreover, an increase in the failure temperature of modified asphalt binder with 9% geopolymer is recorded as 8.58%, 14.2%, and 15.2% for curing times of 2, 7, and 14 days, respectively, compared with virgin asphalt. Furthermore, the nanoparticles appear to be well dispersed in the binder, and increasing the percentage of the geopolymer does not seem to affect the microstructure of the binder. Overall research conclusion is that geopolymer application resulted in a potential enhancement of some of the properties of the asphalt binder.

## 1. Introduction

Modified asphalt binder could be used to reduce pavement distresses such as rutting and cracking. Polymer modification of asphalt binder could be a cost-effective solution to reduce the annual budget for maintenance and rehabilitation of flexible pavements. In the past two decades, growth in the use of polymer-modified asphalt binders in pavement-engineering applications was noticed. Significant improvement of the mechanical and rheological properties of the asphalt binder at different temperatures was reported in the literature [1–3]. Polymers can be defined as large molecules with numerous compositions of small molecules bonded together. These small molecules are called monomers [4]. The binder modification using polymers increases the

sustainability of asphalt binders and asphalt mix designs. In addition, performance enhancement and cost reductions are achieved through polymer modification of asphalt binders [5]. Application of modifiers in asphalt binders would result in a reduction of optimum binder content, increasing stability, increasing the bond between asphalt cement and aggregates, and improving density [6]. In addition, modifiers would minimize the environmental impact on roads, such as traffic noise, the total expenditure for repair, and maintenance of road structures.

Scholars investigated the use of waste materials to improve the performance of asphalt binders. Numerous studies have been conducted to evaluate the benefits of using crumb rubber [7, 8], cylinder oil [9], and palm oil fuel ash (POFA) [10] as binder modifiers. Geopolymer-modified binder is a

new method to capitalize on the use of waste materials in paved roads. Geopolymer concept was first introduced by Davidovits in 1978 [11]. The geopolymers are inorganic polymers with aluminosilicate base. The geopolymers are produced from the interaction between pozzolanic materials with an alkaline solution such as sodium hydroxide (NaOH) and sodium silicate ( $\text{Na}_2\text{SiO}_3$ ), or potassium hydroxide (KOH) and potassium silicate ( $\text{K}_2\text{SiO}_3$ ) [12]. Materials stemming from solid wastes and by-products endowed with silica and/or aluminas such as fly ash, red mud, mine waste, and blast furnace slag qualify as a pozzolanic component of geopolymerization [13]. Geopolymer has also proven its ability to develop mechanical properties rapidly, to improve the high fire-resistance property, and to reduce energy consumption and greenhouse emissions [14–17]. Geopolymer has many applications in the field of manufacturing such as in the aerospace and automobile, metallurgy and nonferrous foundries, civil engineering, and plastic industries [18]. Geopolymeric materials are used in toxic waste management because of their ability to absorb toxic chemical wastes [18].

During the past two decades, geopolymers were widely used as an environment-friendly additive to cementitious construction materials. Geopolymers were noted to reduce the  $\text{CO}_2$  emissions associated with the production of cementitious materials [19]. Geopolymer can also be used in fire-resistant wall panels [13], masonry units, protective coatings, and repairs materials, shotcrete, and high-performance fiber reinforced laminates [15]. Sumajouw et al. [20] investigated the structural behavior of geopolymer concrete columns and noted that the possibility of using the current concrete design standards for fly ash-based geopolymer concrete columns. Twelve columns were tested under axial load and uniaxial bending in the mode of single curvature during this investigation. Six columns were characterized by 40 MPa compressive strength, while the rest had 60 MPa compressive strength. Different reinforcement ratios and load eccentricities were considered. Load carrying capacity, deflection characteristic, and mode of failure were determined. Results showed that the current concrete design standards could be used for designing fly ash-based geopolymer concrete columns.

Geopolymers have many applications in the field of soil stabilization. Recent studies investigated the effectiveness of using geopolymer to improve the physical and mechanical properties of soils. Cristelo et al. [21] experimentally studied the effectiveness of geopolymer on the improvement of rammed-earth construction soils. The ratio of liquid to solid, the ratio of  $\text{Na}_2\text{O}$  to ash, and the alkali concentration were investigated through this study. Furthermore, the influence of concrete superplasticizer, sodium chloride, and calcium hydroxide is also discussed. The results showed that there are only slight effects of sodium chloride or superplasticizer, and there is a significant increase in compressive strength as an optimum value for the ratio of activator: solids and the concentration of alkali. Sukmak et al. [22] investigated the important factors such as sample sizes, heating conditions, and different percentages of silty clay and fly ash that affect the strength development in clay-fly ash geopolymer brick.

In this study, sodium hydroxide and sodium silicate were used as an alkaline activator, and fly ash was used as a pozzolanic material. The results showed that the samples with optimum heat energy per weight (E/W) is  $8.5^\circ\text{C h/g}$  for fly ash/clay ratios of 0.3 and 0.5 whereas the E/W is  $7.57^\circ\text{C h/g}$  for fly ash/clay ratio of 0.7. Moreover, they recommended that a substantial relationship between weight and heat energy should be considered in the bricks production industry.

Recently, geopolymer was used as an additive during the preparation of warm mix asphalt. Tang et al. [23] studied the applications of geopolymer in warm mix asphalt. Sodium hydroxide and sodium silicate were used with different concentrations as an activator for aluminosilicate in meta-kaolin, slag, and silica fume. The results showed that geopolymer could decrease the mixing temperature. Consequently, geopolymers could be used to reduce warm mix asphalt mixing cost.

The need for new additive with high properties is in continuous growth to enhance the asphalt binder properties. The use of by-product materials such as fly ash enhances the sustainability of pavement mixtures and reduces the emission of  $\text{CO}_2$ . Fly ash can be divided into three classes, N, F, and C, based on its composition and source of origin [24]. The concentration of calcium in fly ash has an effective influence on the polymerization process which was noted that fly ash with a low amount of calcium such as Class F is better for the formation of geopolymers than fly ash with a high amount of calcium such as Class C [25]. Xu and van Deventer [26] noted that the addition of sodium hydroxide solution to the sodium silicate solution as the alkaline liquid improved the reaction with fly ash.

The main objective of this project is to study the rheological behavior and performance grading of geopolymer-modified binder with the concentrations of 3%, 6%, and 9% at different temperatures using several laboratory experiments. The impact of curing time variation on the performance of geopolymer was also evaluated in this project. Finally, the microstructure of base and modified asphalt binder was investigated using the environmental scanning electron microscope (ESEM).

## 2. Experimental Methods

### 2.1. Materials

**2.1.1. Geopolymer Preparation.** Geopolymer was the combination of fly ash and the alkali activator. The alkali activator was sodium silicate solution ( $\text{Na}_2\text{SiO}_3$ ) and sodium hydroxide (NaOH) pallet diluted in water to produce 8 Molar (8 M) NaOH solution. A mixture of sodium silicate solution and sodium hydroxide solution was prepared to activate the aluminosilicate precursors in fly ash.

In this study, fly ash with Class F is used which satisfies this chemical composition  $\text{SiO}_2 + \text{Al}_2\text{O}_3 + \text{Fe}_2\text{O}_3 \geq 70\%$  according to the ASTM C618-17a [24]. The chemical compositions of fly ash are listed in Table 1. Geopolymer

TABLE 1: Chemical Composition (%) of Fly ash.

Constituent (%)	SiO <sub>2</sub>	Al <sub>2</sub> O <sub>3</sub>	Fe <sub>2</sub> O <sub>3</sub>	CaO	MgO	SO <sub>3</sub>	Na <sub>2</sub> O
Fly ash	57.2	23.5	3.8	9.3	1.0	0.2	2.43

additives were prepared using the alkaline medium as the chemical activator and fly ash as the aluminosilicate source.

Figure 1 shows the adopted mixing procedure to prepare the geopolymer. The following steps summarize the preparation of geopolymer:

- (1) Prepared alkaline solution using sodium hydroxide (8 M) and sodium silicate solution with percentages of 100 : 50% by mass respectively.
- (2) 200 grams of fly ash powder was mixed with 80 grams of the alkaline medium for 6 minutes.
- (3) The formed slurry was transferred to silicon molds, as shown in Figure 1.
- (4) Geopolymers were cured at room temperature (23–25°C) and in the oven (40°C). Curing was performed in three different curing plans which will be explained in the following section.

In this study, there are three sets of geopolymer prepared based on the curing time as the following: (i) first set was cured for 24 hours at room temperature and then cured in the oven at 40°C for 24 hours, (ii) second set was cured for 6 days at room temperature and then cured in the oven at 40°C for 24 hours, and (iii) third set was cured for 13 days at room temperature and then cured in the oven at 40°C for 24 hours. The particles size greater than 0.25 mm may impact the consistency of results obtained from tests such as DSR. Therefore, geopolymer samples were grinded into powder, as shown in Figure 1 and then were sieved using sieve No. 100 to avoid particles with a diameter of more than 0.15 mm.

**2.1.2. Modified Binder Preparation.** The base asphalt binder used was PG 58-28, and the properties of the virgin asphalt binder are shown in Table 2. The base asphalt binder of 300 g was heated until it becomes fluid then the geopolymer was added into the base asphalt blend with doses of 3%, 6%, and 9% by mass of the asphalt binder. Subsequently, the blends were mixed using a mechanical shear mixer for 120 minutes under a speed of 2000 r/min with a temperature of 150°C ± 5 to produce a homogenous blend, as depicted in Figure 2.

### 3. Experimental Test Procedures

**3.1. Rotational Viscometer Test.** The viscosity of virgin and modified asphalt binder was measured using the rotational viscometer with 10 g of asphalt binder. Three readings were determined for each test temperature, and the average was recognized as the test result. Also, the test temperatures ranged from 90°C to 165°C and using 15°C as an interval.

**3.2. Dynamic Shear Rheometer (DSR) Test.** The dynamic shear rheometer (DSR) is used to study the rheological behavior of asphalt binder at intermediate and high

temperatures. Moreover, DSR measures the complex shear modulus ( $G^*$ ) and the phase angle ( $\delta$ ) of asphalt binder at different temperatures and frequencies of loading, as per AASHTO T315. In this study, DSR-frequency sweep test was performed for the virgin and modified binders using a 25-mm and 8-mm diameter plate and a 1 mm and 2 mm gap, respectively. The tests were performed at sixteen frequencies ranging from 0.159 Hz to 15 Hz while the test temperatures ranged from 11 to 35°C (intermediate temperature) and from 40 to 64°C (high temperature). In this study, sinusoidal shear strains were conducted on asphalt binder samples by placing the samples between two parallel plates, one plate is fixed, and another one is moving freely. Then, the various frequencies are applied under several temperatures. Sinusoidally changing shear strain is expressed as [27, 28]

$$\gamma(t) = \gamma_0 \sin \omega t, \quad (1)$$

with resulting stress

$$\tau(t) = \tau_0 \sin(\omega t + \delta), \quad (2)$$

where  $\gamma_0$  is the peak strain,  $\tau_0$  is the peak stress,  $\omega$  is the radian frequency,  $\delta$  is the phase angle, and  $t$  is the time.

After changing the phase by  $\pi/2$ ,

$$\begin{aligned} \gamma^* &= \gamma_0 e^{i\omega t}, \\ \tau^* &= \tau_0 e^{i(\omega t + \delta)}. \end{aligned} \quad (3)$$

Then, the complex shear modulus is determined by the following equation:

$$\begin{aligned} G^* &= G' + iG'' = \frac{\tau^*}{\gamma^*} = \frac{\tau_0 e^{i(\omega t + \delta)}}{\gamma_0 e^{i\omega t}} = \left(\frac{\tau_0}{\gamma_0}\right) e^{i\delta} \\ &= \left(\frac{\tau_0}{\gamma_0}\right) (\cos \delta + i \sin \delta). \end{aligned} \quad (4)$$

Equation (4) shows that

$$|G^*| = \frac{\tau_0}{\gamma_0} = \sqrt{G'^2 + G''^2}, \quad (5)$$

$$G' = |G^*| \cos \delta,$$

which is called storage modulus,

$$G'' = |G^*| \sin \delta, \quad (6)$$

which is called loss modulus.

$$\tan \delta = \frac{G''}{G'}. \quad (7)$$

The DSR results were used to construct the master curves, isochronal plots, and rutting figures. Also, the failure temperatures were also determined from the DSR-grading test. The development of the master curve helps to make a comparison between the stiffness of asphalt binder over different ranges of temperatures and frequencies. In order to obtain the master curve, a shift factor should be applied to

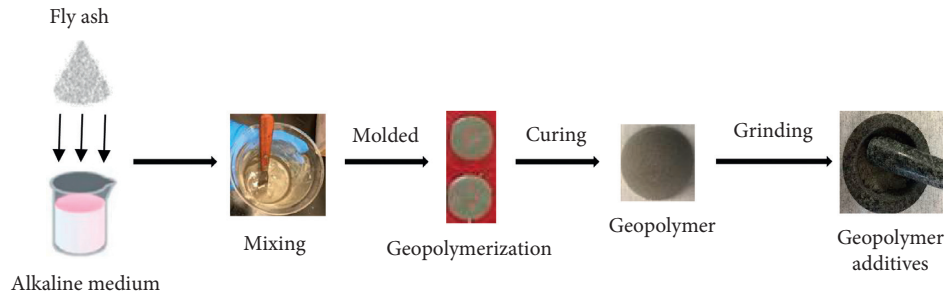


FIGURE 1: Preparation of geopolymer additives.

TABLE 2: Properties of original asphalt binder.

Index	Conditions (°C)	Unit	Results	Requirements
Specific gravity	At 15		1.03	—
Brookfield viscosity	At 135	Pa·s	0.275	3.0 max
Flash point	—	°C	230+	230 min
$G^*/\sin(\delta)$	At 58	kPa	1.195	1.0 min

the experimental complex modulus ( $G^*$ ) and phase angle ( $\delta$ ) values in order to normalize them to a reference temperature. The master curve can be developed using a specified reference temperature and applying a relationship between complex modulus and frequency [29].

**3.3. Environmental Scanning Electron Microscopy (ESEM).** ESEM is a microscope that uses high-pressure gas in a chamber to examine a relatively natural state in which materials are scanned analogously to a standard SEM without routine preparation for compatibility [30]. The model of ESEM unit used to test the specimens was FEI Quanta 250 FEG, as shown in Figure 3.

A stainless-steel sample mold design was developed recently in the Centre for Pavement and Transportation Technology (CPATT) with an 8 mm diameter [31], as depicted in Figure 3.

## 4. Results and Discussion

**4.1. Effects of Geopolymer on Viscosity.** The rotational viscosity of asphalt binder is considered an important index to assess the workability for asphalt binder. Hence, determination of the adequate asphalt binder mixing temperature and compaction is significantly impacted by the geopolymer content. The percentage of geopolymers significantly affects the viscosity of the asphalt binder [23]. Figures 3 and 4 show the average viscosity of asphalt binder with different percentages of geopolymer (0, 3, 6, and 9%).

The virgin binder was characterized by the lowest viscosity, whereas the modified asphalt binder sample with 9% of geopolymer has the highest viscosity which indicates that 9% of geopolymer has better performance regarding rutting resistance. However, using the statistical  $T$ -test to compare

the viscosity of virgin binder and binder with 9% geopolymer at temperatures ranging from 90°C to 165°C resulted in the insignificant difference at 95% confidence level with a  $P$ -value of 0.126. It was noted that the viscosity of the 9% modified binder was higher than that of the virgin binder by 51% at 90°C. The difference between the viscosity of the two binders vanishes at higher temperatures as shown in Figure 4.

The increase in binder viscosity due to the addition of geopolymer materials was reported by previous scholars [1, 28, 32]. Asphalt binders with high viscosity achieve excellent weather resistance and provide strong binding forces between aggregates. In addition, asphalt binders with high viscosity have better resistance to displacement by water than those of low viscosity [33]. The viscosity results of asphalt binder with 3, 6, and 9% geopolymer content fell below the maximum limit of 3 Pa·s at the temperature of 135°C according to the Superpave specifications.

Figure 5 shows the viscosity of asphalt binder samples with 9% geopolymer and conditioned at curing times of 2, 7, and 14 days. Figure 6 presents the viscosity data through two stages. In stage one, the viscosity of both virgin and modified binders with various curing times was subjected to immediate reduction as the temperature increased from 90 to 120°C. The highest viscosity was noted in the modified binder with 7- and 14-day curing time. Stage two witnessed a temperature change from 120°C to 165°C. The results of stage two show that the modified binders still were characterized by higher viscosity compared with the virgin binder.

The statistical analysis of the 9% geopolymer-modified binder confirmed that the curing time period does not have a significant impact on the viscosity. The 2-day curing period was considered the control curing period. The 7-day and 14-day curing period viscosity results were compared with the 2-day curing period to check the impact of curing period on viscosity. The statistical  $T$ -test resulted in  $P$ -values of 0.19 and 0.2 for the viscosity of 7-day and 14-day curing periods compared with the control curing period (2-days). Therefore, the additional curing time has an insignificant impact on viscosity. It should be noted that the percentage increase in viscosity was 30% by increasing the curing period from 2 to 7 days. The viscosity showed 0% change between 7 and 14 day curing periods. Therefore, extending the curing period beyond 7 days will not result in a significant change in the

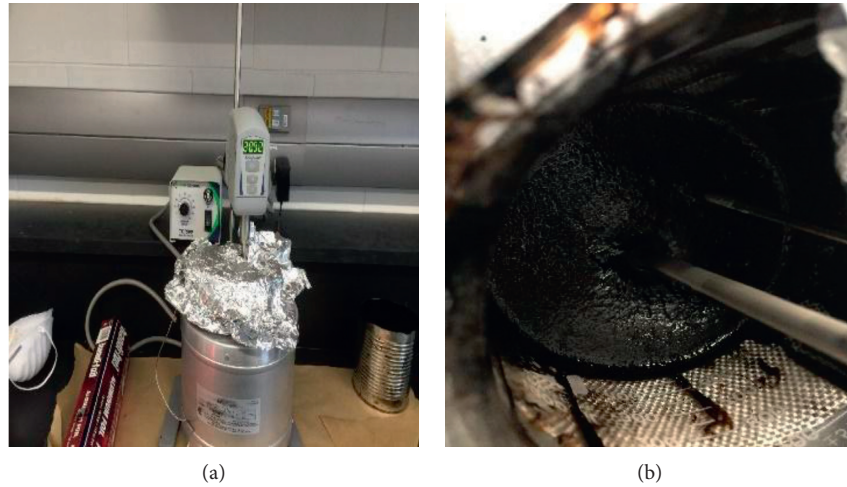


FIGURE 2: Mechanical shear mixer.

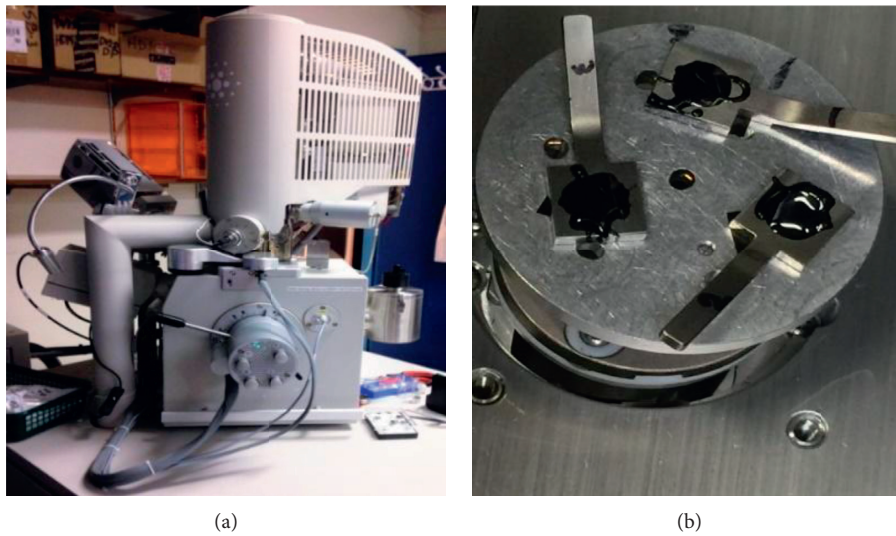


FIGURE 3: ESEM device (a) and sample mould with binder in the ESEM stage (b).

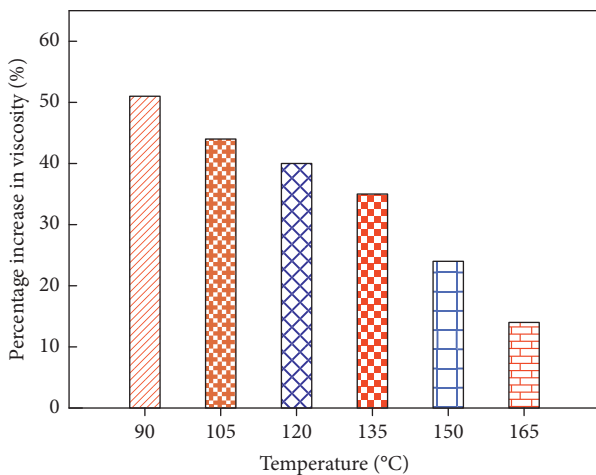


FIGURE 4: Percentage increase of viscosity comparing the 9% geopolymer-modified binder to the virgin binder.

viscosity of geopolymer modified binders, which confirms the findings from [13, 17, 34, 35].

#### 4.2. Effects of Geopolymer on Rheological Properties

4.2.1. *Rheological Master Curve.* Figures 7(a) and 7(b) present the rheological master curve at a reference temperature of 35°C for complex shear modulus and phase angle. Figure 7(a) showed the insignificant difference between the complex shear modulus of modified asphalt binder with 6 and 9% of geopolymer. Airey [1] studied the rheological behavior of styrene butadiene styrene (SBS) modified binder with 3%, 5%, and 7% of geopolymer and reported an increase in complex shear modulus with increasing the modifier percentages. Based on results obtained from specimens tested in CPATT, an increase of geopolymer percentage above 6% did not have a significant impact on

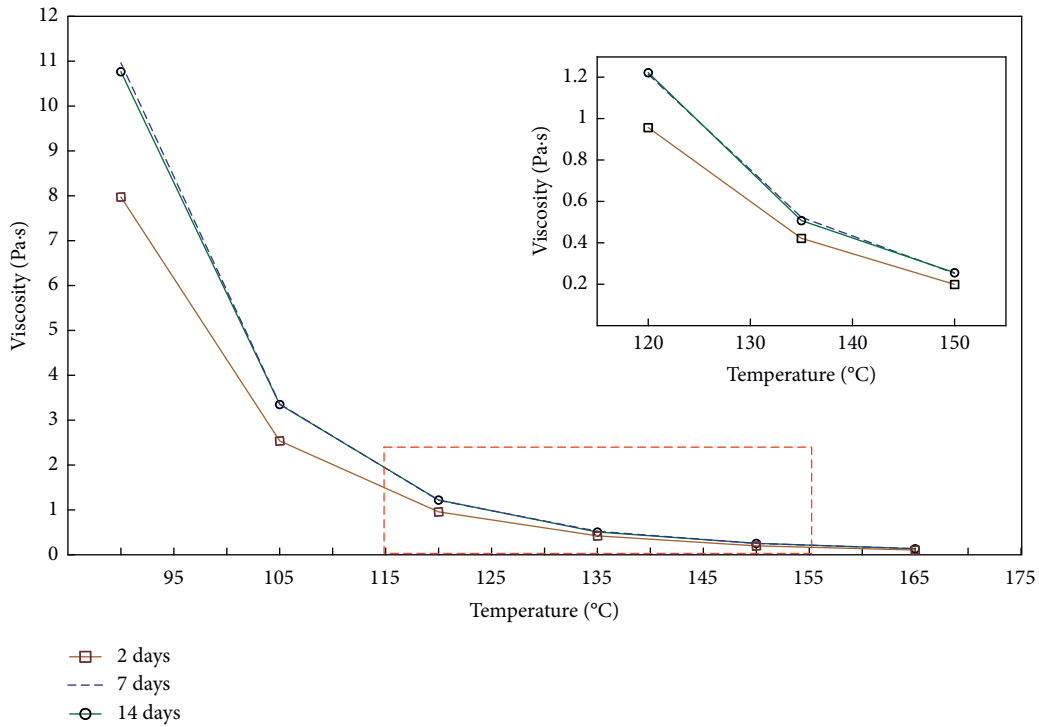


FIGURE 5: Effects of curing time on asphalt binder viscosity for 9% of geopolymer.

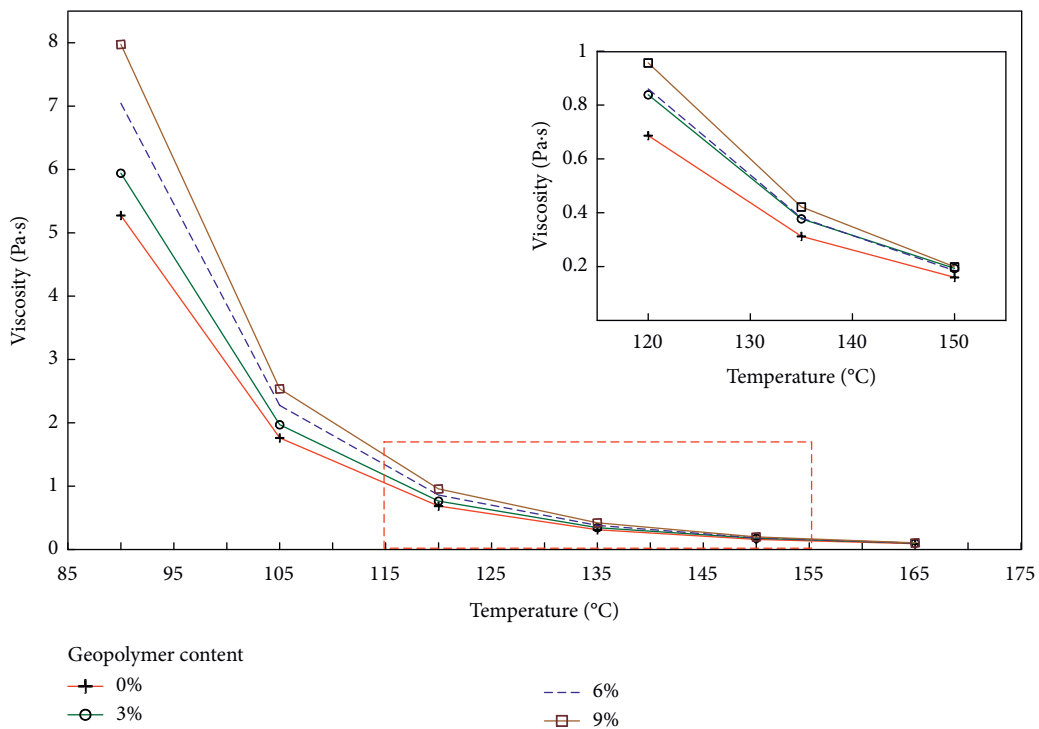


FIGURE 6: Asphalt binder viscosity changing with the temperature at different geopolymer additives.

complex shear modulus. For example, the complex shear modulus at 10 Hz increased by 127%, 214%, and 224% through adding 3, 6, and 9% geopolymers, respectively, compared to the virgin binder.

Figure 7(b) shows that the phase angle at 10 Hz decreased by 2.9%, 5.3%, and 6% due to increasing the geopolymer percentages 3, 6, and 9%, respectively, compared with the virgin binder. This indicates an increase in the elastic response of the

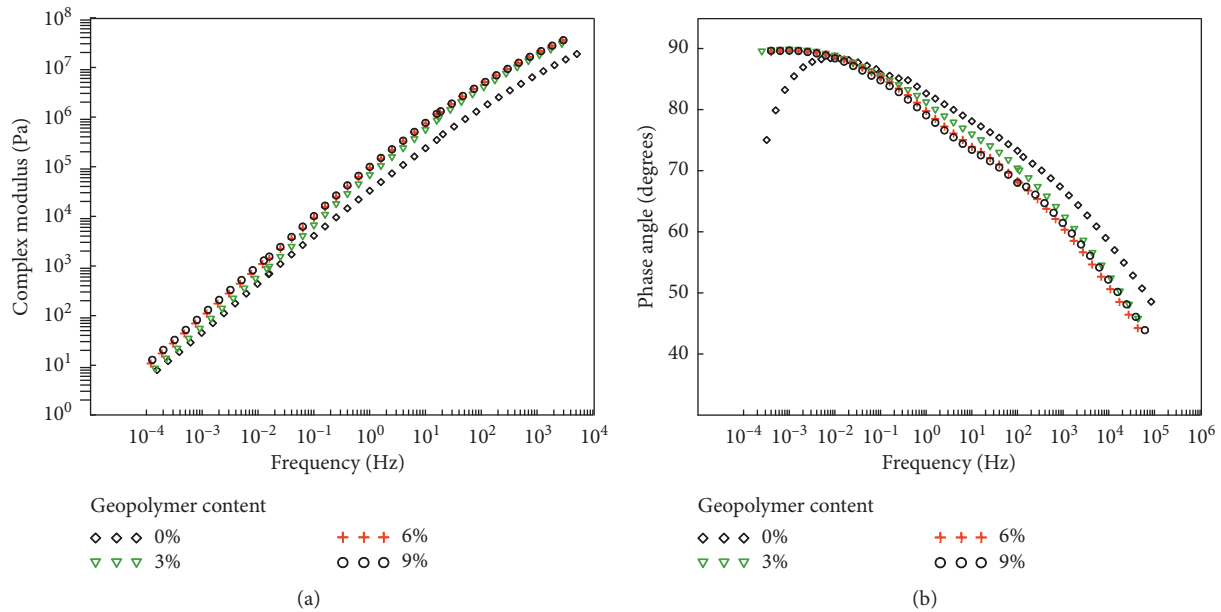


FIGURE 7: Rheological master curve at 35°C for (a) complex modulus and (b) phase angle.

modified binder. Therefore, the elasticity of the modified binder increased along with the increasing of geopolymer additives.

**4.2.2. Isochronal Plot.** Isochronal plots of complex shear modulus ( $G^*$ ) and phase angle versus temperature at 1 Hz and 0.1 Hz of frequency are shown in Figures 8(a) and 8(b). The results presented in Figures 8(a) and 8(b) show that the complex shear modulus significantly increases at various temperatures (59% average increase) by adding 3% geopolymers compared with the virgin binder. The statistical  $t$ -test resulted in a  $P$ -value of 0.003. Therefore, the addition of 3% geopolymers results in a statistically significant increase in complex shear modulus with a confidence level of 95%. However, the insignificant difference is noticed by comparing the complex modulus at 6% and 9% geopolymer modified samples compared with the 3% geopolymer-modified. The  $P$ -values for the 6% and 9% geopolymer modified compared with the 3% are 0.098 and 0.104, respectively. This indicates that the temperature susceptibility is improved. Previous research literature reported temperature susceptibility increase for elastomer modified binders such as epoxidized natural rubber [28] and styrene butadiene styrene (SBS) [1].

**4.2.3. Rutting Factor.** Rutting is a permanent deformation which occurs at temperatures higher than 40°C, leading to ruts in the direction of traffic and can be relevant to the viscosity of the asphalt binder [36]. Figure 9 shows the effect of temperature on the rutting factor ( $G^*/\sin \delta$ ), which represents a measure of the high-temperature stiffness of the asphalt binder's response to repeated load application at high temperatures. According to the Superpave specification, the rutting factor must be a minimum 1.0 kPa for the unaged binder at 10 rad/sec. This specification is set to

minimize the contribution of the asphalt binder to rutting. The results showed that the rutting factor increased by increasing the geopolymer additives which indicates that rutting resistance is improved. The same result for different binder modifiers is also recorded in previous studies [28, 37]. For example, the rutting factor at 58°C increased by 22%, 58.2%, and 86.6% through adding 3, 6, and 9% of geopolymers by mass respectively, compared with the virgin binder.

**4.3. Effects of Geopolymer on Performance Grading.** Figures 10(a) and 10(b) show the results of failure temperature obtained from the DSR-grading test. Figure 10(a) shows that the virgin binder has the lowest failure temperature nearly 60.6°C compared with geopolymer-modified binder with various percentages. Addition of 3%, 6%, and 9% of geopolymers resulted in an increase of 1.98%, 5.78%, and 8.58% in the failure temperature, respectively. This indicates that the geopolymer could be used to increase the high-temperature grading of asphalt binder. Figure 6(b) shows the results of 9% modified binder with curing time 2, 7, and 14 days. The figure shows that failure temperature for 2, 7, and 14-day curing time exceeded that of the virgin binder by 8.58%, 14.2%, and 15.2%, respectively.

**4.4. Effects of Geopolymer on the Microstructure of the Binder.** ESEM technology was used to observe the polymer-modified asphalt binder microstructure [31, 38]. Stangl et al. [38] used ESEM to investigate the microstructure of asphalt binder with and without modifiers in aged and unaged conditions. The results indicated that aging has a significant effect on the microstructure of asphalt binder, whereby RTFOT-aging caused the network structures to become coarser. Meanwhile, Mikhailenko et al. [30] noted that the denser the

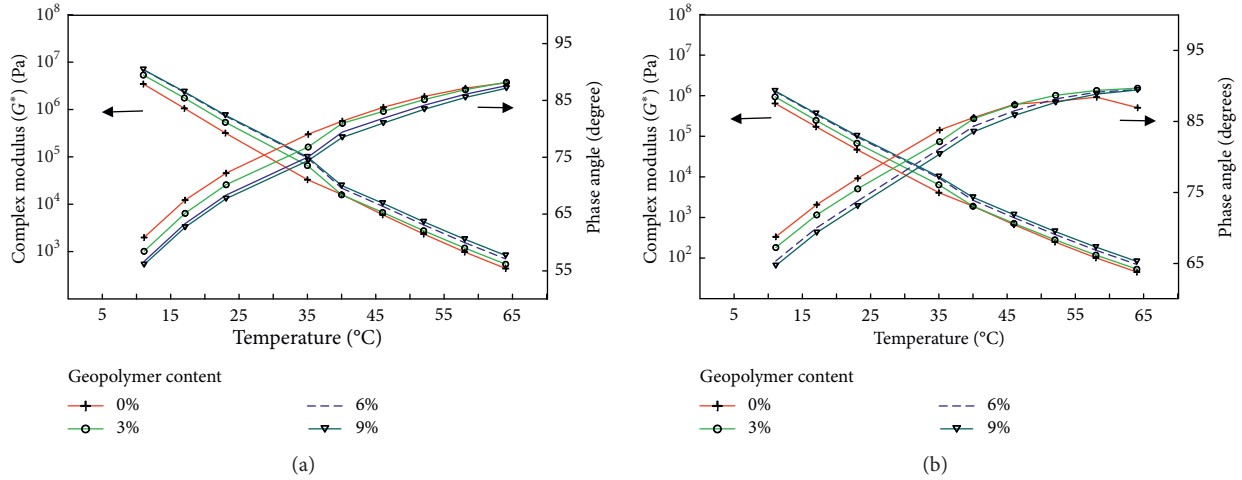


FIGURE 8: Isochronal plots of the complex modulus and phase angle at (a) 1 Hz and (b) 0.1 Hz.

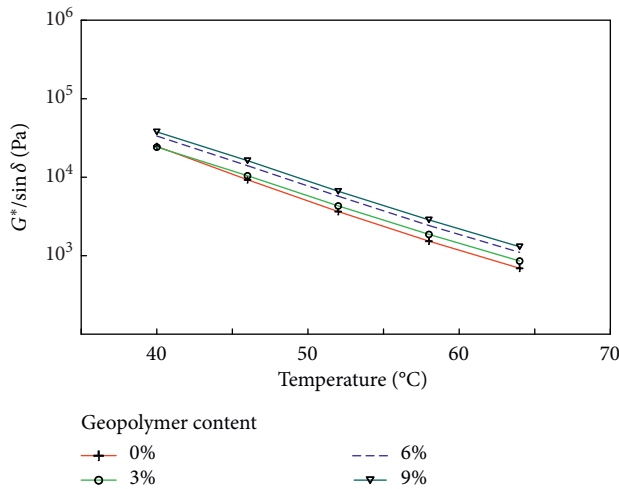


FIGURE 9: Temperature effect on rutting factor ( $G^*/\sin \delta$ ).

structure of the fibrils in ESEM imaging, the stiffer the binder is.

In this investigation, ESEM was used to study the microstructure of asphalt binder with different percentages of geopolymer, 3, 6 and 9%. It is noted that the microstructure of the asphalt binder with 0% of geopolymer matches the microstructure reported by Mikhailenko et al. [39]; whereas, there is no significant effect of adding 3, 6, and 9% of geopolymer on the structure of the fibrils in ESEM imaging. In addition, the nanoparticles of the geopolymer were observed under ESEM, as shown in Figure 11. The examination of the ESEM images indicates that the nanoparticles are well dispersed in the binder, and that the microstructures of the binders with 3, 6, and 9% of geopolymer are quite homogeneous without any visible agglomerations of the geopolymers in the binder.

*4.5. Economic and Environmental Effects of Geopolymer.* Because of its critical impact on the growth of countries' economics, governments tend to facilitate considerable

budgets to improve road-infrastructures. As a result of its severe weather and high traffic load conditions, it is worth nothing that Canada spends millions annually for maintenance of deteriorated pavements for road-infrastructure. Asphalt binder is the world's most commonly used pavement materials, however, is facing several highly sensitive financial and environmental issues. The manufacture of asphalt binder consumes a lot of energy that involves the emission of  $\text{CO}_2$  into the atmosphere. Greenhouse gas (GHG) emissions must be decreased 50 to 80% by 2050 in order to limit the global temperature increase to  $2^\circ\text{C}$  which is considered a challenge to achieve reductions of this magnitude [40]. Meanwhile, Ma et al. [41] noted that reducing (GHG) emission from the construction of asphalt pavement should be focused on the manufacturing stage of raw materials and the mixing process of asphalt concrete. Thus, reducing the usage of the high amount of asphalt binder and decreasing the energy amount during the preparation of hot mix asphalt would have potential financial and environmental effects. Recently, there is a tendency to enhance the asphalt rheological properties using by-product and waste materials that have increased the world over in the last few decades.

It is well known, however, that the potential development of geopolymer has a significant effect on reducing waste and by-product materials, such as fly ash, red mud, mine waste, and blast furnace slag. Into the bargain, using geopolymer as an asphalt modifier has proven its efficiency to improve the rheological properties of asphalt binders thereby enhancing the rutting resistance that results in a reduction of pavement deterioration. Consequently, the reduction in the  $\text{CO}_2$  emission increases, as a result of decreasing in the production amount of asphalt binder. Thus, the geopolymers have significant economical and environmental impacts on the construction of asphalt pavement. Table 3 summarizes the effect of the geopolymer contents on the viscosities; at 135 and 165°C, and the compaction and mixing temperature ranges of asphalt mixture.

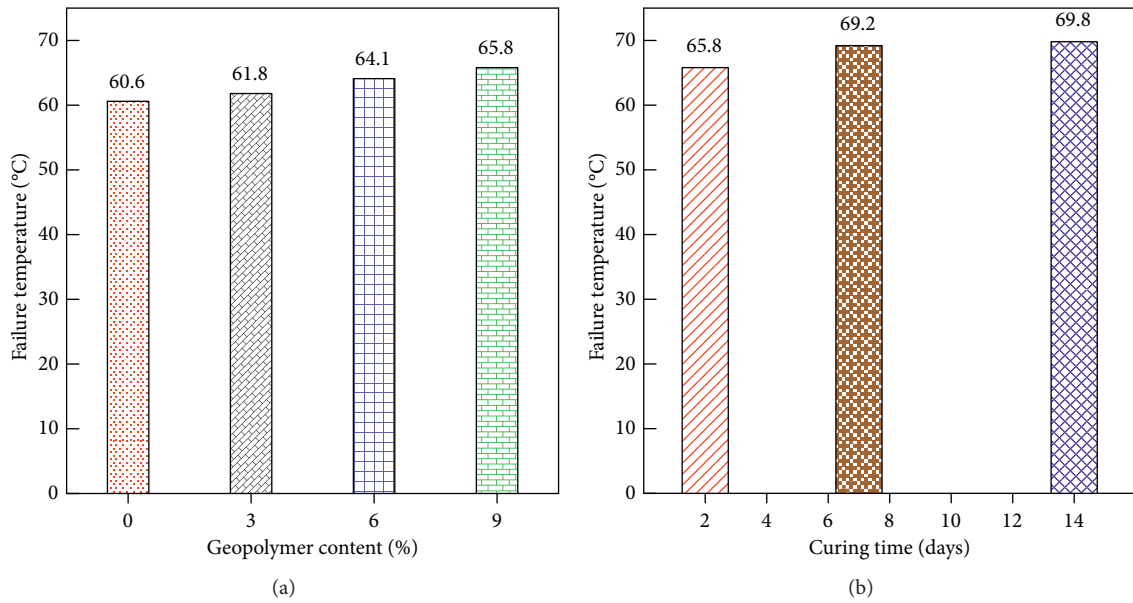


FIGURE 10: Effects of geopolymer on performance grading, (a) effects of geopolymer additives, (b) effects of curing time on 9% of geopolymer.

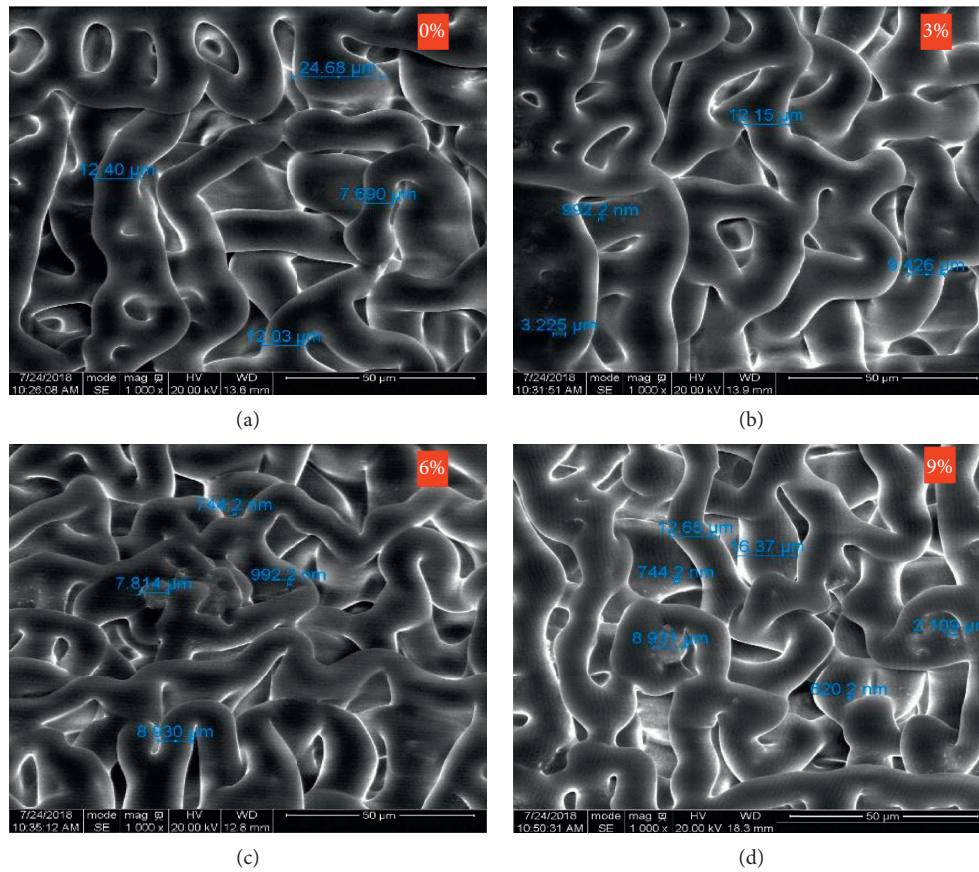


FIGURE 11: ESEM observation of different percentage of geopolymer.

The results revealed a minor effect on the compaction and mixing temperature ranges for modified asphalt binder; in comparison with a virgin asphalt binder. However, a

slight increase is observed in temperature of compaction and mixing processes for modified asphalt binder, for the curing times; for 9% of geopolymer at 7 and 14 days. In overall, we

TABLE 3: Geopolymer effects on compaction and mixing temperature.

Geopolymer content (%)	Curing time (days)	Viscosity (Pa·s)		Compaction range (°C)	Mixing range (°C)
		@135°C	@165°C		
0	2	0.313	0.1	135–140	148–154
3	2	0.345	0.1	138–142	149–154
6	2	0.381	0.1	138–143	149–154
	2	0.422	0.106	140–144	150–155
9	7	0.523	0.137	144–148	154–160
	14	0.508	0.135	144–148	154–159

can draw the conclusion that the geopolymer application in asphalt binder has minor effects on the compaction and mixing temperatures which imply that there is a minor impact on the energy-consuming during compaction and mixing processes for asphalt mixtures.

## 5. Conclusion

Geopolymer was used in many disciplines such as soil and concrete to develop the mechanical properties rapidly and to improve the high fire resistance property. However, the geopolymer is not widely used to enhance the rheological properties of asphalt binder or mixture. Geopolymer could be used as a sustainable and greener alternative to other asphalt modifiers due to its low carbon dioxide footprint and effective by-products/waste better recycling capacity. This paper presented a laboratory study to investigate the effects of geopolymer content on the rheological and microstructure properties of asphalt binder. The following conclusions have been drawn:

- (i) Geopolymer additives had a notable impact on the rheological behavior of asphalt binder. It increased the temperature susceptibility by 1.98%, 5.78%, and 8.58% through adding 3, 6, and 9% geopolymers, respectively. The shear modulus of the modified asphalt binder was increased, and the phase angle was reduced through adding 3, 6, and 9% geopolymers.
- (ii) The rutting factor, at 10 rad/sec and at 58°C, increased by 22%, 58.2%, and 86.6% through adding 3, 6, and 9% of geopolymers by mass of the binder respectively, compared with the virgin binder which indicates that rutting resistance is improved.
- (iii) Geopolymer gained its ultimate properties during the first 7 days, and the curing time crucially impacts the geopolymerization process. The highest increase of failure temperature was for 7- and 14-day curing time with an improvement of 14.2 and 15.2%, respectively which indicates that the geopolymer could be used to increase the high-temperature grading of asphalt binder.
- (iv) The nanoparticles appear to be well dispersed in the binder. The use of geopolymer does not seem to affect the microstructure of the binder.

## Data Availability

The data used to support the findings of this study are available from the corresponding author upon request. All tests were performed in the Centre for Pavement and Transportation Technology (CPATT), University of Waterloo, under supervision of Prof. Hassan Baaj.

## Conflicts of Interest

The authors declare that they have no conflicts of interest.

## References

- [1] G. Airey, "Rheological properties of styrene butadiene styrene polymer modified road bitumens," *Fuel*, vol. 82, no. 14, pp. 1709–1719, 2003.
- [2] H. Baaj, H. Di Benedetto, and P. Chaverot, "Effect of Binder Characteristics on Fatigue of Asphalt Pavement Using an Intrinsic Damage Approach," *Road Materials and Pavement Design*, vol. 6, no. 2, pp. 147–174, 2005.
- [3] M. Aurilio, P. Mikhailenko, H. Baaj, and L. Polikakos, "Properties of asphalt binders with increasing SBS polymer modification," in *Proceedings of the 5th International Symposium on Asphalt Pavement and Environment (APE)*, Padua, Italy, September 2019.
- [4] S. Saoula, K. A. Mokhtar, H. Haddadi, and E. Ghorbel, "Improvement of the stability of a modified bituminous binders within eva," *International Journal of Applied Engineering Research*, vol. 3, no. 4, pp. 575–584, 2008.
- [5] S. Liu, W. Cao, J. Fang, and S. Shang, "Variance analysis and performance evaluation of different crumb rubber modified (CRM) asphalt," *Construction and Building Materials*, vol. 23, no. 7, pp. 2701–2708, 2009.
- [6] S. F. Brown, "Discussion: mechanical properties of bituminous materials for pavement design," *Journal of International Asphalt Technology*, vol. 35, pp. 11–13, 1989.
- [7] F. Moreno-Navarro, M. Rubio-Gómez, E. Tomás-Fortún, F. Valor-Hernández, and A. Ramírez-Rodríguez, "Evaluation of the fatigue macro-cracking behavior of crumb rubber modified bituminous mixes," *Materiales de Construcción*, vol. 64, no. 315, p. e027, 2014.
- [8] F. Cheriet, K. Soudani, and S. Haddadi, "Influence of natural rubber on creep behavior of bituminous concrete," *Procedia—Social and Behavioral Sciences*, vol. 195, pp. 2769–2776, 2015.
- [9] M. N. Borhan, F. Suja, A. Ismail, and R. A. Rahmat, "Used cylinder oil modified cold mix asphalt concrete," *Journal of Applied Science*, vol. 7, no. 22, pp. 3485–3491, 2007.

- [10] M. N. Borhan, A. Ismail, and R. A. Rahmat, "Evaluation of Palm oil Fuel ash (POFA) on asphalt mixture," *Australian Journal of Basic and Applied Sciences*, vol. 4, no. 10, pp. 5456–5463, 2010.
- [11] J. Davidovits, "Geopolymers: inorganic polymeric new materials," *Journal of Thermal Analysis*, vol. 37, no. 8, pp. 1633–1656, 1991.
- [12] G. Görhan and G. Kürklü, "The influence of the NaOH solution on the properties of the fly ash-based geopolymer mortar cured at different temperatures," *Composites Part B: Engineering*, vol. 58, pp. 371–377, 2014.
- [13] R. Shadnia, L. Zhang, and P. Li, "Experimental study of geopolymer mortar with incorporated PCM," *Construction and Building Materials*, vol. 84, pp. 95–102, 2015.
- [14] J. Davidovits, "Global warming impact on the cement and aggregates industries," *World Resource Review*, vol. 6, no. 2, pp. 263–278, 1994.
- [15] J. T. Gourley and G. B. Johnson, "Developments in geopolymer precast concrete," in *Proceedings of the International Workshop on Geopolymers and Geopolymer Concrete*, Perth, Australia, July 2005.
- [16] S. E. Wallah and B. V. Rangan, *Low-Calcium Fly Ash-Based Geopolymer Concrete: Long-Term Properties*, Curtin University of Technology, Perth, Australia, 2006.
- [17] B. Rangan, "Fly ash- based geopolymer concrete," in *Proceedings of the International Workshop on Geopolymer Cement and Concrete*, Mumbai, India, December 2010.
- [18] J. Davidovits, *Geopolymer Chemistry and Applications*, Institut Géopolymère, Saint-Quentin, France, 4th edition, 2015.
- [19] H. E. Elyamany, A. E. M. Abd Elmoaty, and A. M. Elshaboury, "Magnesium sulfate resistance of geopolymer mortar," *Construction and Building Materials*, vol. 184, pp. 111–127, 2018.
- [20] D. M. J. Sumajouw, D. Hardjito, S. E. Wallah, and B. V. Rangan, "Fly ash-based geopolymer concrete: study of slender reinforced columns," *Journal of Materials Science*, vol. 42, no. 9, pp. 3124–3130, 2007.
- [21] N. Cristelo, S. Glendinning, T. Miranda, D. Oliveira, and R. Silva, "Soil stabilisation using alkaline activation of fly ash for self compacting rammed earth construction," *Construction and Building Materials*, vol. 36, pp. 727–735, 2012.
- [22] P. Sukmak, S. Horpibulsuk, S.-L. Shen, P. Chindaprasirt, and C. Suksiripattanapong, "Factors influencing strength development in clay-fly ash geopolymer," *Construction and Building Materials*, vol. 47, pp. 1125–1136, 2013.
- [23] N. Tang, Z. Deng, J.-G. Dai, K. Yang, C. Chen, and Q. Wang, "Geopolymer as an additive of warm mix asphalt: preparation and properties," *Journal of Cleaner Production*, vol. 192, pp. 906–915, 2018.
- [24] ASTM, *Standard Specification for Coal Fly Ash and Raw or Calcined Natural Pozzolan for Use in Concrete*, ASTM, West Conshohocke, PA, US, 2018.
- [25] J. T. Gourley, "Geopolymers; opportunities for environmentally friendly construction materials," in *International Conference and Exhibition on Adaptive Materials for a Modern Society*, The Institute of Materials Engineering Australasia Ltd., Melbourne, Australia, 2003.
- [26] H. Xu and J. S. J. Van Deventer, "The geopolymerisation of alumino-silicate minerals," *International Journal of Mineral Processing*, vol. 59, no. 3, pp. 247–266, 2000.
- [27] X. Lu and U. Isacsson, "Rheological characterization of styrene-butadiene-styrene copolymer modified bitumens," *Construction and Building Materials*, vol. 11, no. 1, pp. 23–32, 1997.
- [28] R. A. Al-Mansob, A. Ismail, A. N. Alduri, C. H. Azhari, M. R. Karim, and N. I. M. Yusoff, "Physical and rheological properties of epoxidized natural rubber modified bitumens," *Construction and Building Materials*, vol. 63, pp. 242–248, 2014.
- [29] T. R. Clyne, X. Li, M. O. Marasteanu, and E. L. Skok, *Dynamic and Resilient Modulus of Mn/DOT Asphalt Mixtures*, Minnesota Department of Transportation, Saint Paul, MN, USA, 2003.
- [30] P. Mikhailenko, C. Kou, H. Baaj et al., "Comparison of ESEM and physical properties of virgin and laboratory aged asphalt binders," *Fuel*, vol. 235, pp. 627–638, 2019.
- [31] P. Mikhailenko, C. Kou, H. Baaj, and S. Tighe, "Observation of polymer modified asphalt microstructure by ESEM," in *Proceedings of the 6th International Conference on Engineering Mechanics and Materials*, Canada, Vancouver, May 2017.
- [32] A. K. Swamy, U. D. Rongali, and P. K. Jain, "Effect of HDPEH polymer on viscoelastic properties of SBS modified asphalt," *Construction and Building Materials*, vol. 136, pp. 230–236, 2017.
- [33] M. A. Taylor and N. P. Khosla, *Stripping of Asphalt Pavements: State of the Art*, Transportation Research Record Journal of the Transportation Research Board, Washington, DC, USA, 1983.
- [34] L. Zhang, S. Ahmari, and J. Zhang, "Synthesis and characterization of fly ash modified mine tailings-based geopolymers," *Construction and Building Materials*, vol. 25, no. 9, pp. 3773–3781, 2011.
- [35] S. Ahmari, L. Zhang, and J. Zhang, "Effects of activator type/concentration and curing temperature on alkali-activated binder based on copper mine tailings," *Journal of Materials Science*, vol. 47, no. 16, pp. 5933–5945, 2012.
- [36] A. Adedeji, T. Grünfelder, F. S. Bates, C. W. Macosko, M. Stroup-Gardiner, and D. E. Newcomb, "Asphalt modified by SBS triblock copolymer: structures and properties," *Polymer Engineering & Science*, vol. 36, no. 12, pp. 1707–1723, 1996.
- [37] A. Khadivar and A. Kavussi, "Rheological characteristics of SBR and NR polymer modified bitumen emulsions at average pavement temperatures," *Construction and Building Materials*, vol. 47, pp. 1099–1105, 2013.
- [38] K. Stangl, A. Jäger, and R. Lackner, "Microstructure-based identification of bitumen performance," *Road Materials and Pavement Design*, vol. 7, no. 1, pp. 111–142, 2006.
- [39] P. Mikhailenko, H. Baaj, C. Kou et al., "ESEM microstructural and physical properties of virgin and laboratory aged bitumen," in *RILEM 252-CMB-Symposium on Chemo Mechanical Characterization of Bituminous Materials*, pp. 150–155, Springer, Cham, Switzerland, 2018.
- [40] A. I. Kay, R. B. Noland, and C. J. Rodier, "Achieving reductions in greenhouse gases in the US road transportation sector," *Energy Policy*, vol. 69, pp. 536–545, 2014.
- [41] F. Ma, A. Sha, R. Lin, Y. Huang, and C. Wang, "Greenhouse gas emissions from asphalt pavement construction: a case study in China," *International Journal of Environmental Research and Public Health*, vol. 13, no. 3, p. 351, 2016.

## Research Article

# Antiageing Performance Evaluation of Recycled Engine Oil Bottom Used in Asphalt Rejuvenation

Miaozhang Yu <sup>1</sup>, Jin Li <sup>1</sup>, Xinzhuang Cui,<sup>1,2</sup> Dedong Guo,<sup>1</sup> and Xinjun Li<sup>1</sup>

<sup>1</sup>School of Transportation Civil Engineering, Shandong Jiaotong University, Jinan 250357, Shandong, China

<sup>2</sup>School of Civil Engineering, Shandong University, Jinan 250061, Shandong, China

Correspondence should be addressed to Miaozhang Yu; [sdjnyumz@163.com](mailto:sdjnyumz@163.com) and Jin Li; [sdzblijin@163.com](mailto:sdzblijin@163.com)

Received 13 May 2019; Revised 6 August 2019; Accepted 26 August 2019; Published 30 September 2019

Guest Editor: Quantao Liu

Copyright © 2019 Miaozhang Yu et al. This is an open access article distributed under the Creative Commons Attribution License, which permits unrestricted use, distribution, and reproduction in any medium, provided the original work is properly cited.

To comprehensively evaluate the antiageing performance of recycled engine oil bottom (REOB) used in asphalt rejuvenation, ageing performance studies were carried out on REOB, REOB-rejuvenated asphalt, and REOB-rejuvenated asphalt mixture. The thin film oven test (TFOT) results of REOB and a professional regenerant, RA5, were compared to verify the ageing resistance of REOB as an asphalt regenerant. The quality and viscosity of REOB-rejuvenated asphalt, RA5-rejuvenated asphalt, and base asphalt were measured after extended TFOT (ageing times for 5 h, 10 h, 15 h, 20 h, and 25 h), and the low-temperature performance of three aged asphalts was evaluated by bending beam rheological tests. The corresponding three kinds of asphalt mixtures were used to design and pave surface layers of a full-scale indoor test road. The long-term fatigue performance of indoor asphalt pavement was investigated by a self-developed rotary accelerated loading test (RALT) system. The results show that when used as an asphalt regenerant, REOB meets the antiageing requirements listed in the technical specification. The short-term (TFOT ageing time less than or equal to 10 h) ageing resistance of REOB-rejuvenated asphalt is better than that of RA5-rejuvenated asphalt but worse than that of base asphalt, whereas the long-term (TFOT ageing time greater than or equal to 15 h) ageing resistance of REOB-rejuvenated asphalt is the worst among the three tested asphalts. After long-term ageing, REOB-rejuvenated asphalt is prone to cracking at low temperatures because of its rapid increase in stiffness and sharp decrease in stress relaxation performance. Increasing temperatures increases the deflection value of asphalt pavement as the number of loading cycles increase. High-temperature ageing significantly aggravates the increase of the deflection value of REOB-rejuvenated asphalt pavement under RALT long-term loading, which makes it most prone to fatigue failure among the three pavements. Therefore, the above test results show that REOB used in asphalt pavement rejuvenation is prone to premature and excessive damage.

## 1. Introduction

At present, the development of asphalt pavement in China has entered the stage of both construction and maintenance. Asphalt pavement recycling technology has become a popular research area for roads because of the ability to recycle large amounts of reclaimed asphalt pavement (RAP) materials generated in the maintenance and repair of asphalt pavement, save ore and asphalt resources, and reduce construction costs. The key to recycling RAP materials is adding appropriate regenerants to rejuvenate the aged asphalt in RAP materials. In the market, professional regenerants are not only generally expensive but also consume

many resources and even cause environmental pollution, which is contrary to the concept of green and sustainable development of asphalt pavement recycling technology. Therefore, the development of new economical and green asphalt regenerants is urgently needed.

China's transportation industry produces 25 to 30 million tons of recycled engine oil (REO) every year [1]. Generally, 70–80% of REO can be effectively recycled through regeneration processes, such as distillation-clay refining or distillation-hydrogenation [2, 3]. However, the remaining residue (accounting for 20–30%) cannot be effectively recycled due to the presence of many impurities; this residue is called recycled engine oil bottom (REOB).

Currently, REOB is mostly treated by discarding, burying, or burning, which causes substantial environmental pollution. To realize the resource reutilization of REOB, based on the similarity and compatibility between REOB and asphalt, research on the use of REOB in asphalt materials has begun at home and abroad. Many relevant patents have been reported on the use of REOB in different asphalt structural layers [4, 5]. However, Hesp and Shurvell [6, 7] found that REOB resulted in premature and excessive cracking of asphalt pavement in northern Ontario, Canada, based on X-ray fluorescence (XRF) analysis. Ding et al. [8, 9] used REOB to modify or rejuvenate asphalt and found through laboratory tests that REOB was unfavourable to the anti-ductile fracture performance and low-temperature cracking resistance of asphalt. The reason may be that paraffin in REOB precipitates asphaltenes, and iron, copper, chromium, and other metals accelerate the oxidation of asphalt. It is considered that the deterioration of performance in the above studies is closely related to the ageing of REOB and asphalt. Therefore, to explore the long-term stability and drawbacks of REOB as an asphalt regenerant, it is necessary to conduct a comprehensive and systematic study on the anti-ageing performance of REOB used for asphalt regeneration.

In this paper, REOB is used as a regenerant for simulated aged asphalt. By comparing and analysing the ageing performance of REOB, REOB-rejuvenated asphalt, and an REOB-rejuvenated asphalt test road, the effect of ageing on the road performance of REOB used as asphalt regenerant is evaluated comprehensively, which provides an improvement basis for REOB used in asphalt pavement.

## 2. Materials and Methods

### 2.1. Test Materials

**2.1.1. Recycled Engine Oil Bottom.** REOB, which cannot be distilled from REO after pretreatment and atmospheric and vacuum distillation in a large REO treatment plant, was selected in this paper. And a professional regenerant RA5 developed with mineral oil as the base oil on the market was selected for comparative study. Four components of REOB and RA5 were analysed using rod-thin-layer chromatography/hydrogen flame ionization detection (TLC-FID), which was produced by Zibo Shanfen Analytical Instrument Co., Ltd. The specific testing steps are described in the following section of experimental methods. The properties and components of REOB and RA5 are shown in Table 1.

**2.1.2. Asphalt Binders.** The original asphalt is 70-A base asphalt with a performance grade (PG) of 70–28. The simulated aged asphalt was prepared from base asphalt by a thin film oven test (TFOT) and a pressure ageing vessel (PAV) according to the Chinese test standard [10]. The REOB-rejuvenated asphalt and RA5-rejuvenated asphalt, which exhibited good performance recovery, were prepared by adding 7% (mass ratio of aged asphalt) REOB and 5% RA5 to the aged asphalt, respectively, at 150°C and shearing

for 10 minutes at 4000 r/min. The performance indexes of different asphalt binders are shown in Table 2.

**2.1.3. Asphalt Mixture.** AC-20 dense-graded asphalt concrete was selected as the surface layer of the indoor test road. The aggregate is made of limestone. Mineral powder is the filler obtained by mechanical grinding of limestone. The gradation design is shown in Figure 1. To accurately compare the influence of three kinds of asphalt on the performance of the asphalt mixture, REOB-rejuvenated asphalt, RA5-rejuvenated asphalt, and 70-A base asphalt were used as binders of AC-20 dense-graded asphalt concrete, and the Marshall design method was used to determine the optimum asphalt-aggregate ratio of the three kinds of asphalt mixtures; three optimum ratios were 4.4%, respectively.

### 2.2. Experimental Methods

**2.2.1. Four-Component Analysis.** Four-component analysis was carried out on REOB and RA5 by using the TLC-FID. Specifically, the samples were first dissolved in toluene to prepare in solutions of 30 mg/mL. Next, samples 0.8–1.0  $\mu\text{L}$  in volume were placed into the 15 mm chromatographic rod. Then, the chromatographic frame was placed into three types of mixtures composed of *N*-heptane, toluene, and toluene/ethanol (volume ratio 55:45) and expanded in sequence on the expansion table. After each expansion, the chromatographic frame was dried, kept warm, and moisturized until the next expansion. Finally, after three rounds of expansion, the chromatographic frame was tested and analysed by a rod-thin-layer chromatography analyser.

**2.2.2. Extended Thin Film Oven Test.** The TFOT protocol can only simulate the short-term ageing of the original asphalt mixture during mixing and paving. The PAV protocol can only simulate the long-term ageing of an asphalt pavement in service for 5 years, but the asphalt at this time has not reached sufficient ageing [11]. Therefore, the modified extended TFOT (ageing time for 5 h, 10 h, 15 h, 20 h, and 25 h) is used to rapidly simulate the ageing of asphalt in long-term use process [12]. The specific test procedure refers to Chinese test standard [10]. Note that the asphalt in the sample dish should be stirred with glass rods every 5 hours during TFOT ageing to avoid the formation of a skin that slows oxygen entering the asphalt [7, 13].

**2.2.3. Brookfield Viscosity Test and Bending Beam Rheological Test.** The viscosity tests were performed with a Brookfield rotary viscometer (model NDJ-1C, Changji Geological Instrument Co., Ltd). The rheological tests were performed with a bending beam rheometer (BBR) (model TE-BBR-F, CANNON Equipment Company). Brookfield viscosity tests used a No. 21 rotor with a rotational speed of 20 RPM. BBR test temperatures were  $-18^{\circ}\text{C}$ . The tests were carried out in

TABLE 1: Basic properties and chemical components of REOB and RA5.

Type	Colour	Density (25°C, g/cm <sup>3</sup> )	Asphaltenes (%)	Resins (%)	Aromatics (%)	Saturates (%)
REOB	Reddish brown	0.904	0.2	15.5	83.5	0.8
RA5	Black	1.08	1.7	12.1	62.7	23.5

TABLE 2: Performance indexes of different asphalt binders.

Type	Penetration (25°C, 0.1 mm)	Softening point (°C)	Ductility (10°C, 5 cm/min, cm)	Viscosity (135°C, Pa·s)	PG
Base asphalt	71	48.7	22	0.397	70–28
Aged asphalt	24	66	0.4	2.352	76–10
REOB-rejuvenated asphalt	72	50	21.6	0.433	70–28
RA5-rejuvenated asphalt	68	51.3	24.2	0.417	70–28

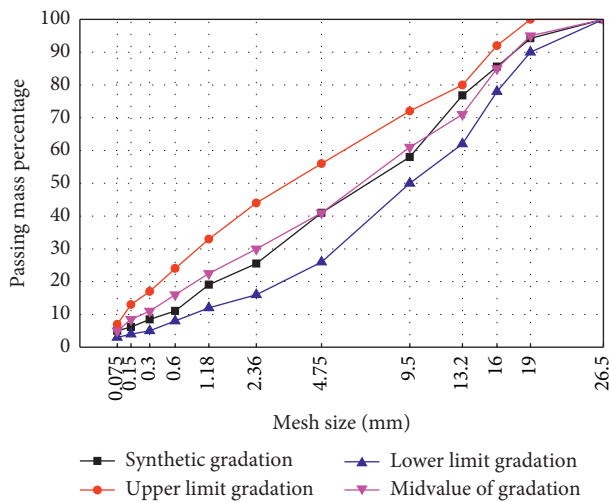


FIGURE 1: AC-20 aggregate gradation curve.

accordance with the relevant methods of Chinese test standard [10].

**2.2.4. Rotary Accelerated Loading Test.** To rapidly simulate the damage to pavement caused by actual traffic loads, our university independently developed the rotary accelerated loading test (RALT) system, as shown in Figure 2. The dimensions of the RALT system are 3360 mm × 2120 mm × 2526 mm. The RALT system can simulate the equivalent axle loads of vehicles less than or equal to 100 kN at rolling speeds of 10~35 km/h (3000–15000 cycles/h). The RALT system has a temperature regulation system that can adjust the temperature from -15°C to 60°C. The effective loading length of the RALT system is 1 m.

**2.2.5. Falling Weight Deflectometer.** A falling weight deflectometer (FWD) can accurately capture the actual deformation of pavement under actual dynamic loads, calculate the modulus of the pavement structure layer, and scientifically evaluate the bearing capacity of pavement [14]. In this paper, PRIMAX 1500 FWD produced by Grontmij

Company in the Netherlands is used to test the deflection of the pavement structure layer.

### 3. Results and Analysis

**3.1. Antiageing Performance of REOB.** When REOB is used as a regenerant, its own ageing resistance is directly related to the antiageing and durability of asphalt rejuvenated with REOB. In the process of thermal oxygen ageing, the mass of the regenerant will increase due to oxidation and polymerization; on the contrary, a mass loss will be caused by the volatilization of light components. However, considering that the regenerant is rich in aromatics, the mass loss of the regenerant will dominate during the thermal ageing process [15]. Therefore, the mass losses and viscosity ratios of REOB and RA5 were measured after a 5 h TFOT, and the results are shown in Table 3.

Table 3 shows that the mass losses and viscosity ratios of REOB and RA5 meet the technical requirements of Chinese technical specification [16], indicating that both regenerants exhibit good thermal stability and ageing resistance, and the feasibility of REOB as a regenerant has been preliminarily verified. Moreover, it can be seen that both the mass loss and viscosity ratio of REOB are less than those of RA5 after a 5 h TFOT, indicating that the antiageing performance of REOB is better than that of RA5. At this time, there is no phenomenon of poor thermal stability and antiageing performance of waste mineral oil as regenerant which has been concerned by predecessors [17, 18].

**3.2. Antiageing Performance of REOB-Rejuvenated Asphalt.** Because short-term simulated ageing (5 h TFOT) cannot evaluate the long-term performance of asphalt [19], the physical and rheological properties of asphalt were tested and analysed after extended TFOT (ageing times for 5 h, 10 h, 15 h, 20 h, and 25 h); hence, the antiageing performance of REOB-rejuvenated asphalt was evaluated in long-term use process [12].

**3.2.1. Mass Loss.** Similar to the above TFOT of REOB, the evaporation loss of rejuvenated asphalt is much greater than the weight gain of oxygen absorption due to the addition of



FIGURE 2: The rotary accelerated loading test (RALT) system. (a) Front view of the RALT, (b) console, and (c) temperature control system.

TABLE 3: Ageing indexes of REOB and RA5 after a 5 h TFOT.

Test objects	Mass loss (%)	Viscosity ratio (%)
REOB	2.48	1.75
RA5	2.75	1.87
Technical requirements	-4 to 4	$\leq 3$

either REOB or RA5. So the mass losses of REOB-rejuvenated asphalt, RA5-rejuvenated asphalt, and base asphalt were measured under the extended TFOT ageing times. The results are shown in Figure 3.

As shown in Figure 3, the mass losses of the three asphalts are less than 0.8% after the 5 h TFOT, which meets the standard requirements. In addition, the mass loss of REOB-rejuvenated asphalt is less than that of RA5-rejuvenated asphalt when the TFOT is less than 10 h, indicating that the antiageing property of REOB-rejuvenated asphalt is better than that of RA5-rejuvenated asphalt at this time, which is consistent with the antiageing performance of REOB. However, when the TFOT is 15 h or longer, the mass loss of REOB-rejuvenated asphalt is greater than that of RA5-rejuvenated asphalt, and the gap between the two increases as the TFOT ageing time increases, indicating that the weakness of poor thermal stability and ageing resistance of REOB as a regenerant is gradually revealed under long-term high-temperature ageing.

**3.2.2. Viscosity Ageing Index.** Asphalt viscosity can accurately reflect the degree of colloidal solubility of asphaltenes in asphalt components [20]. Asphalt ageing increases the asphaltene content due to component migration, and the increase in asphaltenes results in a continuous increase in asphalt viscosity. Therefore, the viscosity change can accurately reflect the ageing process and ageing degree of asphalt. Under extended TFOT ageing times, the dynamic viscosities of the three asphalts at 60°C were measured, and the results are shown in Table 4.

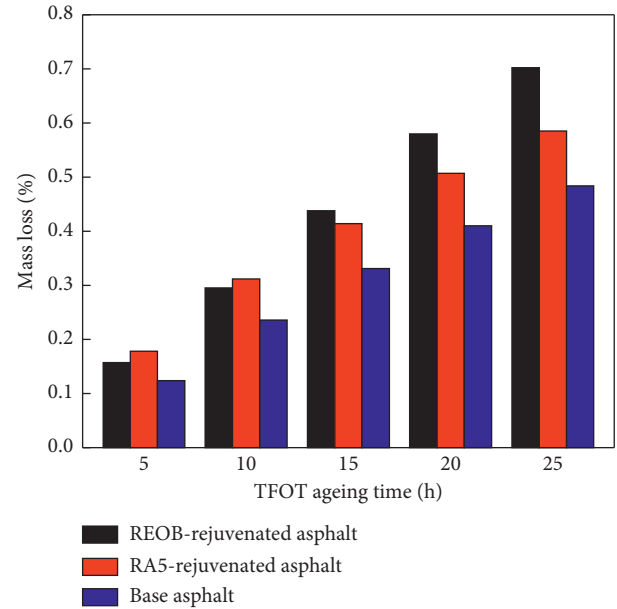


FIGURE 3: Relations between mass loss and TFOT ageing time for three kinds of asphalt.

TABLE 4: Viscosities of the three kinds of asphalt at 60°C under different extended TFOT ageing times (MPa·s).

Asphalt type	TFOT ageing time (h)					
	0	5	10	15	20	25
REOB-rejuvenated asphalt	503	972	1785	2949	4491	5862
RA5-rejuvenated asphalt	475	961	1726	2553	3454	4046
Base asphalt	446	880	1392	2026	2665	3125

According to the data in Table 4, the antiageing performance of the different asphalts can be characterized by the viscosity ageing index  $C$ . The formula for  $C$  is as follows:

$$C = \lg \lg \eta_2 - \lg \lg \eta_1, \quad (1)$$

where  $C$  is the viscosity ageing index,  $\eta_2$  is the viscosity under different TFOT ageing times (MPa·s), and  $\eta_1$  is the viscosity before ageing (MPa·s). Therefore, the relationships between the viscosity ageing index  $C$  and ageing time for the three kinds of asphalt are obtained, as shown in Figure 4.

Figure 4 shows that the viscosity ageing indexes  $C$  of the three kinds of asphalt increase as the TFOT ageing time increases, indicating a decrease in the ageing resistance of the three asphalts. After a 5 h TFOT, the order of the viscosity ageing index is RA5-rejuvenated asphalt > base asphalt > REOB-rejuvenated asphalt, which indicates that REOB-rejuvenated asphalt has the best ageing resistance among the three. After a 10 h TFOT, the order of the viscosity ageing index is RA5-rejuvenated asphalt > REOB-rejuvenated asphalt > base asphalt. At this time, the ageing resistance of REOB-rejuvenated asphalt is not as good as that of base asphalt but is still better than that of RA5-rejuvenated asphalt. As the TFOT ageing time increases, the viscosity ageing index of REOB-rejuvenated asphalt becomes greater than that of the other two asphalts, and the gap between REOB-rejuvenated asphalt and the other two asphalts increases as the ageing time increases, indicating that REOB-rejuvenated asphalt has the worst long-term (at TFOT ageing times greater than or equal to 15 h) antiageing performance. The reason may be that the paraffin in REOB accelerates asphaltene precipitation and that iron, copper, chromium, and other metals in REOB are easily oxidized at high-temperature for a long time, thus intensifying the ageing and hardening of asphalt.

**3.2.3. Creep Stiffness and Creep Rate.** The ageing of asphalt pavement makes the asphalt hard and brittle, wherein the asphalt stiffness increases, and the stress relaxation and ultimate tensile strain decrease; these changes easily result in the low-temperature cracking of asphalt pavement, which shortens the service life of asphalt pavement [21]. Therefore, a low-temperature bending creep test can be carried out using a BBR, as proposed by the Strategic Highway Research Program (SHRP), to evaluate the effect of extended TFOT ageing on the low-temperature crack resistance of asphalt. After the extended TFOTs, the creep stiffnesses and creep rates of the three asphalts at  $-12^\circ\text{C}$  are shown in Figures 5 and 6, respectively.

Figure 5 shows that the creep stiffnesses of the three kinds of asphalt increase with increasing TFOT ageing time, which shows that the asphalt hardens continuously and that the low-temperature performance gradually decreases after ageing. After 5 h and 10 h TFOTs, the increased levels of creep stiffness of the three asphalts are ranked as follows: RA5-rejuvenated asphalt > REOB-rejuvenated asphalt > base asphalt; these results demonstrate that the hardening rate of RA5-rejuvenated asphalt is the highest among the three asphalts and the short-term (TFOT ageing time less than or equal to 10 h) ageing resistance of REOB-rejuvenated asphalt is better than that of RA5-rejuvenated asphalt but worse than that of base asphalt. When the TFOT ageing time is 15 h or longer, the increased levels of creep stiffness of REOB-rejuvenated asphalt are greater than those of RA5-rejuvenated asphalt

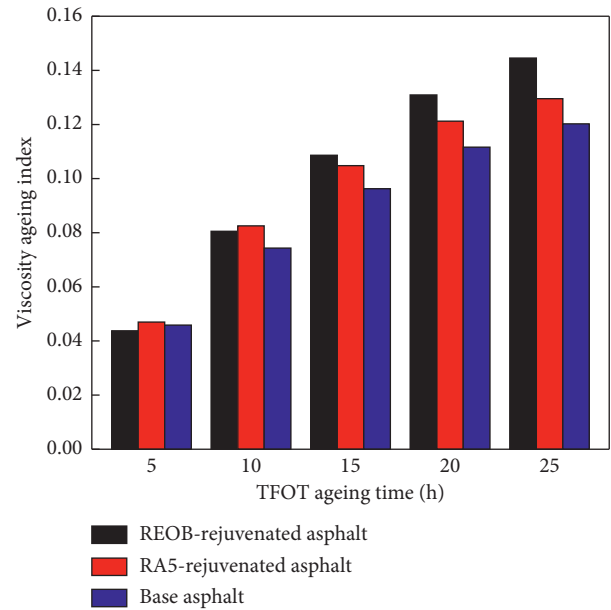


FIGURE 4: Relations between viscosity ageing index and TFOT ageing time for the three kinds of asphalt.

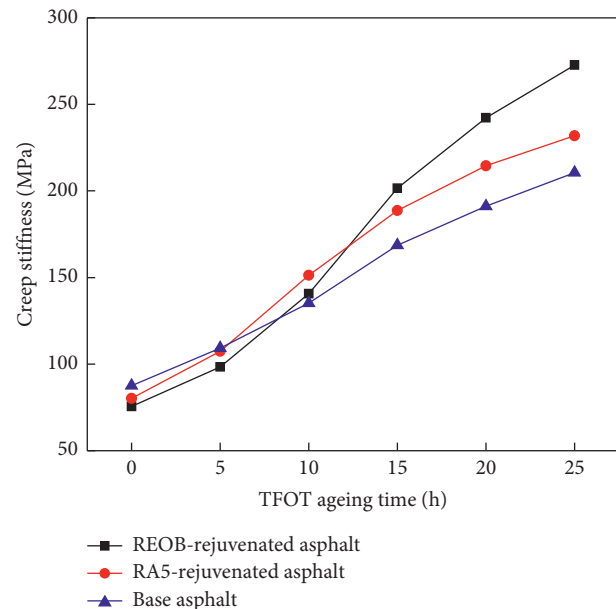


FIGURE 5: Relation between creep stiffness rate and TFOT ageing time.

and base asphalt, indicating that REOB-rejuvenated asphalt has the worst long-term (TFOT ageing time greater than or equal to 15 h) ageing resistance, which is consistent with the mass loss and viscosity ageing index trends shown above.

Figure 6 shows that the creep rates of three asphalts decrease with increasing TFOT ageing time, which indicates that the stress dissipation ability of asphalt at low temperature gradually weakens. After 5 h and 10 h TFOTs, the creep rate of REOB-rejuvenated asphalt falls below that of base asphalt. When the TFOT ageing time is 15 h or longer, the

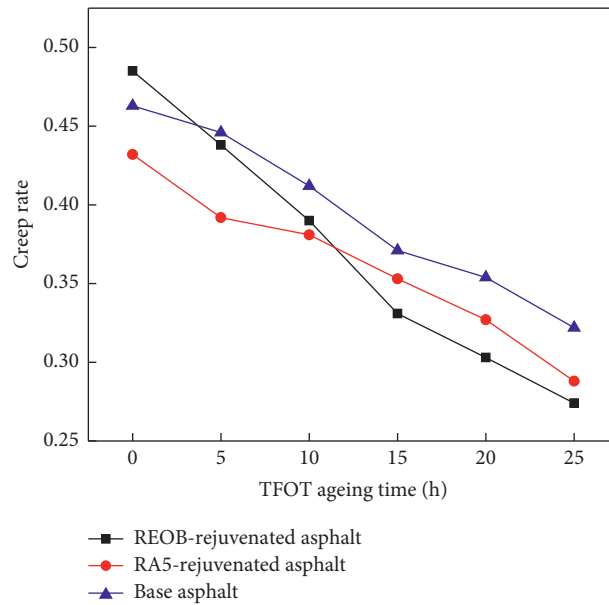


FIGURE 6: Relation between creep and TFOT ageing time.

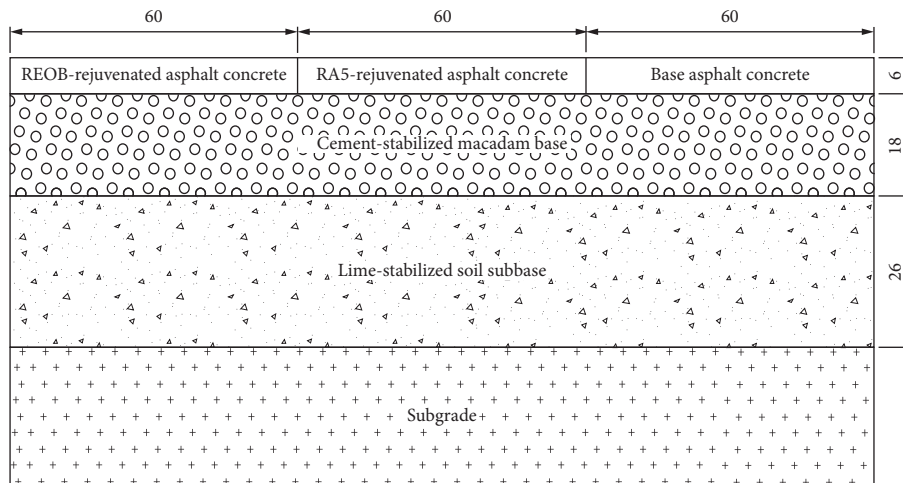


FIGURE 7: Structural sketch of full-scale indoor test road (cm).

creep rate of the REOB-rejuvenated asphalt substantially drops to a point less than that of RA5-rejuvenated asphalt, indicating that the stress relaxation ability of REOB-rejuvenated asphalt decreases to the worst among the three asphalts; therefore, the corresponding asphalt pavement would easily crack when the temperature sharply decreases.

**3.3. Antiageing Performance of an REOB-Rejuvenated Asphalt Mixture Test Road.** Another aspect of the reduction in the service life of asphalt pavement caused by ageing is the attenuation of fatigue resistance. Ageing increases the stiffness of the asphalt mixture, decreases the ultimate failure strain of traffic fatigue and temperature stress fatigue, and reduces the number of loading actions of fatigue damage [21], which ultimately leads to fatigue failure of asphalt pavement.

To study the effects of ageing on the fatigue resistance and service life of asphalt pavement and to explore the practical feasibility of REOB used in rejuvenated asphalt pavement, REOB-rejuvenated asphalt concrete, RA5-rejuvenated asphalt concrete, and base asphalt concrete were used to design and pave surface layers of a full-scale indoor test road (Figures 7 and 8) in this study. Using the RALT system independently developed by our university, the three pavement structures were loaded at normal temperature and high temperature ( $60^{\circ}\text{C}$ ) with a 100 kN axle load and a 15 km/h loading speed. For every 50,000 loads by the RALT system, the deflection values of the three pavement structures were measured using an FWD. The relationship between loading cycles and deflection values is shown in Figure 9.

Figure 9 shows that the deflection values of the three asphalt pavement structures increase but the growth rates



FIGURE 8: Field map of full-scale indoor test road (from left to right in the field map: REOB-rejuvenated asphalt concrete, RA5-rejuvenated asphalt concrete, and base asphalt concrete).

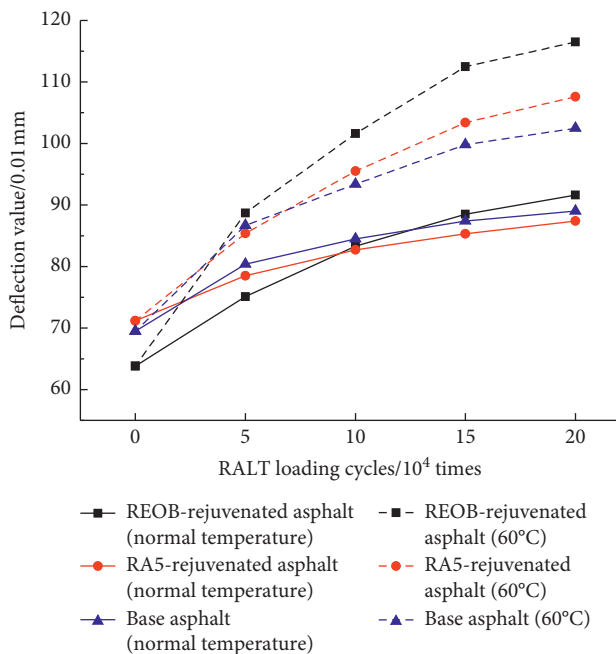


FIGURE 9: Relation between pavement deflection value and RALT loading cycles.

slow as the number of RALT loading cycles increases, indicating that the structural bearing capacity and service life of the asphalt pavement gradually decrease [18]. In addition, the increase in temperature substantially increases the deflection value of asphalt pavement because the deformation resistance and structural modulus of asphalt pavement decrease with increasing temperature. Moreover, according to the time-temperature equivalence principle [22], increasing the temperature is equivalent to increasing the

number of loading cycles; therefore, the deflection values of asphalt pavement are further increased at higher temperatures.

The growth rate of the deflection value of REOB-rejuvenated asphalt pavement is obviously greater than those of RA5-rejuvenated asphalt pavement and base asphalt pavement. After the high temperature accelerates the ageing of the three asphalt pavements, the growth of the deflection value of REOB-rejuvenated asphalt pavement becomes more substantial, which indicates that high-temperature ageing exacerbates the decrease in bearing capacity of asphalt pavement during long-term loading processes and makes REOB-rejuvenated asphalt pavement more prone to fatigue failure than RA5-rejuvenated asphalt pavement and base asphalt pavement.

#### 4. Conclusions

- (1) REOB meets the technical requirements of mass loss and viscosity ratio of asphalt regenerants listed in the technical specification. Moreover, at a TFOT ageing time of 5 h, REOB exhibits a better antiageing performance than professional regenerant RA5.
- (2) At a TFOT ageing time less than or equal to 10 h, the short-term antiageing performance of REOB-rejuvenated asphalt is better than that of RA5-rejuvenated asphalt evaluated by the mass loss and viscosity ageing index. But the long-term antiageing performance of REOB-rejuvenated asphalt is worse than that of RA5-rejuvenated asphalt and base asphalt when the TFOT ageing time is greater than or equal to 15 h.
- (3) The evaluation of creep stiffness for antiageing performance is consistent with the law of mass loss and viscosity ageing index; that is, REOB-rejuvenated asphalt exhibits better short-term antiageing performance and the worst long-term antiageing performance. Moreover, the creep rate of REOB-rejuvenated asphalt is substantially attenuated during extended TFOT ageing, which shows that REOB-rejuvenated asphalt is prone to thermal cracking.
- (4) The full-scale indoor test road shows that both increasing loading cycles and increasing temperatures can increase the deflection value of asphalt pavement and reduce the bearing capacity of pavement. Compared with RA5-rejuvenated asphalt pavement and base asphalt pavement, high-temperature ageing decreases the bearing capacity of REOB-rejuvenated asphalt pavement more substantially in the long-term loading process, which makes REOB-rejuvenated asphalt pavement more prone to fatigue failure.

#### Data Availability

The experimental data in this paper are from the pavement material laboratory of Shandong Jiaotong University, which is the provincial key laboratory. The experimental data in this paper are real and reliable.

## Conflicts of Interest

The authors declare no conflicts of interest.

## Acknowledgments

The authors thank Yanru Shi, Peng Jiang, Chongzhen, and Tonghui Yun for their help in the experiment. This research was funded by Shandong Provincial Natural Science Foundation, China (ZR 2016EEM42) and a Project of Shandong Province Higher Educational Science and Technology Program (J16LA17).

## Supplementary Materials

The video records an actual wheel loading process simulated by the rotary accelerated loading test (RALT) system independently developed by our university on the full-scale indoor test road. The RALT system can rely on temperature control system to set the temperature ( $-15^{\circ}\text{C}$  to  $60^{\circ}\text{C}$ ) of pavement under loading cycles and accelerates and loads pavement under certain axle loading (less than or equal to 100 kN) and speed (10~35 km/h). Each time the pavement is loaded, the console records the times of loading. (*Supplementary Materials*)

## References

- [1] Y. Ma, D. Liu, W. Xu et al., "Study on the current situation and key technology of waste engine oil regeneration in the transportation industry," *Comprehensive Utilization of China's Resources*, vol. 28, no. 11, pp. 25–29, 2010.
- [2] S. Zhou, *Heat and Mass Transfer in Short-Path Distillation Process and Application of the Process to Regeneration of Waste Lubricating Oil*, Sichuan University, Chengdu, China, 2007.
- [3] L. V. Wei-Min, "Principle of asphalt regeneration and technical requirement of regeneration agent," *Petroleum Asphalt*, no. 6, pp. 1–6, 2007.
- [4] D. Guo, Y. Chen, X. Li et al., "A hot recycled asphalt structural layer used recycled engine oil bottom and its construction method," Chinese Patent: CN 107010877 A, 2017.
- [5] D. Guo, Y. Chen, L. I. Jin et al., "A cold recycled asphalt structural layer used recycled engine oil bottom and its construction method," Chinese Patent: CN 107176808 A, 2017.
- [6] S. A. M. Hesp and H. F. Shurvell, "X-ray fluorescence detection of waste engine oil residue in asphalt and its effect on cracking in service," *International Journal of Pavement Engineering*, vol. 11, no. 6, pp. 541–553, 2010.
- [7] S. A. M. Hesp and H. F. Shurvell, "Waste engine oil residue in asphalt cement," *International Journal of Pavement Engineering*, vol. 1, no. 3, pp. 134–143, 2012.
- [8] H. Ding, Y. Qiu, W. Wang et al., "Adverse effect of waste engine oil bottom on asphalt performance and its mechanism," *Journal of Building Materials*, vol. 20, no. 4, pp. 646–650, 2017.
- [9] R. Li, H. Ding, and Q. Sun, "Effect of waste engine oil bottom on the low temperature performance of aged asphalt," *Journal of Building Materials*, pp. 1–8, 2019.
- [10] JTG E20-2011, *Test Procedures for Asphalt and Asphalt Mixture in Highway Engineering*, People's Transportation Press, Beijing, China, 2011.
- [11] K. A. Galal and T. D. White, "SHRP PG classification and evaluation of in-service asphalts after eight years," in *Progress of Superpave—Evaluation and Implementation*, ASTM STP 1322, R. N. Jester, Ed., pp. 135–150, American Society for Testing and Materials, Philadelphia, PA, USA, 1997.
- [12] Z. Di, "Study on the effect of nano- $\text{CaCO}_3$  on anti-ageing performance of asphalt by delayed ageing test," *Journal of Wuhan University of Technology (Transportation Science and Engineering)*, vol. 42, no. 6, pp. 1063–1067, 2018.
- [13] S. Rubab, K. Burke, L. Wright et al., "Effect of engine oil residues on asphalt cement quality," in *Proceedings of the 56th Canadian Technical Asphalt Association*, pp. 1–12, Québec City, Canada, November 2011.
- [14] Z. Yao, "A review on design criteria of asphalt pavements," *Highway*, no. 2, pp. 43–49, 2003.
- [15] R. Liu, K. Liao, H. Wang et al., "Evaluation of aging resistance of recycled asphalt," *Contemporary Chemical Industry*, vol. 42, no. 1, pp. 21–23+27, 2013.
- [16] JTG F41-2008, *Technical Specification for Highway Asphalt Pavement regeneration*, People's Transportation Press, Beijing, China, 2008.
- [17] American Asphalt Regeneration Association (ARRA), *American Asphalt Regeneration Guide*, People's Transportation Press, Beijing, China, 2001.
- [18] Y. Wang, K. Liao, F. Yan et al., "Development of waste asphalt regenerating agent," *Advances in Fine Petrochemicals*, no. 8, pp. 18–21, 2003.
- [19] Z. Zou, "Delayed aging test study on the effect of nano calcium carbonate on the aging resistance of asphalt," *Journal of Wuhan University of Technology (Transportation Science and Engineering Edition)*, vol. 42, no. 6, pp. 1063–1067, 2018.
- [20] Y. Yang, W. Zhao, G. Chen et al., "Experimental study on ageing resistance of recycled asphalt," *Journal of Highway and Transportation Research and Development*, no. 8, pp. 93–95, 2006.
- [21] J. Shen, *Pavement Performance of Asphalt and Asphalt Mixture*, People's Transportation Press, Beijing, China, 2001.
- [22] L. I. Xiao, N. Liang, and L. Chen, "Dynamic modulus and time-temperature equivalence equation of asphalt concrete," *Journal of Chang'an University (Natural Science Edition)*, vol. 34, no. 3, pp. 35–40, 2014.

## Research Article

# Effect of Blending Degree between Virgin and Aged Binder on Pavement Performance of Recycled Asphalt Mixture with High RAP Content

Ying Xu <sup>1,2</sup>, Zhijing Chou,<sup>1</sup> Yunze Li,<sup>1</sup> Jie Ji <sup>1,2</sup> and Shi-fa Xu<sup>1,2</sup>

<sup>1</sup>School of Civil Engineering and Transportation, Beijing University of Civil Engineering and Architecture, Beijing 100044, China

<sup>2</sup>Beijing Urban Transportation Infrastructure Engineering Technology Research Center, Beijing 100044, China

Correspondence should be addressed to Ying Xu; [caacxuying@126.com](mailto:caacxuying@126.com)

Received 29 March 2019; Revised 31 July 2019; Accepted 4 September 2019; Published 25 September 2019

Guest Editor: Hassan Baaj

Copyright © 2019 Ying Xu et al. This is an open access article distributed under the Creative Commons Attribution License, which permits unrestricted use, distribution, and reproduction in any medium, provided the original work is properly cited.

In this study, the influence of the blending degree between virgin and aged binder on the pavement performance of hot-mix recycled asphalt mixture (HMRAM) with high RAP content is analyzed. The aggregate gradation of AC-16 was selected. The RAP contents were 30, 40, and 50%. HMRAMs with different degrees of blending (DOB) were prepared by changing the mixing temperature (150, 165, and 180°C) without the occurrence of excessive aging for asphalt binders. An improved Hirsch dynamic modulus prediction model was then used to quantitatively characterize the DOB of HMRAM. Finally, the high-temperature, low-temperature, moisture stability, and fatigue resistance performance of HMRAM were tested and the effect of the DOB between the virgin and aged asphalt binder on the pavement performance was analyzed. The results showed that the DOB between the virgin and aged asphalt binder cannot reach 100% at the three mixing temperatures for HMRAM with 30, 40, and 50% RAP contents, which is inconsistent with the assumption of complete blending in China's specification. The dynamic stability of the mixture gradually decreases with the increased DOB for HMRAM with a high RAP content, while the moisture stability, low-temperature, and fatigue resistance performance are continuously improved. This means that with the increase in DOB in the stage of open to traffic, meeting high-temperature performance criteria at the design stage may become unsatisfactory for HMRAM. The moisture stability, low-temperature performance, and fatigue resistance performances of HMRAM measured at the design stage were reasonable and conservative. The change in DOB significantly affects the content and properties of total free binder in HMRAM, affecting pavement performance. The content and physical properties of the RAP aggregate also have a significant impact on pavement performance.

## 1. Introduction

More transportation agencies are moving toward the increased use of reclaimed asphalt pavement (RAP) due to the increasing demand for environment-friendly paving mixtures and the significant increase in the costs of raw asphalt binder [1]. In the production and mixing process of the hot-mix recycled asphalt mixture (HMRAM), the aged binder coated outside the old aggregate in the RAP will be blended with a rejuvenator and virgin binder. Based on the mobilized proportion of the RAP binder, the degrees of blending (DOB) between the RAP binder and virgin binder are classified into no-blending ("black rock"), partial blending, and complete blending states [2].

At present, HMRAMs are mostly designed based on the assumption of a complete blending state. Recent studies have shown that under normal production conditions when the RAP content is less than 30%, the DOB for the RAP approaches 100% [2], which conforms to the assumption of the current design specifications. However, for HMRAM with a high RAP content (>30%), only the partial aged binders in the RAP are blended with the virgin binders, which results in inconsistency with the design assumption. Therefore, the DOB quantification between the RAP binder and virgin binder is the key issue for the design of HMRAM with a high RAP content.

In previous research studies, the extents of the RAP binder mobilization and RAP mixture blending have been characterized using chemical and mechanical approaches. In

the chemical approach, after HMRAMs are stage extracted, gel permeation chromatography (GPC), Fourier transform infrared (FTIR) spectroscopy, etc., are used to evaluate the difference between the RAP binders in different layers [3–5]. In the mechanical approach, the amount of blending is indirectly determined by comparing the rheological properties of HMRAM and ideal mixtures in which the extracted RAP binder is already blended with the virgin bitumen prior to mixing [6–8]. The DOB can be characterized by comparing the dynamic modulus of the mixtures to that of those predicted using the Hirsch model or Witzak model based on the complex modulus of the recovered binder [9, 10]. Although the mechanical approach is considered faulty, it is still one of those most commonly used.

Since the RAP binder is usually stiffer than the virgin binder [11], the extent of RAP binder mobilization and RAP mixture blending has a significant impact on the properties of the binder and HMRAM [12, 13]. Carpenter and Wolosick [14] found that the DOB of the recycled asphalt mixture after compaction continues to gradually increase, which results in the decrease of the resilience modulus and rutting resistance of the asphalt mixture. The research studies of Noureldin and Wood also validated these results [15]. McDaniel et al. [16] considered that the DOB has no significant effect on the stiffness and deformation resistance of the mixture at 10% RAP content. However, for HMRAM with a high RAP content of 40%, a lower DOB resulted in a lower stiffness of the mixture and poor deformation resistance. Stephens et al. [17] found that prolonging the preheating of the RAP resulted in a higher DOB, which increased the unconfined compressive strength and splitting strength of the recycled asphalt mixture. Coffey et al. [18] measured the DOB of three kinds of HMRAM with an RAP content of 25%. All the DOBs obtained are higher than 85%. Changes in the DOB have minimal effect on the fatigue and rutting resistance of the mixtures.

The mixing conditions have a significant effect on the DOB of HMRAM. By investigating the effects of the production stages, including the RAP binder transfer, mechanical blending, and diffusion, on the blending of RAP and virgin binders and the mechanical properties of RAP mixtures, Zhang and Muhunthan et al. [19] found that diffusion is the stage that affects the rheological and fracture properties of RAP mixtures the most. They also found that thorough mechanical blending contributes to improvement in the ductility of high-percentage RAP mixtures. Kriz et al. [20] have proposed that production temperature and binder layer thickness in the mix has a significant impact in binder diffusion. As binder thickness in the mix is not uniform, there may be regions where a binder layer is thicker than expected, which results in partial blending status between virgin and aged binder after production and placement of mixture. While the diffusion continues at the ambient temperature, it can take months or even years for blending completion. Rad et al. [21] also proposed that the mixing temperature should be increased in the production stage to promote complete blending between the virgin and aged binders. Bowers [22] studied the influencing factors of the blending state between the virgin and aged binders, demonstrating that the temperature of the mixture had a significant effect on the blending

state between the virgin and aged binders. They found that the higher the temperature was, the faster the diffusion rate between the virgin and aged binders was. Based on the literature above, the mixing temperature has been found to significantly affect the diffusion and DOB between the virgin and aged binders in a recycled asphalt mixture.

In conclusion, many scholars have studied the influence of different RAP content on pavement performance [23–25]. It is considered that with an increasing RAP content, the high-temperature performance and tensile strength of the mixture will improve, but the fatigue performance and moisture stability will deteriorate. However, few studies have focused on the impact of single DOB changes on pavement performance for HMRAM with specific RAP content. As far as HMRAM with high RAP content (>30%) is concerned, complete blending status is difficult for the DOB to achieve at the end of construction, changing gradually after construction [2]. How does this change affect the pavement performance after construction? What is the best means of dealing with this impact in the HMRAM design stage? Additional research is required.

Therefore, the objective of this research is to evaluate the relationship between the DOB and pavement performance, such as the high-temperature, low-temperature, moisture stability, and fatigue resistance performances for HMRAM with high RAP content. Firstly, HMRAMs with three different RAP contents are prepared under different mixing temperature. Secondly, the DOB of HMRAM is quantitatively characterized using the mechanical method based on the improved Hirsch dynamic modulus prediction model. Thirdly, the pavement performances of HMRAMs are tested. Finally, the relationship between the pavement performance and DOB of HMRAM are analyzed.

## 2. Materials and Methods

### 2.1. Raw Materials

*2.1.1. RAP Material.* The RAP material selected in this study comes from the asphalt surface material milled from a municipal road in Beijing. The RAP binder was extracted by the rotavapor method (T 0727-2011), and trichloroethylene was used as the solvent. Three indexes—ductility at 15°C, penetration at 25°C, and softening point for RAP binder—were tested and compared with the technical requirements of AH-70 asphalt binder. The test results are shown in Table 1.

According to the data in the table, the penetration and ductility of the RAP binder are 2.70 mm and 19.2 cm, respectively, which are significantly lower than the technical standard of AH-70 asphalt binder, indicating that the aging degree of the RAP binder is very serious. The properties of extracted RAP aggregates are also tested. They are shown in Table 2.

*2.1.2. Rejuvenator.* In this study, the aged asphalt in RAP was regenerated by adding a rejuvenator, and a commercial rejuvenator was selected. The performance indexes are shown in Table 3. In the mixing process, the rejuvenator can be added in proportion after the dry mixing of RAP material and a new aggregate.

TABLE 1: Properties of RAP binder.

Indexes	Units	RAP binder samples			Mean value	AH-70 asphalt binder
		A	B	C		
Ductility (15°C, 5 cm/min)	cm	18.6	17.8	21.2	19.2	≥100
Penetration (25°C, 5 s, 100 g)	0.1 mm	26.8	25.9	28.4	27.0	60–80
Softening point	°C	59.1	58.5	58.6	58.7	≥46

TABLE 2: Physical properties of the RAP aggregate.

Indexes	Units	Particle size			Test methods
		10~20 mm	3~10 mm	0.075~3 mm	
Crushing value	%	17.6	—	—	T 0316
Los Angeles wear loss	%	19.4	19.4	—	T 0317
Polished value	—	38	—	—	T 0321
Apparent density	g/cm <sup>3</sup>	2.721	2.715	2.708	T 0304
Water absorption	%	0.3	0.4	0.6	T 0304
Adhesion to asphalt	Grade	5	—	—	T 0616

TABLE 3: The properties of rejuvenator.

Indexes	Viscosity (60°C)/ (10 <sup>-3</sup> Pa·s)	Flash point (°C)	Rate of viscosity change before and after TFOT (%)	Rate of mass change before and after TFOT (%)	Density (g·cm <sup>-3</sup> )
Rejuvenator	364.2	256	2.55	-3.29	1.012
Requirements	176~900	≥220	≤3	≤4, ≥-4	—

Relevant specifications and studies have shown that the performance properties of recycled asphalt binder can be evaluated using penetration or a viscosity indicator. The general viscosity test temperature is 60°C, owing to the high aging degree of the RAP binder. This study used the ductility at 15°C, penetration at 25°C, softening point, and viscosity at 135°C as the indexes to determine the adding content of the rejuvenator. The performance properties of the regenerated RAP binder should meet the technical requirements of the AH-70 asphalt binder.

The determining method of the rejuvenator content is explained by 30% RAP content. According to application experience, the adding content of the rejuvenator is suggested as 3%, 4%, 5%, and 6% (the mass ratio of the rejuvenator to the RAP binder). The performance properties of the regenerated RAP binder after adding different rejuvenator content are shown in Table 4.

According to the data in Table 4, with the increase in the rejuvenator content, the penetration and ductility of the regenerated RAP binder shows an upward trend, while the softening point and viscosity at 135°C decrease gradually. When the mass ratio of the rejuvenator to RAP binder is 5%, all the performance index values of the regenerated RAP binder meet the technical requirements of AH-70 asphalt binder. Therefore, an adding content of 5% of rejuvenator is used.

**2.1.3. Virgin Aggregate and Binder.** In this study, the aged binder in RAP is regenerated by adding a rejuvenator. The insufficient amount of total asphalt binder is supplemented with a virgin AH-70 asphalt binder. The virgin aggregate and mineral filler are limestone. The properties are shown in Tables 5~7.

#### 2.1.4. Mix Design of Recycled Mixture with High RAP Content

**(1) Gradation Design of HMRAM.** In this study, three high RAP contents of 30%, 40%, and 50% were selected, which is the ratio of the RAP materials to the total HMRAM mass. The selected gradation is AC-16. To decrease the variability of the RAP material, RAP materials were divided into four grades: 0~1.18 mm, 1.18~4.75 mm, 4.75~13.2 mm, and 13.2~16 mm. RAP material that is too fine will significantly affect the performance of HMRAM and make difficult meeting the specification requirements of AC-16 for the synthetic gradation. Therefore, RAP materials of 0~1.18 mm grade has been removed. The remaining three grades of the RAP materials are mixed according to the mass ratio of 10%, 60%, and 30%. In determining the ratio of the RAP and new aggregate, the RAP is not added as a “black stone,” instead the old aggregates in the RAP after extraction are compounded with the virgin aggregate to ensure that the synthetic gradation of HMRAM meets the requirements of AC-16. The three grades of mixed RAP materials are extracted, and the content of RAP binder is tested at 4.4%. The gradation curve is shown in Figure 1.

**(2) Choice of Mixing Method.** Based on the past research studies, it was found that the mixing temperature has the most significant influence on the DOB [26]. Therefore, to prepare HMRAM with different DOBs, the mixing temperatures with different RAP contents are selected as 150°C, 165°C, and 180°C. HMRAM with a complete blending state is also prepared by mixing the virgin binder and aggregate with a complete separating RAP binder and old aggregate using the RAP extraction method. All other mixing

TABLE 4: Performance properties of regenerated RAP binder.

Indexes	Units	Adding content of rejuvenator					Technical requirements of AH-70 asphalt binder
		0	3%	4%	5%	6%	
Viscosity (25°C)	Pa·s	1.362	0.953	0.696	0.527	0.263	—
Ductility (15°C, 5 cm/min)	cm	19.2	53.8	80.5	143.2	193.5	≥100
Penetration (25°C, 5 s, 100 g)	0.1 mm	27.2	49.5	56.3	69.5	76.3	60~80
Softening point	°C	58.7	54.6	51.3	48.7	44.2	≥46

TABLE 5: Physical properties of the virgin aggregate.

Indexes	Units	Norms requirements	Particle size			Test methods
			10~20 mm	3~10 mm	0.075~3 mm	
Crushing value	%	≤26	19.8	—	—	T 0316
Los Angeles wear loss	%	≤28	17.5	17.5	—	T 0317
Polished value	—	≥40	42	—	—	T 0321
Apparent density	g/cm <sup>3</sup>	—	2.736	2.731	2.726	T 0304
Water absorption	%	≤2.0	0.5	0.4	0.3	T 0304
Adhesion to asphalt	Grade	≥5	5	—	—	T 0616

TABLE 6: The properties of mineral filler.

Indexes	Units	Standard	Test results	Test methods
Apparent density	g/cm <sup>3</sup>	≥2.5	2.697	T 0352
Moisture content	%	≤1	0.3	T 0103
Particle size range	<0.6 mm	%	100	100.0
	<0.15 mm	%	90~100	98.0
	<0.075 mm	%	75~100	95.0
Hydrophilicity coefficient	—	<1.0	0.76	T 0353

TABLE 7: The properties of AH-70 virgin binder.

Indexes	Units	Test results	Test methods
Penetration (25°C, 5 s, 100 g)	0.1 mm	69.9	T 0604
Softening point	°C	48.6	T 0606
Ductility (15°C, 5 cm/min)	cm	149	T 0605
Density (15°C)	g/cm <sup>3</sup>	1.031	T 0603
Residue after RTFOT	Quality loss	%	0.3
	Penetration ratio	%	70.4
	Ductility at 15°C	cm	48

parameters are the same. The four mixing methods are summarized in Table 8.

To truly reflect the influence of thermal history of HMRAM samples on DOB, after 3 min of mixing, the HMRAM will be placed in an oven at 10°C lower than the mixing temperature for 1.5 h to simulate the diffusion process between the virgin and aged binder during the storage and transportation stages. The storage temperature is 10°C lower than the mixing temperature because the temperature of the mixture during storage and transportation is generally 10–15°C lower than the mixing temperature based on construction experience. After 1.5 h in a stored stage, the HMRAM were compacted and then placed in an oven at 20°C for 4 h at the cooling stage. The thermal history of the four mixing methods is shown in Figure 2.

Figure 2 shows that the thermal history of HMRAM samples can be divided into three stages, namely, mixing

stage, storage and transportation stage, and placement and cooling stage. It should be emphasized that when the mixing temperature is different, not only will the diffusion rate between virgin and aged binder in the mixing stage be affected, but the different thermal history of HMRAM samples in the storage and transportation stage and placement and cooling stage will also have a significant impact on the diffusion rate. Therefore, the influence of the mixing temperature on DOB would be caused by the comprehensive thermal history difference in all three stages.

To evaluate whether different mixing temperatures will cause different degrees of aging of HMRAM, the penetration, softening point, and ductility of the extracted binder of HMRAM with 30% RAP content for the four mixing methods are tested. The test results are presented in Table 9. It shows that changing the mixing temperature does not cause significant differences in the degree of aging of the

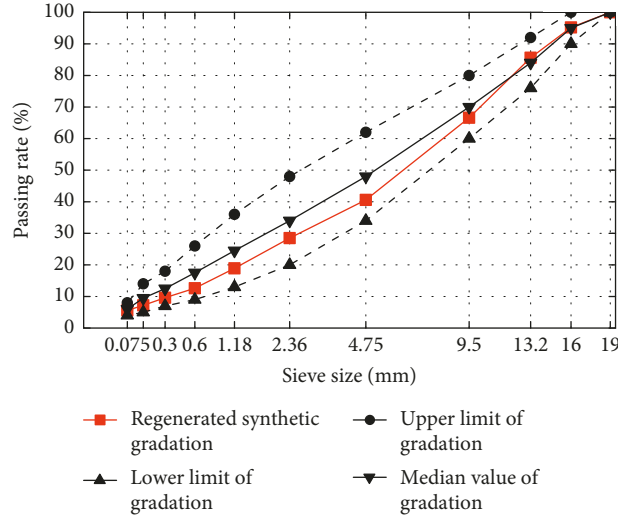


FIGURE 1: Synthetic gradation curve of AC-16.

TABLE 8: Four mixing methods.

Mixing method/mixing temperature	Mixing method 1 150°C	Mixing method 2 165°C	Mixing method 3 180°C	Mixing method 4 (100% DOB) 165°C
RAP preheating time (h) and temperature (°C)			2; 110	
Heating temperature of virgin binder (°C)			165	
Heating temperature of virgin aggregate (°C)			180	
Mixing time (min)			3	
Aggregate gradation			AC-16	
Binder content			Same	
DOB state	Partial blending	Partial blending	Partial blending	Complete blending

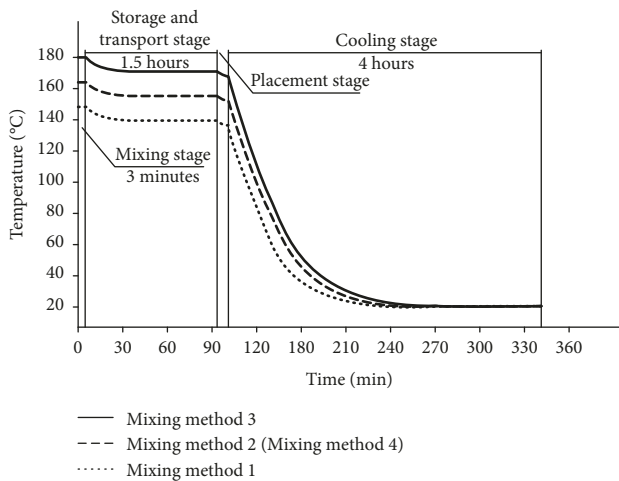


FIGURE 2: Thermal history of samples with different mixing method.

extracted binder. Therefore, the performance of HMRAM is only affected by the DOB.

(3) *Optimum Binder Content.* The Marshall Design method is used to determine the optimum binder content of HMRAM with the four mixing methods. To avoid the influence of a total binder content change on the

pavement performance, we used the same total binder content for all the mixing methods in this study. Thus, only the DOB affects the composition of the effective HMRAM binder and its pavement performance. For HMRAM with mixing method 4, the total binder content is determined as 4.4%. Therefore, 4.4% is determined as the total binder content for all mixing modes. The virgin binder in HMRAM with different RAP contents is calculated using equation (1).

$$P_{nb} = P_b - n \times P_{ab} (1 + P_0), \tag{1}$$

where  $P_{nb}$ —virgin binder content (%)—the proportion of virgin binder in HMRAM;  $P_b$ —total binder content (%)—the proportion of the total content of virgin binder, RAP binder, and virgin binder in HMRAM;  $P_{ab}$ —RAP binder content (%)—the proportion of RAP binder in RAP material;  $n$ —RAP material blending ratio—the proportion of RAP material in HMRAM;  $P_0$ —rejuvenator content (%)—the mass ratio of rejuvenator to RAP binder.

Take 30% of RAP content as an example. The total binder content  $P_b$  (virgin binder plus RAP binder plus rejuvenator) is 4.4%,  $n$  is 30%, and  $P_{ab}$  is 4.4%. Thus, the RAP binder content is 1.32% ( $n \times P_{ab} = 30\% \times 4.4\% = 1.32\%$ ). The rejuvenator content  $P_0$  is 5%. Thus, the rejuvenator content in HMRAM is 0.07%

TABLE 9: Test results of the extracted HMRAM binder for the four mixing methods.

Technical index	Units	Mixing method 1	Mixing method 2	Mixing method 3	Mixing method 4 (100% DOB)	Variance
		150°C	165°C	180°C	165°C	
Penetration (25°C, 5 s, 100 g)	0.1 mm	64.3	64.4	64.3	64.1	0.02
Softening point	°C	49.3	49.3	49.4	49.6	0.02
Ductility (15°C, 5 cm/min)	cm	133	134	133	134	0.33

TABLE 10: The binder composition in HMRAM.

RAP content (%)	Total binder content (%)	RAP binder (%)	Virgin binder (%)	Rejuvenator (%)
30	4.4	1.32	3.01	0.07
40	4.4	1.76	2.55	0.09
50	4.4	2.20	2.09	0.11

( $n \times P_{ab} \times P_0 = 30\% \times 4.4\% \times 5\% = 0.07\%$ ). Finally, the virgin binder content  $P_{nb}$  is 3.01% ( $4.4\% - 1.32\% - 0.07\% = 3.01\%$ ). Similarly, the virgin binder content for 40% and 50% of RAP content can be obtained. The amounts of the RAP binder, virgin binder, and rejuvenator for different RAP contents are listed in Table 10.

## 2.2. Test Method

2.2.1. *Characterization of the DOB between the RAP Binder and Virgin Binder.* The aforementioned mechanical

characterization method is used to determine the DOB of HMRAM [6–8]. However, in this method, the Hirsch model constants were determined based on assumptions and simplifications for conventional asphalt mixtures. Therefore, it may be inappropriate for the prediction of the dynamic modulus of HMRAM with a high RAP content. An improved Hirsch model proposed by Zhang et al. [27] is used in this study, which is defined in formulas (2)–(5). The steps of the characterization are as follows:

$$|E^*|_{\text{mix}} = P_c \left[ E_a \left( 1 - \frac{\text{VMA}}{100} \right) + |E^*_{\text{mastic}}| \left( \frac{\text{VFA} \times \text{VMA}}{10000} \right) \right] + (1 - P_c) \left[ \frac{1 - (\text{VMA}/100)}{E_a} + \frac{\text{VMA}}{\text{VFA} |E^*_{\text{mastic}}|} \right]^{-1}, \quad (2)$$

$$P_c = \frac{(20 + ((\text{VFA} \times |E^*_{\text{mastic}}|)/\text{VMA}))^{0.58}}{650 + ((\text{VFA} \times |E^*_{\text{mastic}}|)/\text{VMA})^{0.58}}, \quad (3)$$

$$\frac{1}{|E^*_{\text{mastic}}|} = \sqrt{\left( \frac{1}{2(1 + \nu) |G^*_{\text{mastic}}| \cos \delta} + \frac{E_2}{E_2^2 + \eta_2^2 \omega^2} \right)^2 + \left( \frac{1}{\eta_1 \omega} + \frac{\eta_2 \omega}{E_2^2 + \eta_2^2 \omega^2} \right)^2}, \quad (4)$$

$$\frac{1}{\eta_1 \omega} + \frac{\eta_2 \omega}{E_2^2 + \eta_2^2 \omega^2} = \frac{|G^*_{\text{mastic}}|}{\sin \delta}, \quad (5)$$

where  $E_a$  is the elastic modulus of aggregates;  $E_2$  is the elastic modulus of spring 2 in Burgers model;  $\eta_1$  is the sticky pot 1 viscosity;  $\eta_2$  is the sticky pot 2 viscosity;  $\omega$  is the angular frequency; VMA is the voids in the mineral aggregate; VFA is the voids filled with asphalt;  $|E^*_{\text{mastic}}|$  is the dynamic modulus of the mastic; and  $|G^*_{\text{mastic}}|$  is the dynamic shear modulus of the mastic.

The usage of equations (2)–(5) is shown as follows. The angular frequency  $\omega$  can be calculated by the formula

$\omega = 2\pi f$ , with the known frequency  $f$ .  $|G^*_{\text{mastic}}|$  and phase angle  $\delta$  of the mastic with known DOB can be measured by the DSR test. Then, the parameters  $\eta_1$ ,  $\eta_2$ , and  $E_2$  can be obtained through error minimization by equation (5), and  $|E^*_{\text{mastic}}|$  can be calculated by equation (4). Then, the values of VMA and VFA of mixtures with known DOB are substituted into equation (3) to solve  $P_c$ . Finally, all parameters are substituted in equation (2) to obtain the dynamic modulus of HMRAM, and the master curve of

the dynamic modulus is drawn based on the dynamic modulus of HMRAM with different testing frequencies.

*Step 1.* Plotting of the master curve of the dynamic modulus of HMRAM

The dynamic modulus of HMRAM is tested by the uniaxial compression test (AASHTO TP 79-2013) method. The test temperatures are 20°C, 35°C, and 50°C. The loading frequencies are 0.1 Hz, 0.5 Hz, 1 Hz, 5 Hz, 10 Hz, and 25 Hz. The master curve of the dynamic modulus is plotted.

*Step 2.* Plotting of the theoretical master curve of the dynamic modulus of HMRAM with the DOB of 70, 80, 90, and 100%.

The mastic with DOB of 70, 80, 90, and 100% is prepared. HMRAM with 30% RAP content is selected to illustrate the calculation process. The asphalt mastic with 100% DOB is prepared with 1.32% of completely activated RAP binder, 3.01% of virgin binder, 0.07% of rejuvenator, and 5.33% of mineral filler. The total free binder is defined as the sum of the activated RAP binder, virgin binder, and rejuvenator. When the DOB is 90%, the content of activated RAP binder is 1.19% (1.32% × 90%). The content of the virgin binder, rejuvenator, and mineral powder remains unchanged. Thus, the asphalt mastic with 90% DOB is prepared with 1.19% of activated aged binder in RAP, 3.01% of virgin binder, 0.07% of rejuvenator, and 5.33% of mineral powder. Based on the same method, the asphalt mastic with 70% and 80% DOB is also prepared. The composition of the asphalt mastic with different DOBs is shown in Table 11.

The dynamic modulus of the mixture of 70, 80, 90, and 100% is obtained as described in Section 2.2.1, and the dynamic modulus master curve is plotted at a reference temperature of 20°C. The principal curve of the dynamic modulus is drawn as shown in Figure 3.

*Step 3.* Determination of the DOB for HMRAM.

The measured dynamic modulus master curve is compared with the theoretical master curve of HMRAM with the DOB of 70, 80, 90, and 100%. As shown in Figure 3, the master curve with red color is measured based on the actual specimen and the other four gray predicted master curves with 70%, 80%, 90%, and 100% DOB. Because the measured master curve is not parallel to the predicted master curve, the average value of the two interpolations for the actual principal curve at a minimum of 0.01 Hz and a maximum of 1000 Hz is adopted to characterize the DOB of the HMRAM specimen. Taking Figure 2 as an example, according to the interpolation relationship, 71% for end point A and 78% for end point B were obtained, and the average value of 74.5% was determined as the DOB of HMRAM. In the same way, the mixing degree of the recycled mixture with other RAP content can be obtained, as shown in Table 12.

*2.2.2. Pavement Performance Test of HMRAM.* According to the China specification (JTG E20-2011), the rutting test (T 0719-2011), the bending failure test (T 0715-2011) and the freeze-thaw splitting test (T 0729-2011) were used to test the high-temperature, low-temperature, and moisture stability performance of HMRAM, respectively. The rutting test (T 0719-2011) was originated from TRRL in Britain, which was tested at a temperature of 60°C, a load of 0.7 MPa, and a rate of 42 times per minute. The low-temperature bending test (T 0715-2011) used a wheel-rolling method to form the rutting board, which is 300 mm × 300 mm × 50 mm. Then, it was cut into a quadrangular beam with 250 mm × 30 mm × 35 mm. Flexural-tensile strain at the failure of the beam specimen was tested under the testing condition of -10°C and a loading rate of 50 mm/min using UTM-25 equipment. The freeze-thaw splitting test (T 0729-2000) originated from AASHTO T 283-98. The splitting strength ratio before and after the freeze-thaw cycle conditions is used to evaluate the moisture stability of the asphalt mixture. The four-point bending fatigue life test (T 0739-2011) originated from AASHTO T 321-03. The standard loading waveform of the fatigue test is a deviated sinusoidal wave. The testing temperature is 15°C, the loading frequency is 10 Hz, and the control strain is 400  $\mu\epsilon$ .

The pavement performance of the HMRAM with three RAP contents and four types of DOB for each RAP content was tested. To ensure the accuracy of the test results, four parallel performance tests were conducted for each DOB. To minimize the variation in test results, a data snooping method based on a Gaussian distribution was used to detect and remove the outliers.

- (1) Calculate the mean  $\mu$  and standard deviation  $\sigma$  using the following equations:

$$\mu = \frac{1}{n} \sum_{i=1}^n R_i, \quad (6)$$

$$\sigma = \sqrt{\frac{\sum_{i=1}^n (R_i - \mu)^2}{(n-1)}},$$

where  $R_i$  is the testing value of pavement performance; and  $n$  is the sample size;

- (2) Assume  $R_i$  obeys the Gaussian distribution with mean  $\mu$  and standard deviation  $\sigma$ :

$$R_i \sim N(\mu, \sigma^2). \quad (7)$$

- (3) Test whether or not the value of  $R_i$  is an outlier by statistic test. The threshold for testing the outliers is set at 1.281 $\sigma$ , i.e., 80% of measurements within the range of  $\mu \pm 1.281\sigma$ :

$$R > \mu \pm 1.281\sigma \text{ (consider outlier)}. \quad (8)$$

TABLE 11: Composition of mastic.

RAP content (%)	DOB (%)	Activated RAP binder (%)	Virgin binder (%)	Rejuvenator (%)	Mineral filler (%)	Total free binder (%)
	100	1.32/1.76/2.20	3.01/2.55/2.09	0.07/0.09/0.11	5.33/5.19/4.98	4.40/4.40/4.40
30/40/50	90	1.19/1.58/1.98	3.01/2.55/2.09	0.07/0.09/0.11	5.33/5.19/4.98	4.27/4.22/4.18
	80	1.06/1.41/1.76	3.01/2.55/2.09	0.07/0.09/0.11	5.33/5.19/4.98	4.14/4.05/3.96
	70	0.92/1.23/1.54	3.01/2.55/2.09	0.07/0.09/0.11	5.33/5.19/4.98	4.00/3.87/3.74

Note. The “/” is used to separate the values of each composition of mastic at 30%, 40%, and 50% RAP content.

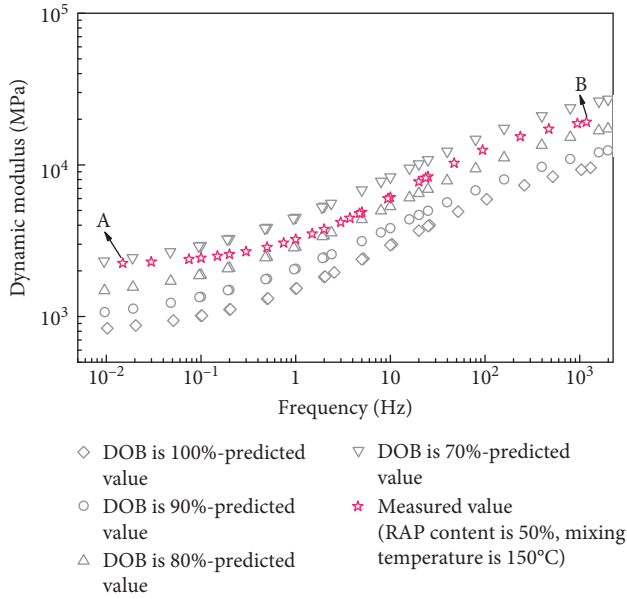


FIGURE 3: Prediction and measured dynamic different modulus master curve.

TABLE 12: Different DOB under four mixing methods.

RAP content (%)	Mixing methods			
	Mixing at 150°C (%)	Mixing at 165°C (%)	Mixing at 180°C (%)	Complete blending (%)
30	85.5	92.5	95.0	100
40	80.5	86.0	87.5	100
50	74.5	77	80.5	100

The dynamic stability data of HMRAM with 40% RAP content under a mixing temperature of 150°C is taken as an example to illustrate the data snooping method. The four parallel test results are 3621 passes/mm, 3598 passes/mm, 3665 passes/mm, and 3752 passes/mm. The mean value  $\mu$  is 3659 passes/mm, and  $\sigma$  is 59 passes/mm. The range of  $\mu \pm 1.281\sigma$  is from 3584 passes/mm to 3734 passes/mm. As the data point of 3752 passes/mm falls outside of the range, it is removed.

### 3. Results and Discussion

**3.1. DOB Results of HMRAM.** As shown in Table 11, the DOBs are between 85.5~95%, 80.5~87.5%, and 74.5~80.5% at the three mixing temperatures for HMRAM with 30, 40, and 50% RAP contents, which is inconsistent with the assumption of complete blending in the China

specification. However, increasing the mixing temperature can significantly increase the DOB. For HMRAM with 30% RAP, the DOB is only 85.5% at a mixing temperature of 150°C. However, the DOB is increased to 95% at 180°C, where a complete blending state is nearly achieved. When the RAP content is 40% and 50%, even with increasing the mixing temperature to 180°C, the DOB can only reach 87.5% and 80.5%, respectively, which is still that of a partial blending state. This conclusion is consistent with the research results of Coffey [18]. Therefore, the current specifications for HMRAM design are not suitable to use. In conclusion, the design method of HMRAM with high RAP content (>30%) should be improved. The influence of the DOB on the effective asphalt content and pavement performance of the mixtures should be fully considered.

Since the increasing the mixing temperature can result in increased DOB, the mobilization of the aged binder coated outside the old aggregate may require more thermal energy and the increase of the mixing temperature can supply more thermal energy. Rad et al. proposed that temperature is the most important factor affecting the diffusion rate, and the development of mixing degree depends on the diffusion rate. The higher the temperature is, the faster the diffusion rate is, resulting in higher DOB [21]. The studies of Kriz et al. [20] and Bowers [22] also show that the increase in mixing temperature increases the DOB. This conclusion is also validated in this paper. However, it should be noted that a simple increase in the mixing temperature might cause excessive aging of the mixture, which negatively affects the pavement performance of HMRAM.

**3.2. Effect of DOB on the Composition of the Total Free Binder.** In this study, the total binder content of HMRAM with three RAP contents is 4.4%, and the gradation is the same; therefore, the change in the total free binder content and properties due to different DOB becomes the important reason affecting the pavement performance of HMRAM. Two situations are considered to analyze the impact of DOB on the total free binder composition. One situation has the DOB remaining unchanged and RAP content changing; the other situation has the RAP content remaining unchanged and the DOB changing.

**3.2.1. DOB Remains Unchanged and RAP Content Changes.** The example of DOB equaling 85% and the RAP content changing from 30% to 50% is taken to illustrate the impact of this change. When the RAP content is 30%, according to equation (1), the content of the activated RAP binder,

virgin binder, and rejuvenator are 1.12%, 3.01%, and 0.066%, respectively. The total free binder content is 4.20%.

When DOB is 100%, the RAP binder can be completely converted to AH-70 binder by adding the rejuvenator. However, when DOB is less than 100%, the activated RAP binder decreases; adding the original amount of rejuvenator in this case results in the addition of too much rejuvenator, which will make the total free binder become softer. Thus, the rejuvenator is divided into two parts. One is named the balanced rejuvenator. The balanced rejuvenator is defined as the amount of the rejuvenator that can make the activated RAP binder exactly reach the requirements of the AH-70 binder. The other part is named excess rejuvenator, that is, the amount of the total rejuvenator minus the balanced rejuvenator, which makes the total free binder become softer.

In this example, the total rejuvenator is 0.066%, the activated RAP binder is 1.12%, the balanced rejuvenator is 0.056% ( $1.12\% \times 5\%$ , 5% is the dosage of the rejuvenator to make RAP binder reach the requirements of the AH-70 binder), and the excess rejuvenator is 0.010% (0.066% minus 0.056%). When the RAP content is 40% and 50%, the composition and content of the binder can be calculated using the same method. The calculation results are shown in Table 13.

According to the table above, when the RAP content decreases from 50% to 30%, the total free binder content increases from 4.07% to 4.20%, while the excess rejuvenator content decreases from 0.017% to 0.010%. With the decrease in excess rejuvenator content, the free binder with a 30% RAP content is stiffer than that with a 50% RAP content under the same DOB.

*3.2.2. RAP Content Remains Unchanged and DOB Changes.* HMRAM with a 30% RAP content is taken as an example for analysis. The composition and content of the binder under different DOBs is calculated and shown in the Table 14.

According to the above table, when DOB decreases from 100% to 70%, the total free binder content decreases from 4.40% to 4.00%, while the excess rejuvenator content increases from 0.00% to 0.02%. The increase in the excess rejuvenator content makes the free binder at 100% DOB is stiffer than that at 70% DOB.

Voids in the mineral aggregate (VMA) and voids filled with asphalt (VFA) are important volume parameters of asphalt mixture. VMA is numerically equal to the air void content plus the effective binder content by volume. VFA is the percentage of VMA filled with asphalt binder [28]. Therefore, the higher the VMA and VFA in the mixture, the higher the effective binder content in the mixture. To verify whether the effective binder in mixtures increases with DOB, the VMA and VFA of HMRAM specimens with different mixing methods are tested. The volume of effective binder is also calculated according to the test results of VMA and VFA. The relationship between VMA, VFA, and effective binder volume and DOB is shown in Figure 4.

The figure shows that the VMA and VFA of HMRAM specimens increase with DOB, irrespective of the RAP content, even if it is 30%, 40%, or 50%. The volume of the effective binder calculated based on VMA and VFA also increases with DOB. Considering 50% RAP content as an example, when DOB increases from 74.5% to 100%, the volume of the effective binder also increases from 9.8% to 10.5%. Such results further verify that when DOB increases, more RAP binders are converted to free binders, which leads to an increase in the volume of free binders in HMRAM. The properties of free binder also change.

### 3.3. Pavement Performance of the HMRAM

*3.3.1. Effect of RAP Content and Mixing Temperature on the Pavement Performance.* This paper considers the influence of RAP content and mixing temperature on the pavement performance of HMRAM. For each pavement performance indicator, there are four repeated tests for each combination of the two influence factors. We use variance of analysis (ANOVA) with dual-factor repeated test method to determine the significance of the two factors. The results of the calculation are shown in Table 15. According to the ANOVA results in Table 15, for the four pavement performance indicators, the mixing temperature and RAP content have a significant impact, which is consistent with the results of previous studies [12, 13].

#### 3.3.2. Effect of DOB on the Pavement Performance

*(1) Data Statistics and Analysis Methods.* For the three different RAP contents, the corresponding mean pavement performance value after removing outliers to different DOBs is shown in Figure 5. The relationship between DOB and pavement performance is fitted into a curve for the same RAP content. The 95% confidence interval of the fitting curve is also used to determine whether each data point is within the confidence interval. If the point falls outside the interval, it is removed. Taking Figure 3 as an example, the 95% confidence interval of the fitting curve shows that the point with a DOB of 81% is within the 95% confidence interval. Therefore, this point cannot be removed, even though this data point appears to be an outlier.

To determine whether the slopes of the fitting curves between DOB and pavement performance are considerably different, we use a covariance analysis (ANCOVA). When the sig. value is less than 0.05, the slopes of two fitting curves are considerably different. The relationship curves between DOB and pavement performance under three RAP contents and ANCOVA results are shown in Figure 6 and Table 16.

*(2) High-Temperature Performance.* From Figure 6(a), the dynamic stability (DS) decreases with the increase of the DOB for HMRAM. With the same DOB, the DS of HMRAM with a high RAP content is relatively high. For different RAP contents, the decline slope of fitting curve for 30% RAP content appears

TABLE 13: Composition of binder in HMRAM with 85% DOB content.

RAP content (%)	Total binder content (%)	RAP binder (%)	Rejuvenator (%)	Virgin binder (%)	Activated RAP binder (%)	Total free binder (%)	Balanced rejuvenator (%)	Excess rejuvenator (%)
30	4.40	1.32	0.066	3.01	1.12	4.20	0.056	0.010
40	4.40	1.76	0.088	2.55	1.50	4.14	0.075	0.013
50	4.40	2.20	0.110	2.09	1.87	4.07	0.094	0.017

TABLE 14: Composition of binder in HMRAM with 30% RAP content.

DOB (%)	Total binder content (%)	RAP binder (%)	Rejuvenator (%)	Virgin binder (%)	Activated RAP binder (%)	Total free binder (%)	Balanced rejuvenator (%)	Excess rejuvenator (%)
70	4.40	1.32	0.066	3.01	0.92	4.00	0.046	0.020
80	4.40	1.32	0.066	3.01	1.06	4.14	0.053	0.013
90	4.40	1.32	0.066	3.01	1.19	4.27	0.059	0.007
100	4.40	1.32	0.066	3.01	1.32	4.40	0.066	0.000

to be considerably less than that of 40% and 50% RAP content. The statistical analysis results listed in Table 16 indicate that the curve slope of 30% and 50% RAP content is considerably different. This indicates that the change of DOB has an even greater effect on the DS of HMRAM with high RAP content, as compared to HMRAM with a low RAP content.

According to the variation trend of high-temperature performance of HMRAM with DOB, it can be inferred that a higher DS presented by HMRAM with a high RAP content is not necessarily safe at the design stage because the DOB will gradually increase after construction based on Carpenter and Wolosick [14]; thus, its DS value will also gradually decrease. The final high-temperature performance may not meet the requirements. Therefore, it is suggested that an HMRAM specimen with a complete blending state be used to measure the high-temperature performance for HMRAM with a high RAP content. HMRAM can be prepared by mixing the virgin binder and aggregate with a completely separating RAP binder and old aggregate using the RAP extraction method.

We try to analyze the reasons why DOB affects high-temperature performance of HMRAM based on the change of content and properties of free binder in HMRAM. According to the results in Section 3.2, when DOB increases, more RAP binders are converted to free binders, which leads to an increase of total free binder in HMRAM. The properties of free binder are also change. It may be the important reason affecting the pavement performance of HMRAM.

The example of HMRAM with a 30% RAP content showed in Table 14 is discussed. With the DOB increasing from 70% to 100%, the total free binder content increases from 4.00% to 4.40%, while the excess rejuvenator content decreases from 0.02% to 0.00%. Figure 6(a) shows that the increase of total free binder content will increase VMA and binder film thickness. Recent research (documented in NCHRP Report 567) suggests that rut resistance of asphalt concrete mixtures decreases with increasing VMA and apparent film thickness. Therefore, the high-temperature

performance will decrease with the total free asphalt. The reduction in the excess rejuvenator content makes the free binder at 70% DOB softer than that at 100% DOB. In general, the softening of asphalt binder will reduce the high-temperature performance of mixtures. Therefore, the changes in the total free binder content and properties have the opposite effects on the high-temperature performance of HMRAM. The results shown in Figure 6(a) indicate that the increase of total free binder has a great impact.

When DOB remains unchanged and RAP content changes, the example of 85% DOB showed in Table 12 is discussed. The RAP content decreases from 50% to 30%, the total free binder content increases from 4.07% to 4.2%, while the excess rejuvenator content decreases from 0.017% to 0.010%. Similar to the analysis above, the changes in the total free binder content and properties also have the opposite effects on high-temperature performance of HMRAM. The change of total free binder has a greater impact based on Figure 6(a).

When the DOB approaches 100%, the DS values of HMRAM with three RAP contents are nearly similar, based on Table 17 and Figure 6(a). The other three pavement performance indicators present similar trends. We use variance of analysis (ANOVA) to determine the significance of effect of the RAP content on high-temperature performance under 100% DOB. The results of the calculation are shown in Table 18. It presents statistical significant difference for the pavement performance of HMRAM with different RAP contents under 100% DOB, especially for fatigue performance.

In this study, the HMRAM specimens with 100% DOB are prepared by mixing the virgin binder and aggregate with a complete separating RAP binder and old aggregate using the RAP extraction method. The RAP binder coated outside the old aggregate is extracted completely and uniformly mixed with virgin binder and rejuvenator; therefore, avoiding the heterogeneous binder across the mixture. For HMRAM with different RAP contents, the gradation of aggregates, the properties and the content of mixed binder

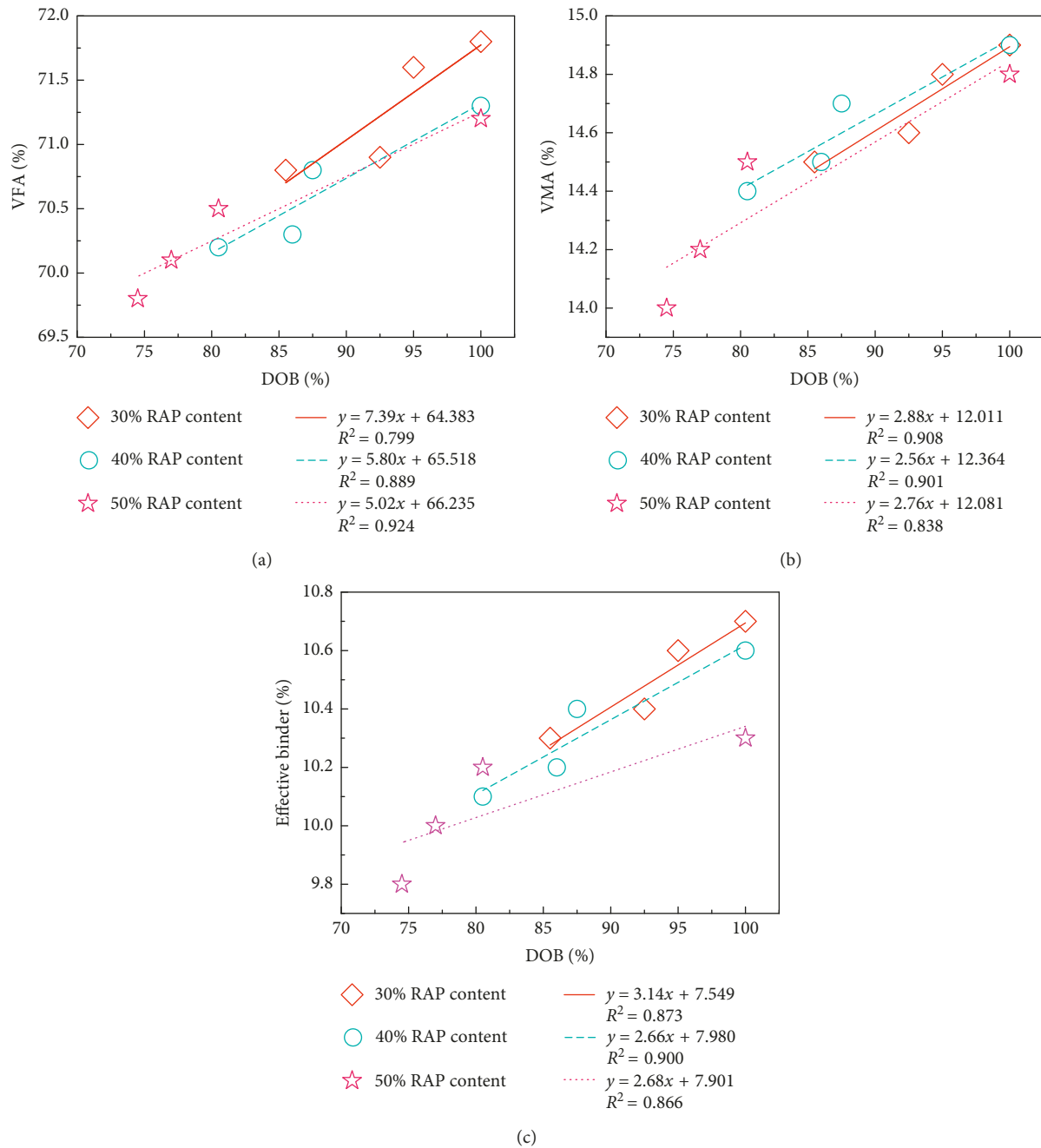


FIGURE 4: The relationship between VMA, VFA, and effective binder volume and DOB.

TABLE 15: Results of ANOVA with dual-factor repeated test ( $\alpha = 0.05$ ).

Pavement performance	Factors	F	F <sub>crit</sub>	F vs. F <sub>crit</sub>	Results
Dynamic stability	Mixing temperature	224.07	3.35	$F > F_{crit}$	Significance
	RAP content	2221.46	3.35	$F > F_{crit}$	Significance
TSR	Mixing temperature	234.06	3.35	$F > F_{crit}$	Significance
	RAP content	2082.01	3.35	$F > F_{crit}$	Significance
Flexural failure strain	Mixing temperature	13.31	3.35	$F > F_{crit}$	Significance
	RAP content	178.37	3.35	$F > F_{crit}$	Significance
Fatigue life	Mixing temperature	25277.95	3.35	$F > F_{crit}$	Significance
	RAP content	2591114.44	3.35	$F > F_{crit}$	Significance

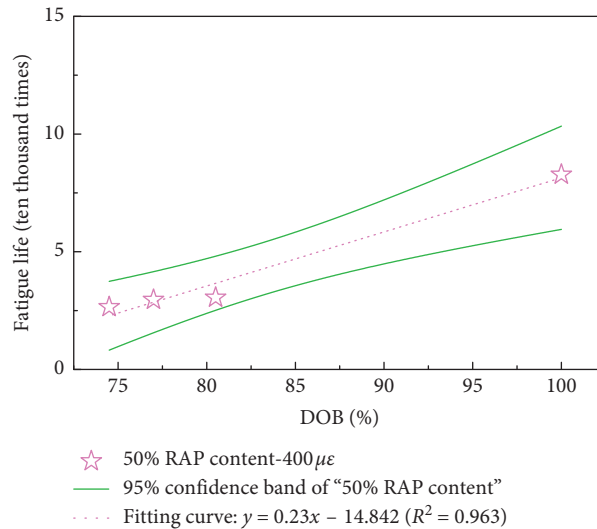


FIGURE 5: Confidence interval of the fitting curve between DOB and pavement performance.

are all the same. The only difference is the proportion of the old aggregate. No RAP binder is coated outside the old aggregate at this time after extraction. Regarding the old aggregate, its physical properties such as angularity, and strength deteriorate with an increase in service periods. Its properties are also different from those of virgin aggregate used in this research. The crushing value and Los Angeles wear loss of old aggregates are worse than those of virgin aggregates, as indicated in Tables 2 and 5. Therefore, when the content of old aggregates varies considerably for HMRAM with different RAP contents, it may slightly influence the performance of HMRAM. However, the rules of influence do not have to be further studied in the future.

(3) *Moisture Stability, Low-Temperature Performance, and Fatigue Performance.* Figures 6(b)–6(d) show the similar effects of DOB on moisture stability, low-temperature performance, and fatigue performance. The three performance indicators increase with an increase in the DOB for HMRAM with the same RAP content and decrease with an increase in the RAP content for HMRAM with the same DOB. If the moisture stability, low-temperature performance, and fatigue performance of HMRAM meets the requirements of specification at the design stage, there is no risk that these pavement performances of HMRAM will decrease with an increase in DOB after construction. Therefore, the moisture stability, low-temperature performance, and fatigue resistance performance of HMRAM measured at the design stage is reasonable and conservative.

As for different RAP contents, the statistical analysis results listed in Table 18 indicate that the curve slopes of 30% and 50% RAP blending rates are significantly different. The change of DOB has a greater impact on moisture stability, low-temperature performance, and fatigue performance of

HMRAM with a high RAP content than that with a low RAP content.

When DOB or RAP content changes, the content and properties of the total free binder in HMRAM are also important factors affecting moisture stability, low-temperature performance, and fatigue performance. Considering the fatigue performance as an example, recent research (documented in NCHRP Report 567) suggests that the primary HMA mixture design factor affecting fatigue life is the effective volumetric binder content of the mixture (VBE). For a given pavement, fatigue life increases with VBE. Considering 50% RAP content as an example, when DOB increases from 74.5% to 100%, total free binder increases. The VBE increased from 9.8% to 10.5%. Although the total free binder is stiffer, the fatigue life of HMRAM increases significantly from 26,534 times to 82,751 times. However, as analyzed in the previous section, we cannot ignore the influence of the difference of the ratio of RAP aggregate on the fatigue performance of HMRAM with different RAP contents.

According to recent studies, when partial blending status is observed between RAP binder and virgin binder, the distribution of total free binder in the blending zone is heterogeneous (Figure 7). The free binder near RAP aggregate is stiffer and that far from RAP aggregate is softer. In this paper, we suggest that the content of total free asphalt will vary with DOB by calculating and measuring the changes of VMA, VFA, and VBE. We also infer that the increasing content of aged RAP binder with DOB results in hardening of total free binder. However, this is only a qualitative explanation for the whole properties of total free binder. In fact, the specific effect of the heterogeneous distribution of free binder on HMRAM with partial blending state is very complex, and further research is required. Simultaneously, when the RAP content is different, the physical properties of the old aggregate such as

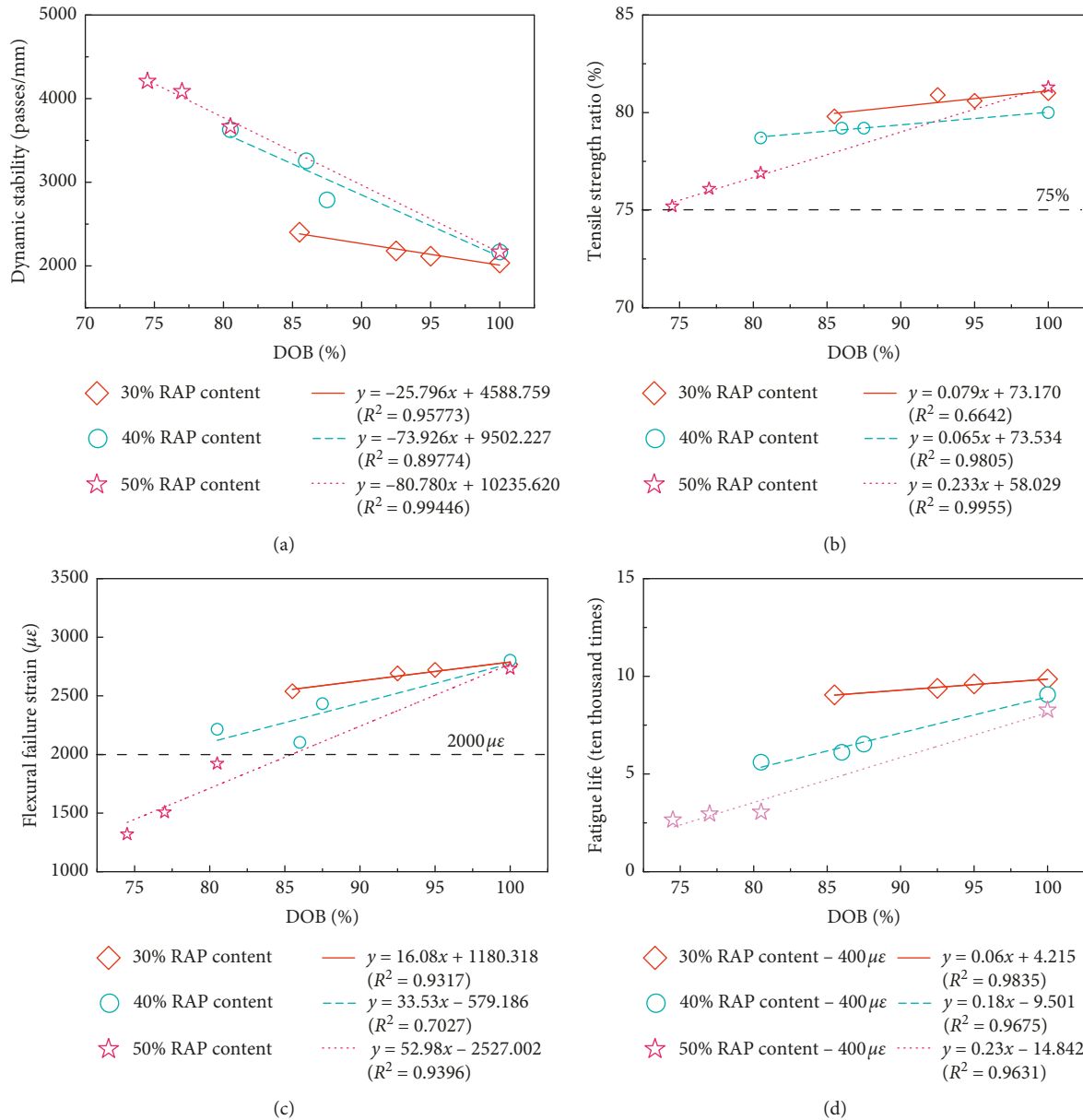


FIGURE 6: Influences of the DOB on the pavement performance. (a) Dynamic stability; (b) moisture stability; (c) low-temperature performance; (d) fatigue performance.

TABLE 16: ANCOVA results of slope difference for different RAP contents.

Pavement performance	RAP contents		
	30% vs. 40%	40% vs. 50%	30% vs. 50%
Dynamic stability	0.048 (Sig.)	0.626	0.001 (Sig.)
TSR	0.621	0.000 (Sig.)	0.005 (Sig.)
Flexural failure strain	0.289	0.233	0.036 (Sig.)
Fatigue life	0.006 (Sig.)	0.273	0.012 (Sig.)

TABLE 17: Mean value of pavement performance under 100% DOB.

RAP content (%)	Dynamic stability (passes/mm)	TSR (%)	Flexural failure strain ( $\mu\epsilon$ )	Fatigue life (times)
30	2035	81.0	2769	98564
40	2166	80.0	2803	90568
50	2168	81.3	2732	82751

TABLE 18: Results of ANOVA ( $\alpha = 0.05$ ).

Pavement performance	Factors	$F$	$F_{crit}$	$F$ vs. $F_{crit}$	Results
Dynamic stability	RAP content	24.99	4.26	$F > F_{crit}$	Significance
TSR	RAP content	25.27	4.26	$F > F_{crit}$	Significance
Flexural failure strain	RAP content	7.06	4.26	$F > F_{crit}$	Significance
Fatigue life	RAP content	1314.87	4.26	$F > F_{crit}$	Significance

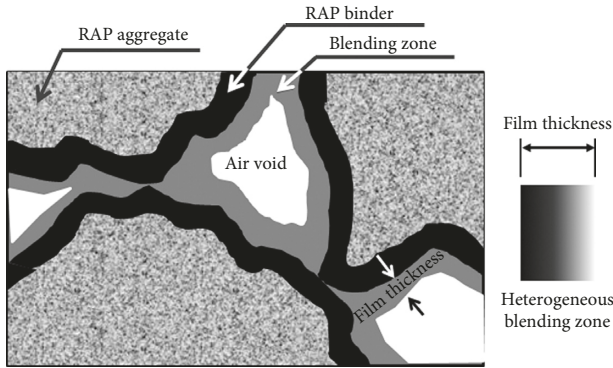


FIGURE 7: Microstructure of heterogeneous blending zone.

angularity and strength, are also different from those of the virgin aggregate. Therefore, its content will also have a significant impact on the performance of HMRAM.

#### 4. Conclusions and Recommendations

In this study, the influence of the DOB between the virgin and aged binder on high-temperature, low-temperature, moisture stability, and fatigue resistance performance of HMRAM with different high RAP contents and mixing methods are investigated. The main conclusions are summarized as follows:

- (1) The DOBs are between 85.5~95%, 80.5~87.5%, and 74.5~80.5% at the three mixing temperatures for HMRAM with 30, 40, and 50%, which is inconsistent with the assumption of a complete blending state in the China specification. The current specifications for the HMRAM design are unsuitable for usage. Therefore, it is necessary to adjust the mixing process and determine the DOB between the virgin binder and RAP binder according to the method proposed in this study. Then, on the premise of avoiding secondary aging, the optimal mixing process should be determined based on the maximum DOB.
- (2) The dynamic stability of the mixture gradually decreases with the increase of the DOB for HMRAM with a high RAP content, while the moisture stability, low-temperature, and fatigue resistance performance are continuously improved. Therefore, it is suggested that HMRAM with a complete blending state be used to measure the high-temperature performance. The moisture stability, low-temperature performance, and fatigue resistance performance of HMRAM measured at the design stage is reasonable and conservative.

- (3) With the change in the DOB between the virgin binder and RAP binder, the content and properties for the total free binder in HMRAM are the important factors affecting pavement performance. The content and physical properties of the RAP aggregate such as angularity and strength also have a significant impact on the performance of HMRAM.

The following improvements for this study should be made in the future. Only HMRAM with 30%, 40%, and 50% RAP contents are discussed in this paper, which corresponds to a gradation of AC-16. More types of mixture with a higher RAP content should be studied. A simpler design method of HMRAM should be proposed in the future. The specific effect of the heterogeneous distribution of free binder on HMRAM with partial blending state is very complex, and further research is needed. The content and physical properties of old aggregate in RAP materials may have an important influence on pavement performance of HMRAM with a high RAP content. Related research is also needed in the future.

#### Data Availability

The data used to support the findings of this study are available from the corresponding author upon request.

#### Conflicts of Interest

The authors declare no conflicts of interest.

#### Acknowledgments

This research was funded by the Science and Technology Project of Beijing Education Commission (SQKM201810016003) and the Fundamental Research Project of Universities Affiliated to Beijing Education Commission (FZ01-48).

#### References

- [1] H. Song-Chang, P. Ming-Wen, and J. Xu, "Application of asphalt pavement recycling technology at home and abroad," *Highway Transportation Technology*, vol. 2006, no. 11, pp. 5-8, 2006.
- [2] I. L. Al-Qadi, M. Elseifi, and S. H. Carpenter, "Reclaimed asphalt pavement—a literature review," Tech. Report No. FHWA-ICT-07-001, Illinois Department of Transportation, Springfield, IL, USA, 2007.
- [3] B. Huang, G. Li, D. Vukosavljevic, X. Shu, and B. Egan, "Laboratory investigation of mixing hot-mix asphalt with reclaimed asphalt pavement," *Transportation Research*

- Record: Journal of the Transportation Research Board*, vol. 1929, no. 1, pp. 37–45, 2005.
- [4] B. F. Bowers, B. Huang, Q. He, X. Shu, X. Jia, and B. C. Miller, “Investigation of sequential dissolution of asphalt binder in common solvents by FTIR and binder fractionation,” *Journal of Materials in Civil Engineering*, vol. 27, no. 8, Article ID 04014233, 2015.
  - [5] S. Zhao, B. Huang, X. Shu, and M. E. Woods, “Quantitative evaluation of blending and diffusion in high RAP and RAS mixtures,” *Materials & Design*, vol. 89, pp. 1161–1170, 2016.
  - [6] I. L. Al-Qadi, S. H. Carpenter, G. Roberts et al., “Determination of usable residual asphalt binder in RAP,” Research Report ICT-R27-11, Illinois Center for Transportation, Rantoul, IL, USA, 2009.
  - [7] T. Bennert and R. Dongré, “Backcalculation method to determine effective asphalt binder properties of recycled asphalt pavement mixtures,” *Transportation Research Record: Journal of the Transportation Research Board*, vol. 2179, no. 1, pp. 75–84, 2010.
  - [8] S. Parashant, Y. A. Mehta, and A. Nolan, “A study to determine the degree of partial blending of reclaimed asphalt pavement (RAP) binder for high RAP hot mix asphalt,” in *Proceeding of the transportation research board, 89th annual meeting*, Washington, DC, USA, January 2010.
  - [9] R. Bonaquist, “Laboratory evaluation of hot mix asphalt (HMA) mixtures containing recycled or waste product materials using performance testing,” Report FHWA-PA-2005-006+98-32(19), Pennsylvania Department of Transportation, Harrisburg, PA, USA, 2005.
  - [10] A. Shah, R. S. McDaniel, G. Huber, and V. Gallivan, “Investigation of properties of plant-produced RAP mixtures,” *Journal of the Transportation Research Board: Journal of the Transportation Research Board*, vol. 1998, no. 1, pp. 103–111, 2007.
  - [11] G. R. Kemp and N. H. Predoehl, “A comparison of field and laboratory environments on asphalt durability,” in *Proceedings of the Association of Asphalt Paving Technologists*, vol. 50, pp. 492–537, San Diego, CA, USA, 1981.
  - [12] I. L. Al-Qadi, S. H. Carpenter et al., “Determination of usable residual asphalt binder in RAP,” Report No. FHWA-ICT-09-031, Illinois Department of Transportation, Springfield, IL, USA, 2009.
  - [13] Q. Aurangzeb, I. L. Al-Qadi, I. M. Abuawad, W. J. Pine, and J. S. Trepanier, “Achieving desired volumetric and performance for high RAP mixtures,” in *Proceedings of the TRB Annual Meeting*, Washington, DC, USA, January 2012.
  - [14] S. H. Carpenter and J. R. Wolosick, “Modifier Influence in the Characterization of Hot-Mix Recycled Material,” pp. 15–22, Transportation Research Board, Washington, DC, USA, 1980.
  - [15] A. S. Noureldin and L. E. Wood, “Rejuvenator diffusion in binder film for hot-mix recycled asphalt pavement,” in *Transportation Research Record: Journal of the Transportation Research Board*, pp. 51–61, no. 1115, Transportation Research Board of National Academies, Washington, DC, 1987.
  - [16] R. S. McDaniel, H. Soleymani, R. M. Anderson, P. Turner, and R. Peterson, “Recommended use of reclaimed asphalt pavement in the superpave mixture design method,” NCHRP Final Report (9–12), TRB, Washington, DC, USA, 2000.
  - [17] J. E. Stephens, J. Mahoney, and C. Dippold, “Determination of the PG binder grade to use in a RAP mix,” Report No. JHR 00-278, Connecticut Department of Transportation, Newington, CT, USA, 2001.
  - [18] S. Coffey, E. Dubois, Y. A. Mehta, and C. Purdy, “Determining impact of blending between virgin and reclaimed asphalt binder on predicted pavement performance using mechanistic-empirical pavement design guide,” in *Proceedings of the 92nd annual meeting compendium of papers*, p. 17, Transportation research board, Washington, DC, USA, January 2013.
  - [19] K. Zhang and B. Muhunthan, “Effects of production stages on blending and mechanical properties of asphalt mixtures with reclaimed asphalt pavement,” *Construction and Building Materials*, vol. 149, pp. 679–689, 2017.
  - [20] P. Kriz, D. L. Grant, B. A. Gale et al., “Blending and diffusion of reclaimed asphalt pavement and virgin asphalt binders,” *Road Materials and Pavement Design*, vol. 15, no. 1, pp. 78–112, 2014.
  - [21] F. Y. Rad, N. R. Sefidmazgi, and H. Bahia, “Application of diffusion mechanism,” *Transportation Research Record: Journal of the Transportation Research Board*, vol. 2444, no. 1, pp. 71–77, 2014.
  - [22] F. B. Bowers, “Investigation of asphalt pavement mixture blending utilizing analytical chemistry techniques,” Doctoral Dissertations University of Tennessee, Knoxville, Tenn, USA, 2013.
  - [23] B. Huang, X. Shu, and D. Vukosavljevic, “Laboratory investigation of cracking resistance of hot-mix asphalt field mixtures containing screened reclaimed asphalt pavement,” *Journal of Materials in Civil Engineering*, vol. 23, no. 11, pp. 1535–1543, 2011.
  - [24] X. Shu, B. Huang, E. D. Shrum, and X. Jia, “Laboratory evaluation of moisture susceptibility of foamed warm mix asphalt containing high percentages of RAP,” *Construction and Building Materials*, vol. 35, pp. 125–130, 2012.
  - [25] S. Zhao, B. Huang, X. Shu, X. Jia, and M. Woods, “Comparative evaluation of warm mix asphalt containing high percentages of reclaimed asphalt pavement,” *Construction and Building Materials*, vol. 44, pp. 92–100, 2013.
  - [26] R. Karlsson and U. Isacson, “Laboratory studies of diffusion in bitumen using markers,” *Journal of Materials Science*, vol. 38, no. 13, pp. 2835–2844, 2003.
  - [27] C. Zhang, S. Shen, and X. Jia, “Modification of the Hirsch dynamic modulus prediction model for asphalt mixtures,” *Journal of Materials in Civil Engineering*, vol. 29, no. 12, Article ID 04017241, 2017.
  - [28] National Academies of Sciences, Engineering, and medicine, “A Manual for Design of Hot-Mix Asphalt with Commentary,” The National Academies Press, Washington, DC, USA, 2011.
  - [29] S. N. Nahar, M. Mohajeri, A. J. M. Schmets, A. Scarpas, M. F. C. van de Ven, and G. Schitter, “First observation of the blending zone morphology at the interface of reclaimed asphalt binder and virgin bitumen,” *Transportation Research Record: Journal of the Transportation Research Board*, vol. 2370, no. 1, pp. 1–9, 2013.

## Research Article

# Properties and Components of Recycled Engine Oil Bottom Rejuvenated Asphalt and Its Grey Relationship Analysis

Jin Li <sup>1</sup>, Miaozhang Yu <sup>1</sup>, Xinzhuang Cui,<sup>1,2</sup> and Wentong Wang<sup>3</sup>

<sup>1</sup>School of Transportation Civil Engineering, Shandong Jiaotong University, Jinan 250357, Shandong, China

<sup>2</sup>School of Civil Engineering, Shandong University, Jinan 250061, Shandong, China

<sup>3</sup>School of Highway, Chang'an University, Xi'an 710064, China

Correspondence should be addressed to Jin Li; [sdzblijin@163.com](mailto:sdzblijin@163.com) and Miaozhang Yu; [sdjnyumz@163.com](mailto:sdjnyumz@163.com)

Received 30 April 2019; Accepted 23 June 2019; Published 2 September 2019

Guest Editor: Jose Norambuena-Contreras

Copyright © 2019 Jin Li et al. This is an open access article distributed under the Creative Commons Attribution License, which permits unrestricted use, distribution, and reproduction in any medium, provided the original work is properly cited.

Numerous environmental pollution and resource waste problems are associated with recycled engine oil bottom (REOB), which cannot be effectively recycled. Based on the similarity compatibility theory and component adjustment theory, comparing the physical and rheological properties of laboratory-aged asphalt under three types of REOB (defined as REOB-1, REOB-2, and REOB-3) with different dosages, the optimum type and dosage of REOB as asphalt regenerant were explored. The rejuvenation mechanism of REOB on aged asphalt was revealed by combined performance, four-component, and infrared spectroscopy analyses. The relationship between the four components and physical rheological indexes in the process of asphalt rejuvenated by REOB was quantitatively obtained by the grey relationship analysis. The results show that only REOB-3 with a dosage of 7% on the aged asphalt has the best comprehensive rejuvenation effect. Also, the high-temperature rutting resistance of rejuvenated asphalt with 7% REOB-3 is better than that of the original asphalt, but the low-temperature flexibility and the crack resistance performance have yet to be improved. The mechanism through which REOB rejuvenates aged asphalt is an incomplete component adjustment; some of the components undergo physical or chemical reactions and transformations. Accordingly, the asphaltene content and the intensity of sulfoxide functional groups in aged asphalt decrease, thereby achieving rejuvenation gradually with the addition of REOB. A grey relationship analysis demonstrates that asphaltenes have the greatest influence on high-temperature performance and that low-temperature performance requires a reasonable combination of four components. Moreover, a comprehensive advantage analysis reveals that REOB is the most sensitive to the softening point and that the asphaltene content has the greatest influence on the physical and rheological properties of REOB-rejuvenated asphalt. Therefore, the asphaltene content should be strictly controlled during the addition of REOB to rejuvenate aged asphalt.

## 1. Introduction

Oxidation, product wear, pollutant mixing, additive consumption, and water absorption all occur throughout the use of engine oil, leading to the decline in the functionality of the oil; unfortunately, these processes invalidate the production of recycled engine oil (REO). In most developed industrial countries at present, REO is primarily subjected to standardized recycling into fuel oil or lubricant oil through various recovery technologies, including ultrafiltration, centrifugal separation, molecular distillation, flocculation treatment, and solvent refining [1]. However, the traditional sulfuric acid-clay regeneration process is still widely used in

China, although some improved regeneration processes, such as distillation-clay refining [2] and distillation-hydrotreating [3], have also been developed in recent years; these new technologies not only improve the quality and efficiency of REO regeneration but also reduce the secondary pollution of acid residue, wastewater, and waste gas in traditional recycling process [1]. Generally, 70–80% of REO can be effectively recycled by the aforementioned processes. However, the remaining residue (accounting for 20–30%) cannot be effectively recycled due to the presence of many impurities; this residue is ultimately called recycled engine oil bottom (REOB). Various functional additives in engine oil containing sulfur, calcium, zinc, phosphorous, and

molybdenum in addition to oxidation products and metals (including mainly iron and copper) that become worn during engine operation all remain in REOB after these regeneration processes; consequently, REOB cannot be effectively utilized. Currently, REOB is mainly treated by directly discarding, burying, or burning the residue, all of which lead to irreparable pollution of the soil, water, and atmosphere; this pollution is detrimental to human health and could even cause cancer once it comes into contact with the human body. Therefore, REOB has been listed as one of the three main control points in the field of environmental protection for the 21st century, and thus, an effective recycling and treatment procedure for REOB is urgently needed [1, 2].

Research on the use of REO and REOB in asphalt materials has already begun both domestically and internationally. Villanueva et al. [4] used different REO contents to soften asphalt and found that the addition of REO increases the penetration of asphalt, decreases the softening point, and reduces the high-temperature performance of asphalt after softening but also significantly improves the low-temperature performance. Through a rheological test on Trinidad Lake Asphalt mixed with different amounts of REO, Ackbarali and Maharaj [5] proved that REO can be used as a modifier to soften hard asphalt. Furthermore, Dedene [6] used REO to modify reclaimed asphalt binders and carried out rutting tests and tensile strength ratio tests on the corresponding asphalt mixture; the results showed that REO can be used as a rejuvenating agent to chemically restore the properties of asphalt pavements containing reclaimed asphalt pavements. In addition, Jia et al. [7] studied the infrared spectra and rheological properties of different asphalt binders containing REO and analysed the microcosmic interactions of REO and different types of asphalt binders. Moreover, Xu [8] studied the pavement performance of an REO-rejuvenated asphalt mixture and analysed its economic and social benefits. In conclusion, research on the modification or rejuvenation of asphalt binders with REO has achieved moderate success. The technology through which REO is employed to regenerate lubricating oil advances daily, and the production source of lubricating oil depends largely on crude oil [1]. Currently, the application of REO to regenerate lubricating oil is more economical, energy-friendly, and promotional than the application of REO in asphalt materials. However, an effective method for utilizing the REOB that remains after the regeneration of REO has yet to be developed, and thus, it will be more necessary to develop application prospects for REOB by conducting research on the use of REOB in asphalt materials.

Through X-ray fluorescence analysis in Canada, Hesp and Shurvell [9] confirmed that REOB can be used in asphalt binders and discussed the adverse effects of REOB on the early cracking of asphalt pavement. Rubab et al. [10] conducted rolling thin film oven (RTFO) and pressure ageing vessel (PAV) tests after mixing REOB with two different types of asphalt binders in Canada and found that REOB may accelerate the oxidation speed of modified asphalt while improving the performance grade of asphalt binders. Ding

et al. [11] used REOB produced by vacuum distillation and atmospheric distillation processes in China to modify straight asphalt; by employing the extended ageing test, it was found that REOB is unfavourable to the ductile fracture performance and cracking resistance performance of asphalt at low temperatures. However, previous studies on REOB are limited to the modification of an asphalt matrix. Moreover, insufficient research has been conducted on the relationship and correlation mechanism between REOB and asphalt binders. In addition, the properties of REOB may vary widely with source and regeneration process, thereby affecting asphalt modification and action performance. Therefore, it is necessary to carry out systematic studies on several types of REOB used for aged asphalt, particularly because the application of REOB to the rejuvenation of aged asphalt can broaden the effective utilization of REOB and have great economic and engineering significance for reclaimed asphalt pavement (RAP).

In this paper, three types of REOB were selected from the recycling plant. Physical and rheological tests were carried out in addition to four-component and infrared spectroscopic analyses on aged asphalt containing various REOB contents. Upon comparing and analysing the rejuvenation effects of aged asphalt blended with different dosages of REOB, the correlation mechanism between REOB and aged asphalt was revealed based on the combined performance, component, and structure. Furthermore, the relationship between the properties and components of rejuvenated asphalt with REOB was established by means of grey relationship analysis. To explore the feasibility of utilizing REOB for rejuvenating asphalt, this study provides a basis for further research into the application of waste oil to rejuvenate asphalt binders.

## 2. Materials and Methods

**2.1. Raw Materials.** In China, the chemical compositions and properties of REOB produced by different REO regeneration processes may vary greatly due to the different sources of REO and the different degrees of oxidation and wear during their use. Three types of REOB were recovered from a large REO treatment plant after pretreatment and atmospheric and vacuum distillation. Their basic properties and chemical components are shown in Table 1, respectively. The 70-A petroleum asphalt binders, which are widely used in North China, were selected as the control binders; their main technical properties are shown in Table 2.

**2.2. Preparation of the Aged Asphalt Binders.** According to the standard highway engineering testing specification of China for asphalt and asphalt mixtures (JTG E20-2011), an RTFO test was used to simulate the short-term ageing of the original asphalt mixture during mixing and paving. Similarly, a PAV test was used to simulate the long-term ageing of an asphalt pavement in service for 5 years [12]. Finally, the aged asphalt binders were obtained by implementing a PAV test after an RTFO test on the original 70-A asphalt binders.

TABLE 1: Basic properties and chemical components of three types of REOB.

Type	Colour	Viscosity (60°C, cSt)	Density (25°C, g/cm <sup>3</sup> )	Asphaltenes (%)	Resins (%)	Aromatics (%)	Saturates (%)
REOB-1	Brown	293	0.873	0.9	6.8	73.1	19.2
REOB-2	Black brown	535	0.912	8.1	0.1	91.7	0.1
REOB-3	Reddish brown	340	0.885	0.2	15.5	83.5	0.8

TABLE 2: Properties indices of 70-A matrix asphalt binders.

Indices	Test results	Engineering requirements	Test methods	
Penetration (25°C, 0.1 mm)	71	60~80	JTG E20-2011 T0604	
Softening point (°C)	48.7	≥46	JTG E20-2011 T0606	
Ductility (10°C, cm)	22	≥20	JTG E20-2011 T0605	
Brookfield viscosity (135°C, Pa·s)	0.397	—	JTG E20-2011 T0625	
	Mass loss (%)	-0.12	-0.8~0.8	JTG E20-2011 T0610
After RTFO (163°C, 75 min)	Penetration ratio (%)	65.3	≥61	JTG E20-2011 T0604
	Ductility (10°C, cm)	7.2	≥6	JTG E20-2011 T0605

**2.3. Preparation of the Rejuvenated Asphalt Binders.** The aged asphalt binders were heated to 150°C in an oven while adding 3%~8% (mass ratio of aged asphalt) REOB with an interval of 1%. To prepare different proportions of REOB-rejuvenated asphalt during this preparation process, the blended samples consisting of aged asphalt binders and REOB were continuously stirred by a glass rod until the REOB was evenly dispersed within the aged asphalt binders.

**2.4. Physical Property Tests.** To evaluate the influences of the various physical characteristics of REOB on aged asphalt, the conventional physical indices of aged asphalt containing REOB of different contents, including the 25°C penetration, softening point, and 10°C ductility, were tested in accordance with JTG E20-2011 specifications T0604, T0606, and T0605.

**2.5. Rheological Property Tests.** The rutting factor ( $G^*/\sin \delta$ ) obtained by a dynamic shear rheometer (DSR) was used to characterize the high-temperature stability of different proportions of REOB-rejuvenated asphalt according to JTG E20-2011 T0628; the rejuvenated asphalt was measured at a fixed frequency of 10 rad/s with increments of 6°C in the strain control mode. Moreover, the creep stiffness ( $S$ ) and creep rate ( $m$ ) obtained by a bending beam rheometer (BBR) were used to characterize the low-temperature crack resistance of the aged asphalt binders with different content of REOB in accordance with JTG E20-2011 T0627, in which the test temperatures were -12°C, -18°C, and -24°C.

**2.6. Four-Component Analysis.** Four-component analysis was carried out on the asphalt binders and REOB by using the rod-thin-layer chromatography/hydrogen flame method. The specific testing steps are described as follows. The samples were dissolved in toluene and prepared in solutions of 30 mg/mL. Next, samples 0.8–1.0  $\mu$ L in volume were placed into the 15 mm chromatographic rod five to six times, and the diameter of each point sample was controlled at 1–3 mm. Then, the chromatographic frame was placed into

three types of mixtures composed of *N*-heptane, toluene, and toluene/ethanol (volume ratio 55:45) and expanded in sequence on the expansion table. After each expansion, the chromatographic frame was dried, kept warm, and moisturized until the next expansion. Finally, after three rounds of expansion, the chromatographic frame was tested and analysed by a rod-thin-layer chromatography analyser.

**2.7. Infrared Spectra Test.** The molecular structures and functional groups of asphalt binders and REOB were analysed by Fourier transform infrared (FTIR) spectrometry. The specific steps of the test are described as follows. The samples were dissolved in carbon disulfide (CS<sub>2</sub>), an organic solvent, with a concentration of 5 wt.%. Then, one drop of the prepared solution was dropped into a small groove with a diameter of 10 mm on a potassium bromide wafer. After evaporating the CS<sub>2</sub>, the sample film was tested by FTIR spectrometry. The test employed scanning wavenumbers of 4000–500 cm<sup>-1</sup>, and a total of 64 scans were performed.

### 3. Results and Discussion

#### 3.1. Physical Properties

**3.1.1. Penetration.** As one of the important classification indices of asphalt binders, the penetration, which represents the conditional viscosity of an asphalt binder at a specified temperature, can reflect the degree of softening and consistency of an asphalt binder. Figure 1 shows the influence of three types of REOB on the penetration of aged asphalt under different contents. Figure 1 explains that the penetration of the aged asphalt binders increases with the addition of all three types of REOB, which indicates that REOB can soften aged asphalt and reduce its consistency and viscosity. However, the improvement effect of the three types of REOB differs. Among the types of REOB analysed, the increase degree of REOB-1 is the largest, and the rate of increase is basically unchanged throughout the process; the increase degree of REOB-2 is the smallest, and when both the content of REOB-2 and REOB-3 ranges from 3% to 6%, the rate of increase is obviously higher than that when the

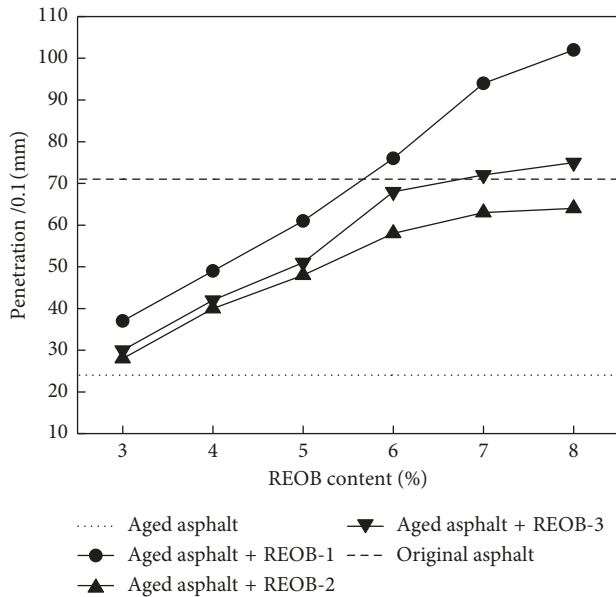


FIGURE 1: Influence of three types of REOB on penetration of aged asphalt.

content ranges from 6% to 8%. Furthermore, when REOB-1 content is 6% and REOB-3 content is 7%, penetration can be restored to the original asphalt level; when REOB-2 content is more than 6%, penetration tends to be stable and lower than that of the original asphalt. These differences are observed because the viscosities of all three types of REOB are lower than that of aged asphalt; thus, REOB can infiltrate deeper to aged asphalt, thereby softening and increasing the overall penetration.

**3.1.2. Softening Point.** The softening point represents the temperature of an asphalt binder when it reaches a certain viscosity under a particular test condition. A higher softening point represents a greater asphalt viscosity and a better stability at high temperatures. The influences of the three types of REOB on the softening point of aged asphalt are illustrated in Figure 2, which demonstrates that the softening point of aged asphalt binders decreases with an increase in REOB dosage ranging from 3% to 7%. Moreover, when the dosage of REOB-1 reaches 6% and the dosage of REOB-3 reaches 7%, the softening points of the corresponding aged asphalt binders decrease to nearly the level of an original 70-A asphalt, thereby showing that the high-temperature viscosity and stability of binders are reduced by the addition of REOB. When the three REOB contents all reach 8%, the softening point of aged asphalt continued to decrease with REOB-2, but the decrease rate of that obviously slowed; conversely, both REOB-1 and REOB-3 increase the softening point of binders to a certain extent, indicating increases in both high-temperature stability and viscosity. However, there is a difference between the penetration analysis in Section 3.1.1 and the above analysis at an 8% dosage of both REOB-1 and REOB-3. The possible reason for this difference is that an oil film forms on the surface of aged asphalt samples containing 8%

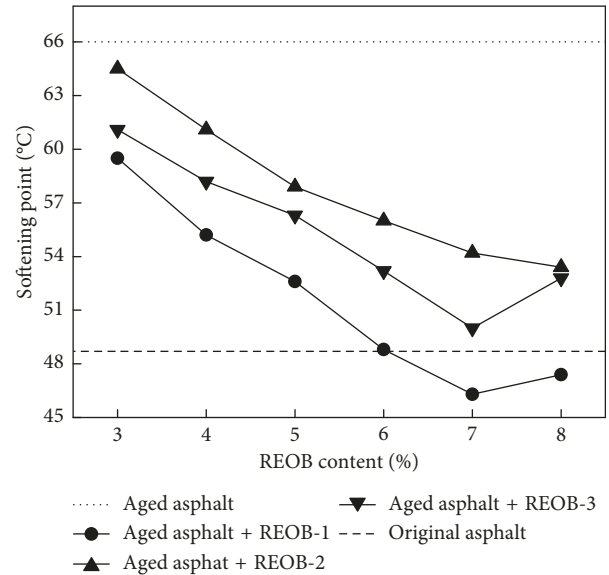


FIGURE 2: Influence of three types of REOB on softening point of aged asphalt.

REOB-1 or 8% REOB-3 that are kept at room temperature over a period of time. As a result, the penetration value is affected by the thickness of the surface oil film, and the formation of the surface oil film has an impact on the softening point of asphalt binders.

**3.1.3. Ductility.** The ductility is an index used to evaluate the plastic deformation capacity of asphalt; this index can measure the ability to undergo tensile deformation without being destroyed under an external force. The influences of three types of REOB on the ductility of aged asphalt are displayed in Figure 3, which shows that the ductility of aged asphalt binders with an REOB dosage ranging from 3% to 7% increases with an increase in REOB dosage, revealing that the plastic deformation and crack resistance of binders at low temperatures will gradually increase with the increase in REOB dosage. In addition, when the REOB content reaches 7%, the ductility of aged asphalt with REOB-3 increases to nearly the level of an original 70-A asphalt; REOB-1 maximizes the ductility of aged asphalt but cannot meet the requirements of the asphalt pavement specification. However, when the amount of REOB reaches 8%, the ductility of aged asphalt with REOB-2 continues to increase but remains much lower than that of the original asphalt. Additionally, the ductility of aged asphalt binders containing either 8% REOB-1 or 8% REOB-3 suddenly decreases, which clearly indicates that the low-temperature crack resistance of binders is poor, which is not in accordance with the technical pavement performance requirements.

**3.1.4. Determination of the REOB Optimal Type and Dosage.** A comprehensive analysis of the penetration, softening point, and ductility indices shows that the three types of REOB have a certain recovery effect on the physical properties of aged asphalt and that the recovery effect is closely

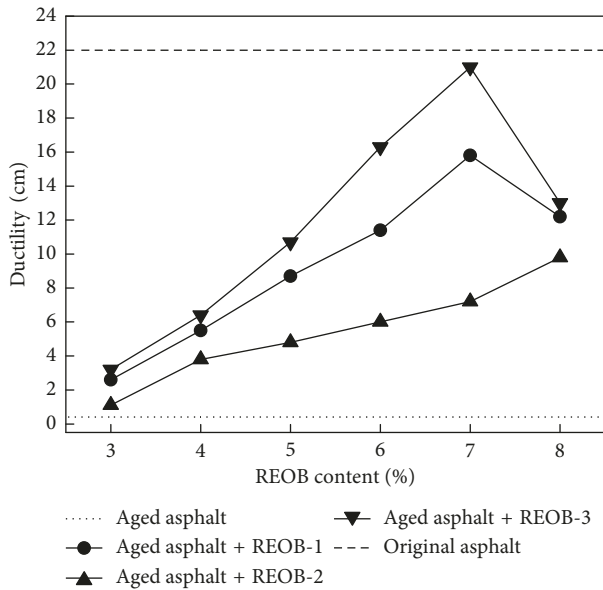


FIGURE 3: Influence of three types of REOB on ductility of aged asphalt.

related to the type and content of REOB. With these three conventional physical indices of an original 70-A asphalt as benchmark values, the ratios between the three conventional physical indices of aged asphalt binders containing different types and dosages of REOB and the benchmark values are defined as the degrees of recovery; the closer the degree of recovery to 100%, the better the rejuvenation effect of REOB on aged asphalt [13]. Therefore, the degrees of recovery for the ductility of aged asphalt with 6% REOB-1 and 8% REOB-2 are 51.8% and 44.5%, respectively, which are far from the standard of original asphalt. For an REOB-3 dosage of 7%, the degrees of recovery for penetration, softening point and ductility are 101.4%, 102.7%, and 95.5%, respectively. The comprehensive recovery effect is the best, and these three conventional physical indices can meet the technical pavement performance requirements; thus, according to physical properties, the best choice for the rejuvenation of aged asphalt is 7% REOB-3. In addition, based on the above test results, REOB-3 was selected for the following rheological tests and the rejuvenation mechanism was discussed; hereafter, REOB refers to REOB-3.

### 3.2. Rheological Properties

**3.2.1. Rutting Factor.** Because the rutting of asphalt pavement mainly occurs during the initial stage of pavement construction, the Strategic Highway Research Program (SHRP) proposed the rutting factor ( $G^*/\sin \delta$ ) of original asphalt or asphalt subjected to short-term ageing using the RTFO test as an evaluation index of the high-temperature stability. The SHRP requires that the  $G^*/\sin \delta$  value of original asphalt is no less than 1.0 kPa and that the  $G^*/\sin \delta$  value of asphalt after RTFO ageing is no less than 2.2 kPa. Figures 4(a) and 4(b) show the influence of REOB content on the  $G^*/\sin \delta$  values of original asphalt and asphalt after

RTFO ageing, respectively. Both figures show that the  $G^*/\sin \delta$  value of asphalt binders decreases with an increase in the testing temperature for both original and RTFO-aged asphalt, indicating that rutting occurs easily within asphalt pavement at high temperatures. At the same testing temperature, the  $G^*/\sin \delta$  value of aged asphalt decreases with an increase in the REOB content from 4% to 7%; this finding indicates that the addition of REOB decreases the rutting resistance of aged asphalt at high temperatures. However, the sudden increase in the  $G^*/\sin \delta$  value of asphalt rejuvenated by 8% REOB indicates that the rutting resistance of binders will increase at this dosage, which is consistent with the softening point analysis in Section 3.1.2. For original binders and RTFO-aged binders, the  $G^*/\sin \delta$  values of aged asphalt with an REOB dosage of 4% to 8% are higher than that of original asphalt; simultaneously, the stability of rejuvenated asphalt with 7% REOB at a high temperature is the closest to that of original asphalt. Additionally, comparing Figure 4(a) with 4(b), the  $G^*/\sin \delta$  values of all binders increase at the same temperature after short-term ageing, which indicates that asphalt binders are hardened. Meanwhile, the high-temperature grade of aged asphalt containing various REOB contents does not lose after short-term ageing.

**3.2.2. Creep Stiffness and Creep Rate.** Contrary to its ability to resist rutting at high temperatures, asphalt pavement will exhibit shrinkage cracking at low temperatures; this cracking is usually due to an increase in the stiffness modulus in addition to the constant ageing of asphalt binders during use and the gradual transition of asphalt from flexible to brittle at low temperatures [12]. Therefore, the SHRP claims that the creep stiffness ( $S$ ) and creep rate ( $m$ ) of asphalt binders after performing RTFO and PAV tests should be used as evaluation indices of the low-temperature cracking resistance, where  $S$  should not exceed 300 MPa and  $m$  should not be less than 0.3 after 60 seconds of testing. The  $m$  value reflects the rate of release of the shrinkage stress during the viscoelastic flow of asphalt binders. Larger values of  $m$  and smaller values of  $S$  correlate with a more favourable cracking resistance of asphalt pavement at low temperatures. The influence of REOB content on the creep stiffness and creep rate of aged asphalt is illustrated in Figures 5(a) and 5(b), respectively, both of which show that the  $S$  value of an asphalt binder will increase and the  $m$  value will decrease with a decrease in the testing temperature, indicating that cracking will occur more easily in asphalt pavement at lower service temperatures. At the same testing temperature, the  $S$  value of aged asphalt decreases and the  $m$  value increases with an increase in the REOB content from 4% to 7%. However, the  $S$  value of rejuvenated asphalt with 8% REOB increases, while the  $m$  value suddenly decreases; this reflects the drop in the low-temperature performance, which is consistent with the ductility analysis in Section 3.1.3. At  $-12^\circ\text{C}$ , an  $S$  value of less than 300 MPa and an  $m$  value exceeding 0.3 will meet the technical standard requirement for aged asphalt containing either 6% or 7% REOB; in addition, the

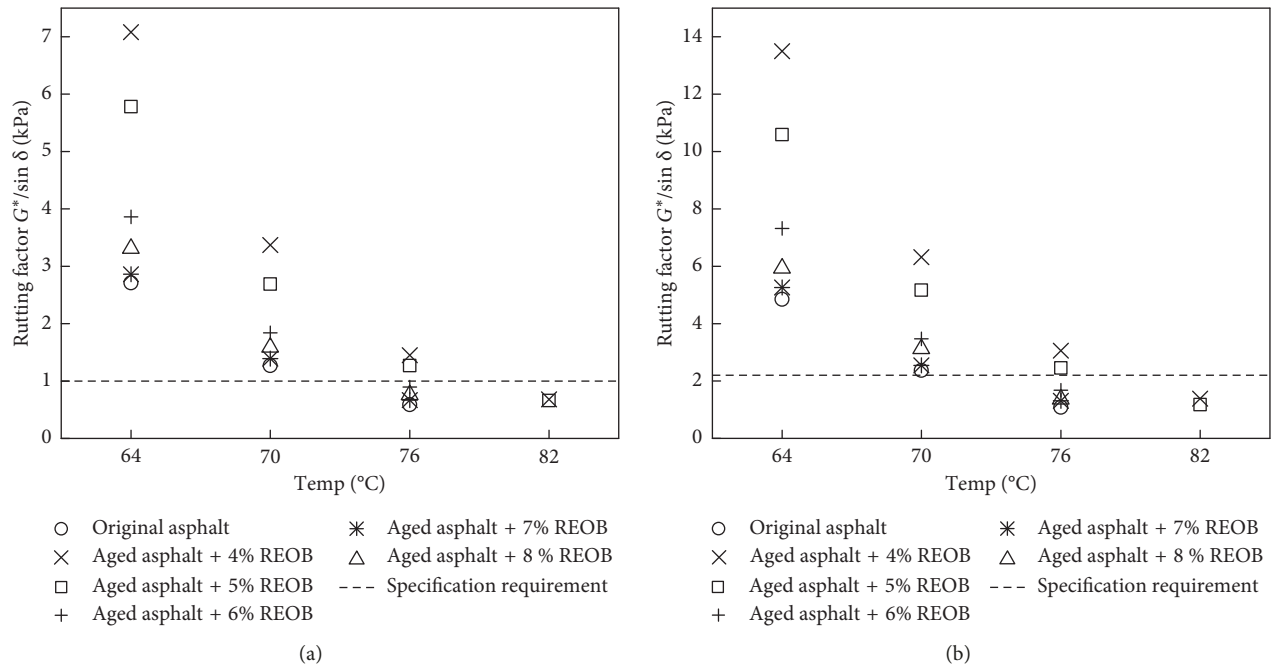


FIGURE 4:  $G^*/\sin \delta$ —temperature for aged asphalt with different REOB content. (a) Original. (b) After RTFO.

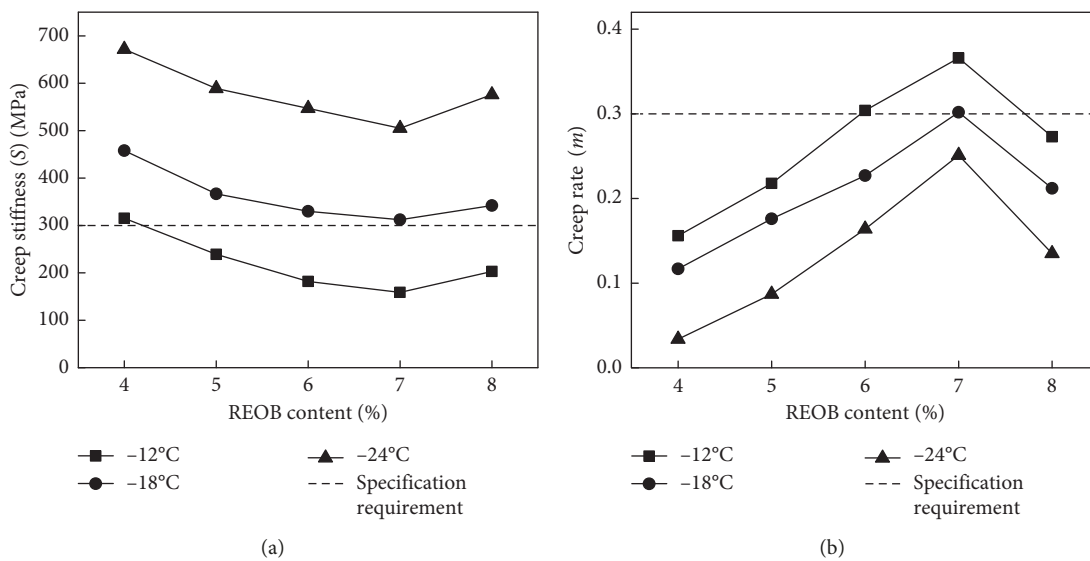


FIGURE 5: Influence of REOB content on creep stiffness and creep rate of aged asphalt. (a) Creep stiffness. (b) Creep rate.

low-temperature cracking resistance of asphalt rejuvenated by 7% REOB is superior to that of asphalt rejuvenated by 6% REOB.

**3.2.3. Performance Grade Classification.** The performance grade can be obtained based on the above analysis performed with a DSR and a BBR, as shown in Table 3. As asphalt continues to age, the high-temperature grade will increase, while the low temperature grade will decrease. Therefore, adding an appropriate REOB dosage can improve the low-temperature performance of aged asphalt, but this will compromise its high-temperature performance.

Nevertheless, under the optimum dosage of REOB for aged asphalt, the performance grade of asphalt rejuvenated by 7% REOB will reach PG70-22. Moreover, its high-temperature grade will be the same as that of original asphalt, while the low-temperature grade of the rejuvenated asphalt will be lower by one grade. At excessively high or low REOB content, the low-temperature performance of rejuvenated asphalt will be even worse, and it will no longer satisfy the SHRP requirements.

**3.3. Four-Component Analysis.** Table 4 shows the content of the four components of different asphalt binders and REOB

TABLE 3: Performance grade of different asphalt binders.

Test objects	High temperature grade	Low temperature grade	Performance grade (PG)
Original asphalt	70	-28	70-28
Aged asphalt	76	-10	76-10
Aged asphalt + 4% REOB	76	-10	76-10
Aged asphalt + 5% REOB	76	-16	76-16
Aged asphalt + 6% REOB	70	-22	70-22
Aged asphalt + 7% REOB	70	-22	70-22
Aged asphalt + 8% REOB	70	-16	76-16

TABLE 4: Content of four components of REOB and different asphalt binders (%).

Test objects	Asphaltenes	Resins	Aromatics	Saturates	
Original asphalt	5.4	13.4	39.1	42.1	
REOB	0.2	15.5	83.5	0.8	
Aged asphalt	13	38.1	11.1	37.8	
Rejuvenated asphalt with 6% REOB	Theoretical value	12.23	36.74	15.45	35.58
	Measured value	8	38.2	15.7	38.1
	Difference value	4.23	-1.46	-0.25	-2.52
Rejuvenated asphalt with 7% REOB	Theoretical value	12.1	36.52	16.17	35.21
	Measured value	4.8	41.5	18.4	35.3
	Difference value	7.3	-4.98	-2.23	-0.09
Rejuvenated asphalt with 8% REOB	Theoretical value	11.98	36.29	16.89	34.84
	Measured value	10.6	14.9	25.8	48.7
	Difference value	1.38	21.39	-8.91	-13.86

and demonstrates that the content of asphaltenes and resins will increase as asphalt ages, while the content of aromatics and saturates will correspondingly decrease. The main reason for this is that the light components composed of aromatics and saturates will oxidize and polymerize as the asphalt ages, and they will gradually transform into recombinant components comprising resins and asphaltenes.

Most of the components of REOB are aromatics with some resins and few asphaltenes and saturates. Therefore, on the one hand, adding certain dosages of REOB to aged asphalt will supplement the aged asphalt with aromatics that are otherwise missing, thereby harmonizing the four components and achieving a stable asphalt colloid structure. On the other hand, the volatile saturates content in REOB is very small, indicating that REOB exhibits a good heat resistance as an asphalt rejuvenator, which is consistent with the technical requirements of asphalt rejuvenators [14].

According to the theory of pure component adjustment, the mechanism through which REOB rejuvenates aged asphalt is the pure supplement of components, that is, no reactions and transformations occur among the four components [15]. So each component conforms to the formula (1):

$$P = m_a P_a + m_r P_r, \quad (1)$$

where  $P$  is the proportion of one component in rejuvenated asphalt (%);  $m_a$  is the blending ratio of aged asphalt in rejuvenated asphalt;  $P_a$  is the proportion of one component in aged asphalt (%);  $m_r$  is the blending ratio of REOB in rejuvenated asphalt; and  $P_r$  is the proportion of one component in REOB (%).

However, Table 4 illustrates that the theoretical results for the four components calculated by formula (1) of pure adjustment theory are substantially different from those measured through actual testing, which indicates that the rejuvenation mechanism of REOB in aged asphalt can be defined as incomplete component adjustment, in which some components undergo physical or chemical reactions and transformations during the rejuvenation process.

Comparing with the results calculated by formula (1) of pure component adjustment, the measured asphaltene content of rejuvenated asphalt with 6% REOB is reduced by 4.23%, while the contents of resins, aromatics, and saturates correspondingly increase to varying degrees. These differences are observed because when 6% REOB is added to aged asphalt, aromatics are used as a dispersing medium for the asphalt colloidal structure; these aromatics can peptize and disperse asphaltenes, making them undergo an inverse transformation, and some of the asphaltenes are converted into resins, aromatics, and saturates. For rejuvenated asphalt with 7% REOB, the degree of asphaltene dissolution is greater and the amount of transference out of the structure reaches 7.3%; thus, its content is reduced to the nearest level of original asphalt; the amounts of resins and aromatics taken in are also more for rejuvenated asphalt with 7% REOB than for that with 6% REOB. However, different conditions are observed for rejuvenated asphalt with 8% REOB; the amount of asphaltenes transferred out is sharply reduced at this time, and thus, the asphaltene content reaches 10.6% compared with the amount in rejuvenated asphalt with 6% and 7% REOB. The largest proportion of resin transferred out reaches 21.5%, and the largest proportions of aromatics and saturates transferred in are 13.7% and 9.3%, respectively.

According to asphalt colloid structure theory, asphaltene are hydrophobic to oil components, which are composed of aromatics and saturates, but they exhibit an affinity to resins. Therefore, asphaltene need to be encapsulated by a sufficient amount of resins to form micelles and be dispersed in oil components to develop stable colloidal structures [16]. However, the resin content is too small relative to the asphaltene content for rejuvenated asphalt with 8% REOB; asphaltene would flocculate too easily due to the lack of resins for encapsulating the asphaltene, and as a consequence, a stable colloidal structure cannot be formed. In summary, the colloidal structure of rejuvenated asphalt with 7% REOB is the most stable. Moreover, adding REOB can achieve a good rejuvenation effect by reducing the asphaltene content and increasing the resin content in aged asphalt.

**3.4. Infrared Spectroscopic Analysis.** The technical properties of asphalt are related not only to the content of chemical components but also to the chemical structure. Figure 6 shows infrared spectrograms of REOB, original asphalt, aged asphalt, and rejuvenated asphalt with 7% REOB. The infrared spectrogram of REOB demonstrates a strong asymmetric stretching vibration peak at  $2925\text{ cm}^{-1}$  and the symmetric stretching vibration peak of methylene ( $-\text{CH}_2-$ ) at  $2854\text{ cm}^{-1}$ . At  $1464\text{ cm}^{-1}$  and  $1377\text{ cm}^{-1}$ , the asymmetric and symmetric bending vibration peaks of methyl ( $-\text{CH}_3$ ), respectively, are observed. The strong absorption peak at  $722\text{ cm}^{-1}$  is the bending vibration peak of long-chain methylene  $-(\text{CH}_2)_n-$ , and the position of the absorption peak can be used to determine that  $n > 4$ . The strong absorption peaks at  $1744\text{ cm}^{-1}$  and  $1711\text{ cm}^{-1}$  can prove the existence of carbonyl groups ( $\text{C}=\text{O}$ ) composed of acids and ketones in REOB. The vibration absorption peak of the carbon skeleton ( $\text{C}=\text{C}$ ) on the benzene ring is near  $1450\text{ cm}^{-1}$ , and the absorption peak near  $900\text{ cm}^{-1}$  is caused by C-H on the benzene ring. In addition, there are acid amides (at  $1260\text{ cm}^{-1}$ ), phosphorous compounds (at  $1247\text{ cm}^{-1}$ ), and sulfur compounds (at  $1163\text{ cm}^{-1}$ ) in the REOB. In conclusion, REOB is composed of base oil and complex mixtures containing a variety of polar functional groups. The main components of REOB are alkanes, naphthenes, and aromatic hydrocarbons, which have chemical compositions that are very similar to that of asphalt. According to the theory of similarity compatibility, REOB is compatible with asphalt and can form a stable colloidal structure.

Comparing the infrared spectrum of aged asphalt with that of original asphalt, the positions of the vibration peaks of both asphalts are basically the same, but some peak strengths are different. Owing to the oxidation reaction of asphalt during ageing, the ketone carbonyl ( $\text{C}=\text{O}$ ) vibration peak appears at  $1710\text{ cm}^{-1}$ , which is the characteristic peak of ageing asphalt, and the sulfoxide group ( $\text{S}=\text{O}$ ) vibration peak at  $1060\text{ cm}^{-1}$  is significantly enhanced. In addition, the methylene ( $-\text{CH}_2-$ ) and methyl ( $-\text{CH}_3$ ) vibration peaks at  $2925\text{ cm}^{-1}$ ,  $2854\text{ cm}^{-1}$ ,  $1475\text{ cm}^{-1}$ , and  $1376\text{ cm}^{-1}$  are weakened, and the C-H vibration peaks on benzene rings at  $750\text{--}900\text{ cm}^{-1}$  are also weakened; these effects are the result

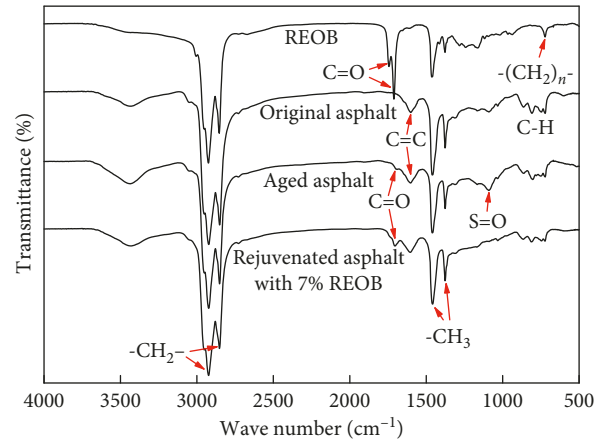


FIGURE 6: Infrared spectrograms of REOB and asphalt binders.

of condensation and dehydrogenation during asphalt ageing.

Due to the small content of REOB, the infrared spectrum of rejuvenated asphalt with 7% REOB is similar to that of aged asphalt. Compared with that of aged asphalt, the ketone carbonyl ( $\text{C}=\text{O}$ ) vibration peak of rejuvenated asphalt at  $1710\text{ cm}^{-1}$  is obviously enhanced because of the addition of REOB carbonyl groups to the rejuvenated asphalt, but the sulfoxide ( $\text{S}=\text{O}$ ) vibration peak at  $1060\text{ cm}^{-1}$  is significantly weakened. In summary, the characteristic peaks of REOB also exist in rejuvenated asphalt, and some vibration peaks of functional groups evidently change both before and after rejuvenation, indicating that chemical reaction and transformation of the structures occur within rejuvenated asphalt; these findings are consistent with the correlation mechanism between REOB and aged asphalt ascertained in the four-component analysis presented in Section 3.3.

#### 4. Grey Relationship Analysis of Properties and Components

The differences in the asphalt properties depend on the chemical composition of the asphalt [17]. The addition of REOB changes the components in addition to the physical and rheological properties of aged asphalt. The relationship between the four components and the physical rheological properties of asphalt rejuvenated by REOB are obtained quantitatively by the grey relationship analysis to improve the asphalt pavement performance by controlling the REOB content.

The penetration, softening point, ductility, rutting factor (after RTFO ageing at a testing temperature of  $70^\circ\text{C}$ ), creep stiffness, and creep rate (at a testing temperature of  $-12^\circ\text{C}$ ) of aged asphalt and rejuvenated asphalt with 6%, 7%, and 8% REOB were selected as reference sequences  $X_{01}$ ,  $X_{02}$ ,  $X_{03}$ ,  $X_{04}$ ,  $X_{05}$ , and  $X_{06}$ , respectively, and the content of asphaltene, resins, aromatics, and saturates were used as comparison sequences  $X_1$ ,  $X_2$ ,  $X_3$ , and  $X_4$ , respectively. The relationship degrees in Table 5 are calculated from the data in Table 6 according to the calculation steps of grey relationship analysis method [17, 18].

TABLE 5: Relationship degrees between the properties indices and four components.

Projects	Asphaltenes $X_1$	Resins $X_2$	Aromatics $X_3$	Saturates $X_4$
Penetration $X_{01}$	0.524	0.545	0.656	0.563
Softening point $X_{02}$	0.860	0.785	0.587	0.802
Ductility $X_{03}$	0.544	0.545	0.550	0.547
Rutting factor $X_{04}$	0.905	0.788	0.565	0.701
Creep stiffness $X_{05}$	0.787	0.730	0.552	0.655
Creep rate $X_{06}$	0.539	0.545	0.594	0.558

TABLE 6: Raw data of aged asphalt and rejuvenated asphalts with REOB.

Projects	Aged asphalt	Rejuvenated asphalt with 6% REOB	Rejuvenated asphalt with 7% REOB	Rejuvenated asphalt with 8% REOB
$X_{01}$	24	68	72	75
$X_{02}$	66	53.2	50	52.8
$X_{03}$	0.4	16.3	21	13
$X_{04}$	6.84	3.47	2.55	3.13
$X_{05}$	1172	182	159	203
$X_{06}$	0.057	0.304	0.366	0.273
$X_1$	13	8	4.8	10.6
$X_2$	38.1	38.2	41.5	14.9
$X_3$	11.1	15.7	18.4	25.8
$X_4$	37.8	38.1	35.3	48.7

For asphalt rejuvenated by REOB, Table 5 shows that the relationship degree with the penetration is greatest for aromatics, followed by saturates, resins, and asphaltenes, while the relationship degree with the softening point is greatest for asphaltenes, followed by saturates, resins, and aromatics; for ductility, the difference in relationship degree between the four components is very small, indicating that good ductility requires a reasonable combination of the four components. These correlations are basically consistent with the qualitative relationships between the four components and the properties of asphalt in the blending method [19]. As the dispersing medium of an asphalt colloid solution, aromatics can play the role of a glue dissolution and softening agent; that is, it can make the asphalt softer, thereby increasing penetration. In contrast, asphaltenes are thickening agents, and saturates are used as a softener. The plasticization of aromatics is stronger than that of saturates, and asphaltenes require more softener than resins. Therefore, asphaltenes could increase the softening point, while saturates could reduce the softening point. Furthermore, the reasonable combination of the four components can improve the plasticity and ductility of asphalt binders at low temperature.

For the rheological indices, the order of the relationship degree with  $G^*/\sin \delta$  is as follows: asphaltenes > resins > saturates > aromatics; the order of the relationship degree with  $S$  is the same as that of  $G^*/\sin \delta$ , which indicates that asphaltenes have the greatest influence on the deformation resistance of binders at both high and low temperatures. The order of the relationship degree with  $m$  is as follows: aromatics > saturates > resins > asphaltenes; this order is consistent with the correlation order of ductility, and the difference in relationship degrees among the four components is very small, which indicates that the reasonable combination of four components can ensure a good deformation rate.

In order to better compare each row or column in Table 5, the correlation and advantage between the four-component and physical rheological indexes of rejuvenated asphalt with different REOB contents are comprehensively analysed, and the grey relationship matrix ( $\gamma$ ) with the coefficients  $\gamma_{0xy}$  according to Table 5 is established, as shown below. Among them,  $x$  corresponds to the row order of performance indexes in Table 5, and  $y$  corresponds to the column order of four-component in Table 5.

$$\gamma = \begin{bmatrix} \gamma_{011} & \gamma_{012} & \gamma_{013} & \gamma_{014} \\ \gamma_{021} & \gamma_{022} & \gamma_{023} & \gamma_{024} \\ \gamma_{031} & \gamma_{032} & \gamma_{033} & \gamma_{034} \\ \gamma_{041} & \gamma_{042} & \gamma_{043} & \gamma_{044} \\ \gamma_{051} & \gamma_{052} & \gamma_{053} & \gamma_{054} \\ \gamma_{061} & \gamma_{062} & \gamma_{063} & \gamma_{064} \end{bmatrix} = \begin{bmatrix} 0.524 & 0.545 & 0.656 & 0.563 \\ 0.860 & 0.785 & 0.587 & 0.802 \\ 0.544 & 0.545 & 0.550 & 0.547 \\ 0.905 & 0.788 & 0.565 & 0.701 \\ 0.787 & 0.730 & 0.552 & 0.655 \\ 0.539 & 0.545 & 0.594 & 0.558 \end{bmatrix}. \quad (2)$$

Comparing the relationship degree of each row in the matrix, the relationship degrees among the four components and the softening point in the second row are relatively large, indicating that REOB is the most sensitive to softening point; thus, the main function of REOB is to reduce the viscosity of aged asphalt, which meets the relevant technical standards of asphalt rejuvenators at home and abroad [14]. Moreover, a comparison of the relationship degree of each column in the matrix reveals that the relationship degree between the physical rheological indices and asphaltenes in the first column is relatively large, which reflects the fact that the asphaltene content has the greatest influence on the properties of rejuvenated asphalt. Therefore, the asphaltene content should be strictly controlled during the addition of REOB to rejuvenate aged asphalt. These results also confirm the analysis of the four components in Section 3.3.

## 5. Conclusions

- (1) An analysis of physical properties shows that the three types of REOB can increase the penetration and ductility and decrease the softening point of aged asphalt under proper dosage, but the recovery effect of REOB-1 and REOB-2 on ductility is too poor. Only when 7% REOB-3 is used are the three physical indices of aged asphalt restored to the level of original asphalt.
- (2) An analysis of the rheological properties shows that a suitable dosage of REOB can reduce the rutting factor  $G^*/\sin \delta$  of aged asphalt and decrease the creep stiffness while increasing the creep rate. A performance grade classification indicates that a moderate REOB content can decrease the high-temperature grade and increase the low-temperature grade of aged asphalt, thereby showing a good consistency with the analysis of physical properties. In comparison, the high-temperature and low-temperature performances of rejuvenated asphalt with 7% REOB are the closest to those of original asphalt, but its low-temperature performance is slightly worse and thus needs further improvement.
- (3) Four-component analysis indicates that most of the components of REOB are aromatics. The mechanism through which REOB rejuvenates aged asphalt is incomplete component adjustment; that is, some of the components undergo physical or chemical reactions and transformations. The addition of REOB can achieve a rejuvenation effect mainly by reducing the asphaltene content and increasing the resin content in aged asphalt.
- (4) Infrared spectra analysis indicates that the main components of REOB are similar and compatible with asphalt. Adding 7% REOB to aged asphalt can significantly reduce the strength of sulfoxide functional groups, thereby achieving a rejuvenation effect.
- (5) The grey relationship analysis reveals that asphaltenes have the greatest influence on the high-temperature performance of asphalt rejuvenated by REOB and low-temperature performance requires a reasonable combination of the four components. Moreover, a comprehensive advantage analysis demonstrates that the addition of REOB has the greatest sensitivity to softening point, and asphaltene content has the greatest influence on the physical and rheological properties of asphalt rejuvenated by REOB. In addition, the rejuvenation performance of modified asphalt should be further studied by using different REOB.

## Data Availability

The experimental data in this paper are from the pavement material laboratory of Shandong Jiaotong University, which is the provincial key laboratory. The experimental data in this paper are real and reliable.

## Conflicts of Interest

The authors declare that they have no conflicts of interest.

## Acknowledgments

The authors would like to acknowledge the staff of Shandong Natural Science Foundation and Shandong University Science and Technology Program of China for their assistance. Moreover, the authors thank Professor Xinjun Li and Professor Dedong Guo of Shandong Jiaotong University for their help in the experiment. This research was funded by the project "Study on the Effect and Mechanism of Recycled Engine Oil Bottom on the Modification Performance of Asphalt" (ZR2016EEM42) of Shandong Natural Science Foundation and the project "Research on Modification Behavior Mechanism of Recycled Engine Oil Bottom on Recycled Asphalt" (J16LA17) of Shandong University Science and Technology Program.

## Supplementary Materials

S1: the basic theory of grey relationship analysis. S2: the calculation steps of grey relationship analysis. (*Supplementary Materials*)

## References

- [1] Y.-F. Ma, D.-X. Liu, W.-L. Xu et al., "Study on the current situation and key technology of waste engine oil regeneration in the transportation industry," *Comprehensive Utilization of China's Resources*, vol. 28, no. 11, pp. 25–29, 2010.
- [2] S.-R. Zhou, *Heat and Mass Transfer in Short-Path Distillation Process and Application of the Process to Regeneration of Waste Lubricating Oil*, Sichuan University, Chengdu, China, 2007.
- [3] H.-Q. Xie, Z.-T. Ma, Y. Han et al., "Test of regeneration processes of waste gasoline engine oil," *Petroleum Processing and Petrochemicals*, vol. 48, no. 1, pp. 85–88, 2007.
- [4] A. Villanueva, S. Ho, and L. Zanzotto, "Asphalt modification with used lubricating oil," *Canadian Journal of Civil Engineering*, vol. 35, no. 2, pp. 148–157, 2008.
- [5] D. S. Ackbarali and R. Maharaj, "The viscoelastic properties of Trinidad Lake asphalt-used engine oil blends," *International Journal of Applied Chemistry*, vol. 7, pp. 1–8, 2011.
- [6] C. Dedene, "Investigation of using waste engine oil blended with reclaimed asphalt materials to improve pavement recyclability," Master Thesis, Michigan Technological University, Houghton, Michigan, 2011.
- [7] X. Jia, B. Huang, B. F. Bowers, and S. Zhao, "Infrared spectra and rheological properties of asphalt cement containing waste engine oil residues," *Construction and Building Materials*, vol. 50, no. 3, pp. 683–691, 2014.
- [8] P.-P. Xu, *Study on the Properties of Waste Oil Recycled Asphalt and its Mixtures*, Jilin University, Changchun, China, 2015.
- [9] S. A. M. Hesp and H. F. Shurvell, "X-ray fluorescence detection of waste engine oil residue in asphalt and its effect on cracking in service," *International Journal of Pavement Engineering*, vol. 11, no. 6, pp. 541–553, 2010.
- [10] S. Rubab, K. Burke, L. Wright, S. A. M. Hesp, P. Marks, and C. Raymond, "Effect of engine oil residues on asphalt cement quality," in *Proceedings of the Fifty-Sixth Annual Conference of*

- the Canadian Technical Asphalt Association*, pp. 1–12, Québec City, Canada, November 2011.
- [11] H.-B. Ding, Y.-J. Qiu, W.-Q. Wang et al., “Adverse effect of waste engine oil bottom on asphalt performance and its mechanism,” *Journal of Building Materials*, vol. 20, no. 4, pp. 646–650, 2017.
- [12] J.-A. Shen, *Road Performance of Asphalt and Asphalt Mixture*, People’s Communications Press, Beijing, China, 2001.
- [13] Y. Zhang, M.-Z. Chen, S.-P. Wu et al., “Study on physical properties and structure of recycled asphalt with different waste oil,” *Journal of Wuhan University of Technology (Transportation Science and Engineering Edition)*, vol. 41, no. 1, pp. 104–108, 2017.
- [14] J.-G. Geng, *Study on Asphalt Aging Mechanism and Regeneration Technology*, Chang’an University, Xi’an, China, 2009.
- [15] Y.-H. Nie, P. Liu, Z.-G. Zhou et al., “Study on the effects of regenerator on the mechanism of asphalt regeneration,” *Highway Engineering*, vol. 37, no. 6, pp. 65–68, 2012.
- [16] Z.-H. Wang, J.-H. Fang, and M.-F. He, “Discussion on the aging process and regeneration mechanism of asphalt,” *Qinghai Transportation Technology*, no. 4, pp. 45–48, 2017.
- [17] H.-X. Chen, M.-S. He, X.-H. Ji et al., “Grey relationship analysis of asphalt properties and asphalt composition,” *Journal of Chang’an University (Nature Science Edition)*, vol. 34, no. 3, pp. 1–6, 2014.
- [18] J.-L. Deng, *Basic Methods of Grey System*, East China University of Technology Press, Shanghai, China, 1987.
- [19] Y.-G. Wang, K.-J. Liao, F. Yan et al., “Reclaimed waste asphalt by blending method,” *Chemical Technology*, no. 2, pp. 22–24, 2003.

## Research Article

# Usage of Reclaimed Asphalt Material in Stone Mastic Asphalt

**Petr Hyzl, Ondrej Dasek , Iva Coufalikova, Michal Varaus, and Dusan Stehlik**

*Institute of Road Structures, Faculty of Civil Engineering, Brno University of Technology, Brno, CZ 60200, Czech Republic*

Correspondence should be addressed to Ondrej Dasek; [dasek.o@fce.vutbr.cz](mailto:dasek.o@fce.vutbr.cz)

Received 16 April 2019; Revised 19 June 2019; Accepted 21 July 2019; Published 4 August 2019

Guest Editor: Jose Norambuena-Contreras

Copyright © 2019 Petr Hyzl et al. This is an open access article distributed under the Creative Commons Attribution License, which permits unrestricted use, distribution, and reproduction in any medium, provided the original work is properly cited.

The paper focuses on the issue of using reclaimed asphalt (RA) in asphalt mixtures used for highly traffic-loaded asphalt pavements—in asphalt mixtures of the stone mastic asphalt (SMA) type. It is a skeleton-type mixture, where the traffic load is bore by a skeleton of coarse aggregates bonded with mastic (i.e., bitumen and fine aggregates). It is therefore essential to pay close attention to the properties of this coarse aggregate. Higher demands on properties of the aggregate are probably due to the fact that RA is not currently being used in SMA-type mixtures. Most standards do not allow usage of RA in this type of mixtures. Given that traffic load of road networks is constantly increasing, the ratio of SMA-type asphalt mixtures also increases in the road network. This paper presents results of 5-year research focused on the possibility of using RA in SMA-type asphalt mixtures. This included laboratory design of these mixtures with various dosages and types of RA. Their empirical and functional properties were verified. Based on the positive results of the laboratory testing, a test section was subsequently constructed using several variants of the mixtures containing up to 50% of RA. This test section is regularly being monitored, and despite very intense traffic load, there are no failures apparent after 2 and half years of operation. Based on the laboratory research and subsequent construction and monitoring of a test section, it can be said that RA can be used in SMA-type mixtures without any negative impacts on functional properties or mixture lifetime.

## 1. Introduction

Based on the European Asphalt Pavement Association (EAPA), the total length of the European road network is more than 5 million kilometres, out of which 66,700 km is classified as highways. Vast majority of these roads have asphalt surface [1]. Annual production of the total number of 4700 European asphalt mixing plants is approximately 282.5 million tons of the asphalt mixture [2]. Given the limited amount of natural resources, it is in long term essential to use materials already built-in to current road constructions, as much as possible. Literature [3] shows that the European road network contains approximately 950 billion tons of asphalt mixtures.

Using various recycling methods of these building materials, it is possible to maintain the natural material resources (aggregates and bitumen) and decrease the energy and economical demands of construction works. Given the fact that the cost of basic components for the manufacture of asphalt mixtures constantly increases in long term, the use of reclaimed

asphalt (RA) in asphalt mixture manufacturing is advantageous from the economical perspective as well [4, 5]. It is not just the cost of the aggregate but also the cost of the bitumen, which is the most expensive component in the asphalt mixture.

RA is already used in some countries routinely in asphalt concrete (AC) mixtures (dense graded), even in relatively high ratio, often above 50% [6–8]. In contrast, use of RA is not very common in mixtures of the stone mastic asphalt (SMA) type. It is especially because these mixtures have high demands on aggregate gradation, which is gap graded and usually dense gradation of RA often does not satisfy this gap-graded gradation requirement. Nevertheless, there are studies which describe high ratios of RA in SMA mixtures. Vast majority of countries, however, currently do not allow the use of RA in SMA mixtures.

This paper, based on laboratory research and realization using a test section with various mixture variants, shows that usage of SMA mixtures with a certain ratio of RA is well possible in practice without any negative impacts on functional parameters and lifetime of the layer.

The study [9] focused on determination of optimum content of cellulose fibres in RA in the SMA asphalt mixture. RA ratios used were 0%, 8%, 16%, and 24%. Based on the results of the Marshall stability, rutting test, and indirect tensile strength, it was found that the optimum ratio of RA is 16%.

The study [10] included comparison of resistance against deformation of stone mastic asphalt with various RA contents (0% to 50%). As the RA content increased, the resistance of the SMA mixtures against deformation also increased, which was affected by polymer-modified bitumen contained in the RA. This study assumed dosages of RA to the SMA mixture up to 50%; however, this only included mixtures prepared in a laboratory. Similar issue is dealt with in the study [11], where stone mastic asphalt with RA content up to 30% and AC with RA content up to 50% were designed. Results of laboratory functional tests (stiffness, fatigue, and rutting) proved little differences between the properties of asphalt mixtures with low and high RA content.

The issue of adding RA into SMA mixtures was dealt with as part of the project [12] solved not just by representatives of the technological institute but also by a representative of an investor, and the conclusion was recommendation of adding 30% of RA into all SMA mixtures.

## 2. Scope

Scope of this paper is to summarize and describe the results of a 5-year research focused on the possibilities of using RA in asphalt mixtures of the stone mastic asphalt (SMA) type, which is, thanks to its skeleton, used in most traffic-loaded asphalt pavements (highways, etc.). The paper also introduces the concept of high dosage of RA in SMA (up to 50%), which is currently a relatively new technology with very little experiences worldwide. The paper describes a design of an SMA mixture with aggregate gradation up to 11 mm (SMA 11) with various dosages of RA (0% to 50%), results of laboratory tests of these mixtures, and realization of test sections including evaluation of lifetime of these sections after 2.5 years in operation. Another goal was determination of parameters for standards and regulations with respect to RA dosages in SMA.

## 3. Methods

Three tests were chosen to assess the mechanical properties of SMA mixtures: the wheel tracking test was used to determine rutting resistance (EN 12697-22), the two-point bending test was used to determine the stiffness (EN 12697-26, Annex A), and the thermal stress-restrained specimen test (TSRST) with a temperature decrease was used to determine low-temperature properties (EN 12697-46).

**3.1. Wheel Tracking Test.** The wheel tracking test was performed according to EN 12697-22 method B (wheel tracking test with a small size device in air) under constant temperature (50°C and 60°C). Dimensions of slabs were 260 mm × 320 mm and 50 mm high. The slabs were compacted in a laboratory by using a compactor with a roller

running on vertical sliding steel plates. Resistance to permanent deformation was assessed by proportional rut depth at  $10^4$  cycles ( $PRD_{AIR}$ ), and wheel tracking slope was calculated as the average rate at which the rut depth increases with repeated passes ( $WTS_{AIR}$ ).

**3.2. Stiffness Test.** Stiffness of the individual mixtures was determined based on the EN 12697-26 using the two-point bending test on trapezoidal-shaped specimens performed at 15°C and a load frequency of 5, 10, 15, 20, and 25 Hz. The slabs were compacted similarly to the wheel tracking test. The degree of compaction of slabs was between 99% and 101%. Trapezoidal-shaped specimens were cut from slabs using the sliding table circular saw. For the purposes of the stiffness modulus test, 15 trapezoidal-shaped specimens were produced from each mixture.

**3.3. Low-Temperature Properties.** The low-temperature properties were determined according to EN 12697-46. The critical temperature and the tensile stress in the tested specimen was determined using a uniaxial tension test—thermal-stress restrained specimen test (TSRST). When a crack forms by cooling of the prismatic beam (50 mm × 50 mm × 200 mm) at a constant rate of 10°C/h from the initial temperature, the given specimen is restricted from contracting, i.e., with no longitudinal strain.

**3.4. Asphalt Binder Tests.** Binders were extracted from the asphalt mixtures manufactured for the test sections, and these were subjected to the multiple stress creep and recovery (MSCR) test in accordance with EN 16659 at a temperature 60°C in a dynamic shear rheometer. The main aim of this test was to verify the functionality of the rejuvenators and modification additives and set standard requirements.

## 4. Materials

**4.1. Aggregate.** The crushed split aggregates used in this study came from the Zbečno quarry, and the fractions used were 0/2 mm, 2/5 mm, 4/8 mm, and 8/11 mm and limestone filler, which satisfied the requirements of the EN 13043 standard.

**4.2. Asphalt Binder.** Polymer-modified bitumen PMB 45/80-55 was used for the manufacture of the asphalt mixtures. Basic properties of this bitumen are given in Table 1.

**4.3. Reclaimed Asphalt (RA).** Two types of RA were used for the manufacture of SMA:

- (a) Standard RA was obtained from milling of asphalt layers containing paving (nonmodified) bitumen. The age of the milled layers from the 1st class road was 8 years. Such RA is hereafter referred to as “RAP.” Content of the asphalt binder determined by extraction was found to be 5.16% (Table 2).

TABLE 1: Basic parameters of PMB 45/80-55.

Test	Determined values	Requirements of the EN 14023 standard
Needle penetration in accordance with EN 1426	65 (0.1 mm)	45–80 (0.1 mm)
Softening point in accordance with EN 1427	61.6°C	Minimum 55°C
Elastic recovery in accordance with EN 13398	86%	Minimum 60%

TABLE 2: Basic properties determined for reclaimed binder from RA of gradation 0/11 mm (RAP) for SMA 11.

Test	Determined values
Needle penetration in accordance with EN 1426	24.7 (0.1 mm)
Softening point in accordance with EN 1427	64.4°C
Dynamic viscosity at 135°C in accordance with EN 13302	0.81 Pa·s
Elastic recovery in accordance with EN 13398	7%
PG grade	76-10
Fraass breaking point in accordance with EN 12593	-2°C

TABLE 3: Basic properties determined for reclaimed binder from RA of gradation 0/11 mm (RAP SMA) for SMA 11.

Test	Determined values
Needle penetration in accordance with EN 1426	16.9 (0.1 mm)
Softening point in accordance with EN 1427	69.8°C
Dynamic viscosity at 135°C in accordance with EN 13302	1.23 Pa·s
Elastic recovery in accordance with EN 13398	43%
PG grade	76-4
Fraass breaking point in accordance with EN 12593	-3°C

(b) RA was obtained by milling wearing course, made from SMA mixtures with polymer-modified bitumen. The age of the milled surface layer from the motorway was 9 years. Such RA is hereafter referred to as “RAP SMA.” Asphalt binder content determined by extraction was found to be 6.4% (Table 3).

Dynamic shear rheometer (DSR) was used to compare the functional properties of reclaimed binders made from both of the RAs. Black diagram (relationship between complex shear modulus and phase angle) is given in Figure 1.

The curve shows a specific wavy trend of the Black diagram of the modified bitumen in RAP SMA, which differs from a Black diagram of a nonmodified bitumen especially in the area of low complex shear modulus values. The modified RAP SMA bitumen has a lower value of phase angle at the equivalent value of complex shear modulus.

Both RAs were crushed to gradation 0/11 mm prior to use. Aggregate gradation of both RAs is compared in Figure 2. This graph shows a more gap-graded curve in case of RAP SMA, which was subsequently (due to favourable gradation) used in the mixture with the highest dosage of RA.

**4.4. Other Materials Used.** To limit binder drainage, 0.3% of cellulose fibres S-CEL 7 G was added to all asphalt mixtures. To improve binder adhesion to the aggregate, the Addibit L300 additive was added to all the mixtures (0.2% of binder weight). Storflux rejuvenator was applied in order to soften the aged asphalt binder contained in the RA.

**4.5. Laboratory Designs of SMA 11 with RA.** When designing SMA 11 mixtures with various RA ratios in a laboratory (Marshall design with requirements specified in EN 13108-5), the main aim was to set (if possible) equivalent sieve size

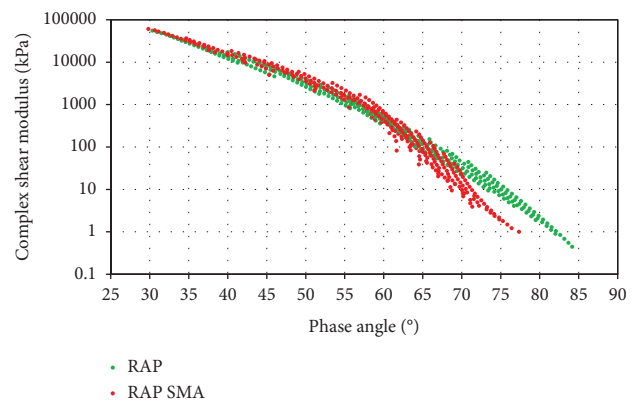


FIGURE 1: Black diagram—reclaimed binders from used RA.

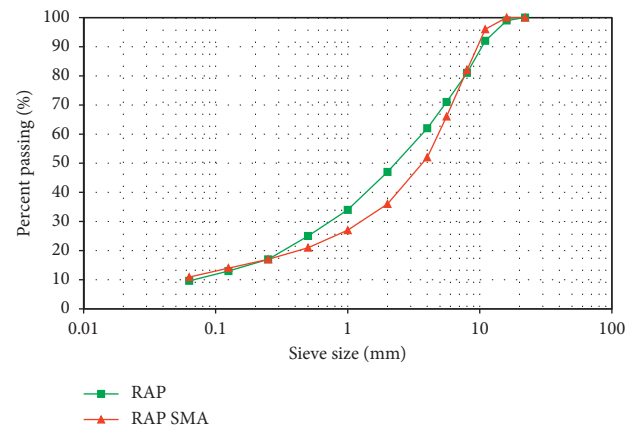


FIGURE 2: Sieve size distribution of used RAs.

distribution and final overall content of asphalt binders in the individual mixtures so that the designed mixtures could be compared with one another during subsequent functional laboratory tests and on test sections. Binder optimum was

chosen based on evaluation of the results of air void content for the individual laboratory-prepared sets with a binder content of 6.3%, 6.5%, and 6.7%, which are not further mentioned in this paper in order to keep the text concise.

In particular, an optimization of six variants of asphalt mixtures of the SMA 11 type was performed:

- (a) SMA 11 with 0% RA was used as a reference mixture
- (b) SMA 11 with 10%, 20%, and 30% "RAP"
- (c) SMA 11 with 30% and 50% "RAP SMA"

Overall optimum ratio of asphalt binder in all mixtures was 6.5%. Binder contained in the RA was included in this overall binder content. Binder content in RA was always subtracted from the added amount of new polymer-modified bitumen PMB 45/80-55. Table 4 shows composition of the individual mixture variants, and Figure 3 provides the sieve size distribution of the final mixture designs. In case of the design of the SMA mixtures, the rejuvenating additive Storflux (producer Storimpex Group) was used both for the laboratory design and for the trial section. The recommended dosing by the producer was 20 kg of Storflux per 1 ton RA.

## 5. Results and Discussion

**5.1. Wheel Tracking Test.** Wheel tracking test results determined at temperatures of 50°C and 60°C are given in Table 5 and Figure 4. The standard deviation values are shown in brackets. Upon increasing the test temperature from 50°C to 60°C, the value of parameters  $WTS_{AIR}$  and  $PRD_{AIR}$  increased. Resistance against deformation of all mixtures was similar, and increasing the ratio of RA does not significantly worsen the resistance of the SMA mixture against permanent deformation. All the compared asphalt mixtures satisfied the required resistance against deformation (the maximum value of parameter  $PRD_{AIR}$  is 5.0%, and the maximum value of parameter  $WTS_{AIR}$  is 0.07 mm/10<sup>3</sup> cycles at a temperature of 50°C).

**5.2. Stiffness.** Stiffness modulus results are given in Table 6 and graphically assessed in Figure 5.

Based on the assessment of the above provided results for determination of stiffness modulus, it can be said that stiffness moduli of all variants lie in a relatively narrow range and there are only relatively small differences between them. In case of the mixture with standard RA (RAP), the values of stiffness modulus at a temperature of 15°C and load frequency of 10 Hz ranged between 6434 MPa and 7207 MPa. Mixtures with RA from the SMA mixture (RAP SMA) under same conditions showed stiffness moduli between 6683 MPa and 7321 MPa, i.e., slightly higher values. Therefore, if a rejuvenator is used to soften an aged RA binder, there is no excessive increase in stiffness of the SMA mixtures with a high RA content.

**5.3. Low-Temperature Properties.** The determined parameters of maximum tensile strength and temperature of the test specimen upon crack formation are summarized in Table 7.

The resulting maximum tensile strength upon crack formation is in case of all tested mixture variants practically identical when taking into account uncertainties of the measurement. Similarly, the tested specimen temperatures upon frost crack appearance are very similar. Variants with RA from SMA (RAP SMA) show slightly better results, which can be explained by the presence of polymer-modified bitumen in the RA. It can therefore be deduced that using higher dosage of RA does not lead to worse low-temperature behaviour of SMA mixtures (assuming usage rejuvenator to soften the aged binder in RA).

**5.4. Test Section.** During September 2016, a test section was built in the Czech Republic based on the above described laboratory research. This section included a total of six variants of wearing layers, created from SMA 11 mixture with two types of RA (RAP and RAP SMA) and their various dosages (0% to 50%). For comparison, a section containing unmodified paving bitumen 50/70 was built (Section 7). No problems were encountered during the manufacture of all asphalt mixture variants in the asphalt mixing plant (using parallel drum), rejuvenator dosage or subsequent laying, and compaction of the mixtures with no negative impact of added RA on the asphalt mixtures.

Drilled cores from all subsections were sampled in 2017. Subsequently, mixture analyses and functional tests were performed on the obtained binders, especially to verify functionality of the rejuvenators and set the standard requirements. In the meantime, regular monitoring of the test section state was started, which is done by visual inspection.

Below are results of the authors' work, where comparison was made between the sampled drilled cores from all the sections, with the aim to set a criterion for the maximum content and type of RA in SMA mixtures based on standard regulations.

Samples of SMA were taken for subsequent laboratory analyses of all mixture variants. Asphalt binder was reclaimed from these mixtures for performing basic empirical tests and rheological measurements, and also sieve analysis of the aggregate was performed.

Rheological measurements were performed in order to assess the effect of differences between rheological behaviour of reclaimed binders from mixtures, containing both of the used RA types. Because these mixtures underwent coating process and were approximately one year in operation in a pavement, the authors consider the results very important for determination of standard requirements.

Aggregate sieve analyses were performed especially to assess the effect of dosage of standard RA (RAP) with dense-graded sieve size distribution and RA from SMA mixture (RAP SMA) with gap-graded sieve size distribution curve on the overall gradation of the asphalt mixture.

A dynamic shear rheometer Kinexus was used to determine the rheological properties of the reclaimed binders. In particular, the MSCR test (multiple stress

TABLE 4: Composition of the individual SMA 11 mixture variants with various ratios of RA (RAP and RAP SMA).

Mixture	SMA 11					
	0% RAP	10% RAP	20% RAP	30% RAP	30% RAP SMA	50% RAP SMA
Filler (%)	10.5	9.5	8.0	7.5	6.5	3.7
Fraction 0/2 (%)	15.0	10.0	6.0	3.0	3.0	—
Fraction 2/5 (%)	18.0	18.0	16.0	8.0	9.5	1.0
Fraction 4/8 (%)	8.0	8.0	6.0	9.0	8.5	7.0
Fraction 8/11 (%)	48.5	44.5	44.0	42.5	42.5	38.3
RAP (%)	—	10.0	20.0	30.0	—	—
RAP SMA (%)	—	—	—	—	30.0	50.0
S-CEL 7G (%)	0.3	0.3	0.3	0.3	0.3	0.3
Total binder content (%)	6.5	6.5	6.5	6.5	6.5	6.5
Colflex 45/80-55 (new binder) (%)	6.5	6.0	5.5	5.0	4.6	3.3
Addibit L300 (%)	0.2	0.2	0.2	0.2	0.2	0.2
Air void content (%)	3.8	3.6	3.7	3.6	3.6	3.6
Maximum specific gravity (kg/m <sup>3</sup> )	2563.8	2564.8	2537.9	2545.0	2567.2	2579.0
Bulk specific gravity (kg/m <sup>3</sup> )	2468.1	2473.1	2444.4	2452.6	2475.0	2490.8
Voids in mineral aggregates (%)	19.5	19.3	19.3	19.3	19.4	19.3
Voids filled by bitumen (%)	81	82	81	81	81	82
Total binder content (%-vol.)	15.7	15.8	15.6	15.6	15.8	15.9

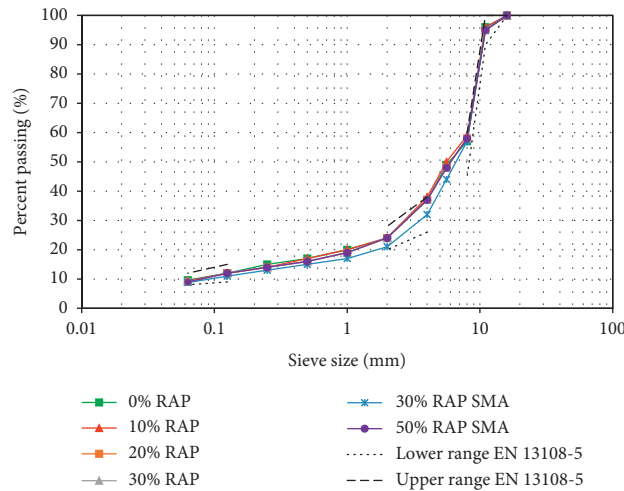


FIGURE 3: Sieve size distribution of the individual variants of the designed SMA 11 mixtures with various ratios and both types of RA.

TABLE 5: Determined parameters of resistance against permanent deformation of SMA 11 mixture.

Mixture Temperature (°C)	50		60	
	WTS <sub>AIR</sub> (mm/10 <sup>3</sup> cycles)	PRD <sub>AIR</sub> (%)	WTS <sub>AIR</sub> (mm/10 <sup>3</sup> cycles)	PRD <sub>AIR</sub> (%)
SMA 11 0% RAP	0.012 (0.001897)	1.8 (0.366824)	—	—
SMA 11 10% RAP	0.018 (0.002898)	2.0 (0.288097)	—	—
SMA 11 20% RAP	0.028 (0.002530)	2.3 (0.209762)	—	—
SMA 11 30% RAP	0.026 (0.002191)	1.7 (0.244949)	0.048 (0.002608)	2.1 (0.275681)
SMA 11 30% RAP SMA	0.026 (0.001265)	1.6 (0.260768)	0.049 (0.00228)	2.6 (0.126491)
SMA 11 50% RAP SMA	0.019 (0.002000)	2.0 (0.192354)	0.046 (0.003578)	3.0 (0.289828)

creep and recovery test) was performed in accordance with the EN 16659, which also allows assessing and differentiating the degree of binder modification. This issue is described in detail in [13]. The table below shows test results of selected binder variants. The binders below were chosen with the aim to determine the parameters for the standard:

- (a) From Section 1, the “reference mixture”, containing modified asphalt and no reclaimed asphalt material

- (b) From Section 5, a mixture containing polymer-modified bitumen PMB 45/80-55 and 30% RAP SMA
- (c) From Section 7, for comparison, mixture containing paving bitumen 50/70 and no reclaimed asphalt material

The results of shear strain during multiple stress creep and recovery test (Figure 6) and the obtained parameters (Table 8) show that binders recovered from Sections 1 and 5

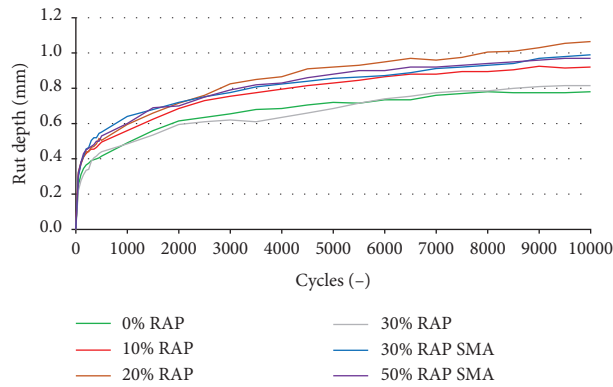


FIGURE 4: Course of the wheel tracking test at a temperature of 50°C.

TABLE 6: Stiffness of SMA 11 mixture variants with various RA ratios (RAP and RAP SMA).

Mixture	Stiffness modulus (MPa) at 15°C and load frequency				
	5 Hz	10 Hz	15 Hz	20 Hz	25 Hz
SMA 11 0% RAP	6405 (52.4)	7082 (36.4)	7492 (35.0)	7835 (34.8)	8156 (34.8)
SMA 11 10% RAP	5765 (34.9)	6434 (26.4)	6864 (39.7)	7178 (34.8)	7443 (38.5)
SMA 11 20% RAP	6235 (42.7)	6923 (23.5)	7400 (51.3)	7736 (38.4)	8047 (38.2)
SMA 11 30% RAP	6467 (24.8)	7207 (45.7)	7703 (32.6)	8075 (21.1)	8393 (46.2)
SMA 11 30% RAP SMA	6076 (19.4)	6683 (38.1)	7083 (48.0)	7382 (30.0)	7868 (35.0)
SMA 11 50% RAP SMA	6691 (37.1)	7321 (30.3)	7760 (38.0)	8111 (35.2)	8521 (43.2)

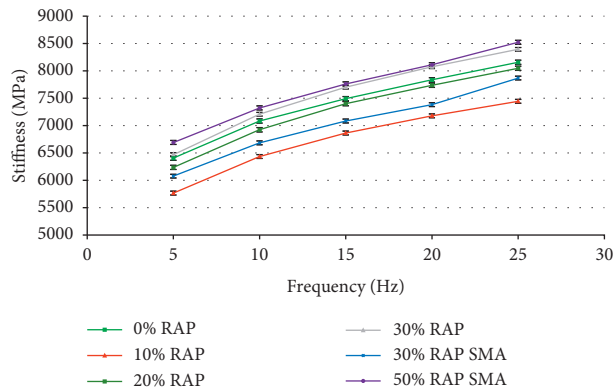


FIGURE 5: Stiffness of the individual SMA 11 mixture variants with various ratios and both types of RA.

TABLE 7: Low-temperature parameters of SMA 11 mixtures with various ratios of RA (RAP and RAP SMA).

Mixture	Low-temperature properties based on EN 12697-46	
	Maximum tensile strength (MPa)	Temperature at crack formation (°C)
SMA 11 0% RAP	3.60 (0.228)	-22.9 (0.638)
SMA 11 10% RAP	4.08 (0.207)	-21.9 (0.603)
SMA 11 20% RAP	3.72 (0.273)	-21.0 (0.566)
SMA 11 30% RAP	4.04 (0.236)	-21.6 (0.579)
SMA 11 30% RAP SMA	4.24 (0.361)	-24.4 (0.603)
SMA 11 50% RAP SMA	3.84 (0.305)	-23.1 (0.609)

(i.e., with 0% of reclaimed asphalt material and 30% RAP SMA) behave very similarly, unlike bitumen from Section 7 (i.e., 50/70) which behaves differently. Given the fact that nonmodified paving bitumen was used in Section 7, the lowest value of  $J_{nr3,2}$  and highest value of  $R_{3,2}$  were achieved.

Figure 7 shows results of sieve analyses of the aggregate from all asphalt mixtures. Sieve size distribution of recovered aggregates from all mixtures lies in a relatively narrow range. Given the particular drops on the standard-required sieves, it was determined that the requirements of

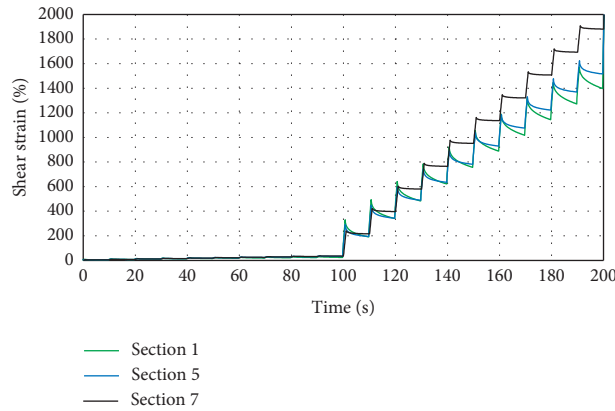


FIGURE 6: Progress of multiple stress creep and recovery test for chosen recovered bitumens.

TABLE 8: Results of multiple stress creep and recovery test according to EN 16659 for selected recovered binders.

Binder recovered from	MSCR test results					
	$J_{nr,0,1}$ ( $\text{kPa}^{-1}$ )	$J_{nr,3,2}$ ( $\text{kPa}^{-1}$ )	$J_{nr,diff\ 3,2-0,1}$ (%)	$R_{0,1}$ (%)	$R_{3,2}$ (%)	$R_{diff\ 3,2-0,1}$ (%)
Section 1	0.24	0.43	75.77	71.46	54.52	23.71
Section 5	0.32	0.46	42.72	54.96	41.78	23.98
Section 7	0.35	0.58	65.63	35.82	12.18	66.00

$J_{nr}$  is the nonrecoverable creep compliance (at two shear stresses: 0.1 kPa and 3.2 kPa) in  $\text{kPa}^{-1}$ ;  $R$  is the average percent recovery in %.

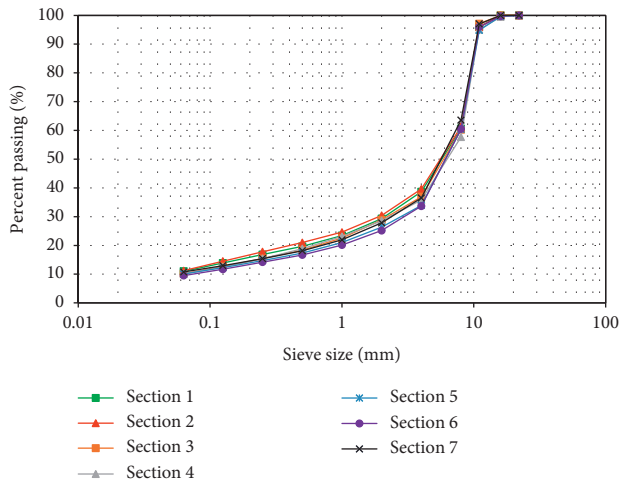


FIGURE 7: Sieve size distribution of recovered aggregates from test sections.

the standard were satisfied with regard to aggregate gradation of mixture.

Upon closer analysis of the sieve size distribution curves, it can be seen that mixtures where RAP SMA was used show better results (more gap graded) of the sieve size distribution curve, which is closer to gradation of SMA-type asphalt mixtures.

## 6. Conclusions

The paper presents and analyzes results of a 5-year research focused on the possibility of using the reclaimed asphalt material (in a dosage up to 50%) in stone mastic asphalt

(SMA), which is, thanks to its skeleton structure, used predominantly in very heavily traffic-loaded pavements (highways, etc.). For concluding, the following are considered:

- (i) The abovementioned results (stiffness, resistance against permanent deformations, and low-temperature properties) of the individual laboratory-prepared SMA mixtures with various dosages of the reclaimed asphalt material (10% to 50%) and comparison with reference mixture with no reclaimed asphalt material
- (ii) Trouble-free real manufacture of these mixtures in an asphalt mixing plant and subsequent laying of all variants of SMA mixtures in the test section
- (iii) Analysis of properties of the taken asphalt mixtures and recovered asphalt binders, which were in operation and performed well with no issues until now despite being heavily traffic loaded

Based on the above results, it can be said that it is possible to use the reclaimed asphalt material in SMA-type mixtures without any negative impacts on functional properties or layer lifetime. Based on the above results and experience, the authors currently recommend change of the standard (in particular proposal of national parameters in standard EN 13 108-5) regarding content of the reclaimed asphalt material in SMA-type mixtures. The current prohibition of adding the reclaimed asphalt material to SMA-type mixtures is replaced with possibility of adding the processed reclaimed asphalt material in the ratio up to 20%, given the reclaimed asphalt material must be obtained by separate milling of wearing

course of the pavement made from the SMA-type mixture (i.e., with modified asphalt binder—RAP SMA). Proper processing means not just precrushing of the material to the required fraction, roofing of RA deposits, its separation by milling layer by layer, but especially usage of rejuvenators for restoration of properties of the aged bitumen in the reclaimed asphalt material.

### Data Availability

The data used to support the findings of this study are included within the article.

### Conflicts of Interest

The authors declare that there are no conflicts of interest.

### Acknowledgments

This paper has been worked out under the project TA04031328 “Recycling of stone mastic asphalts and development of special cellulose fibres for this type of asphalt mixtures” and project no. LO1408 “AdMaS UP—Advanced Materials, Structures and Technologies,” supported by Ministry of Education, Youth and Sports under the “National Sustainability Programme I.”

### References

- [1] D. Cihlářová, I. Fencl, S. Čápayová, and P. Pospíšil, “Use of adhesion promoters in asphalt mixtures,” *Slovak Journal of Civil Engineering*, vol. 26, no. 1, pp. 19–24, 2018.
- [2] “EAPA statement,” <https://eapa.org/asphalt/>.
- [3] EAPA Position Paper, *Asphalt the 100% Recyclable Construction Product*, European Asphalt Pavement Association, Brussels, Belgium, 2014, [https://eapa.org/wp-content/uploads/2018/07/EAPApaper\\_Asphalt\\_the%20100%20recyclable\\_construction-product.pdf](https://eapa.org/wp-content/uploads/2018/07/EAPApaper_Asphalt_the%20100%20recyclable_construction-product.pdf).
- [4] R. Izaks, V. Haritonovs, I. Klasa, and M. Zaumanis, “Hot mix asphalt with high RAP content,” *Procedia Engineering*, vol. 114, pp. 676–684, 2015.
- [5] G. Liu, G. Leegwater, E. Nielsen, J. Komacka, and M. van de Ven, “Evaluating the rheological properties of PMB-containing RA binders from surface-layer asphalt mixtures to be recycled,” *Construction and Building Materials*, vol. 49, pp. 8–14, 2013, ISSN 0950-0618.
- [6] T. Koudelka and M. Varaus, “Asphalt mixtures with a high amount of RAP—case study,” *IOP Conference Series: Materials Science and Engineering*, vol. 236, pp. 1–10, 2017.
- [7] E. Hagos, M. Shirazi, and A. van de Wall, “The development of 100% RAP asphalt mixture with the use of innovative rejuvenator,” in *Proceedings of the 6th Eurasphalt & Eurobitume Congress*, Prague, Czech Republic, June 2016.
- [8] A. M. Abu Abdo, “Utilizing reclaimed asphalt pavement (RAP) materials in new pavements—a review,” *International Journal of Thermal & Environmental Engineering*, vol. 12, no. 1, pp. 61–66, 2016.
- [9] H. S. Jagadeesh and M. Kadayyanvarmath, “Studies on SMA mixes with partial rap replacement in addition with fiber,” *International Journal of Science and Research (IJSR)*, vol. 6, no. 8, pp. 65–73, 2017, ISSN (Online): 2319-7064.
- [10] A. Liphardt, J. Król, and P. Radziszewski, “Influence of polymer modified binder content from RAP on stone mastic asphalt rutting resistance,” *Procedia Engineering*, vol. 153, pp. 407–413, 2016.
- [11] F. Perez, M. Rodriguez, J. De Visscher, A. Vanelstraete, and L. De Bock, “Design and performance of hot mix asphalts with high percentages of reclaimed asphalts: approach followed in the paramix project,” in *Proceedings of the 3rd Eurasphalt & Eurobitume Congress*, Vienna, Austria, May 2004.
- [12] O. G. Andersson, A. Christiansen, U. Helk, L. Josephsen, H. F. Larsen, and E. Nielsen, “MUDP projekt: cirkulær asfalt produktion i Danmark,” 2018, ISBN: 978-87-93710-95-5, <https://www2.mst.dk/Udgiv/publikationer/2018/10/978-87-93710-95-5.pdf>.
- [13] P. Coufalík, *Rheological Properties of Asphalt Binders*, Dissertation thesis, Brno University of Technology, Faculty of Civil Engineering, Brno, Czech Republic, 2017.

## Research Article

# Wetting Model of Asphalt on the Aggregate Surface and Its Effect Factors

YuHui Pi,<sup>1</sup> Yan Li ,<sup>2</sup> YingXing Pi,<sup>1</sup> XiaoYong Tan,<sup>2</sup> and MingMing He<sup>3</sup>

<sup>1</sup>Chongqing Vocational Institute of Engineering, Chongqing 402260, China

<sup>2</sup>School of Highway, Chang'an University, Xi'an, Shaanxi 710064, China

<sup>3</sup>CCCC First Highway Consultants Co., Ltd., Xi'an, Shaanxi 710075, China

Correspondence should be addressed to Yan Li; [liyan@chd.edu.cn](mailto:liyan@chd.edu.cn)

Received 27 March 2019; Revised 3 June 2019; Accepted 15 July 2019; Published 25 July 2019

Guest Editor: Lily Poulidakos

Copyright © 2019 YuHui Pi et al. This is an open access article distributed under the Creative Commons Attribution License, which permits unrestricted use, distribution, and reproduction in any medium, provided the original work is properly cited.

Wetting is the process where asphalt infiltrates into the aggregate surface, which is important for the bonding between asphalt and aggregates. In this paper, the aggregate surface textures were simplified to V shape, and a wetting model was established to research the effects of initial temperature and cooling rate of asphalt and aggregate surface texture sizes on the wetting process. The results show that the asphalt infiltrates into the aggregate surface texture faster in the preliminary stage and slower in the later stage. Cooling rate and lower initial temperature of asphalt affect the surface tension and viscosity, resulting in a longer wetting process, but the effects of cooling rate could be ignored in actual practice. The relationship between the infiltration ending time and surface texture size was established, and it is found that the infiltration ending time is essentially proportional to the texture depth squared and inversely proportional to the texture width.

## 1. Introduction

Water damage is one of the most important failures for highway asphalt pavement, and many highway asphalt pavements face more and more serious water damage after serving for more than one year in South China. Water damage is mainly derived from the loss of the bonding between asphalt and aggregates, which is closely related to the viscosity and cohesion of asphalt, the alkalinity or acidity property, and the surface roughness of aggregates. Some authors demonstrated that moisture could damage the asphalt that lost in strength and durability due to the presence of water [1–3]. Now, the mechanism of bonding between asphalt and aggregates has become the hottest topic currently, and lots of researches have been conducted. So far, there are five theories to explain the bonding mechanism between asphalt and aggregates, including the mechanics theory, chemical reaction theory, surface energy theory, electrostatic theory, and molecular orientation theory, where the surface energy theory has been widely applied [4]. The bonding between asphalt and aggregates was analyzed by

measuring the surface energy parameters and calculating the bonding work between asphalt and aggregates [5]. Hefer et al. applied the Wilhelmy plate method to measure contact angle and then, the bonding of different asphalt and aggregates was evaluated [6]. The USD (Universal Sorption Device) was used to measure the specific surface area of aggregates and the surface energy parameters of asphalt, and the bond strength was calculated, which could provide the basis of selecting asphalt and aggregates [7]. Also, the microcalorimetric could measure the heat change at the moment of adhering of asphalt to the aggregates and then evaluated the bonding effect between asphalt and aggregates [8]. Previous research established a bonding model between asphalt and aggregates based on the surface energy theory, and the bonding work between three kinds of asphalt and three kinds of aggregates was calculated according to this model, which were applied to evaluate the bonding properties of asphalt aggregate interface [9].

Surface energy theory could be used to analyze the bonding mechanism between asphalt and aggregates, but most of the current research studies focus on the properties

evaluation after the asphalt had adhered on the aggregates and rarely involve in how the asphalt was adhered on the aggregates. The bonding of asphalt and aggregates was the result of asphalt wetting on the aggregates, which is important in the bonding or adherence between asphalt and aggregates [10]. Some of researches were conducted to study the wetting process. The effects of the surface characteristics of the aggregates on the wetting process were analyzed [11], and it was found that the smoother the aggregate surface, the faster the asphalt wetting speed and the smaller the contact area between asphalt and aggregates. Coarse surface of aggregates was beneficial to increase the contact area and improve the adhesive strength [12]. However, the wetting process between asphalt and aggregates not only depended on the roughness of aggregate surface, but also was closely related to the asphalt properties, such as the surface tension and viscosity. Therefore, in this paper, the surface textures of aggregates were simplified, and a wetting model was modified by considering the asphalt parameters variation on the temperature to describe the wetting process of asphalt on the aggregate surface. Then, the changing law of surface tension and viscosity of asphalt on the temperature was established, and the effects of initial temperature and cooling rate of asphalt and surface texture size of aggregates on the wetting process were evaluated.

## 2. Law of Change with Temperature of Viscosity, Surface Tension, and Contact Angle of Asphalt with Aggregates

Viscosity and surface tension of asphalt are the basic properties of asphalt and the important index of asphalt cohesion [13]. This property is closely related to the infiltration and bonding of asphalt aggregates. The law of change with time of the viscosity, surface tension, and contact angle of asphalt with aggregates is the parameter basis of asphalt aggregate infiltration and bonding.

*2.1. Law of Change with Temperature of the Viscosity of Asphalt.* In this experiment, the 70# virgin asphalt is selected and the asphalt rotation viscometer is used to determine the viscosity. The experimental program is identical to the specification. Viscosity at different temperatures was measured as shown in Table 1.

According to the Saal formula, the viscosity and temperature of asphalt have the following relationship:

$$\lg \lg \eta = 8.9059 - 3.2533 \lg(T + 273), \quad (1)$$

where  $\eta$  is the viscosity of asphalt, MPa·s, and  $T$  is the asphalt temperature, °C.

The results showed that the viscosity of asphalt decreased significantly with the increase of temperature and showed a double logarithmic linear relationship.

*2.2. Law of Change with Temperature of the Surface Tension of Asphalt.* In this experiment, the 70# virgin asphalt is selected, and the hanging line method is used to determine the

TABLE 1: Viscosity of asphalt at different temperatures (MPa·s).

Temperature (°C)	180	160	140	120	100	80	60
The matrix asphalt	69	230	302.5	855	2800	39296	101772

surface tension [14] and calculate the surface tension of asphalt at different temperatures as shown in Table 2.

According to the data in Table 2, the relationship between asphalt surface tension and temperature can be obtained by using the Matlab software:

$$\gamma = 22.22 - 0.061T, \quad (2)$$

where  $\gamma$  is the surface tension of asphalt, N·m<sup>-1</sup>, and  $T$  is the asphalt temperature, °C.

With the increase of temperature, the surface tension decreases significantly and has a strong linear rule.

### 2.3. Law of Change with Temperature of the Contact Angle of Asphalt with Aggregates

*2.3.1. Advancing and Receding Angle.* When we place a liquid drop on a clean, planar, solid surface, we can observe a contact angle  $\theta_E$ , which is precisely the angle contained in Young's formula. Quite often, though, the surface is marred by defects.

On a nonideal surface, the static contact angle turns out not to be unique. If, for instance, we inflate a drop, as shown in Figure 1(a), the contact angle  $\theta$  can exceed  $\theta_E$  without the line of contact moving at all. Eventually,  $\theta$  reaches a threshold value  $\theta_A$  beyond which the line of contact finally moves.  $\theta_A$  is referred to as the advancing angle. Likewise, when deflating a drop as shown in Figure 1(b),  $\theta$  can decrease down to a limiting value  $\theta_R$  known as the receding angle [15].

*2.3.2. Contact Angle Test.* The contact angle between the 70# virgin asphalt and aggregates at different temperature was obtained as shown in Table 3 by means of the hanging line method and hanging plate method.

Through analysis, it can be seen that asphalt temperature has an effect on the contact angle of asphalt aggregates. When the temperature increases, the contact Angle decreases. But overall, the contact Angle varies little.

## 3. Basic Wetting Model and General Wetting Process

*3.1. Basic Wetting Model and Model Parameters.* Wetting is the process of asphalt to maintain contact with aggregate surface and actually is a process of the asphalt to infiltrate into the aggregate surface texture [16]. But the aggregate surface is extremely complex with different texture shapes and texture dimensions, as shown in Figure 2(a) [17]. For simplification, the surface textures of aggregates were assumed to be V-shape with different widths and depths, as shown in Figure 2(b). The research shows that the aggregate surface is generally wedge-shaped, which is simplified to V shape. Among the assumptions include the concave part of the aggregate surface structure is made into a smooth through crack with wide upper surface and narrow lower surface. This paper mainly

TABLE 2: Surface tension of asphalt at different temperatures (mN/m).

Temperature (°C)	60	80	100	120	140	160	180
Matrix asphalt	18.54	17.39	16.12	14.90	13.64	12.45	11.27

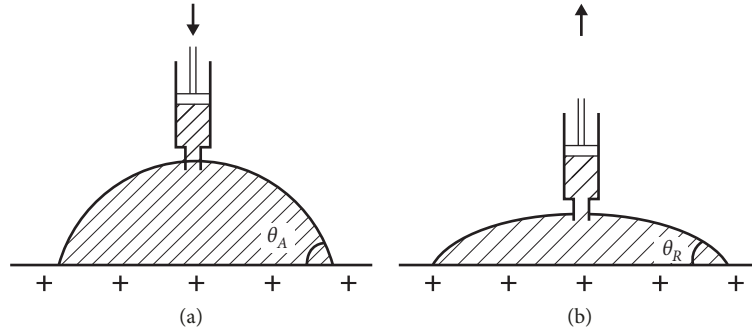


FIGURE 1: (a) Advancing angle when the drop is inflated. (b) Receding angle when the drop is deflated.

TABLE 3: Contact angle between asphalt and aggregates at different temperatures (°).

Temperature (°C)	60	80	100	120	140	160	180
Aggregates	20.41	19.83	19.39	19.02	18.89	18.73	18.61

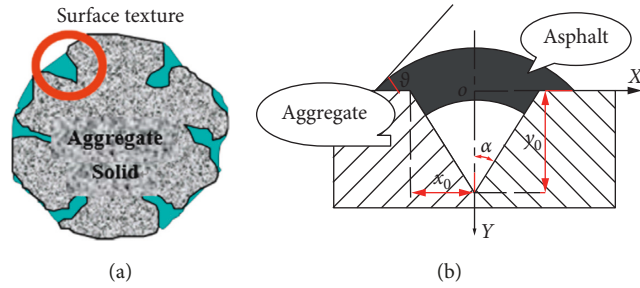


FIGURE 2: Aggregate surface texture and the model of asphalt infiltrating into aggregates. (a) Aggregate surface; (b) simplification of aggregate surface texture.

studies the asphalt infiltration into the aggregates and the raised part is less, ignoring the raised part.

According to the general wetting theory [18], the temperature of asphalt in the mixing process is about 160°C, which is regarded as Newtonian fluid state. The aggregate surface is rough and porous. When asphalt infiltrates the aggregate surface, these tiny pores act as capillaries. The combined effect of surface tension, cohesion, and adhesion of asphalt makes it enter the pore to a certain depth. The mechanism of transport is viscocapillary. The basic wetting process of asphalt on the aggregate surface could be expressed as equation (3) without considering the effect of temperature on the surface extension and viscosity of asphalt [19]. So, the parameters of asphalt, including the surface tension, viscosity, and contact angle, are considered to be constant, not varying with temperature.

$$\frac{\gamma \cos(\theta - \alpha)}{3\eta} \frac{x_0}{y_0} t = y_0 \ln\left(\frac{y_0}{y_0 - y}\right) - y, \quad (3)$$

where  $x_0$  is the half width of the V shape texture, mm;  $y_0$  is the depth of the V shape texture, mm;  $y$  is the depth of asphalt infiltrating into the V shape texture;  $\gamma$  is the surface tension of asphalt, N·m<sup>-1</sup>;  $\eta$  is the viscosity of asphalt, MPa·s;  $\theta$  is the contact angle between asphalt and aggregates, degree;  $\alpha$  is half angle of the V shape texture, degree; and  $t$  is time of asphalt infiltrating into the V shape texture, s.

With the change of aggregate size and shape, its surface texture depth and width changes. According to the existing literature [20], a laser profilometer was designed based on the reflective fiber sensor method to measure and evaluate the aggregate surface texture quantitatively. Measurement results accorded with real condition of surface texture, and results show that the absolute value of dispersion between profile peak and valley distributed in 800~1800 μm; this parameter happens to be the depth of V shape surface texture,  $y_0$ ; also, the distance between the adjacent two peak or two trough is about 500~900 μm, and it just is the double width of V shape surface texture,  $x_0$ ; therefore,  $x_0$  is about 250~450 μm.

**3.2. General Wetting Process.** It is known that  $y_0$  goes from 800 to 1800 μm and  $x_0$  from 250 to 450 μm. To simplify the calculation and combine with above values, we took the average of  $x_0$  and the maximum, minimum, and average of  $y_0$  as variables. In this paper, the half width of V shape surface texture,  $x_0$ , is assumed as 300 μm, and the depth,  $y_0$ , is assumed as 800 μm, 1000 μm, and 1800 μm, respectively. Then, the half angle of the V shape texture,  $\alpha = \arctan(y_0/x_0)$ .

In the basic wetting model, the parameters of asphalt are considered to be constant, not varying with temperature. So, the 70# virgin asphalt was selected, and the technical parameters were measured at 160°C. The surface tension of SK70# virgin asphalt is 12.45 mN/m, the viscosity is 230 MPa·s, and using the contact test, the obtained contact angle between asphalt and aggregates is 18.73°.

The above model parameters are substituted in equation (3), and the Matlab program is applied to obtain the solutions. The infiltration curves of asphalt on the aggregate surface with different texture depths are shown in Figure 3.

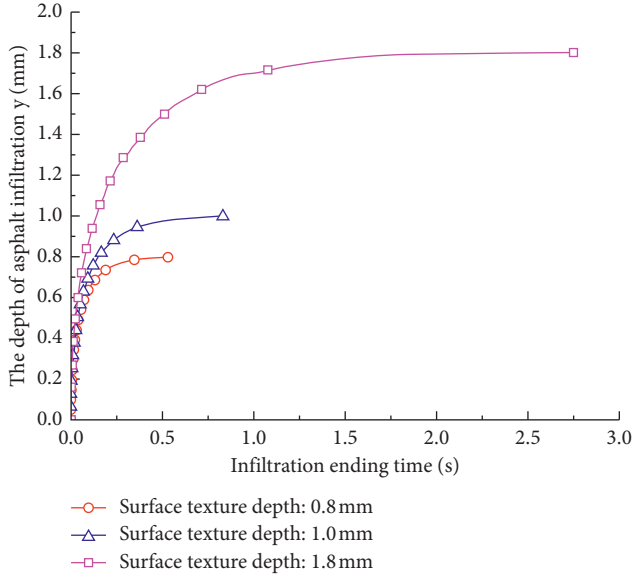


FIGURE 3: Infiltration curves of asphalt on the aggregate surface.

The results show that the asphalt infiltrates into the aggregate surface texture faster in the preliminary stage and slower in the later stage, and the infiltrating asphalt could be only more and more closer to the bottom of surface texture but never reach to. But there is a moment at which the infiltration rate becomes very slow, and the infiltration process could be considered as approximately completed. This time is defined as infiltration ending time. The infiltration ending time is obtained by estimating the infiltration curves as in Figure 3. It is the time when the tangent of infiltration curves is horizontal. In this paper, the end of the infiltration curves just are the infiltration ending times and the later curves are omitted.

#### 4. Modified Wetting Model and the Effect of Temperature

The above discussion is based on the assumption that the technical parameters of asphalt are not varied with temperature during the wetting process. But in fact, the asphalt surface tension, viscosity, and the contact angle between asphalt and aggregates are closely related to the temperature. With consideration of the influence of temperature on asphalt parameters, the basic wetting model should be modified.

**4.1. Variation of Asphalt Parameters with the Temperature.** The surface tension of the liquid is caused by its surface molecules suffering unbalanced force, and usually varied with the temperature [21]. According to the surface tension experiment, the relationship between surface tension of asphalt and temperature can be expressed as equation (2).

According viscosity experiment, the variation of asphalt viscosity with temperature could be expressed as equation (1).

In order to obtain the variation law of temperature with the time, the asphalt was firstly heated to 160°C and then placed in air for cooling to 80°C, so as to simulate the cooling process of asphalt in the construction period. During the simulated cooling process, the asphalt temperatures over

cooling time were recorded and analyzed. The relationship between asphalt temperature and cooling time is expressed as

$$T = T_0 - 0.068t, \quad (4)$$

where  $T$  is the asphalt temperature, °C;  $T_0$  is the initial asphalt temperature, °C; and  $t$  is the cooling time, s.

In fact, the contact angle between asphalt and aggregates is changing with the asphalt temperature. While the experiment proved that the influence is very small, this paper takes no account of its effect and considers the contact angle is constant.

**4.2. Modified Wetting Model and Effects of Cooling Temperature.** Rewrite equation (3) in the differential expression as [19]

$$\frac{d_y}{d_t} = \frac{\gamma \cos(\theta - \alpha)x_0}{3\eta} \left( \frac{1}{y} - \frac{1}{y_0} \right). \quad (5)$$

Substitute equations (1), (2), and (4) in equation (5) and obtain

$$\frac{d_y}{d_t} = \frac{[a - bT] \cos(\theta - \alpha)x_0}{3(g/10^{(T+273)^d})} \left( \frac{1}{y} - \frac{1}{y_0} \right), \quad (6)$$

where  $d$  and  $g$  are the two temporary variables.

The integral form of equation (6) is expressed as

$$y_0^2 \ln(y_0 - y) + y_0 y = \frac{\cos(\theta - \alpha)}{3k} x_0 \cdot \int [a - bT] 10^{c/(T+273)^d} dT + C_1. \quad (7)$$

In equation (7),  $\int [a - bT] 10^{c/(T+273)^d} dT$  is too complex to solve. In order to simplify the calculation,  $[a - bT] 10^{c/(T+273)^d}$  was transformed into a simple function  $1.42 \times 10^{-4} e^{0.041T}$  ( $R^2 = 0.9965$ ) by using the Matlab program, and  $\int [a - bT] 10^{c/(T+273)^d} dT$  could be expressed as

$$\int [a - bT] 10^{c/(T+273)^d} dT = 3.46 \times 10^{-4} e^{0.041T}. \quad (8)$$

Substitute the initial conditions in equation (7);  $y$  is 0 mm when  $T$  is 160°C and the constant  $C_1$  could be obtained as  $C_1 = -3.64 \times 10^{-4}$ . Then substitute equation (8), (4) and the constant  $C_1$  in equation (7), and the wetting process could be solved by using the Matlab program. The comparison of infiltration curves deduced from the basic and modified wetting models is shown in Figure 4.

From the infiltration curves, the infiltration ending time could be determined, and the comparison of the infiltration ending times deduced from the basic and modified models is expressed in Table 4. After modification, the infiltration ending time becomes longer because viscosity increases and surface tension decreases with the decreasing temperature during the infiltrating process. It is more realistic, and the cooling of asphalt affects the surface tension and viscosity and results in a longer infiltration ending time. However, the total mixing time of asphalt mixture in practice is generally

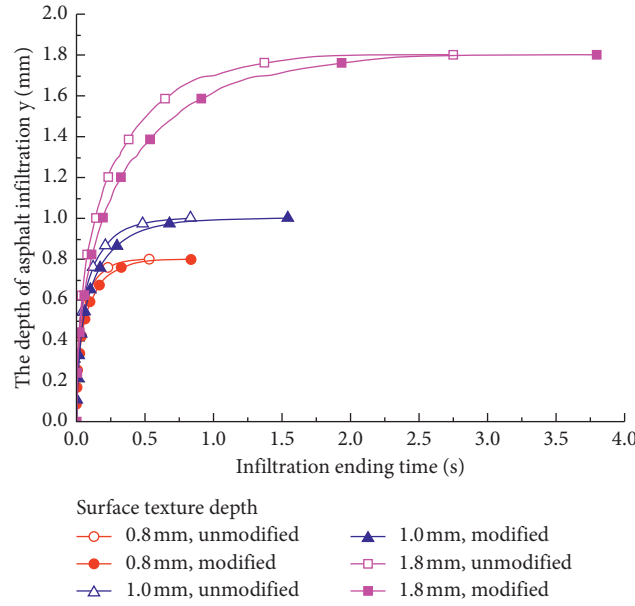


FIGURE 4: Comparison of infiltration curves deduced from the basic and modified models.

TABLE 4: Comparison of infiltration ending time deduced from basic and modified model.

Surface texture depth (mm)	Infiltration ending time from basic model (s)	Infiltration ending time from modified model (s)	Amplitude of variation (s)	Relative error (%)
0.8	0.53	0.83	0.30	56.6
1.0	0.83	1.54	0.71	85.5
1.8	2.75	3.80	1.05	38.2

more than 45 s [22]; the modification on the infiltration ending time could be ignored.

4.3. *Effects of the Initial Temperature on the Infiltration Process.* Though the effects of cooling temperature could be ignored during mixing, the initial temperature affects the surface tension and viscosity significantly and may have an important influence on the infiltration time.

In order to analyze the abovementioned influence, this paper takes the constant value of  $x_0 = 350 \mu\text{m}$  and  $y_0 = 1300 \mu\text{m}$ , which are the midvalues of V shape surface texture distribution and only change the initial temperature to solve the modified wetting model. The infiltration curves of asphalt are shown in Figure 5.

According to Figure 5, the infiltration ending times at different initial temperatures are shown in Figure 6. The result shows that the initial asphalt temperature has a significant influence on the infiltration process, and the higher the initial temperature, the shorter the infiltration ending time. The key factor to improve the bonding between asphalt and aggregates is to ensure that the temperature of asphalt does not decrease during mixing.

### 5. Effects of Surface Texture Size on the Infiltration Process

The surface texture sizes are also the important parameters in the infiltration of asphalt on the aggregate surface [23]. So

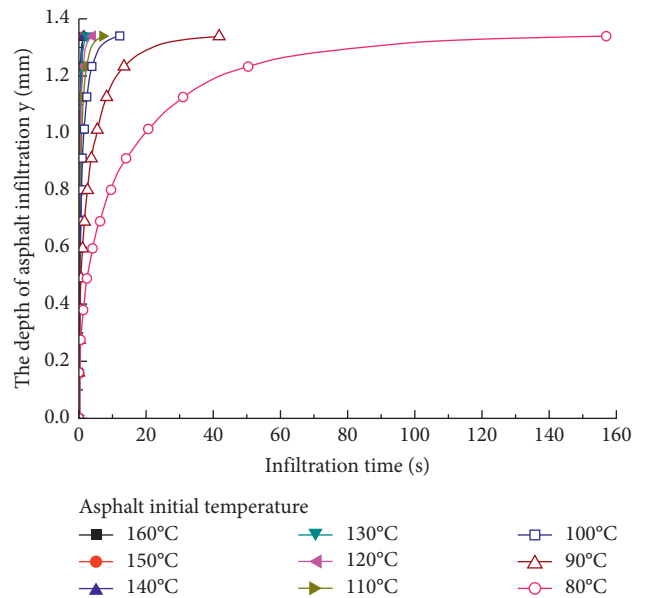


FIGURE 5: Infiltration curves of asphalt at different initial temperature.

the initial temperature of asphalt is assumed as 160°C, and the surface tension, viscosity, and contact angle are kept as constant but the V shape width and depth are changed to solve the modified wetting model. The infiltration ending times with different V shape textures are shown in Figure 7.

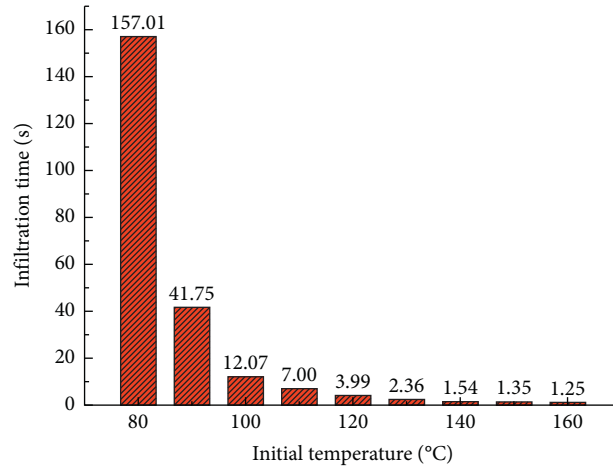


FIGURE 6: Infiltration ending time at different initial temperatures.

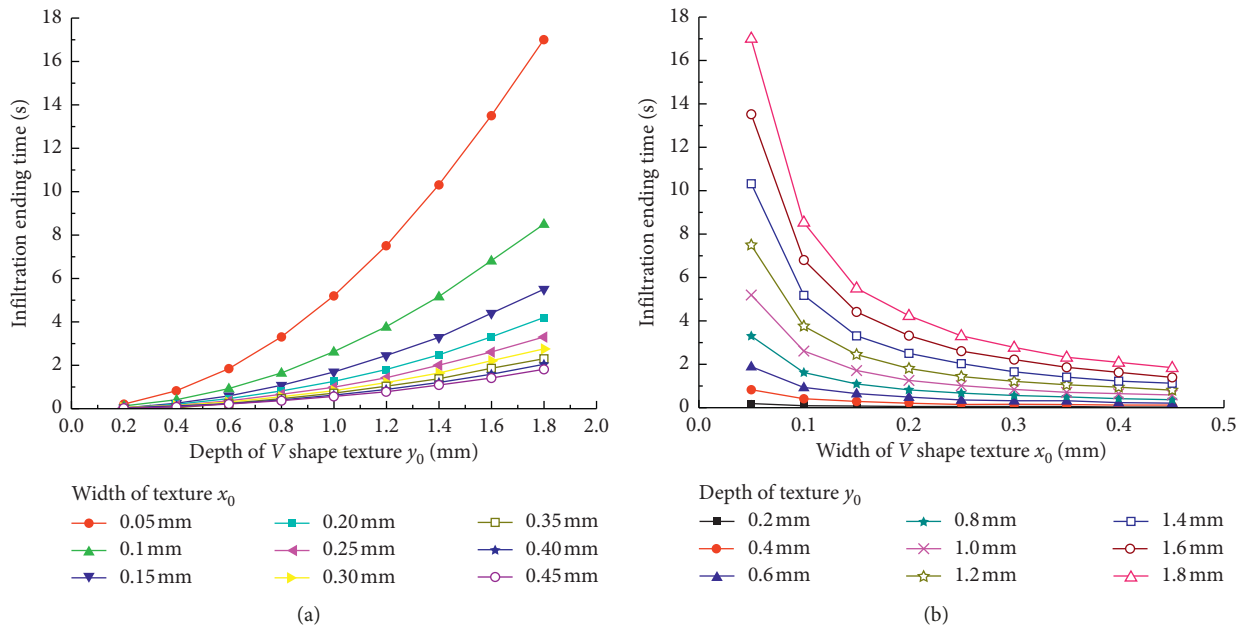


FIGURE 7: Infiltration ending times with different V shape textures. (a) Infiltration ending time vs. depth of texture. (b) Infiltration ending time vs. width of texture.

It could be found that the coarser the surface texture of aggregates, the better the bonding between asphalt and aggregates. The infiltration ending time increases with the depth of the surface texture, but decreases with the width; that is to say, the deeper and narrower the aggregate surface texture is, the longer the asphalt wetting process is. So we should choose aggregates with rough surfaces and large voids. The relationship between the infiltration ending time and surface texture size is expressed as

$$J = 0.25\lambda \frac{h^2}{w}, \tag{9}$$

where  $J$  is the infiltration ending time, s;  $h$  is the depth of surface texture, mm;  $w$  is the width of surface texture, mm; and  $\lambda$  is the correction coefficient, related to the shape of

surface texture, and is expressed as  $h/w = 1, \lambda = 1; h/w < 1, \lambda > 1; h/w > 1, \lambda < 1$ .

## 6. Conclusions

This paper analyzed the general wetting process of asphalt on the aggregate surface based on the surface energy theory and established a modified wetting model by considering the asphalt parameters variation on the temperature, according to which the effects of initial temperature and cooling rate of asphalt and aggregate surface texture size on the wetting process were evaluated. Some conclusions are obtained as following.

- (i) According to the basic wetting model, the asphalt infiltrates into the aggregate surface texture faster in

the preliminary stage and slower in the later stage, and the infiltrating asphalt could be only more and more closer to the bottom of surface texture but never reach to.

- (ii) The basic wetting model should be modified with consideration of the influence of temperature on asphalt properties, and the cooling and lower initial temperature result in a longer wetting process. However, the effects of cooling rate could be ignored in actual practice.
- (iii) The relationship between the infiltration ending time and surface texture size has been established with a shape-related correction coefficient and indicates that the infiltration ending time of asphalt on the aggregates is essentially proportional to the texture depth squared but inversely proportional to the texture width.

## Data Availability

The data used to support the findings of this study are available from the corresponding author upon request.

## Conflicts of Interest

All authors have no conflicts of interest to declare.

## Acknowledgments

This work was supported by National Key R&D Program of China (no. 2018YFE0103800), China Postdoctoral Science Foundation (no. 2017M620434), Shaanxi Postdoctoral Grant Program (no. 2017BSHYDZZ17), and the Special Fund for Basic Scientific Research of Central College of Chang'an University (no. 310821173501). The authors gratefully acknowledge their financial support.

## References

- [1] S. G. Jahromi, "Estimation of resistance to moisture destruction in asphalt mixtures," *Construction and Building Materials*, vol. 23, no. 6, pp. 2324–2331, 2009.
- [2] U. Bagampadde, U. Isacson, and B. M. Kiggundu, "Impact of bitumen and aggregate composition on stripping in bituminous mixtures," *Materials and Structures*, vol. 39, no. 3, pp. 303–315, 2006.
- [3] J. S. Buckley, K. Takamura, and N. R. Morrow, "Influence of electrical surface charges on the wetting properties of crude oils," *SPE (Society of Petroleum Engineers) Reservoir Engineering*, vol. 4, no. 3, 1989.
- [4] J. P. Zhang, H. Q. Tan, J. Z. Pei, T. Qu, and W. L. Liu, "Evaluating crack resistance of asphalt mixture based on essential fracture energy and fracture toughness," *International Journal of Geomechanics*, vol. 19, no. 4, article 06019005, 2019.
- [5] S. Han, Y. M. Liu, O. M. Xu, and B. Li, "Influence of material characteristics on bonding at interface between asphalt and aggregates," *Journal of Chang'an University (Natural Science Edition)*, vol. 30, no. 3, pp. 7–9, 2010.
- [6] A. W. Hefer, A. Bhasin, and D. N. Little, "Bitumen surface energy characterization using a contact angle approach," *Journal of Materials in Civil Engineering*, vol. 18, no. 6, pp. 759–767, 2006.
- [7] A. Bhasin and D. N. Little, "Characterization of aggregate surface energy using the universal sorption device," *Journal of Materials in Civil Engineering*, vol. 19, no. 8, pp. 634–641, 2007.
- [8] A. Bhasin and D. N. Little, "Application of microcalorimeter to characterize adhesion between asphalt binders and aggregates," *Journal of Materials in Civil Engineering*, vol. 21, no. 6, pp. 235–243, 2009.
- [9] Y. Y. Wang, D. M. Yue, Z. H. Shi, and D. Huo, "The research based on the surface energy theory to evaluate asphalt/stone interface bonding performance," *Chinese and Foreign Road*, vol. 33, no. 3, pp. 247–250, 2013.
- [10] X. P. Cao and Y. M. Jiang, "Frictional property of wetting contact line and wenzel behavior of solid surface tension," *Journal of Physics*, vol. 54, no. 5, pp. 2202–2206, 2005.
- [11] C. X. Zhou, G. M. Chen, and Y. Q. Tan, "Roughness measurement of aggregates surface texture," *Journal of Traffic and Transportation Engineering*, vol. 9, no. 1, pp. 51–55, 2009.
- [12] W. C. Kong, *Impacts of Aggregates Characteristics on Asphalt/Aggregates Interface Properties*, Chang'an University, Xi'an, China, 2012.
- [13] J. P. Zhang, X. Li, W. Ma, and J. Pei, "Characterizing heterogeneity of asphalt mixture based on aggregate particles movements," *Iranian Journal of Science and Technology, Transactions of Civil Engineering*, vol. 43, no. 1, pp. 81–91, 2019.
- [14] J. P. Zhang, Z. P. Fan, H. Wang, W. Sun, J. Z. Pei, and D. Wang, "Prediction of dynamic modulus of asphalt mixture using micromechanical method with radial distribution functions," *Materials and Structures*, vol. 52, no. 2, pp. 1–12, 2019.
- [15] D. Gennes, P. Gilles, B. Wyart, and S. Françoise, *Capillarity and Wetting Phenomena*, Springer, Berlin, Germany, 2004.
- [16] E. Masad, D. Little, and R. Sukhwani, "Sensitivity of HMA performance to aggregate shape measured using conventional and image analysis methods," *Road Materials and Pavement Design*, vol. 5, no. 4, pp. 477–498, 2004.
- [17] J. Z. Corey, *Application of Surface Energy Measurements to Evaluate Moisture Susceptibility of Asphalt and Aggregates*, Texas A&M University, College Station, TX, USA, 2005.
- [18] X. R. Teng, *Surface Physical Chemical Properties*, Chemical Industry Press, Beijing, China, 2009.
- [19] E. W. Washburn, "The dynamics of capillary flow," *Physical Review*, vol. 17, no. 3, pp. 273–283, 1921.
- [20] G. M. Chen, Y. Q. Tan, Z. R. Wang, L.-H. Liu, and H.-P. Ma, "Experimental design for measurement on aggregates surface texture," *China Journal of Highway and Transport*, vol. 19, no. 2, pp. 36–41, 2006.
- [21] E. J. Henry, "Analytical and numerical modeling assessment of capillary barrier performance degradation due to contaminant-induced surface tension reduction," *Journal of Geotechnical and Geoenvironmental Engineering*, vol. 133, no. 2, pp. 231–236, 2007.
- [22] JTG F40-2004, *Technical Specifications for Construction of Highway Asphalt Pavements*, China Communications Press, Beijing, China, 2004.
- [23] J. P. Zhang, X. Li, G. Liu, and J. Pei, "Effects of material characteristics on asphalt and filler interaction ability," *International Journal of Pavement Engineering*, vol. 20, no. 8, pp. 928–937, 2019.

## Research Article

# Evaluation of the Effect of Fly Ash and Slag on the Properties of Cement Asphalt Mortar

Tri H. M. Le <sup>1</sup>, Dae-Wook Park <sup>1</sup>, Jin-Yong Park,<sup>2</sup> and Tam M. Phan <sup>1</sup>

<sup>1</sup>Dept. of Civil Engineering, Kunsan National University, 558 Daehak Ro, Jeonbuk, Republic of Korea

<sup>2</sup>Korea Rail Network Authority, 242 Jungang-Ro, Dong Gu, Daejeon 34618, Republic of Korea

Correspondence should be addressed to Dae-Wook Park; [dpark@kunsan.ac.kr](mailto:dpark@kunsan.ac.kr)

Received 25 March 2019; Accepted 26 June 2019; Published 10 July 2019

Guest Editor: Quantao Liu

Copyright © 2019 Tri H. M. Le et al. This is an open access article distributed under the Creative Commons Attribution License, which permits unrestricted use, distribution, and reproduction in any medium, provided the original work is properly cited.

The application of cement asphalt mortar (CAM) in modern high-speed railways has been gaining attention due to its combined merits between asphalt and cement hydration product characteristics. To promote sustainable development, it is promising to utilize by-products in the making of new CAM instead of using only cement. In this research, the cement content was partly replaced by fly ash or ground-granulated blast furnace (GGBS) slag to achieve this objective. Then, laboratory experiments were conducted to determine the effect of these admixtures on the fresh and hardened characteristics of CAM. The test results revealed that the CAM mixture with slag received better fresh properties compared to the controlled mixture. However, the poor pozzolanic property of these by-product materials may lead to the low strength development. Meanwhile, although the mixture with fly ash suffered from slow strength establishment compared to the control mix at an early age, the strength of this condition increases dramatically after 28 days. Based on the findings, the application of appropriate fly ash content in the CAM mixture will not only provide ideal workable time and mixing stability but also ensure the required strength for the design target. This combination also serves as a cost-effective and environmental solution.

## 1. Introduction

Progressive ballast deterioration and geometry degradation have been seriously impacting the performance of railway track systems associated with high traffic pressure. The weakening structure will impose critical safety effects on the track system and reduce the comfort of railway users. Recently, some innovative solutions have been proposed to solve this issue [1–4]. One of the rehabilitation strategies of ballast degradation is to reduce track vibration by using crumb rubber. However, tracks incorporated with this technique have suffered from high vertical settlement and low bearing capacity [4]. Another solution was introduced in the study of Kennedy et al. [5], in which the authors utilize geosynthetics in the ballast layer. It was noticed that injecting polyurethane into the ballast will not only improve the settlement resistance of the ballast structure but also ensure the railway structural integrity. However, the significantly high construction cost limits the wide application of this method.

In Japan and Europe, a cost-effective concept has been applied for decades to enhance the performance of the track system and reduce the maintenance effort [6–10]. In this method, cement asphalt mortar was utilized as an interlayer between the track slab and the concrete roadbed [7, 8]. Reports indicated that stress dissipation characteristics from the asphalt membrane will reduce the pressure for the whole structure, thereby sustaining the long-time service life [7–10]. Meanwhile, the cement hydration product will ensure the vertical settlement resistance of the railway track. Another advantage of CAM is simple application with self-leveling behavior. The fresh material can be pumped without compaction machine support [7–10].

Also, the main components of CAM can be easily provided by the local construction company such as asphalt emulsion (AE), cement (C), sand (S), and water (W). However, this nonballast slab track method with CAM can only be applied at the initial stage of construction [6–10]. This drawback may hinder its application in actual ballast

degradation rehabilitation projects. Therefore, this research objective is to generate a new strategy named “cement asphalt mortar-stabilized ballast” which not only can achieve the merits of the above nonballast method but can also be applied as a fouled ballast rehabilitation solution.

The present technique evaluates the possibility of stabilizing ballast with cement asphalt mortar, as a prominent solution to reduce the loss in track quality due to particle degradation and ballast settlement. By pouring fresh CAM above the ballast layer, the self-leveling CAM mixture will flow throughout the whole ballast system. The CAM mixture will coat the ballast particles and create strong bonding between them [3]. This bonding will achieve the stiffness from cement hydration products and viscoelasticity from the asphalt membrane [3]. It is expected that the connection between CAM and fouled ballast structure will behave as a new stress dissipation system with high rutting resistance. Moreover, due to the fast application with simple preparation, this technique will also save time for traffic closure.

Prior research about this technique has brought promising results for wide application. The preliminary test results show that optimum C/AE ratios can propose a good mixture with both merits from asphalt and merits from cement hydration products [6–11]. The incorporation of sand and proper initial water will noticeably improve the mixing stability of the fresh CAM mixture which not only shortens the flow time but also contributes to the homogeneous distribution of CAM particles [11, 12]. Prior research also found that the application of quick-hardening admixture as a replacement of cement (14%) provides fast strength gain at an early age without impact on the mixing stability characteristic [11].

In recent decades, research has demonstrated that fly ash can be applied in many structural applications, providing good mechanical properties and durability of concrete [13–16]. In the operation of thermal power plants, fly ash is collected by an electrostatic precipitator from the combustion of powdered coal. This by-product has been found to possess pozzolanic, hydraulic characteristics with glassy, spherical particles of finer size compared to cement [14].

The application of fly ash in cement mortar not only enhances the workability at an early age but also contributes to long-term strength gain of concrete [15]. Based on related research [13–16], it is suggested that the content of fly ash should be designed from 20 to 30% by weight of cement in concrete or mortar to achieve optimum performance. In massive structures (foundation, dams, etc.), reports suggest that higher levels of fly ash should be used (up to 50%) to help control the thermal cracking. In the hydration process of cement, the internal temperature of concrete will be reduced remarkably by using fly ash, thereby lowering the temperature gap between inner and outer parts of concrete [15].

With regard to the use of fly ash in asphalt pavement, most recent studies have focused on the application of fly ash as a mineral filler for asphalt pavement [13]. The authors confirm that the incorporation of fly ash improves the performance of the asphalt mixture because of its unique spherical shape, beneficial particle size distribution, and

chemical properties. Some studies show that these characteristics of fly ash enhance the workability and flexibility and improve the rutting and freeze-thaw resistance of asphalt concrete [16]. In the research of Ramme et al., the authors prove that the fatigue life and tensile strength of asphalt concrete can be slightly increased by using an appropriate amount of Class F fly ash [16]. Moreover, reports found that replacement of natural fillers by fly ash will provide better antistripping and moisture resistance properties for asphalt pavement because of the strong connection between fly ash hydration products and asphalt membrane [13, 16]. The findings of these demonstrations established the foundation for further study on the practical application of fly ash.

The application of GGBF slag in the production of the concrete mixture has been gaining attention recently through some important improvements in engineering properties [17–19]. From iron production, slag is defined as a nonmetallic by-product which is composed mainly of silicates of calcium. Compared to cement, the particles size of slag is much smaller (less than 45 microns) which provides noticeable improvements in the ease of concrete pumping and placement [18]. With appropriate mixing content, this mineral admixture can provide much better workability and enhance the durability of concrete by improving the interface with the cement hydration product. Slag shares relatively the same characteristic with fly ash that has both pozzolanic and cementitious properties [18].

Based on related research [17–19], this mineral admixture can significantly affect certain engineering characteristics of both fresh and hardened concrete [19]. By eliminating the amount of reactive element (such as calcium) needed for expansive sulfate reaction, GGBF slag can significantly protect concrete from sulfate attack. Also, reports confirmed that GGBF slag can reduce the potential of concrete to expand due to alkali-silica reaction [19]. Slag-blended cement will provide ecological advantages by resource conservation to energy efficiency.

Recently, the investigation of CAM mechanical properties has gained attention from many research studies [6–10]. However, there has been lack of investigations as to the utilization of by-products in the production of CAM. Therefore, in this research, slag and fly ash will be first introduced as admixtures in the CAM mixture. The incorporation of the two by-products is expected to improve the fresh properties of CAM and long-time strength gain. The aim of the conducted research is to identify the influence of different dosages of fly ash or slag on the mechanical properties of CAM.

To acquire this objective, cement used in the CAM mixture was replaced by fly ash/slag with contents varying from 10% to 30% with an increment of 10%. Based on preliminary research on obtaining efficient CAM mixtures, this research has asphalt emulsion/cement (AE/C), quick-hardening admixture/cement (QA/C), and water/cement (W/C) ratios of 0.75, 0.14, and 0.5, respectively. The behavior of the fresh CAM mixture was evaluated by conducting the flow cone test, mixing stability test, bleeding test, and workable time test. Then, the hardened stage of CAM was assessed by employing the unconfined compressive strength

(UCS) test on the samples 2 h after casting them into molds and after 28 days. Finally, to identify the microstructure of hardened CAM after 28 days, the FEI Quanta 200F scanning electron microscopy (SEM) test was conducted on CAM samples.

## 2. Materials and Test Methods

Type II Portland cement was used in this study. Class F fly ash was provided by the Korean Western power plant, while GGBF slag was supplied by the Korean iron manufacturing company. The overall chemical properties of cement, fly ash, and slag are displayed in Table 1. The asphalt emulsion is of an anionic type with properties shown in Table 2. Presented in Table 3 is the mix design based on cement weight. The mixing water (W) and asphalt emulsion (AE) contents were selected from the trial mixing test which produced ideal rheology performance at an early age. Based on the suggestion from related studies [10–12], when the fly ash or slag content is increased, less water should be used to ensure the stable workability of all mixtures. This study also incorporates the use of a quick-hardening admixture (QA) at a level of 14% by mass of cement based on a trial test to achieve the fast strength development and mitigate the bleeding phenomenon. In addition, the excessive air bubbles from asphalt emulsion are reduced by using 0.1% defoaming agent (D) (by weight of cement) [10–12]. The initial adding water was mixed with 2% polycarboxylate superplasticizer (SP) based on the author team's experience.

**2.1. Mixing Method.** Based on the authors' experience and after preliminary research [10–12, 20], the wet mixing method was employed in this research. In this method, solid contents (C, QA, and S) were premixed with a water + SP mixture to create the cementitious slurry. The mixing of the slurry was done for approximately 2 minutes at a mixing rate of 120 rpm. Then, the AE + D mixture was then added into the cementitious slurry and mixed together for at least 3 minutes with a mixing rate of 60 rpm before casting them into cylindrical test sample molds ( $\varnothing 50 \times 100$  mm).

The AE + D mixture will improve the mixing stability of asphalt droplets in the asphalt emulsion. The demulsification process of the AE is mitigated, thereby developing a fresh CAM mixture with homogeneous particle sizes and with rare signs of agglomeration. With regard to the replacement of cement by slag or fly ash, this solid content was added into the initial premixed stage as cement.

**2.2. Mixing Stability Test.** Based on preliminary research suggestion, the CAM mixture should obtain proper mixing stability to achieve good flowability and homogeneous particle distribution without agglomeration phenomenon. Therefore, the mixing stability test is first conducted among all tests in this study (Figure 1(a)). Based on KSM 2203 [21], 50 g of asphalt emulsion (50% solid) is poured into a can with 50 g dry cement. Then, the mixture is thoroughly mixed for around 2 min at a stirring rate of 120 rpm. 150 ml of deionized water is then added to the mix and slowly stirred

TABLE 1: Percentage chemical composition of cement, fly ash, and slag.

Chemical composition (%)	SiO <sub>2</sub>	Al <sub>2</sub> O <sub>3</sub>	Fe <sub>2</sub> O <sub>3</sub>	SO <sub>3</sub>	CaO	MgO	K <sub>2</sub> O
Cement	21.56	4.15	2.64	3.01	61.18	2.35	0.65
Fly ash	49.9	24.0	14.4	0.88	3.23	0.98	2.46
Slag	32.7	14.5	0.4	0.4	41.4	4.7	0.6

at a rate of 60 rpm in this second stage for additional 3 min. Finally, the fresh mixture is poured through a 1.18 mm sieve to collect the remaining residue which will be oven-dried and weighted for calculating the mixing stability status:

$$P_r = \frac{m}{m_1 + m_2} * 100\%, \quad (1)$$

where  $P_r$  = percentage of the residue content,  $m$  = oven-dried weight of the residue retained on a 1.18 mm sieve (g),  $m_1$  = weight of asphalt (g), and  $m_2$  = weight of cement (g).

In the optimum mixture, the CAM combination includes cement, asphalt emulsion, sand, water, superplasticizer, and defoaming agent. In preliminary research, the sand and water content will improve the stability of asphalt droplets in asphalt emulsion by lowering the adsorption energy of cement particles. It is predicted that the partial replacement of cement by fly ash or slag will also improve the mixing stability of the mixture. Hence, the new mixing stability was developed with the aim of focusing only on the reaction between cement, slag, and fly ash with asphalt emulsion. The mix design for this new test is shown in Table 4.

**2.3. Flowability Test.** One of the interesting merits of CAM is the self-leveling ability which allows this fresh material to be applied in a narrow place in a short time. Hence, the flow cone test is used to evaluate this characteristic in accordance with Korean Standard KSF 2432 [22]. In this test, a steel cone with a closed end nozzle, a steel plate (50 cm  $\times$  50 cm), a digital watch with counting function, and 400 ml of the fresh mixture are prepared. After thorough mixing, the flow time is determined by recording the required time for 400 ml fresh CAM mixture to completely flow out from the steel cone to the steel plate (Figure 2).

**2.4. Bleeding and Workable Time.** Bleeding is one of the critical problems during the fresh stage of CAM mixtures which imposes segregation, reduces the initial shear stress in mortar, and retards the setting time of cement. The workable time in this research is defined as the amount of time in which the sample is able to retain an acceptable flowability similarly during the initial stage. After this period, the mixture hardens and could not be appropriately cast. In the research of Ouyang et al. [23], the cement hydration is significantly high in the initial 5 min. In this period, the effect of cement on asphalt droplets is more prominent. However, after this time, the asphalt emulsion may be less impacted by the cement hydration process because of thermodynamic stability. Hence, the bleeding phenomenon is tracked after

TABLE 2: Properties of anionic asphalt emulsion.

Density (g/cm <sup>3</sup> )	1-day storage stability (%)	Residue after distillation (%)	Residue on 1.18 mm sieve (%)	Penetration depth at 25° (0.1 mm)	Solid content (%)
1.02	0.3	50	0.01	70	50

TABLE 3: Mix design (by weight of cement/by weight of cement + by-product).

	By-product	Cement (%)	QA (%)	AE (%)	S (%)	W (%)	SP (%)	D (%)
C	0	100	14	75	50	40	2	0.1
FA10	10	90	14	75	50	35	2	0.1
FA20	20	80	14	75	50	32.5	2	0.1
FA30	30	70	14	75	50	30	2	0.1
S10	10	90	14	75	50	35	2	0.1
S20	20	80	14	75	50	32.5	2	0.1
S30	30	70	14	75	50	30	2	0.1

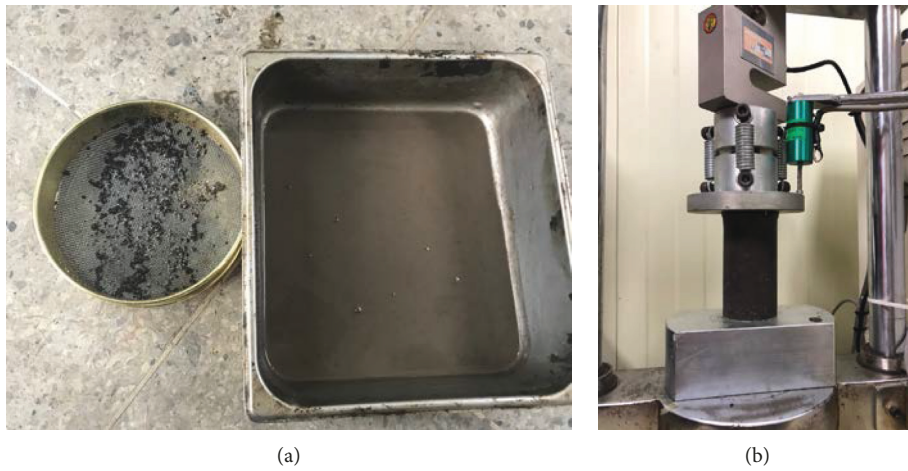


FIGURE 1: Mixing stability test (a) and UCS test (b).

TABLE 4: Mix design for a new mixing stability test.

Condition	Cementitious content (each 50 g)	Asphalt emulsion (g)	Mixing	Residue sieving	Residue drying	Weighing
C	Cement	50				
S	Slag	50	3 min		24 h	
FA	Fly ash	50				

the workable time instead of the initial time. The differences between bleeding of the CAM mixture after the first 5 min and after workable time will be studied in further research. The bleeding water after the workable time is recorded by calculating the mass of bleeding water to the mass of the specimen:

$$\text{bleeding (\%)} = \frac{M_w}{M_s} \times 100, \quad (2)$$

where  $M_w$  = mass of bleeding water and  $M_s$  = mass of the specimen.

**2.5. Unconfined Compressive Strength Test.** The UCS test was employed in this research to quantify the strength development of CAM, especially the cement hydration product [24]. After thorough mixing, the fresh material was cast into

the precut paper mold ( $\varnothing 50 \times 100$  mm). Although the CAM mixture can obtain the strength of about 0.35 MPa after the first two hours, all 28-day strength samples are cured in the mold for 1 day before subjecting them to the unmolding process to ensure the shape stability of the sample. With regard to the curing condition, the environment was controlled at 95% relative humidity and 20°C until the testing day. In the UCS test, the universal compression machine with a loading rate of 1 mm/min is employed to generate accurate test results. 3 replicates will be used to determine the average result of 1 mix design (Figure 1(b)).

**2.6. SEM Test.** Under a high-vacuum condition, the Hitachi FE-SEM S-4700 was used to determine the microstructure of the 28-day strength CAM. Mixes F30, S30, and C were three mixtures employed and evaluated in this test. These mixtures

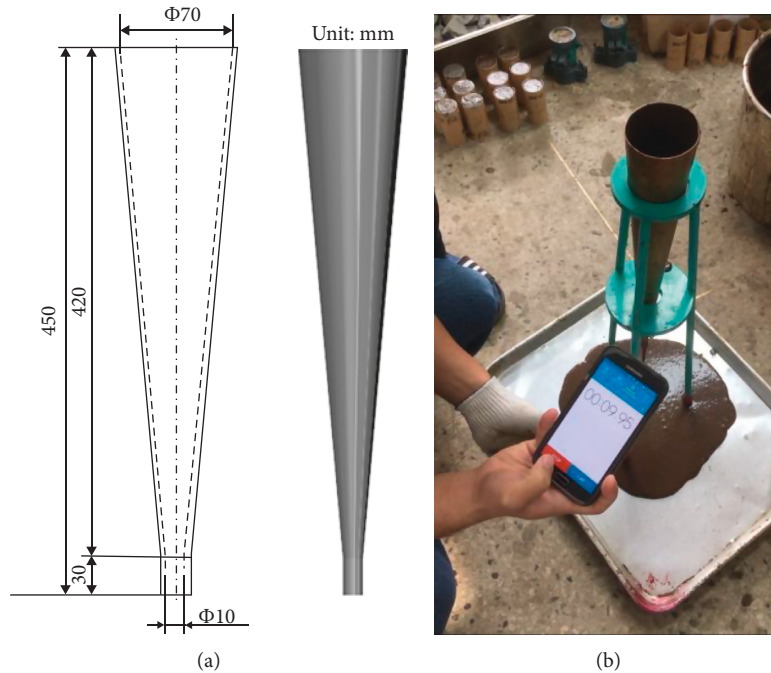


FIGURE 2: Flow cone funnel test (a) and flowability test (b).

were expected to clearly display the main differences in SEM morphologies of CAM mixtures with slag or fly ash.

### 3. Results and Discussion

#### 3.1. Mixing Stability Test

**3.1.1. Mixing Stability Test on Normal Mixtures.** The mixing stability test results of CAM mixtures are illustrated in Figure 3. The test results revealed that the lower residue content was recorded in mix FA and mix S. This can be attributed to the strong reaction of cement to the demulsification process of asphalt emulsion. The application of fly ash or slag will reduce the adsorption energy of cement to asphalt droplets in asphalt emulsion to some extent. For instance, when 30% of the cement content is replaced by fly ash, the residue content of the control mix reduced remarkably to nearly three times (from 3.15 to 1.15%). A higher fly ash or slag content will protect the mixing stability of asphalt droplets in asphalt emulsion, thereby prolonging the demulsification process of the mixture. Evidently, the CAM particles formed in the fresh mixture with fly ash and slag obtain better homogeneous distribution.

It should be noted that fly ash may impose less energy adsorption to the asphalt droplets compared to slag. Consequently, the residual content of mixtures with fly ash is noticeably lower. At the same cement content substitution of 30%, the residual content of mix FA30 and mix S30 is 1.15 and 1.75%, respectively. This may be due to the CaO content in the fly ash mixture that is much lower than that in slag. The high CaO content in slag is nearly the same in cement that may accelerate the demulsification process of asphalt droplets at an early stage of fresh CAM paste (Table 1).

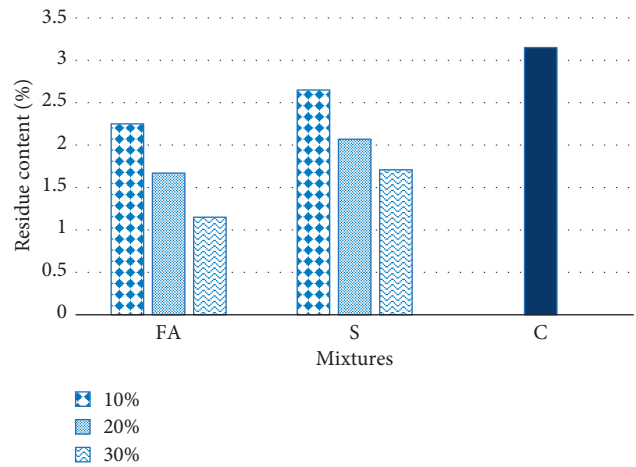


FIGURE 3: Mixing stability test results of normal mixtures.

**3.1.2. Mixing Stability Test on the New Mixture (Only Cement (Slag/Fly Ash) with Asphalt Emulsion).** As can be seen from Figure 4, the residual content of mixes FA, S, and C is 3.1%, 5.3%, and 7.6%, respectively. Without support from water and sand layer, the mixtures are significantly suffering from the fast demulsification process of asphalt emulsion based on preliminary research [10–12]. However, the gaps between the residue contents of cement, slag, and fly ash can be observed. This test confirmed the results from the above normal mixing stability test. It can be concluded that cement imposes the strongest reaction to the asphalt droplets in asphalt emulsion followed by slag and then fly ash. Overall, reducing the cement content to proper values will not only ensure the stability of asphalt emulsion in the mixture but also propose a sustainable cost-effective method.

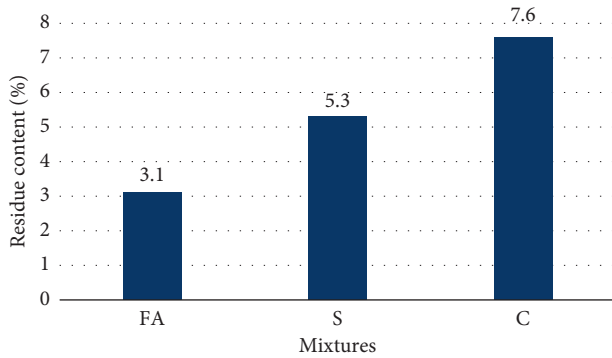


FIGURE 4: Mixing stability test results of new mixtures.

**3.2. Flowability Test.** Figure 5 presents the flowability of CAM mixtures. With the same AE, S, and W conditions, the replacement by fly ash or slag shortened the flow times of all conditions. The higher the cement replacement content, the faster the flow time. Mixtures with fly ash obtain a very good flow time value with mix FA30 having the fastest flow time of around 11 s (two times faster than that of mix C). The test results indicated that mixtures with slag and fly ash exhibited a rare sign of agglomeration at the nozzle of the flow cone. This may be due to the homogeneous CAM particles established when less cement is used. It can also be due to the unique spherical shape, beneficial size distribution, and chemical properties of fly ash or slag. The test results reassure the findings from the mixing stability test with a lower residue content recorded in mix FA and mix S. Hence, it can be concluded that the mixing stability is related to the demulsifying behavior during mixing, which may also affect the mechanical properties of hardened CA mortar [25]. Besides, the fast flow time value may impose a high bleeding phenomenon which triggers a slow setting time for the CAM mixture. Hence, the following bleeding test will determine this concern.

**3.3. Bleeding Test.** Figure 6 describes the bleeding problem of CAM mixtures with slag and fly ash. Based on preliminary research about the use of slag or fly ash [14, 17], it is expected that using by-products as a replacement for cement can mitigate the bleeding phenomenon issue. The test results show that slag and fly ash mixtures exhibit outstanding results with low signs of bleeding phenomenon. When cement contents are reduced in the fly ash or slag mixture, the bleeding value reduced sharply. For example, the bleeding values of mix C, mix S30, and mix FA30 are 1.75%, 0.86%, and 0.66%, respectively. It can be explained by the fast demulsification process of asphalt emulsion in the mixture with only cement. In this stage, asphalt droplets are coalesced, creating a continuous asphalt membrane which will cover the cement particle. The trapped water in asphalt emulsion will be extracted out, and it will cause a high bleeding value. Therefore, it is suggested to apply a proper amount of these mineral admixtures in the CAM mixture to reduce bleeding.

**3.4. Workable Time Test.** With regard to the workable time of CAM, Figure 7 shows the overall results of this property.

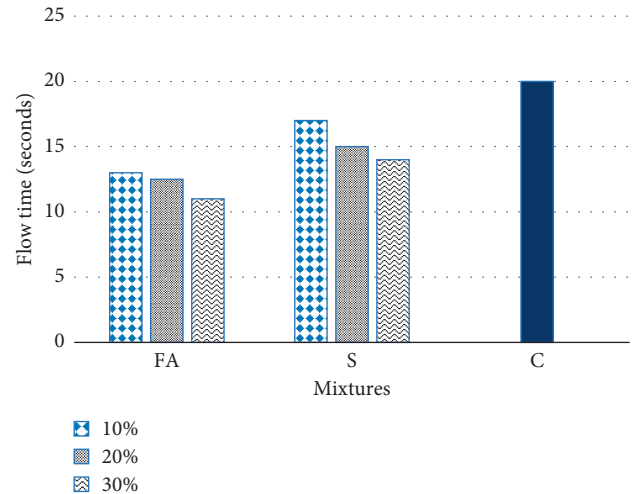


FIGURE 5: Flowability test results.

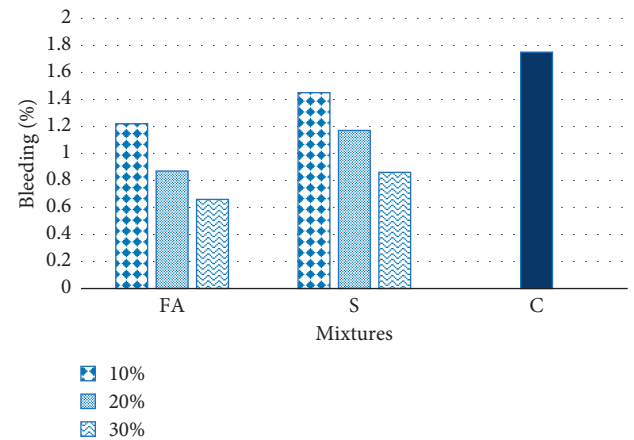


FIGURE 6: Bleeding test results.

In general, the addition of by-product generates a longer workable time for the CAM mixture.

When the FA or slag content is increased, the workable time of the CAM mixture is increased. As can be seen from Figure 7, the workable time of mix S30 is 75 min which is about two times higher than that of the control mix (30 min). This may be due to the slow hydration rate of slag and fly ash compared to cement. Besides, the test results also indicated that adding slag provides better workable time for CAM mixtures compared to fly ash. For instance, mix FA10 maintained the optimum workable condition for around 40 min, and meanwhile, mix S10 maintained it for 10 more minutes in this stage. The workable time shares a strong correlation with the early strength development of the CAM mixture. Slag mixtures had the longest workable time, and therefore, the CAM mixture with this by-product may suffer low early strength gain. This phenomenon will be justified in the succeeding 2-hour UCS test.

**3.5. 2-Hour UCS Test.** Figure 8 shows the 2-hour UCS test results of CAM mixtures with fly ash and slag. Due to the

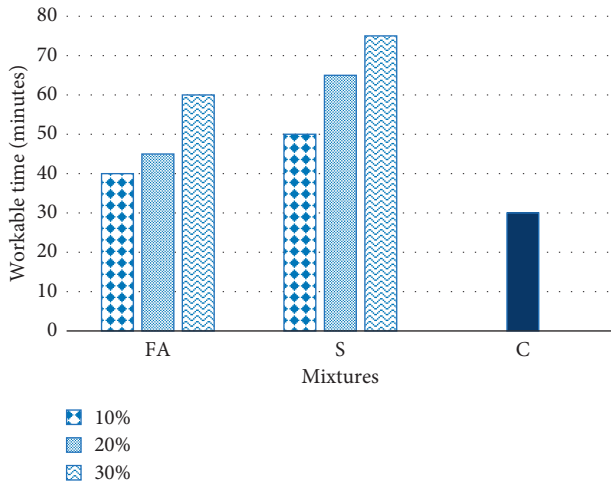


FIGURE 7: Workable time test results.

much longer workable time of the CAM mixture of fly ash or slag, those conditions obtained noticeably lower UCS compared to the controlled mixture. It can be concluded that the replacement of cement by fly ash and slag will prolong the overall setting time and retard the early strength gain of the CAM mixture. When 10% of the cement content was replaced by fly ash and slag, there was a critical drop in the strength of the CAM mixture with a UCS value of 0.28 and 0.26 MPa, respectively. This result agrees with the findings from other research about the impact of fly ash and slag on the UCS of cement mortar at an early age. Hence, the required time for actual application when using fly ash or slag in the CAM mixture should be taken into consideration.

As can be seen from Figures 7 and 8, the mixture with slag has a longer workable time compared to the mixture with fly ash. This result explains why the slag mixture has lower UCS compared to the mixture with fly ash after 2 h. However, the differences in UCS between the two by-products can be neglected. For example, at a cement replacement level of 30%, mix FA30 has a UCS value of 0.19 compared to 0.17 of mix S30.

**3.6. 28-Day UCS Test.** The 28-day UCS test results of CAM mixtures with slag and fly ash are portrayed in Figure 9. Although both fly ash and slag mixtures share the same trend in strength at an early age, there is a reverse trend in strength development after 28 days.

At an early age, the mixture with fly ash has lower strength compared to the control mix, and it is interesting that the replacement of cement by this mineral admixture promotes a promising long-term strength achievement. A higher fly ash content leads to a higher strength gain after 28 days. It can be considered that the UCS of control mix and mix F30 is relatively the same (around 3.7 MPa). Because of the unique spherical shape, beneficial size distribution, and chemical properties of fly ash, the fly ash hydration product proposed a good connection with the asphalt membrane. The homogeneous distribution of asphalt droplets in the CAM mixture with fly ash also contributed to a uniformly

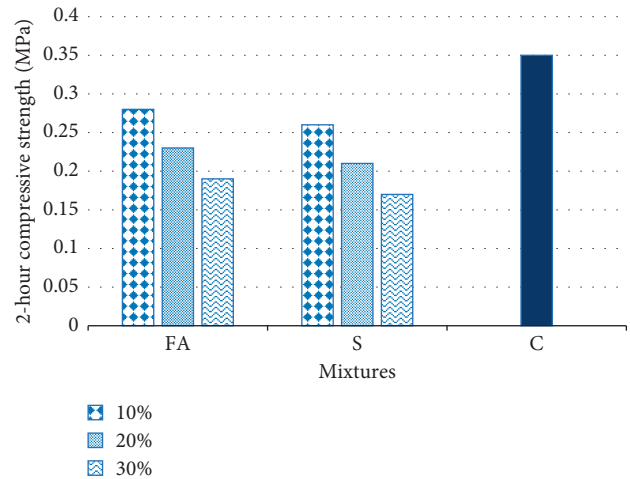


FIGURE 8: 2-hour unconfined compressive strength test results of CAM mixtures.

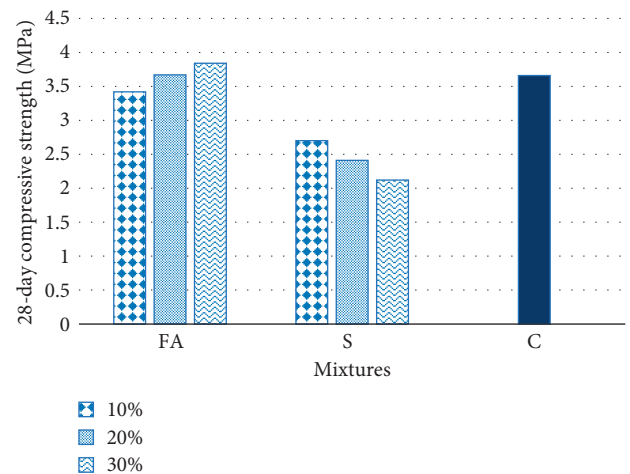


FIGURE 9: 28-day unconfined compressive strength test results of CAM mixtures.

structured formation. Moreover, based on related research about fly ash [14–17], the hydration process of this mineral admixture increases strength gradually through time with low hydration heat release. This mechanism of fly ash may help the CAM mixture build up a better strength-bearing structure with less chance of internal cracking and shrinkage. Hence, the application of fly ash in the CAM mixture not only utilizes the by-product material but also improves the overall mechanical properties of CAM in both fresh and hardened stages.

With regard to mixtures with slag, the slag mixture obtains ideal mixing stability with good flow time and workable time and the UCS results at both ages show poor values which indicated that the replacement of cement by slag does not contribute to the mechanical property of CAM. This may be because the pozzolanic reaction of CA mortar with slag is not effective. For example, there is a sudden drop in the UCS for the control mixture from 3.66 MPa to 2.7 MPa when only 10% of the cement content is replaced by

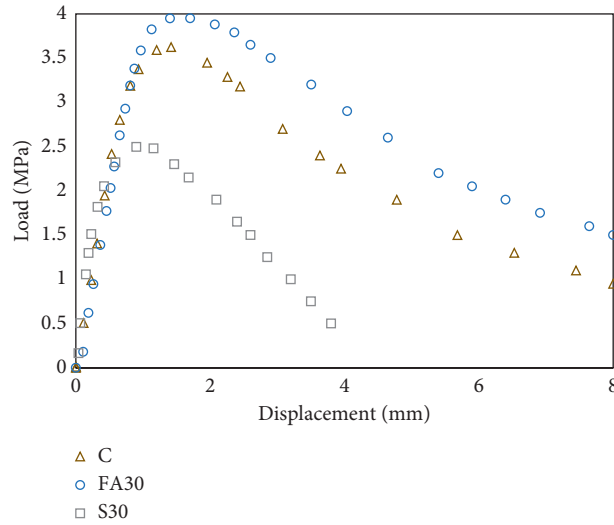


FIGURE 10: Load-displacement behavior of the CAM mixture after 28-day strength.

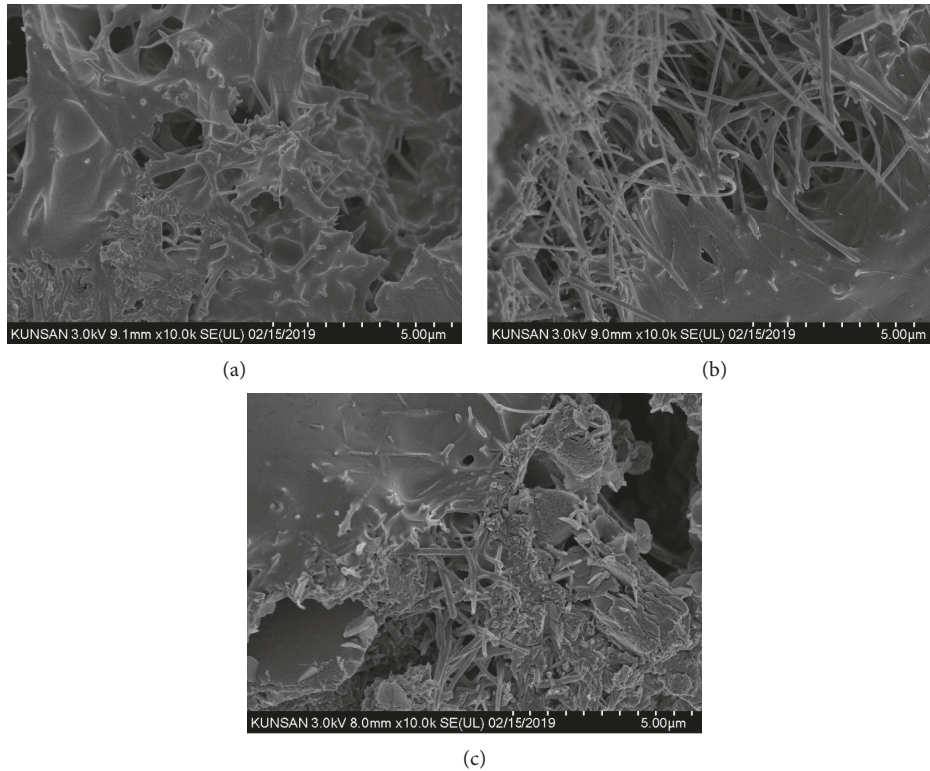


FIGURE 11: SEM test results of CAM mixtures: (a) mix FA30; (b) mix S30; (c) mix C.

slag. Therefore, although the application of slag in cement shows some promising results for the concrete mixture, this combination may otherwise impose critical effects on the production of CAM.

**3.7. Load-Displacement Analysis.** Figure 10 shows the load-displacement trends of CAM mixtures after 28 days. To identify the effect of fly ash or slag on this property of CAM,

mix FA30, mix S30, and mix C are selected for comparison. It is obvious that mix C and mix FA30 share the same trend in load-displacement behavior. After reaching the peak stress, they appear to be ductile with a gradual decrease in strength until the failure point [12, 26]. However, it can be seen that the performance of the CAM mixture with fly ash is relatively better than that of the controlled mixture. In general, it can be explained by the homogeneous distribution of CAM particles in the mixture with fly ash. The finer

particle size of fly ash may propose a denser structure with thorough mixing condition between the cement hydration product and the asphalt membrane. Based on the mixing stability test results, the residue content of the cement mixture is higher than that of the fly ash mixture (FA30), and this may form bigger particle size with poor particle distribution. Also, the gradual increase in strength may contribute to better structure development in the fly ash mixture.

Regarding the CAM mixture with slag, mix S30 not only showed poor peak stress but also suffered from a steep drop in strength after this highest point. It may be attributed to the high CaO content of slag which accelerates the demulsification process of asphalt emulsion, thereby forming inhomogeneous particles and developing a poor structure.

**3.8. SEM Analysis.** The SEM analysis results of the CAM mixture with slag and fly ash are presented in Figure 11. To justify the conclusion from the load-displacement test, mix F30, mix S30, and mix C were employed in this analysis. In general, the findings from the SEM test reassured the UCS test results.

Based on related research [14–17], microstructural investigation of the asphalt binders with fly ash demonstrated crack-mitigating behavior of the spherical fly ash particles incorporated into the bitumen matrix. In this research, the FA mixture has the best homogeneous distribution of the asphalt membrane along with the hydration product material. From the SEM test, a dense structure between mixing components is developed with a low air void content (Figure 11(a)). This finding agrees with that of UCS and load-displacement test analysis which shows that the fly ash mixture obtained better ductile behavior after reaching peak load compared to mix C.

In the SEM of the mixture with slag shown in Figure 11(b), the hydration product has a poor connection with the asphalt membrane which is the reason why mix S30 obtained the lowest strength with a minor ductile behavior.

Regarding control mix, the hydration product of cement has acceptable bonding with the asphalt membrane. However, large air voids were observed in the mixture that may prove why mix C achieved lower strength and ductile performance compared to mix F30 (Figure 11(c)).

## 4. Conclusions

This study evaluates the potential of utilizing fly ash and slag in the production of CAM as a stabilization method for fouled ballast. By assessing the effect of these by-products on the mechanical properties of CAM, optimum mix formulation will be proposed to serve further research on the sustainable development of CAM. The following conclusions can be drawn from this manuscript:

- (i) The replacement of cement by slag or fly ash improves the overall fresh properties of CAM, especially the mixing stability. The higher the cement by by-product replacement, the better the effectiveness.

This can be explained by the reduction of the strong reaction of cement particles to asphalt droplets in asphalt emulsion by using by-products.

- (ii) The application of slag or fly ash to the CAM mixture does not only prolong the demulsification process of asphalt emulsion but also retard the hardening process of CAM.
- (iii) After 28 days, the poor pozzolanic reaction in the slag mixture may result in the lowest strength gain compared to the remaining mixtures. Meanwhile, the 28-day UCS test shows promising results with the fly ash mixture, especially mix F30. Although the mixture with fly ash suffered from strength reduction compared to the control mix at an early age, the strength of this condition increases dramatically after 28 days.
- (iv) The load-displacement behavior of the mixture with fly ash shows a higher ductile characteristic compared to the control mixture and slag mixture. This is attributed to the homogeneous distribution and proper bonding of the asphalt membrane along with the hydration products in mixtures with fly ash.
- (v) SEM analysis also points out that the fly ash mixture is denser than the controlled mix. The air void systems in the fly ash mixture are relatively lower than those in the mixture with only cement. Based on the above ideal engineering properties, the CAM mixture with fly ash is suggested to be applied in further research as a cost-effective strategy.

## Data Availability

The data used to support the findings of this study are available from the corresponding author upon request.

## Conflicts of Interest

The authors declare that there are no conflicts of interest regarding the publication of this paper.

## Acknowledgments

This research was supported by a grant (18RDRP-B076564-05) from Regional Development Research Program funded by the Ministry of Land, Infrastructure, and Transport of the Korean Government.

## References

- [1] E. T. Selig and J. M. Waters, *Track Geotechnology and Substructure Management*, T. Telford, London, UK, 1994.
- [2] J. Pires and A. G. Dumont, "Railway ballast degradation," in *Proceedings of the 15th Swiss Transport Research Conference*, Ascona, Switzerland, April 2015.
- [3] G. D'Angelo, N. Thom, and D. L. Presti, "Bitumen stabilized ballast: a potential solution for railway track-bed," *Construction and Building Materials*, vol. 124, pp. 118–126, 2016.
- [4] S. F. Brown, J. Kwan, and N. H. Thom, "Identifying the key parameters that influence geogrid reinforcement of railway

- ballast,” *Geotextiles and Geomembranes*, vol. 25, no. 6, pp. 326–335, 2007.
- [5] J. H. Kennedy, P. K. Woodward, G. M. Medero, and J. McKinney, “Full-scale cyclic geopavement & railway accelerated fatigue testing,” in *Proceedings of the 10th International Railway Engineering Conference*, London, UK, June 2009.
- [6] Z. Leiben, X. Wang, Z. Wang, B. Yang, Y. Tian, and R. He, “Damping characteristics of cement asphalt emulsion mortars,” *Construction and Building Materials*, vol. 173, pp. 201–208, 2018.
- [7] W. Qiang, Y. Peiyu, A. Ruhan, Y. Jinbo, and K. Xiangming, “Strength mechanism of cement-asphalt mortar,” *Journal of Materials in Civil Engineering*, vol. 23, no. 9, pp. 1353–1359, 2011.
- [8] J. Ouyang, L. Hu, H. Li, and B. Han, “Effect of cement on the demulsifying behavior of over-stabilized asphalt emulsion during mixing,” *Construction and Building Materials*, vol. 177, pp. 252–260, 2018.
- [9] Y. Tan, J. Ouyang, and Y. Li, “Factors influencing rheological properties of fresh cement asphalt emulsion paste,” *Construction and Building Materials*, vol. 68, pp. 611–617, 2014.
- [10] J. Ouyang, J. Zhao, and Y. Tan, “Modeling mechanical properties of cement asphalt emulsion mortar with different asphalt to cement ratios and temperatures,” *Journal of Materials in Civil Engineering*, vol. 30, no. 10, article 04018263, 2018.
- [11] T. H. M. Le, D.-W. Park, and J.-W. Seo, “Evaluation on the mechanical properties of cement asphalt mortar with quick hardening admixture for railway maintenance,” *Construction and Building Materials*, vol. 206, pp. 375–384, 2019.
- [12] T. H. M. Le, D. W. Park, and J. W. Seo, “Effect of water and emulsifier on the mechanical properties of cement asphalt mortar,” *MATEC Web of Conferences*, vol. 271, article 03002, 2019.
- [13] K. Sobolev, I. Flores, and J. D. Bohler, “Application of fly ash in asphalt concrete: from challenges to opportunities,” in *Proceedings of the World of Coal Ash Conference*, St. Louis, MO, USA, May 2013.
- [14] N. Longarini, P. G. Crespi, M. Zucca, N. Giordano, and G. Silvestro, “The advantages of fly ash use in concrete structures,” *Journal of the Polish Mineral Engineering Society*, vol. 15, no. 2, pp. 141–145, 2014.
- [15] S. C. K. Bendapudi and P. Saha, “Contribution of fly ash to the properties of mortar and concrete,” *International Journal of Earth Sciences and Engineering*, vol. 04, no. 6, pp. 1017–1023, 2011.
- [16] B. W. Ramme, A. Covil, A. Faheem, and K. Sobolev, “Fly ash—an important ingredient for use in hot-mix asphalt concrete,” in *Proceedings of the Fourth International Conference on Sustainable Construction Materials and Technologies*, Las Vegas, NV, USA, August 2016.
- [17] K. V. Schuldyakov, L. Y. Kramar, and B. Y. Trofimov, “The properties of slag cement and its influence on the structure of the hardened cement paste,” *Procedia Engineering*, vol. 150, pp. 1433–1439, 2016.
- [18] D. Suresh and K. Nagaraju, “Ground granulated blast slag (GGBS) in concrete—a review,” *Journal of Mechanical and Civil Engineering*, vol. 12, no. 4, pp. 76–82, 2015.
- [19] J. Tao and X. Wei, “Effect of ground granulated blast-furnace slag on the hydration and properties of cement paste,” *Advances in Cement Research*, vol. 31, no. 6, pp. 251–260, 2019.
- [20] J. Q. Zuo, Q. B. Jiang, and B. F. Cai, “Experimental study on emulsified asphalt for CA mortar used in slab track,” *Railway Construction Technology*, vol. 2, no. 2, pp. 68–70, 2005.
- [21] KSM 2203, Emulsified Asphalt.
- [22] KSF 2432, Testing Method for Consistency of Mortar Grouting.
- [23] J. Ouyang, Y. Tan, D. J. Corr, and S. P. Shah, “The thixotropic behavior of fresh cement asphalt emulsion paste,” *Construction and Building Materials*, vol. 114, pp. 906–912, 2016.
- [24] KSF 2351, Testing Method for Compressive Strength of Asphalt Mixture.
- [25] J. Ouyang, Y. Tan, D. J. Corr, and S. P. Shah, “Investigation on the mixing stability of asphalt emulsion with cement through viscosity,” *Journal of Materials in Civil Engineering*, vol. 28, no. 12, article 04016149, 2016.
- [26] J. Ouyang, B. Pan, W. Xu, and L. Hu, “Effect of water content on volumetric and mechanical properties of cement bitumen emulsion mixture,” *Journal of Materials in Civil Engineering*, vol. 31, no. 6, article 04019085, 2019.

## Research Article

# Investigating the Effects of Chopped Basalt Fiber on the Performance of Porous Asphalt Mixture

Sheng Wang , Aihong Kang , Peng Xiao, Bo Li, and Weili Fu

*College of Civil Science and Engineering, Yangzhou University, Yangzhou, Jiangsu 225009, China*

Correspondence should be addressed to Aihong Kang; [kahyzu@163.com](mailto:kahyzu@163.com)

Received 17 March 2019; Revised 21 May 2019; Accepted 18 June 2019; Published 2 July 2019

Guest Editor: Jose Norambuena-Contreras

Copyright © 2019 Sheng Wang et al. This is an open access article distributed under the Creative Commons Attribution License, which permits unrestricted use, distribution, and reproduction in any medium, provided the original work is properly cited.

Porous asphalt mixture is a type of asphalt mixture with good drainage. However, it has poor tensile strength performance and durability. Chopped basalt fibers (CBF) have been proved to be an effective additive to improve the mechanical and fatigue performance of asphalt mixtures, but little attention has been paid on porous asphalt mixture. This paper examined the effect of chopped basalt fibers with different lengths (nonfiber, 3 mm, 6 mm, 9 mm, and 12 mm) and contents (3% and 4%) on the performance of the porous asphalt mixture. A series of tests were conducted to figure out the optimum fiber length and content, including draindown test, cantabro abrasion test, freeze-thaw split tensile test, wheel tracking test, low-temperature cracking resistance test, and four-point bending beam test. Thereafter, indirect tensile tests at different temperatures were conducted to investigate the tensile strength properties of porous asphalt mixtures with optimum fiber length and content. Besides, the macroscopic and microscopic morphology of fracture sections of the samples after indirect tensile tests were studied by using a single-lens reflex (SLR) camera and scanning electron microscopy (SEM) so as to further explore the reinforced mechanism of chopped basalt fibers. The results show that the addition of chopped basalt fibers can generally improve the performance of porous asphalt mixture since chopped basalt fibers form a three-dimensional network structure in the porous asphalt mixture.

## 1. Introduction

Porous asphalt mixture is widely used for its remarkable water permeability, good skid resistance performance, and the function of reducing the pavement temperature [1]. However, due to the stone skeleton structure and big air voids, the structural strength of the porous asphalt mixture mainly comes from the point-to-point intercontact of coarse aggregates [2, 3]. Compared with the conventional dense-graded asphalt mixtures, the contact area between the aggregates decreased by about 25%, resulting in stress concentration at the contact points. Therefore, the tensile strength of the porous asphalt mixture is greater than that of the conventional asphalt mixture, which will make the porous asphalt mixture suffer more thermal cracking or low-temperature cracking and prone to be loose or raveling [4–6]. Besides the limitations of porous asphalt mixtures, the increasing traffic volume is another challenging for the use of porous asphalt mixtures. Thus, it is necessary to comprehensively improve the performance of porous drainage pavement.

Adding additives to the asphalt or asphalt mixture has become one of the technical means to solve this problem [7]. In recent years, fibers have widely been used as an additive in asphalt mixtures. The outstanding characteristics of fiber asphalt mixture can prevent the expansion of asphalt pavement cracks, reduce the occurrence of high-temperature rutting, make up for the shortcomings of low-temperature brittleness, and relieve water damage on the pavements so as to significantly extend the service life of asphalt pavements.

At present, most of the fibers used in asphalt mixtures include organic fibers (lignin fibers, polymer fibers, and polyester fibers) and inorganic fiber (chopped basalt fibers, etc.) [8–10]. Previous studies have shown that organic fibers have some disadvantages such as low strength and modulus, poor resistance to high and low temperatures, and high water absorption. Besides, they also present degradation, oxidation reaction, and curling problems during mixing and paving process [7, 11, 12]. The chopped basalt fiber is made of natural basalt rocks, which are broken and thrown into a

melting furnace. After being melted at 1450°C to 1500°C, the continuous fibers were formed by drawing from the platinum-rhodium alloy wire drawing plate [13–15]. As a new type of mineral fiber, chopped basalt fiber has the advantages of high strength, good acid and alkali resistance, high- and low-temperature resistance, good dispersibility, and environment friendly [16–18]. A large number of previous studies have focused on the effects of chopped basalt fiber on the performance of conventional asphalt mixture and proved the positive effects. However, little attention has been paid on porous asphalt mixture [19–22]. Therefore, the effect of chopped basalt fiber on the performance of porous asphalt mixture needs to be comprehensively studied [23, 24].

Therefore, this paper examined the effect of chopped basalt fibers with varied lengths (nonfiber, 3 mm, 6 mm, 9 mm, and 12 mm) and contents (3% and 4%) on the performance of the porous asphalt mixture. And draindown test, cantabro abrasion test, freeze-thaw split test, wheel tracking test, low-temperature bending test, and four-point bending test were conducted, respectively. The tensile properties of porous asphalt mixture with chopped basalt fiber at different temperatures (−25°C, −15°C, −5°C, 5°C, 15°C, and 25°C) were explored by the indirect tensile test. Morphology analysis of fracture sections was also studied to further understand the reinforced mechanism of CBF by SEM.

## 2. Materials and Methods

### 2.1. Materials

**2.1.1. Asphalt.** A type of radial styrene-butadiene-styrene-(SBS-) modified asphalt was used in the research. The properties of asphalt are shown in Table 1.

**2.1.2. Aggregates.** Basalt coarse aggregates (minimum size of aggregate  $\geq 4.75$  mm) and limestone fine aggregates (maximum size of aggregate  $< 4.75$  mm) were used, respectively. The properties of the aggregates are listed in Tables 2 and 3, respectively.

**2.1.3. Mineral Filler.** The mineral filler was produced by limestone. Some properties are shown in Table 4.

**2.1.4. Additives.** High-viscosity agent (HVA) and chopped basalt fiber were used as additives in this study. HVA is a commonly used additive for porous asphalt mixture to enhance the viscosity of asphalt and improve the bonding between asphalt and aggregates, as shown in Figure 1. HVA is added with the aggregates and blended during the mixing process, which is called “dry process.” The dose of HVA was 0.3% by weight of the asphalt. Some properties are shown in Table 5.

Chopped basalt fiber was obtained from Jiangsu Province (Figure 2). Chopped basalt fiber was added by weight of the total aggregates. Properties of CBF are shown in Table 6.

Figure 3 shows the scanning electron microscope (SEM) micrographs of chopped basalt fibers with the magnification

TABLE 1: Properties of the asphalt.

Properties	Results	Specification requirements
Penetration (25°C, 0.1 mm)	66.0	$\geq 50$
Softening point (°C)	80	$\geq 75$
Ductility (cm)	29	$\geq 20$
Viscosity (Pa·s)	2.302	2.2~3.0
Elastic recovery (25°C, %)	98.7	$\geq 90$
Density ( $\text{g}\cdot\text{cm}^{-3}$ )	1.023	Measured
Penetration ratio (25°C, %)	85.7	$\geq 65$

TABLE 2: Properties of the coarse aggregates.

Properties	Results		Specification requirements
	5~10 mm	10~15 mm	
Apparent density ( $\text{g}/\text{cm}^3$ )	3.002	2.955	$\geq 2.70$
Water absorption (%)	0.43	0.57	$\leq 2.0$
$< 0.075$ mm grain content (%)	0.1	0.4	$\leq 1$
Soft stone content (%)	0.1	0.1	$\leq 1$
LA abrasion value (%)		9.9	$\leq 20$
Crushing value	11.0	13.0	$\leq 18$

TABLE 3: Properties of fine aggregates.

Properties	Results	Specification requirements
Apparent density ( $\text{g}/\text{cm}^3$ )	2.936	$\geq 2.60$
Sturdiness (%)	0.2	$\leq 3$
Angularity (s)	33	$\geq 30$

TABLE 4: Properties of mineral filler.

Properties	Results	Specification requirements
Apparent density ( $\text{g}/\text{cm}^3$ )	2.700	$\geq 2.60$
Hydrophilic coefficient (%)	0.7	$\leq 1$
Water content (%)	0.4	$\leq 1$



FIGURE 1: High-viscosity agent (HVA).

level of 1000. As shown in Figure 3, chopped fiber was of regular cylinders with circular cross sections and large specific surface areas, which can absorb a certain amount of asphalt binder.

TABLE 5: Properties of the high-viscosity agent (HVA).

Properties	Results	Specification requirements
Density ( $\text{g}/\text{cm}^3$ )	0.985	0.90~1.00
Single particle quality (g)	0.029	$\leq 0.03$
Melt index ( $\text{g}/10 \text{ min}$ )	9.0	$\geq 2.0$



FIGURE 2: Chopped basalt fibers.

TABLE 6: Properties of chopped basalt fiber.

Properties	Results	Specification requirements
Relative density ( $\text{g}\cdot\text{cm}^{-3}$ )	2.71	—
Length (mm)	3, 6, 9, 12	—
Diameter ( $\mu\text{m}$ )	13	—
Water content rate (%)	0.13	$\leq 0.2$
Oil absorption rate (%)	52	$\geq 50$
Melting point ( $^{\circ}\text{C}$ )	1600	—
Tensile strength (MPa)	2218	$\geq 1200$

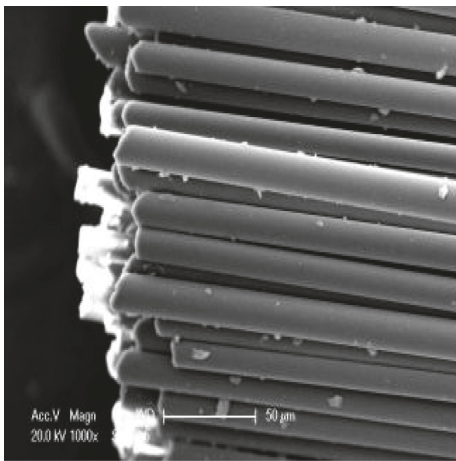


FIGURE 3: SEM micrograph of chopped basalt fibers.

Besides, some crystalline particles can be observed on the fiber surface, which results in increased surface roughness, and the anchoring effect can be formed when the fibers

interact with the asphalt binder, thereby effectively improving the interfacial adhesion between the fiber and the asphalt and improving the overall performance of the asphalt mixture subsequently.

2.2. Test Methods. The test methods are illustrated in Figure 4.

2.2.1. Mixture Design. The gradation of porous asphalt mixture is presented in Table 7.

The porous asphalt mixtures with basalt fibers were fabricated for laboratory tests according to the Chinese technical specification [25]. The minimum asphalt content was determined through Cantabro tests, and the maximum asphalt content was determined through draindown tests. Table 8 summarizes the mixture design parameters of each porous asphalt mix.

2.2.2. Draindown Test and Cantabro Abrasion Test. The draindown test and cantabro abrasion test based on JTG E20-2011 were used to evaluate the draindown resistance and antishedding ability of the porous asphalt mixture [26]. Five replicates are used for each test, and the final data are the average value of every experiment.

2.2.3. Freeze-Thaw Split Strength Test. The freeze-thaw split test was performed according to the JTG E20-2011 procedure to evaluate the water stability of the porous asphalt mixtures [26]. The Marshall specimens are compacted under 50 blows per side. After absorbing water to the saturated state in vacuum, the specimens were placed in a refrigerator at  $-18^{\circ}\text{C} \pm 2^{\circ}\text{C}$  for  $16 \text{ h} \pm 1 \text{ h}$ . Then, the specimens were kept in a water tank at  $60^{\circ}\text{C} \pm 0.5^{\circ}\text{C}$  for 24 h and then loaded at a ratio of 50 mm/min until failure. Three replicates are used for each test, and the final data are the average value.

2.2.4. Wheel Tracking Test. The wheel tracking tests were performed according to the JTG E20-2011 procedure to evaluate the high-temperature stability of the porous asphalt mixture [26]. The wheel tracking test was conducted at  $60^{\circ}\text{C}$  on rectangular specimens, with the dimension of  $300 \text{ mm} \times 300 \text{ mm} \times 50 \text{ mm}$ . Three replicates are used for each test, and the final data are the average value of every experiment.

2.2.5. Low-Temperature Bending Beam Test. The low-temperature bending beam test based on JTG E20-2011 was used to evaluate the low-temperature cracking resistance of the porous asphalt mixture [26]. The specimens, which were  $30 \text{ mm} \times 35 \text{ mm} \times 250 \text{ mm}$  rectangular beams, were tested to determine the bending strain at  $-10^{\circ}\text{C}$  with a loading rate of 50 mm/min until cracking failure, and the load and deflection at the center of beam specimens were measured. Three replicates are used for each test, and the final data are the average value of every experiment. The bending strain was calculated according to the following equation:

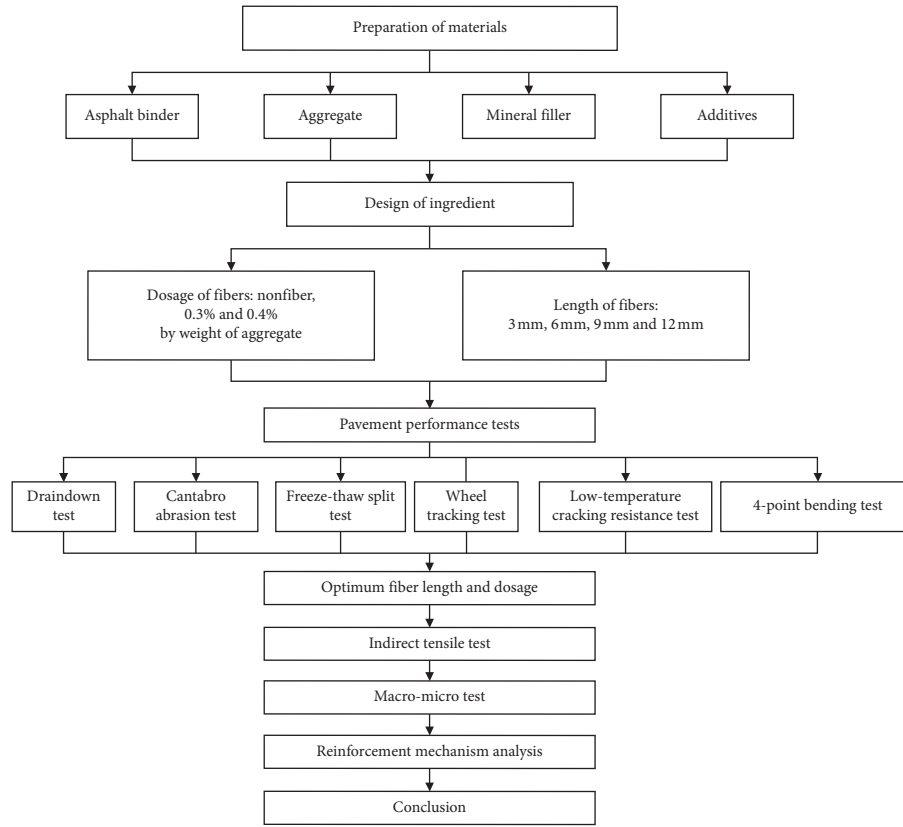


FIGURE 4: Flowchart of test methods.

TABLE 7: Porous asphalt mixture gradation.

Sieve size (mm)	16	13.2	9.5	4.75	2.36	1.18	0.6	0.3	0.15	0.075
Passing ratio (%)	100.0	92.8	60.8	13.6	11.6	9.6	8.4	7.2	6.2	5.1

TABLE 8: Design parameters of each porous asphalt mix.

Mixture type	No.	Fiber length (mm)	Fiber content (%)	Binder content (%)	Air void (%)
Porous asphalt mixture	01	—	—	4.6	20.3
	02	3	0.3	4.8	20.1
	03	3	0.4	4.8	20.1
	04	6	0.3	4.8	19.9
	05	6	0.4	4.8	19.8
	06	9	0.3	4.8	19.6
	07	9	0.4	4.8	19.5
	08	12	0.3	4.9	19.3
	09	12	0.4	4.9	19.2

$$\varepsilon_B = \frac{6 \times h \times d}{L^2}, \quad (1)$$

where  $\varepsilon_B$  is the maximum bending strain when the specimen failed,  $h$  is the height of the cross section of the specimen,  $d$  is the deflection of the cross section of the specimen, and  $L$  is the span of the specimen.

**2.2.6. Four-Point Bending Beam Fatigue Test.** In this study, the four-point bending beam fatigue test was performed using an UTM-25 testing apparatus according to JTG E20-2011 and a rectangular beam with the dimension of 380 mm × 63 mm × 50 mm was used. A haversine loading with the frequency of 10 Hz was used at 15°C, and the experiment was conducted by constant strain mode at different strain levels of 650, 850, and 1050 microstrain. Three replicates are used for each test, and the final data are the average value of every experiment.

**2.2.7. Indirect Tensile Test.** The indirect tensile test is used to determine the tensile properties of the asphalt mixture at a specified temperature and loading rate. This test was carried out in accordance with JTG E20-2011 [26], chopped basalt fibers with a length of 9 mm, content of 0.3% and length of 12 mm and content of 0.3% were mixed into porous asphalt mixture, respectively. The test temperatures were −25°C, −15°C, −5°C, 5°C, 15°C, and 25°C, and the loading rate was 50 mm/min. The indirect tensile test is illustrated in Figure 5. Three replicates are used for each test, and the final data are the average value.

**2.2.8. Fracture Morphology Analysis.** The fractured section of the specimens after the indirect tensile test was chosen to observe the fracture mode by using a Nikon D5300 SLR camera and an XL-30ESEM environmental scanning electron microscope. The size of each observation section was

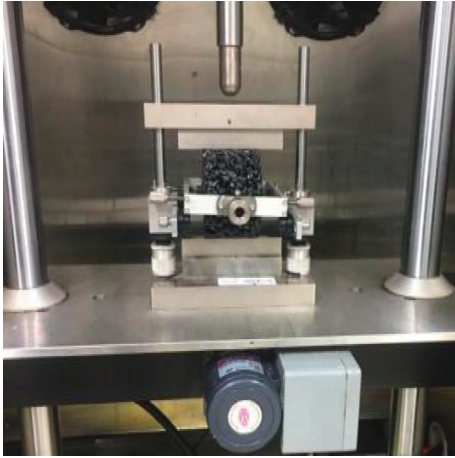


FIGURE 5: Indirect tensile test.

approximately  $20\text{ mm} \times 20\text{ mm} \times 20\text{ mm}$ . The sample should be gold coated before the SEM test, as shown in Figure 6.

### 3. Results and Discussion

**3.1. Pavement Performance Tests.** The pavement performance results of porous asphalt mixtures are shown in Figures 7–12. The results of the draindown test and cantabro abrasion test are shown in Figures 7 and 8, respectively.

It can be seen from Figures 7 and 8 that all the results met the specification's requirements. Clearly, the porous asphalt mixture blended with chopped basalt fiber presented the lower draindown ratio and cantabro mass loss, which means that chopped basalt fiber can improve the antishedding ability of the porous asphalt mixture. As for the effect of fiber length, with the increased fiber length, the draindown ratio and cantabro mass loss firstly decreased and then increased. And the length of 9 mm presented the lowest values. As for the effect of fiber contents, 0.3% of fibers always presented lower values than that of 0.4% of fibers. Therefore, it referred that porous asphalt mixture blended with 9 mm length and 0.3% of basalt fibers acquired the best antistripping ability.

The results of freeze-thaw split strength test are shown in Figure 9.

From Figure 9, it can be seen that the tensile strength ratios of all the specimens were in the range of 81%–84%, which met the requirement of no less than 80%. However, there was no significant difference between specimens with or without CBF, though the tensile strength ratios presented a slight increasing trend when CBF were used. It indicates that the chopped basalt fibers have no significant impact on the water stability of the porous asphalt mixture.

The results of the wheel tracking test are shown in Figure 10.

Based on Figure 10, all the dynamic stability (DS) results met the requirement of no less than 6000 cycles/mm, and compared with the no-fiber porous asphalt mixture, all the porous asphalt mixture with chopped basalt fiber presented much higher dynamic stability. As for the effect of fiber length, with the increased fiber length, the DS values firstly



FIGURE 6: Sample after gold plating.

decreased and then increased. And the length of 9 mm presented the highest value. As for the effect of fiber contents, 0.3% of fibers always presented higher DS values than that of 0.4% of fibers. Therefore, it infers that porous asphalt mixture blended with 9 mm length and 0.3% of basalt fibers acquires the best rutting resistance ability.

The results of low-temperature bending beam test are shown in Figure 11.

It can be seen from Figure 11 that all the destructive strain results met the requirement of no less than  $2800\ \mu\epsilon$ . And compared with the no-fiber porous asphalt mixture, porous asphalt mixture with 3 mm or 6 mm length of CBF presented a slight increment in destructive strains. However, there was an abrupt increment in the strain when 9 mm length of fibers was added into the porous asphalt mixture. When using longer fibers with a length of 12 mm, the strain was slightly reduced. As for the effect of fiber contents, similarly, 0.3% of fiber always presented higher destructive strain values than that of 0.4% of the fibers. Therefore, it refers that porous asphalt mixture blended with 9 mm and 0.3% of CBF acquires the best low-temperature cracking resistance.

The results of the four-point bending fatigue test are shown in Figure 12.

From Figure 12, it is clearly seen that porous asphalt mixtures with CBF have much higher cycles to failure. It means that chopped basalt fiber can significantly improve the fatigue performance of the porous asphalt mixture. For the same kind of porous asphalt mixture, the fatigue life change trend is the same under different strain modes, and the fatigue life decreases with the increase of strain. As for the effect of fiber length, with the increased fiber length, the failure cycles firstly increased and then decreased. And specimens with 9 mm CBF presented the highest fatigue values. As for the effect of fiber contents, 0.3% of fibers mostly presented the higher values than that of 0.4% of fibers. Therefore, it indicates that porous asphalt mixture with 9 mm length and 0.3% of basalt fibers shows the best fatigue performance.

From Figures 7–12, it can be seen that all of the tested performance of the designed porous asphalt mixtures can meet the specifications' requirements, and the addition of chopped

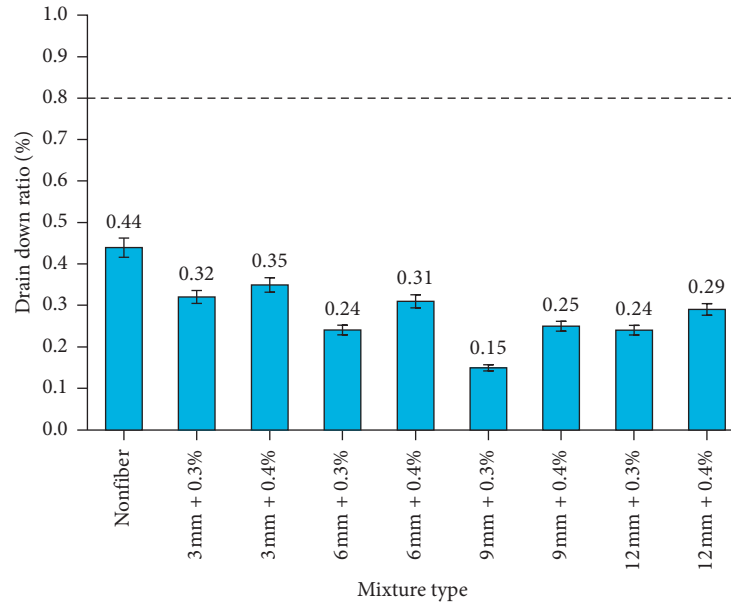


FIGURE 7: Draindown test results.

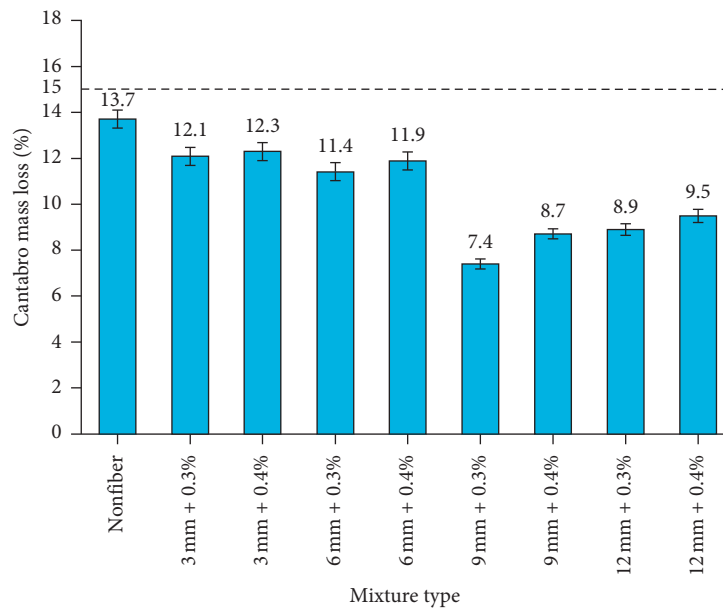


FIGURE 8: Cantabro abrasion test results.

basalt fibers can generally improve the performances of the porous asphalt mixtures. Furthermore, the fiber length and content did impact the performance to some extent. Porous asphalt mixture with 9 mm length and 0.3% of basalt fibers acquires the best pavement performance and followed by the mixtures with 12 mm length and 0.3% of fibers.

### 3.2. Indirect Tensile Strength Test at Different Temperatures.

The tensile properties of the porous asphalt mixture can indicate the thermal cracking resistance performance. Therefore, it is important to further study the effects of chopped basalt fiber on the tensile properties of porous asphalt mixtures. Indirect tensile tests were explored to

evaluate the tensile properties of porous asphalt mixtures at different temperatures. According to the results of Figures 7–12, samples with CBF of 9 mm, 12 mm length, and 0.3% content were used. The indirect tensile strengths of porous asphalt mixtures and temperature are plotted in Figure 13.

As can be seen from Figure 13, the addition of both 9 mm and 12 mm CBF provides a considerable positive effect on the tensile strength of the porous asphalt mixture at all the test temperatures. For instance, compared with no-fiber mixtures, the indirect tensile strength of porous asphalt mixture with fibers increased by 7.1% and 46% at  $-25^{\circ}\text{C}$  and  $25^{\circ}\text{C}$ , respectively. Furthermore, with the increasing temperature, the indirect tensile strength of all mixtures with

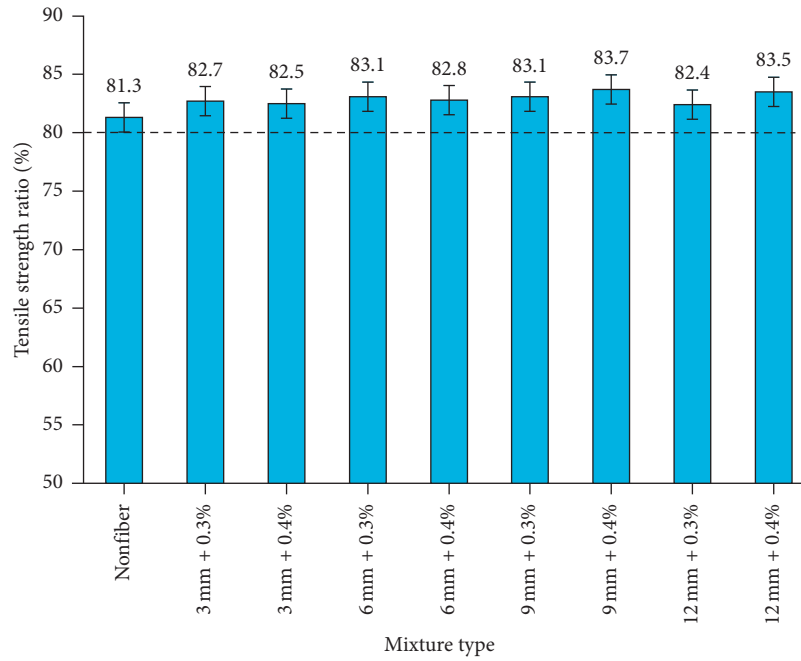


FIGURE 9: Freeze-thaw split test results.

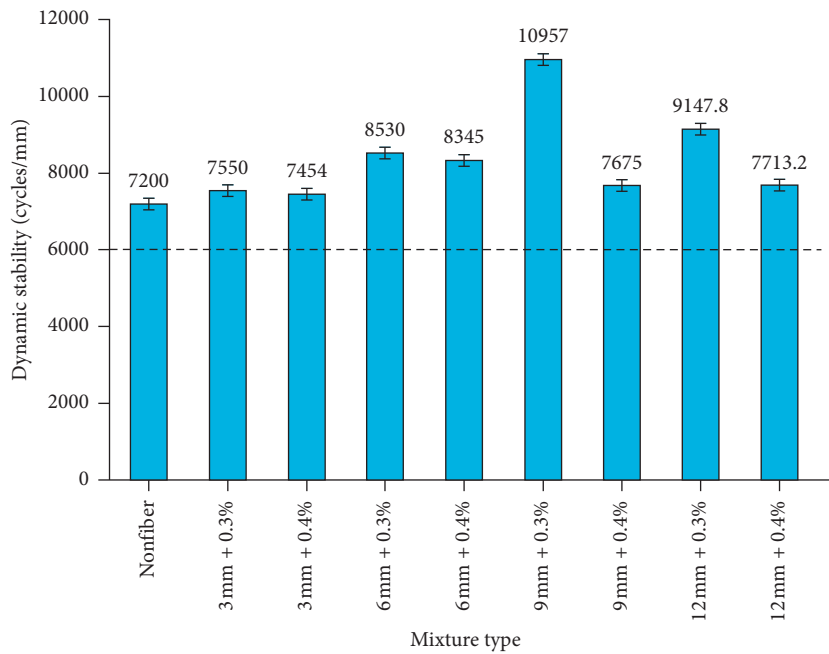


FIGURE 10: Wheel tracking test results.

fibers increased firstly from  $-25^{\circ}\text{C}$  to  $-5^{\circ}\text{C}$  and then decreased from  $-5^{\circ}\text{C}$  to  $25^{\circ}\text{C}$ , and the indirect tensile strength reaches the highest point when the temperature is  $-5^{\circ}\text{C}$ . It was also observed that fiber length had no obvious impact on the indirect tensile strength. However, mixtures with 9 mm fibers presented higher indirect tensile strength at several temperatures. Thus, combined with the results from Figures 7–12, 9 mm length and 0.3% content of fiber is recommended to improve the tensile properties of the porous asphalt mixture.

**3.3. Morphology Analysis.** The morphology of fracture sections of the samples is highly related to the temperatures. When the temperature is over  $10^{\circ}\text{C}$ , the samples cannot produce a fracture section by indirect tensile tests. Therefore, typical fracture sections of samples from indirect tensile tests (ITTs) at the temperatures of  $-15^{\circ}\text{C}$ ,  $-5^{\circ}\text{C}$ , and  $5^{\circ}\text{C}$  were selected for morphology analysis, and the results are shown in Figures 14–16. Porous asphalt mixture is a type of continuous open-grade asphalt mixture, which presents three typical cracking mode aggregate fractures, asphalt tack coat

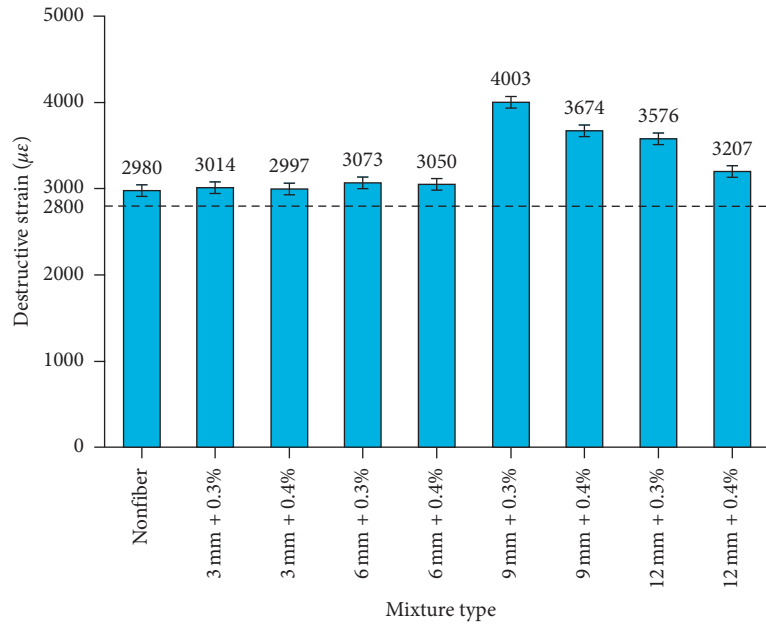


FIGURE 11: Low-temperature bending test results.

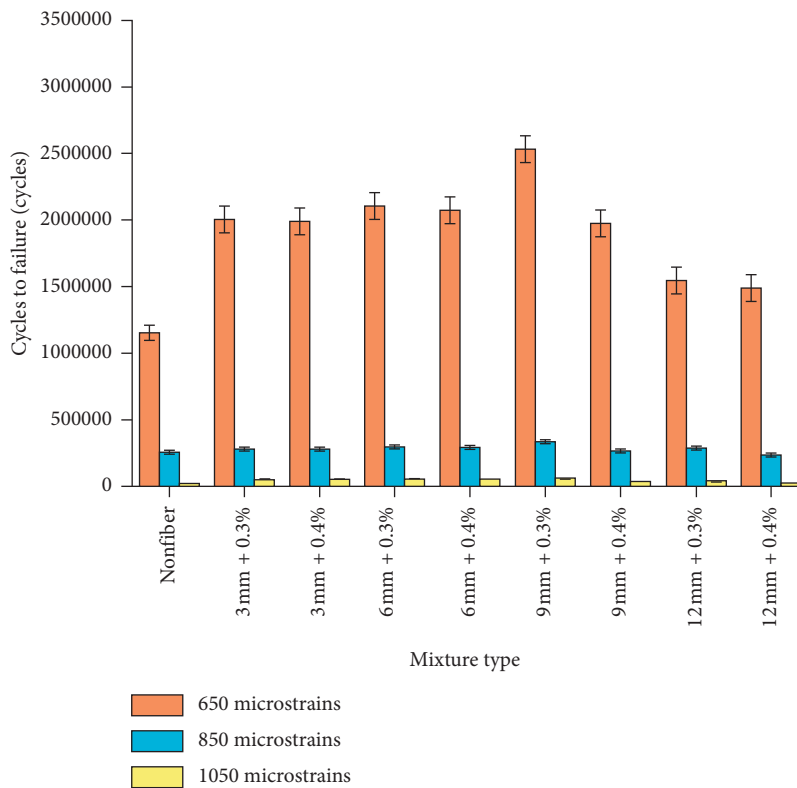


FIGURE 12: Four-point bending beam fatigue test results.

fracture, and asphalt mortar layer fracture [27]. As shown in Figures 14–16, the aggregate fracture is grayish white (marked as green dots); the asphalt tack coat fracture is grayish black, and fracture is relatively smooth, and the fracture of the asphalt mortar layer is black and white [28].

It can be seen from Figures 14–16 that the fracture sections of all the three types of samples from  $-5^{\circ}\text{C}$  ITT

presented much more grayish white parts than the samples from  $-15^{\circ}\text{C}$  and  $5^{\circ}\text{C}$  ITT, and the fracture sections of all the three types of samples from  $-15^{\circ}\text{C}$  ITT presented more grayish white parts than the samples from  $5^{\circ}\text{C}$  ITT. It indicates that at  $-5^{\circ}\text{C}$ , aggregate fracture became an important contributor to the total indirect tensile fracture failure, along with asphalt tack coat fracture and asphalt mortar layer

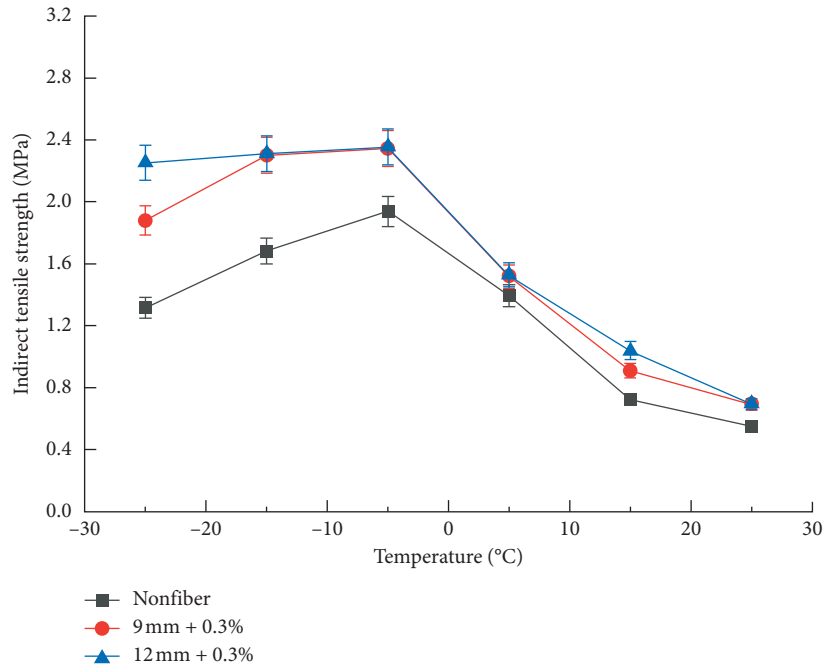


FIGURE 13: Results of indirect tensile strength.

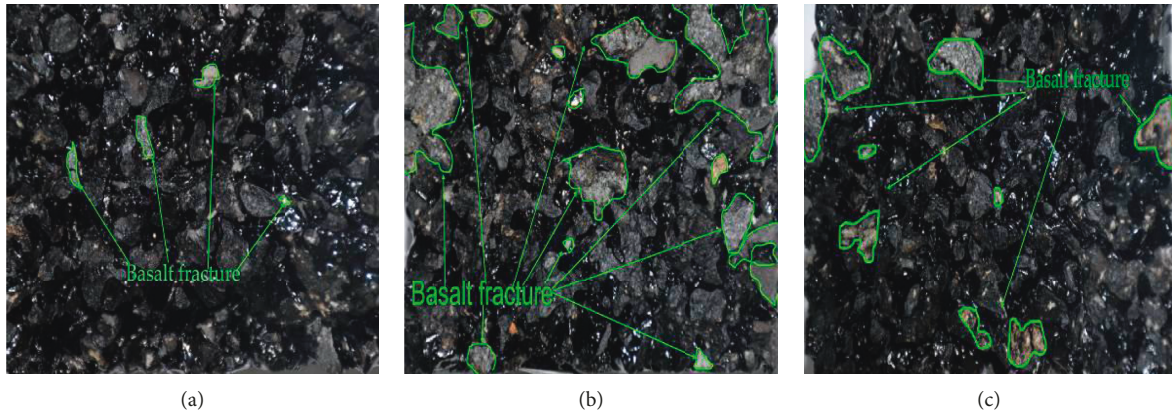


FIGURE 14: Typical sections of no-fiber samples. (a) 5°C. (b) -5°C. (c) -15°C.

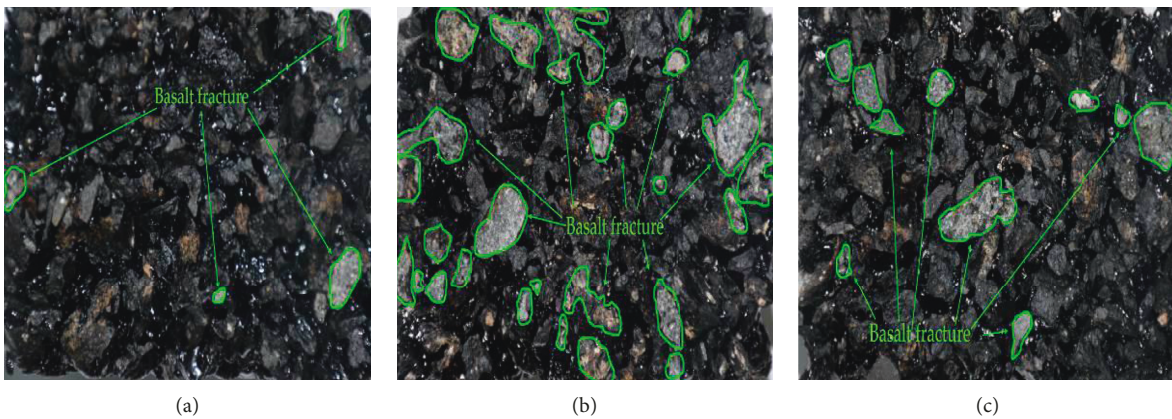


FIGURE 15: Typical sections of samples with fibers of 9 mm + 0.3%. (a) 5°C. (b) -5°C. (c) -15°C.

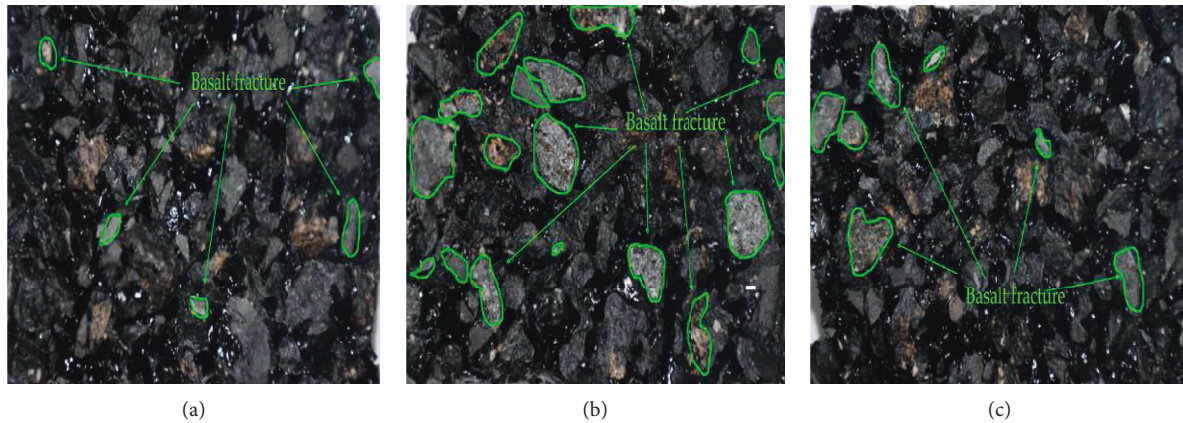


FIGURE 16: Typical sections of samples with fibers of 12 mm + 0.3%. (a) 5°C. (b) -5°C. (c) -15°C.

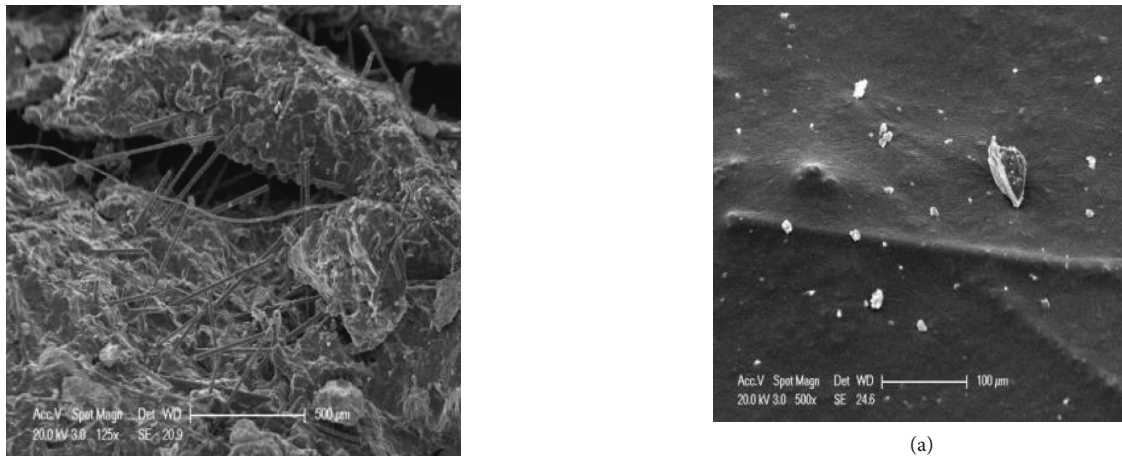


FIGURE 17: SEM micrographs of the crack of the porous asphalt mixture.

fracture. Since the strength of the basalt aggregates themselves becomes a part of the indirect tensile strength of the whole test specimen, the tensile strength of the porous asphalt mixture at -5°C is much higher than that at 5°C and -15°C. At -15°C, asphalt turns stiffer, and the mortar layer fracture becomes the dominant fracture mode. As a result, the tensile strength at -15°C is lower than that at -5°C but higher than that at 5°C, which is consistent with the results from Figure 13.

**3.4. Microstructure Analysis by SEM.** Samples with 9 mm length and 0.3% of fibers after -5°C ITT were selected for microstructure analysis by XL-30ESEM environmental scanning electron microscopy. Typical fiber distribution in porous asphalt mixture is shown in Figure 17. Interface between CBF and asphalt is shown in Figure 18.

It can be observed from Figure 17 that the chopped basalt fibers are randomly distributed in the asphalt mixture. However, the distribution formed a three-dimensional spatial network structure, which is significant for the reinforcement of asphalt mixtures. The three-dimensional

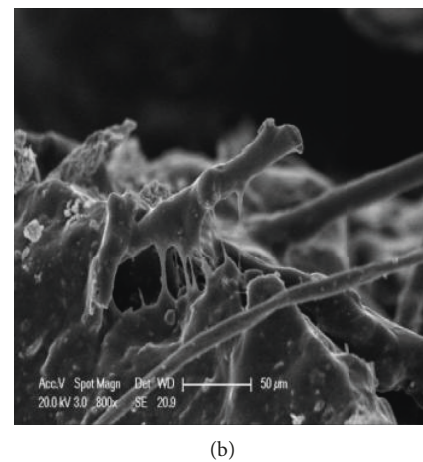


FIGURE 18: SEM micrographs of bonding interface between the fiber and asphalt. (a) Asphalt wrapped with chopped basalt fiber; (b) distribution of fibers in asphalt.

network structure cannot only bear and transfer stress but also improve the inner defects of the asphalt mixtures. Moreover, it can enhance the integrity of the asphalt mixtures so as to prevent crack propagation.

In Figure 18(a), chopped basalt fiber is dispersed in the asphalt and has good wettability with asphalt, and it absorbs

a part of free asphalt and makes it become structural asphalt. Meanwhile, chopped basalt fiber can absorb a certain amount of asphalt so as to maintain the free asphalt, resulting in a positive improvement effect on the asphalt mixture performance.

In Figure 18(b), the surface of the fiber is covered with asphalt, which means the chopped basalt fiber is well bonded to the asphalt. Furthermore, even the broken end of the BCF was covered with asphalt, indicating an excellent interface bonding force between the chopped basalt fiber and the asphalt.

#### 4. Conclusions

According to the results of this study, the following conclusions can be drawn:

- (1) The addition of chopped basalt fibers can improve the pavement performance of porous asphalt mixture, and the recommended length and content of fiber are 9 mm and 0.3%, respectively.
- (2) The addition of chopped basalt fiber can improve the indirect tensile strength of porous asphalt mixture. No obvious difference was observed between the 9 mm and 12 mm length of fibers. The indirect tensile strength reaches the maximum value at  $-5^{\circ}\text{C}$ .
- (3) At  $-5^{\circ}\text{C}$ , the strength of aggregates contributes to the indirect tensile strength of the test sample, resulting in the maximum indirect tensile strength.
- (4) The chopped basalt fiber is well combined with the asphalt and distributed in a three-dimensional network structure in the porous asphalt mixture, which can reinforce the performance of asphalt mixture significantly.

#### Data Availability

The data used to support the findings of this study are available from the corresponding author upon request.

#### Conflicts of Interest

The authors declare that they have no conflicts of interest regarding the publication of this paper.

#### Acknowledgments

The authors would like to appreciate the financial support of the National Natural Science Foundation of China (nos. 51578481 and 51578480), the Practice and Innovation Plans for Graduates of Yangzhou University (XSJCX17\_023), and Natural Science Foundation of the Higher Education Institutions of Jiangsu Province (16KJB580010).

#### References

- [1] T.-W. Hsu, S.-C. Chen, and K.-N. Hung, "Performance evaluation of asphalt rubber in porous asphalt-concrete mixtures," *Journal of Materials in Civil Engineering*, vol. 23, no. 3, pp. 342–349, 2011.
- [2] D. M. Colwill, G. J. Bowskill, J. C. Nicholls, and M. E. Daines, "Porous asphalt trials in the United Kingdom," *Transportation Research Record*, pp. 13–21, 1994.
- [3] T. F. Fwa, S. A. Tan, C. T. Chuai, and Y. K. Guwe, "Expedient permeability measurement for porous pavement surface," *International Journal of Pavement Engineering*, vol. 2, no. 4, pp. 259–270, 2001.
- [4] K. W. Kim and M. E. Hussein, "Variation of fracture toughness of asphalt concrete under low temperatures," *Construction and Building Materials*, vol. 11, no. 7–8, pp. 403–411, 1997.
- [5] E. Zegeye, J.-L. Turos, M. Turos, and M. Marasteanu, "Investigation of size effect in asphalt mixture fracture testing at low temperature," *Road Materials and Pavement Design*, vol. 13, no. 1, pp. 88–101, 2012.
- [6] X. Li and M. Marasteanu, "The fracture process zone in asphalt mixture at low temperature," *Engineering Fracture Mechanics*, vol. 77, no. 7, pp. 1175–1190, 2010.
- [7] S. M. Abtahi, M. Sheikhzadeh, and S. Mahdi Hejazi, "Fiber-reinforced asphalt-concrete—a review," *Construction and Building Materials*, vol. 24, no. 6, pp. 871–877, 2010.
- [8] S. Tapkin, "The effect of polypropylene fibers on asphalt performance," *Building & Environment*, vol. 43, no. 6, pp. 1065–1071, 2008.
- [9] Y. Z. Chen and Z. X. Li, "Study of road property of basalt fiber asphalt concrete," *Applied Mechanics and Materials*, vol. 238, pp. 22–25, 2012.
- [10] J. Sim, C. Park, and D. Y. Moon, "Characteristics of basalt fiber as a strengthening material for concrete structures," *Composites Part B: Engineering*, vol. 36, no. 6–7, pp. 504–512, 2005.
- [11] K. Krayushkina, O. Prentkovskis, A. Bieliatynskiy et al., "Perspectives on using basalt fiber filaments in the construction and rehabilitation of highway pavements and airport runways," *Baltic Journal of Road & Bridge Engineering*, vol. 11, no. 1, pp. 77–83, 2016.
- [12] B. J. Putman and S. N. Amirkhanian, "Utilization of waste fibers in stone matrix asphalt mixtures," *Resources, Conservation and Recycling*, vol. 42, no. 3, pp. 265–274, 2004.
- [13] J.-S. Chen and K.-Y. Lin, "Mechanism and behavior of bitumen strength reinforcement using fibers," *Journal of Materials Science*, vol. 40, no. 1, pp. 87–95, 2005.
- [14] N. Morova, "Investigation of usability of basalt fibers in hot mix asphalt concrete," *Construction and Building Materials*, vol. 47, no. 10, pp. 175–180, 2013.
- [15] W. X. Fan, S. F. Zhang, and L. Q. Liu, "Laboratory study of marshall of basalt fiber-modified asphalt mixture," *Applied Mechanics & Materials*, vol. 256–259, pp. 1851–1857, 2013.
- [16] J. Wu, R. Hong, and C. Gu, "Influence of fiber type on low-temperature fracture performance of presawed asphalt mixture beams," *Advances in Materials Science and Engineering*, vol. 2018, Article ID 5087395, 7 pages, 2018.
- [17] J. Singletary, R. W. Baines, W. Beckett, and K. Friedrich, "Examination of fundamental assumptions of an analytical model of fiber pull-out test," *Mechanics of Composite Materials & Structures*, vol. 4, no. 2, pp. 95–112, 1997.
- [18] C. Yongchun, Z. Chunfeng, T. Guojin et al., "Laboratory study on properties of diatomite and basalt fiber compound modified asphalt mastic," *Advances in Materials Science and Engineering*, vol. 2017, Article ID 4175167, 10 pages, 2017.
- [19] R. Muniandy and B. B. K. Huat, "Laboratory diametral fatigue performance of stone matrix asphalt with cellulose oil palm fiber," *American Journal of Applied Sciences*, vol. 3, no. 9, pp. 2005–2010, 2006.

- [20] Y. Gao, Q. Guo, Y. Guo, P. Wu, W. Meng, and T. Jia, "Investigation on reinforced mechanism of fiber reinforced asphalt concrete based on micromechanical modeling," *Advances in Materials Science and Engineering*, vol. 2017, Article ID 4768718, 12 pages, 2017.
- [21] S. Wu, Q. Ye, N. Li, and H. Yue, "Effects of fibers on the dynamic properties of asphalt mixtures," *Journal of Wuhan University of Technology—Materials Science Edition*, vol. 22, no. 4, pp. 733–736, 2007.
- [22] Z. Chen, S. P. Wu, Z. H. Zhu, and J. S. Liu, "Experimental evaluation on high temperature rheological properties of various fiber modified asphalt binders," *Journal of Central South University of Technology*, vol. 15, no. S1, pp. 135–139, 2008.
- [23] A. Mahrez, M. R. Karim, and H. Y. B. Katman, "Fatigue and deformation properties of glass fiber reinforced bituminous mixes," *Journal of the Eastern Asia Society for Transportation Studies*, vol. 6, pp. 997–1007, 2008.
- [24] S. Serin, N. Morova, M. Saltan, and S. Terzi, "Investigation of usability of steel fibers in asphalt concrete mixtures," *Construction and Building Materials*, vol. 36, no. 4, pp. 238–244, 2012.
- [25] The Ministry of Communications of the People's Republic of China, *Technical Specifications for Construction of Highway Asphalt Pavements*, The Ministry of Communications of the People's Republic of China, Beijing, China, 2005.
- [26] The Ministry of Communications of the People's Republic of China, *Standard Test Methods of Bitumen and Bituminous Mixtures for Highway Engineering*, The Ministry of Communications of the People's Republic of China, Beijing, China, 2011.
- [27] L. Mo, M. Huurman, S. Wu, and A. A. A. Molenaar, "Ravelling investigation of porous asphalt concrete based on fatigue characteristics of bitumen-stone adhesion and mortar," *Materials & Design*, vol. 30, no. 1, pp. 170–179, 2009.
- [28] L. H. Zhao, J. Y. Chen, and S. W. Wang, "Analysis of the crack fracture morphology of the asphalt mixture under tensile stress effects," *Advanced Materials Research*, vol. 250–253, pp. 3533–3537, 2011.

## Research Article

# Aesthetic and Mechanical Suitability of a Clear Synthetic Resin as a Unconventional Binder for Road Pavements

Marco Pasetto , Andrea Baliello , Giovanni Giacomello , and Emiliano Pasquini 

*Department of Civil, Environmental and Architectural Engineering, University of Padova, Padova 35131, Italy*

Correspondence should be addressed to Marco Pasetto; marco.pasetto@unipd.it

Received 29 March 2019; Revised 13 May 2019; Accepted 18 May 2019; Published 23 June 2019

Guest Editor: Jose Norambuena-Contreras

Copyright © 2019 Marco Pasetto et al. This is an open access article distributed under the Creative Commons Attribution License, which permits unrestricted use, distribution, and reproduction in any medium, provided the original work is properly cited.

Current environmental awareness interests several aspects of civil engineering, including road construction. Indeed, new challenges related to environmental pollution and landscape preservation must be faced. In this sense, clear road pavement surfaces represent an effective technology aimed at guaranteeing environmental-friendly aesthetic pavements. The use of clear synthetic resin as a binder involves several benefits for the mitigation of in-service reached temperatures and the heat distribution within pavements (with appreciable effects on pavement mechanical performance too). The present paper illustrates an experimental study aimed at analysing the chromatic and mechanical properties of a clear synthetic resin and thus its suitability as a binder for road pavement mixes. Chromatic characteristics were assessed through digital image analysis at different aging conditions. A dynamic shear rheometer was used to evaluate the linear viscoelastic properties as well as fatigue and rutting potential of the binder in a wide range of temperatures and frequencies. A conventional 35/50 penetration grade bitumen was also investigated for comparison purposes. The clear resin exhibited limited changes in colour (darkening effects), mainly in the case of short-term aging. On the other hand, a low temperature-dependency of such a binder was observed up to 58°C. Slightly increased aptitude to rutting at the higher temperatures was detected, even if it is worth noting that clear in-service mixtures would achieve lower temperatures than traditional “black” materials at a given environmental condition (air temperature, solar radiation, etc.). The resin also exhibited a softer behaviour, along with an enhanced fatigue resistance. Overall, the studied innovative binder showed promising results in view of its effective use in road paving.

## 1. Introduction

Actually, environmental awareness interests the most part of our society, and it especially concerns the civil construction field. Road construction is a core sector, since road pavements are widely diffused involving huge amounts of materials. In particular, they cover considerable surfaces in urban areas, where their dark colour negatively contributes to the quality of the environment [1]. Therefore, a growing attention is paid to the implementation of new materials for road surfaces (i.e., coloured-aesthetic pavements) able to promote the landscape preservation [2, 3]. Initially, these solutions were principally aimed at fulfilling specific safety requirements complying with the needs of eco-friendly design and realization of pavements. Recently, applications of clear or coloured pavements were proposed also as a way to mitigate the heat concentration within anthropized

environments which causes the so-called Urban Heat Island (UHI) phenomenon.

UHI effect is related to the different air temperatures observed between cities and rural regions; they highlight the seasonal and daily dynamics of local heating and global warming (average temperature of earth and atmosphere/climatic changes). UHI is a complex phenomenon affected by many variables, for example, related to urban space morphology composing the texture of the town (dimensional ratios of items, sky view factor, orientation of urban texture, presence of urban canyon, etc.). Furthermore, urban microclimate is characterized by considerable time and space variations of environment conditions; this is due to different material types and depends on several factors such as air temperature, relative humidity, wind (speed and type), solar radiation (direct sunlight and diffuse light), and infrared surface radiation (heat released). Thus, research

studies concerning urban heat islands mitigation strategies are of fundamental importance and involve multidisciplinary expertise.

In regard to this issue, since the detrimental increase in temperature is mainly related to the large presence of nonreflective and high-absorbing surfaces, optimized solutions for road construction (clear or coloured pavements) could effectively contribute to the reduction of heat concentration and diffusion (i.e., mitigation of the UHI effects), thus improving the human health and the life quality [4–6]. In fact, it is well known that the thermal properties of the materials such as the albedo (reflected energy of solar shortwave radiation), the emissivity (ratio of the radiant energy emitted by the surface to that emitted by a black element), and the Solar Reflex Index (SRI, ability to maintain a cool temperature) are related to the colour and the texture of the surfaces [5–8]. Thus, the importance of road surfaces in the UHI phenomenon is crucial since, as anticipated, roads cover a significant part of urban areas and are traditionally manufactured with black/dark high-emissivity materials which strongly enhance heat absorption and diffusion [9, 10]. Moreover, several studies also reported that clear/coloured pavements are able to guarantee benefits in road illumination, night visibility, driving safety, and, for given light conditions, cost savings (especially in road tunnels); moreover, the use of synthetic binders can also reduce the increasing consumption of the petroleum reserves [2], thus enhancing the related environmental benefits.

According to the literature [11–15], clear binders are generally constituted by adhesive materials (having similar mechanical properties with respect to the bitumen) characterized by a yellowish/transparent colour. Regardless of different formulations and peculiarities, such synthetic products cover a significant part of the clear binder market. It is worth specifying that they totally differ from clear modified bitumens, which are obtained by the extraction of the asphaltenes (responsible of the dark colour).

Given this introduction, the aim of the present research is addressed to the analysis of the suitability of a clear synthetic resin to be used as a binder for road pavement mixes instead of traditional bitumen. Given the fact that little research exists on clear, coloured, or solar-reflective road materials for UHI mitigation [16–18], this paper would like to enlarge the existing literature, representing the preliminary phase of a comprehensive research program aimed at developing high-reflective pavements for UHI mitigation with the final goal of a proper quantification of cooling benefits due to pavement chromatic characteristics. Even if the clear colour of the studied material can strongly affect in-service temperatures, heat distribution within the pavement, and its diffusion into the environment, the mixes prepared with such a binder can be used only if they are also able to guarantee adequate mechanical properties and durability as well as to preserve chromatic characteristics over time. Thus, the present paper shows the results of an experimental characterization of clear synthetic resin in comparison of a traditional bitumen: the first phase of the study concerned the evaluation of chromatic characteristics of the resin and

the effect of aging processes on these characteristics, whereas the second phase dealt with a comparative rheological characterization of resin and bitumen evaluating the linear viscoelastic properties as well as the fatigue and rutting potentials.

## 2. Materials and Methods

*2.1. Materials.* The studied clear synthetic resin (hereafter coded CSR) was a proprietary product composed by a thermoplastic bicomponent resin (solid granular elements and liquid catalyst) with bonding properties similar to those of a traditional bitumen. The colour of the material varies from amber-orange to straw-yellow. Such a binder can allow the preparation of clear or coloured pavement surfaces since it can be used instead of the traditional black bitumen (dosed with similar volumetric contents) and by utilizing the same conventional preparation and construction paving procedures (plants, equipment, etc.). A reference unmodified bitumen with a 35/50 penetration grade (hereafter coded 35/50 pen) was also studied for comparison purposes.

Table 1 summarizes the main basic properties of CSR and 35/50 pen. Based on these basic characteristics, CSR demonstrated a noticeably lower consistency at midservice temperature, whereas it seemed to be less temperature-dependent with higher short-term aging resistance. Moreover, a noticeably higher elastic response was observed in the case of the synthetic binder. A reduced ductility is also reported, and a higher thermal cracking potential can be also hypothesized due to the higher Fraass breaking point. A specific rheological study would be recommended in this regard.

*2.2. Chromatic Analysis.* The first phase of the research was aimed at assessing the chromatic characteristics of the studied binders, with particular emphasis on the aging effects on the clear binder colour. Thus, CSR samples were replicated as unaged resin, RTFO resin (short-term aging simulation—EN 12607-1), and PAV resin (long-term aging simulation—EN 14769). The 35/50 pen sample was also studied for comparison purposes. To prepare the test samples, materials were first oven-heated at 160°C and poured into circular glass containers in order to obtain specimens with a layer thickness able to prevent the transparency (i.e., 1.0 mm). The specimens were then placed in a confined chamber, opportunely set up to achieve high-quality images. The setup was composed by a rectangular box (1000 × 800 × 700 mm) with white paper walls useful to permit the light transition. Four light sources were placed on the sides of the box in order to prevent shades or reflections. A centred circular hole ( $\Phi = 300$  mm) on the upper side of the box allowed the image acquisition using a digital high-resolution camera. Additional details concerning chamber setup are reported in Figure 1. In order to acquire images not affected by different exposures or light noises, all samples (35/50 pen, unaged CSR, RTFO-aged CSR, and PAV-aged CSR) were contemporarily photographed in the same picture.

TABLE 1: Basic properties of tested binders.

Property	Standard	35/50 pen	CSR
Penetration at 25°C (0.1 mm)	EN1426	38	69
Penetration at 25°C after RTFO (0.1 mm)	EN1426	23	54
Softening point (°C)	EN1427	65	61
Softening point after RTFO (°C)	EN1427	72	64
Penetration index	EN12591	1.3	2.1
Ductility at 25°C (mm)	ASTM D-113	>1000	210
Elastic recovery (%)	EN13398	9	91
Fraass breaking point (°C)	EN12593	-5.8	-7.5

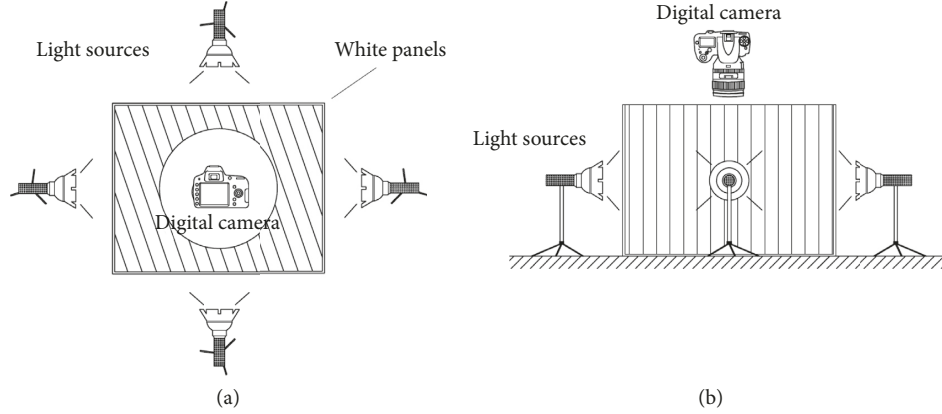


FIGURE 1: Confined chamber for image acquisition: top (a) and side (b) views.

A back analysis was performed with specific graphic software to determine material RGB (Red-Green-Blue) properties. RGB colour model (described by Commission Internationale de l'Éclairage since the 1931) is a common representation to display images in electronic/photographic systems that reproduce an array of colours from the three primary colours (red, green, and blue). In this way, the single colour could be represented by the numerical triad R-G-B (with digits ranging between 0 and 255 intervals), where each number indicates the mean value of the Gauss distribution for each colour. As a consequence, an image with limited chromatic variations could define localized curve distributions, improving the dominant RGB code accuracy (small standard deviations in Gauss curves). For this reason, the target of the picture acquisition was a high-resolution clean image, not influenced by reflections, shades, or flaws. However, an alternative analysis that considered an objective physical representation (based on human perception) was also proposed, since RGB actually defines a device-dependent colour model, not strictly related to an engineering property.

Colour perception is linked to the perceptive feedback of the optical system in relationship with electromagnetic light stimuli. Considering the eye composition with three retinal photoreceptor cones, three numerical functions are enough to model the colours. In this regard, the Hue-Saturation-Lightness (HSL) model was used, since it represents one of the most utilized models based on human perception of colours [19, 20]. According to this model, the parameter hue ( $H$ ) reproduces the colour tonality (in the range of  $0^\circ$ - $360^\circ$ ), the saturation ( $S$ ) indicates the power of light emission (as

percentage), and the lightness ( $L$ ) represents the colour brightness (as percentage). Thus, the conversion from RGB to HSL values was developed through the following steps according to [21]: (i) expressing red, green, and light values in the range between 0 and 1 (dividing RGB digits by 255); (ii) identifying the minimum (min) and maximum (max) normalized RGB values; (iii) following the mathematical procedure hereafter reported (equations (1)-(3d)).

Figure 2 illustrates the RGB and HSL model's interpretation in a 3D space. Once the HSL codifications for unaged, RTFO-aged, and PAV-aged resin samples are defined, comparisons to understand the aging effects on their chromatic characteristics were carried out.

$$L = 100 \cdot \frac{(\max + \min)}{2}, \quad (1)$$

$$S = 100 \cdot \frac{(\max - \min)}{\max + \min}, \quad \text{if } L \leq 0.5, \quad (2a)$$

$$S = 100 \cdot \frac{(\max - \min)}{2 - \max - \min}, \quad \text{if } L > 0.5, \quad (2b)$$

$$H = 0, \quad \text{if } S = 0, \quad (3a)$$

$$H = 60 \cdot \frac{(G - B)}{\max - \min}, \quad \text{if } \max = R, \quad (3b)$$

$$H = 60 \cdot \left[ 2 + \frac{(B - R)}{\max - \min} \right], \quad \text{if } \max = G, \quad (3c)$$

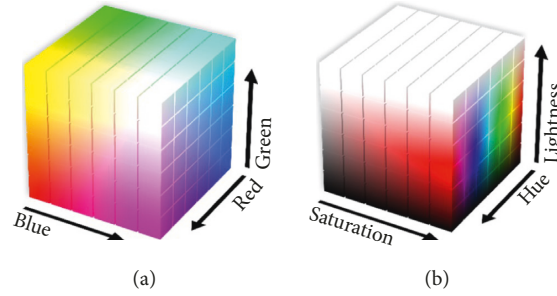


FIGURE 2: Cubic interpretation of RGB (a) and HSL (b) models.

$$H = 60 \cdot \left[ 4 + \frac{R - G}{\max - \min} \right], \quad \text{if } \max = B. \quad (3d)$$

**2.3. Rheological Analysis.** The main rheological properties of the studied binders were then assessed through a Dynamic Shear Rheometer (DSR). According to EN 14770, the rheological tests were carried out using plate-plate geometry with 25.00 mm diameter plate and 1.00 mm gap or 8.00 mm diameter plate and 2.00 mm gap depending on the test temperature. A conditioning period of at least 15 minutes was fixed for each testing temperature, in order to guarantee a homogeneous thermal distribution within the specimens.

First, strain sweep tests were performed to identify the linear viscoelastic (LVE) domain at the different test temperatures and frequencies. The LVE limit of studied materials was established in correspondence of the decrease to 95% of the initial complex modulus  $G^*$  [22, 23]. This was accomplished by performing amplitude sweep (AS) oscillatory tests at the standard angular frequency  $\omega$  of 10 rad/s (1.59 Hz) and in the range of temperature from 10 to 50°C (with 10°C steps), recording the evolution of  $G^*$  as a function of the strain amplitude  $\gamma$  (varied from 0.01% to 100% as represented in Figure 3(a)). Two test replicates were carried out for each test condition.

Then, oscillatory temperature sweep (TS) tests were carried out to detect the temperature dependency of the studied materials. The experimental results were plotted in terms of isochronal curves of the storage modulus  $G'$  (i.e., the elastic component of the complex modulus) and the loss modulus  $G''$  (i.e., the viscous component of the complex modulus) as a function of the test temperature ( $T$ ). In this case, the binders were subjected to strain-controlled oscillatory tests applying a constant amplitude within the LVE domains ( $\gamma = 0.05\%$ ) and using the 8 mm parallel plate geometry at a constant  $\omega$  of 10 rad/s (1.59 Hz). During this test, the temperature was increased linearly from 4 to 76°C (Figure 3(b)). Three test replicates were carried out for each test condition.

Frequency sweep (FS) tests were then executed in oscillatory strain-controlled loading conditions (within the LVE domain), varying the frequency from 100 to 0.1 rad/s (ramp log decreased with a slope of 10 points/decade) and adopting a range of temperatures between 4 and 76°C, with steps of 6°C. In particular, 8 and 25 mm diameter parallel plates were selected for tests between 4°C and 34°C and

between 34 and 76°C, respectively. All tested samples were previously subjected to PAV procedure to simulate the long-term aging, i.e., the worst conditions for midservice temperature cracking resistance. Frequency sweeps allow the construction of the master curves by using the well-known Time-Temperature Superposition Principle (TTSP), generally valid for thermorheologically simple materials (e.g., traditional bitumens). In this case, a single smooth master curve of the selected LVE characteristics (e.g.,  $G^*$ ) is obtained by shifting the experimental data series with horizontal shift factors  $a_T$  related to test frequency (or time) and vertical shift factors  $b_T$  proportional to the material density. In this regard, frequency sweep test results were elaborated to construct master curves both for the complex modulus  $G^*$  and the phase angle  $\delta$  at the reference temperature  $T_0$  of 34°C. To this aim, the reduced angular frequency  $\omega_r$  is defined in the following equation:

$$\omega_r(T_0) = a_T \cdot \omega(T), \quad (4)$$

where  $\omega$  indicates a generic experimental frequency. The horizontal shift factors  $a_T$  were chosen to fit with the Williams-Landel-Ferry (WLF) formulation [24]:

$$\log a_T = -\frac{C_1 \cdot (T - T_0)}{C_2 + (T - T_0)}, \quad (5)$$

where  $C_1$  and  $C_2$  represent empirical material constants related to the free volume and its thermal expansion coefficient. Despite the specific elaboration used for bituminous materials, vertical shifting is also possible. It could be realized with  $b_T$  vertical factors according to the following equation:

$$T_0 \cdot \rho_0 = b_T \cdot T \cdot \rho, \quad (6)$$

where  $\rho$  is the material density at the given temperature  $T$  and  $\rho_0$  is the density at the reference temperature  $T_0$ . Due to the synthetic nature of the studied resin, a tentative vertical shifting was also applied.

The fatigue resistance of the studied binders was also investigated through the linear amplitude sweep (LAS) test which consists of a time-saving and effective (especially for comparative purposes) laboratory procedure to obtain the fatigue law of a bituminous binder with respect to the traditional time sweep analysis, i.e., a series of oscillatory shear tests at a selected frequency and different constant strain amplitudes [25–28]. According to AASHTO TP 101-14, LAS tests were performed on 8 mm diameter specimens by

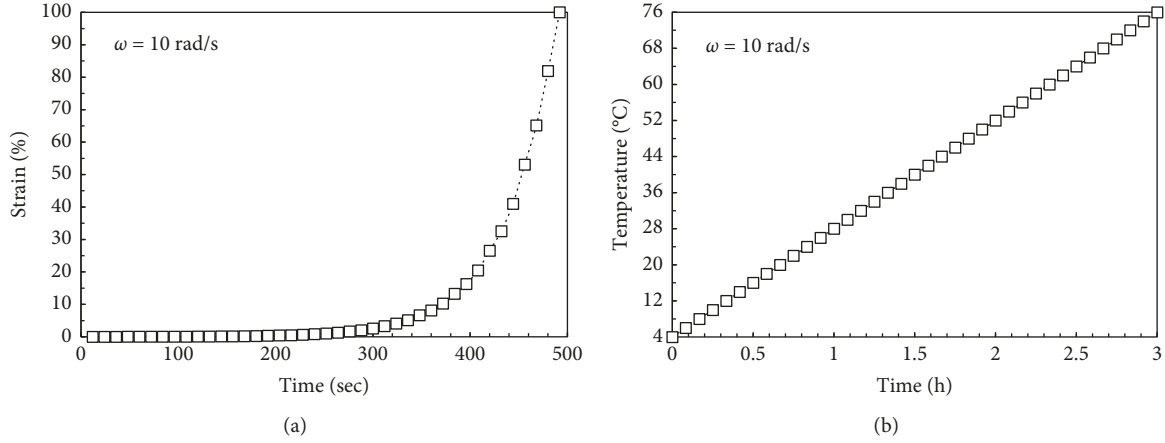


FIGURE 3: Preliminary test configuration: amplitude sweep (a) and temperature sweep (b) tests.

performing a two-phase test protocol, consisting of a preliminary frequency sweep followed by a series of amplitude sweeps progressively increasing the strain amplitude to cause accelerated fatigue damage [29]. In particular, the frequency sweep was carried out by applying an oscillatory strain having a constant amplitude of 0.1% over a frequency interval ranging from 0.2 to 30 Hz (linear continuous ramp depicted in Figure 4(a)). Then, the following amplitude sweeps were performed at the constant frequency of 10 Hz, linearly increasing the strain from 0 to 30% over 3,100 loading cycles (Figure 4(b)) and recording  $G^*$  and  $\delta$  values. LAS test temperature was fixed at 20°C. Three replicates for each material were carried out.

The fatigue law of the tested materials (i.e., the cycles to fatigue failure  $N_f$  as a function of the strain amplitude  $\gamma$ ) was defined based on (i) the determination of undamaged material properties ( $\alpha$  parameter) from the frequency sweep phase; (ii) the viscoelastic continuum damage (VECD) analysis from the amplitude sweep phase (based on the VECD theory) [29]. Despite some literature ambiguity about the first-undamaged phase [30, 31],  $\alpha$  was calculated according to standard specifications:

$$\alpha = \frac{1}{m}, \quad (7)$$

where  $m$  represents the slope of the regression line applied to the first-phase bilogarithmic plot reporting  $G'$  as a function of  $\omega$ :

$$\log G' = m \cdot (\log \omega) + b, \quad (8)$$

where  $b$  is the curve intercept. Assuming  $C(t)$  as the material integrity (i.e., the ratio of  $G^*$  at a given time  $t$  to the initial  $G^*$ ) and  $\gamma$  as the related applied strain amplitude (in percent), the damage  $D(t)$  accumulated during the second phase of test (amplitude sweep) was calculated according to the following equation:

$$D(t) = \sum_{i=1}^N \left[ \pi \cdot \gamma^2 \cdot (C_{i-1} - C_i) \right]^{\alpha/(1+\alpha)} \cdot (t_i - t_{i-1})^{1/(1+\alpha)}, \quad (9)$$

where  $i$  indicates the given loading step. Figure 5(a) represents a typical  $C(t)$  vs.  $D(t)$  plot. The logarithmic plot of  $C_0 - C(t)$  vs.  $D(t)$  (i.e., integrity loss vs. damage) represented in Figure 5(b) allowed the determination of the fitting coefficients  $C_1$  and  $C_2$  ( $C_0$  was assumed equal to 1 according to AASHTO TP 101-14).

Thus, the fatigue law reported in equation (10) can be calculated as follows:

$$N_f = A \cdot \gamma^{-B}, \quad (10)$$

$$A = \frac{f \cdot (D_f)^{1+(1-C_2)\alpha}}{(1 + (1 - C_2) \cdot \alpha) (\pi \cdot C_1 \cdot C_2)^\alpha}, \quad (11)$$

$$B = 2 \cdot \alpha, \quad (12)$$

where  $f$  is the test frequency (10 Hz), whereas  $D_f$  indicates the damage value at sample failure as defined in the following equation:

$$D_f = \left[ \frac{C_0 - C_{\text{at Peak Stress}}}{C_1} \right]^{1/C_2}. \quad (13)$$

Finally, Multiple Stress Creep Recovery (MSCR) tests were performed in order to evaluate the rutting potential of the studied binders at high-service temperatures. According to EN 16659, the test consists of ten creep-recovery cycles (1 s constant loading and 9 s unloading) carried out at two different consecutive stress levels (0.1 and 3.2 kPa). In particular, temperature and stress dependencies were evaluated on RTFO-aged materials (worst condition for rutting potential) using 25 mm diameter samples at temperatures of 52, 58, 64, 70, and 76°C. Three test replicates were carried out for each material and test condition.

The rutting potential was then assessed by representing the strain evolution over time and calculating the non-recoverable creep compliance ( $J_{nr}$ ) as well as the  $J_{nr}/J_{TOT}$  ratio.  $J_{nr}$  and  $J_{nr}/J_{TOT}$  formulations are described in equations (14) and (15), respectively:

$$J_{nr}^n = \frac{\epsilon_r^n - \epsilon_0^n}{\tau^n}, \quad (14)$$

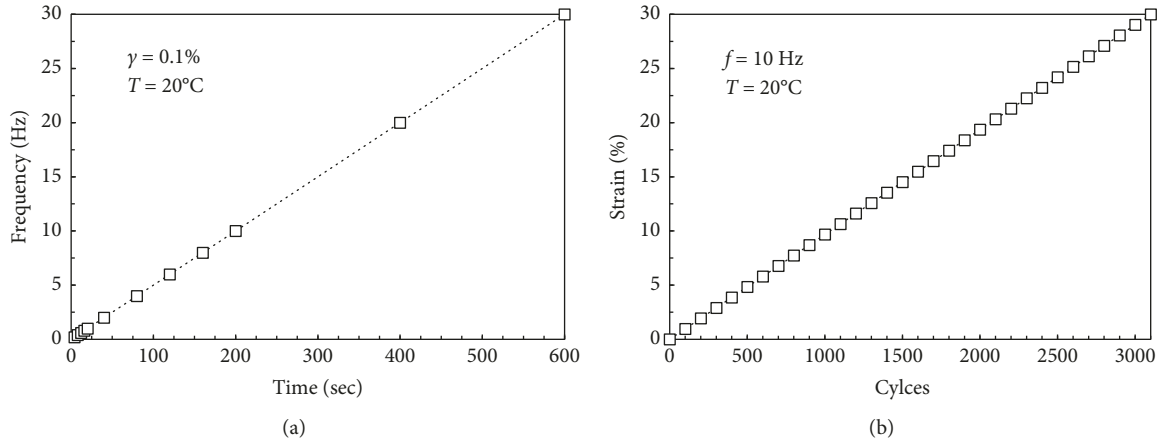


FIGURE 4: LAS test: 1st phase frequency sweep (a) and 2nd phase amplitude sweep (b).

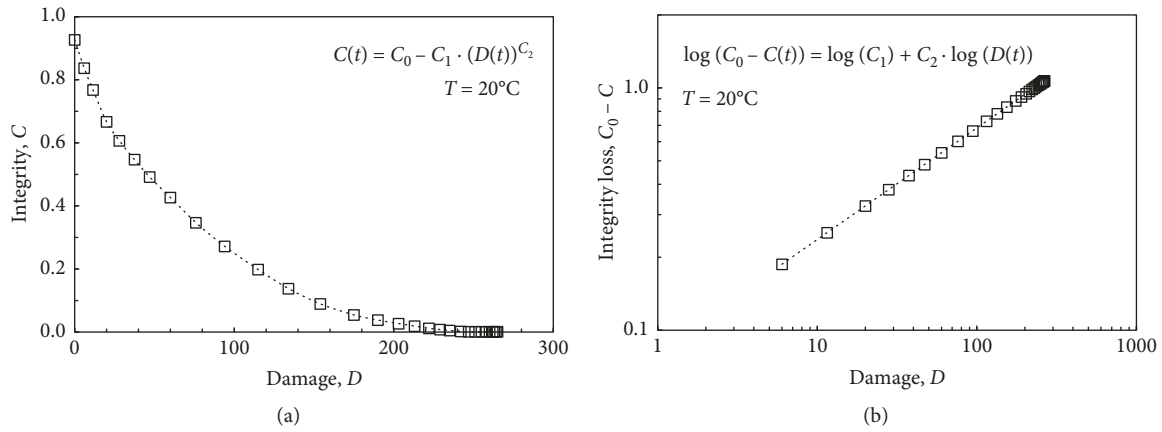


FIGURE 5: Typical LAS test results: integrity vs. damage (a); integrity loss vs. damage (b).

$$\frac{J_{nr}}{J_{TOT}} = \frac{(\varepsilon_r^n - \varepsilon_0^n)/\tau^n}{(\varepsilon_c^n - \varepsilon_0^n)/\tau^n} = \frac{\varepsilon_r^n - \varepsilon_0^n}{\varepsilon_c^n - \varepsilon_0^n} \quad (15)$$

where  $n$  indicates the cycle number,  $\tau$  the applied stress at the  $n$ -cycle,  $\varepsilon_r^n$  the final strain after the entire  $n$ -cycle (10 s),  $\varepsilon_0^n$  the strain at the beginning of  $n$ -cycle, and  $\varepsilon_c^n$  the strain at the end of the creep phase (1 s) at the  $n$ -cycle.

As it can be noted,  $J_{nr}$  refers only to the nonrecovered (i.e., plastic) strains at the end of each cycle, whereas  $J_{nr}/J_{TOT}$  normalizes  $J_{nr}$  with respect to the creep compliance at the end of creep phase (corresponding to the maximum measured strain  $\varepsilon_c$ ). For each sample, the average  $J_{nr}$  and  $J_{nr}/J_{TOT}$  for each stress magnitude are then calculated.

As a summary, Figure 6 schematizes the overall experimental plan of the proposed research.

### 3. Results and Discussion

**3.1. Chromatic Results.** The chromatic test results are summarized in Table 2, whereas Figures 7 and 8 report an example of the captured images of the samples and the visual representation of the corresponding chromatic HSL properties, respectively.

As expected, the tested bitumen demonstrated a deeply dark aspect, almost close to the pure black colour, whereas the synthetic binder showed completely different chromatic characteristics. As far as the influence of the aging process on the CSR colour is concerned, it can be noted that the tonalities of the three samples (unaged, RTFO-aged, and PAV-aged) were similar at the different aging conditions. In particular,  $H$  coordinates exhibited only slight variations due to aging, whereas the saturation  $S$  seemed more affected by the aging processes, changing from 34% (unaged resin) to 98% and 99% in aged conditions. Analogous considerations could be extended to lightness ( $L$ ) values, which moved from 47% in the unaged condition to 35–38% for the aged samples, with a minor difference between RTFO-aged and PAV-aged CSR. Thus, it could be stated that the colour of virgin CSR product did not exactly correspond to that of the material after the paving operations (simulated by RTFO laboratory procedure), whereas long-term aging effects on the CSR colour (simulated by PAV laboratory procedure) should be considered nearly negligible. However, it is worth noting that the colour of the pavement surface over its service life is strongly affected by the colour of the aggregates used (in particular when a clear binder is used) and also due

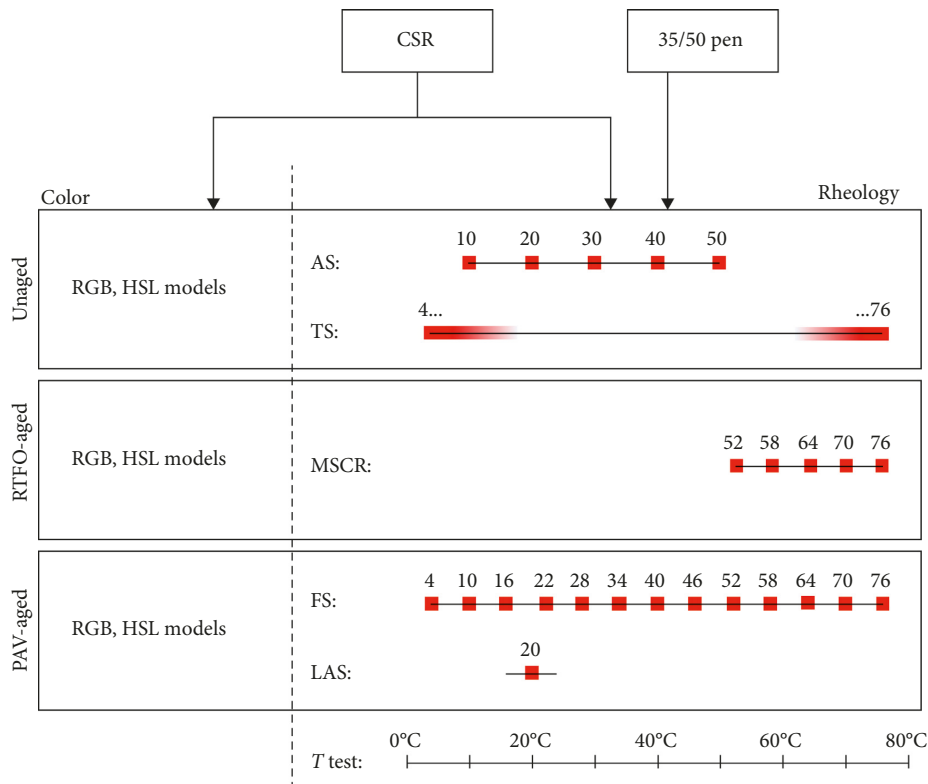


FIGURE 6: Summary of the experimental plan.

TABLE 2: Summary of chromatic test results.

Material	Colour model					
	RGB			HSL		
	R	G	B	H (°)	S (%)	L (%)
35/50 pen	1	4	2	140	60	1
CSR (unaged)	200	130	38	34	68	47
CSR (RTFO-aged)	193	114	2	35	98	38
CSR (PAV-aged)	177	76	1	26	99	35

to other “external” factors such as the interactions with vehicle tires, spillages (fuel, oil, etc.), and “environmental” dirt. A specific research study addressing the above-mentioned aspects is already planned.

**3.2. Rheological Results.** Amplitude sweep (AS) tests were preliminarily carried out in order to investigate the strain-dependency of the studied materials and to identify their linear viscoelastic domains. Average experimental data collected during the AS tests are depicted in Figures 9 and 10 and summarized in Table 3.

Both the traditional bitumen (Figure 9) and the CSR resin (Figure 10) exhibited the typical behaviour represented by a  $G^*$  not dependent on the strain level until the corresponding LVE limit, after which a rapid decrease of the complex modulus occurred highlighting the nonlinear viscoelastic domain. Comparing 35/50 pen and CSR binders, it can be observed that the reference bitumen is evidently stiffer than the clear resin at low temperatures, whereas this difference

progressively decreased with the increase of the test temperature (CSR and the traditional bitumen showed comparable  $G^*$  values at 50°C) denoting a lower temperature-dependence of CSR. Overall, the LVE strain limits reported in Table 3 showed a conventional proportional relation with the measured  $G^*$  for both 35/50 pen and CSR binders [32].

Figure 11 reports the temperature sweep oscillatory test results in terms of storage  $G'$  and loss  $G''$  moduli as a function of the test temperature in order to highlight the temperature dependencies of the studied materials.

Overall, reduced slopes of CSR curves were well recognized, thus indicating a lower temperature susceptibility of the studied resin with respect to the reference bitumen; this is also in accordance with the basic characteristics reported in Table 1 and already discussed. Similarly to what was arising from the preliminary amplitude sweep test results, the synthetic resin revealed to be softer than the 35/50 penetration grade bitumen at the lower temperatures, whereas both  $G'$  and  $G''$  of CSR seemed to be equivalent (or even slightly higher) at the highest analysed temperatures with respect to the corresponding characteristics of the reference bitumen. This could represent a promising finding both for low-temperature cracking phenomenon and mid-temperature fatigue resistance without a clear reduction of the rutting resistance at higher temperatures. However, a lower structural contribution of the CSR-based mixtures can be hypothesized due to its reduced  $G^*$ . Some of these aspects are specifically addressed in the following. Moreover, it is worth noting that the 35/50 pen bitumen was characterized by a predominant viscous behaviour at a temperature higher



FIGURE 7: Acquired pictures: bitumen (a); unaged CSR (b); RTFO-aged CSR (c); PAV-aged CSR (d).

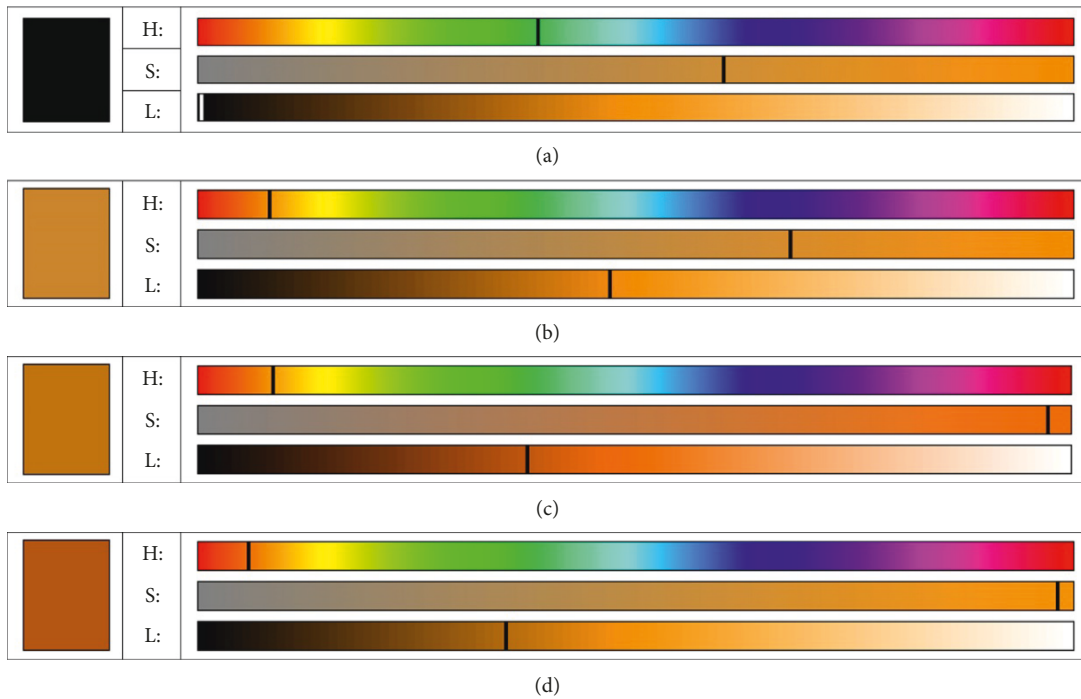


FIGURE 8: HSL colour model results: bitumen (a); unaged CSR (b); RTFO-aged CSR (c); PAV-aged CSR (d).

than 20°C ( $G''$  significantly higher than  $G'$ ), whereas CSR showed very similar values of  $G'$  and  $G''$  at all the tested temperatures, being  $G''$  only slightly higher than  $G'$ .

The main linear viscoelastic response of the tested materials is discussed below through the frequency sweep test results. The validity of TTSP for the tested materials was

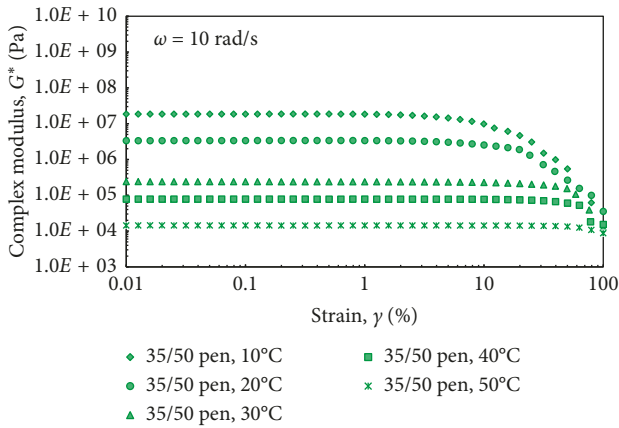


FIGURE 9: Amplitude sweep experimental test results ( $G^*$  vs.  $\gamma$ )—35/50 pen.

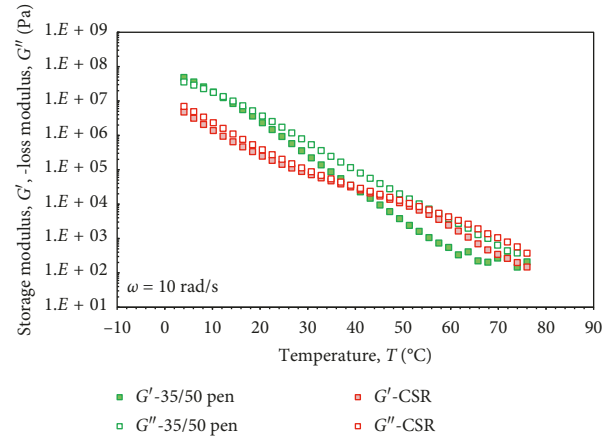


FIGURE 11: Temperature sweep test results at 10 rad/s:  $G'$ ,  $G''$  vs.  $T$  (35/50 pen and CSR).

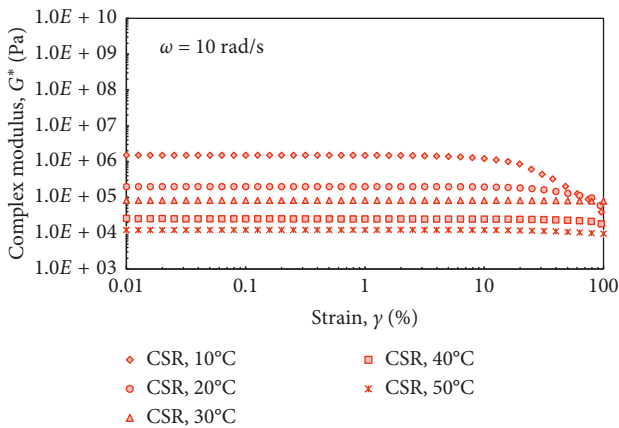


FIGURE 10: Amplitude sweep experimental test results ( $G^*$  vs.  $\gamma$ )—CSR.

TABLE 3: Summary of amplitude sweep test results: initial  $G^*$  and LVE limit.

Temperature (°C)	35/50 pen		CSR	
	Initial $G^*$ (Pa)	LVE limit (%)	Initial $G^*$ (Pa)	LVE limit (%)
10	18 556 338	1.82	1 507 503	3.57
20	3 358 052	3.47	200 186	15.96
30	241 327	8.21	82 764	32.82
40	78 802	18.97	26 111	37.61
50	14 439	42.55	10 595	45.73

preliminarily checked by analysing the measured complex moduli and phase angles in the Black space ( $\delta$  vs.  $G^*$  plot), since it is ascertained that smooth curves in this space indicate the validity of such a superposition principle [14, 33] avoiding inconsistent data fitting with horizontal and vertical shifting. Given this background, the 35/50 pen bitumen exhibited a practically smooth trend in the Black space (Figure 12), thus allowing the consistent construction of  $G^*$  master curve (Figure 13) and  $\delta$  master curve (Figure 14) at the reference temperature of 34°C. It can be noted that the complex shear modulus (Figure 13) smoothly increased with

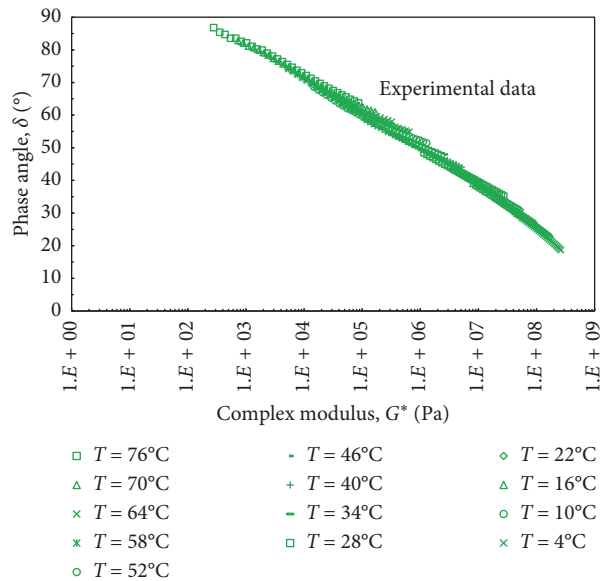


FIGURE 12: Black diagram ( $\delta$  vs.  $G^*$ )—35/50 pen.

the test frequency and seemed to approach the glassy asymptote ( $G^* = 10^9$  Pa) at the lower tested temperature and highest frequency. On the other hand, the measured phase angle increased with the test temperature (thus decreasing the reduced frequency) achieving values of about 80°. In the tested temperature range, a prevalent elastic behaviour ( $\delta < 45^\circ$ ) was guaranteed up to 28 ÷ 40°C, depending on the corresponding test frequency.

The measured  $G^*$  and  $\delta$  of the CSR resin are shown in the Black space of Figure 15. In this case, the experimental data did not provide a smooth curve, indicating the partial inconsistency of the TTSP, at least for the analysed temperatures and frequencies. Therefore, the construction of  $G^*$  and  $\delta$  master curves for CSR was not possible. In any case, different behaviours seemed to be recognizable depending on the test temperatures. This experimental finding could be rationally explained considering the bicomponent nature of the tested resin and the fact that the melting processes could cause the discontinuity and the transition since different

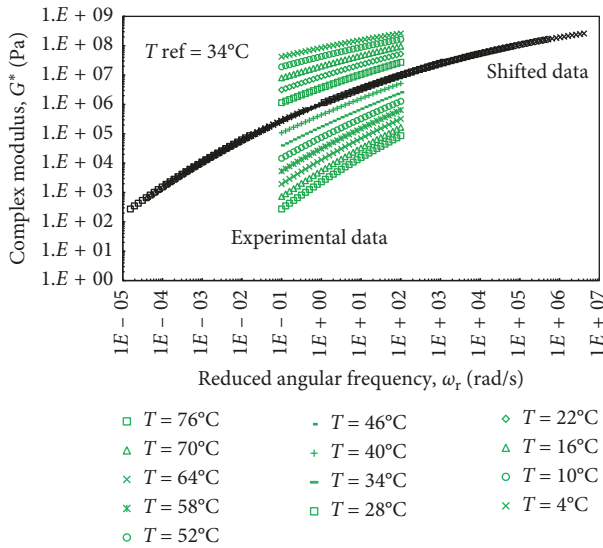


FIGURE 13: Complex modulus master curve ( $G^*$  vs.  $\omega_r$ )—35/50 pen.

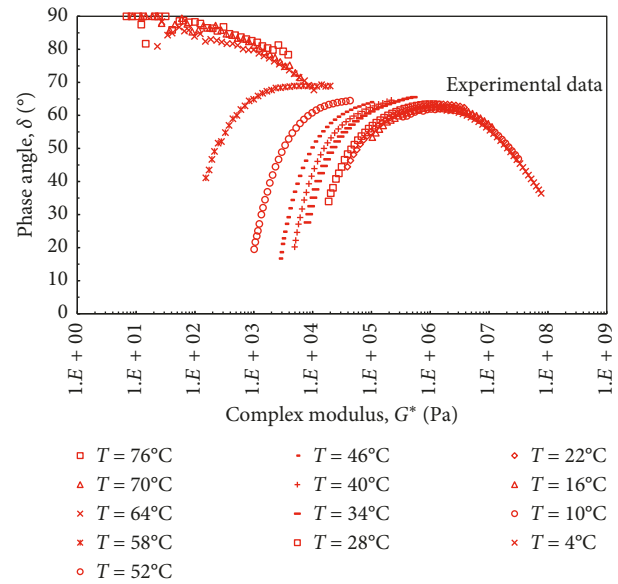


FIGURE 15: Black diagram ( $\delta$  vs.  $G^*$ )—CSR.

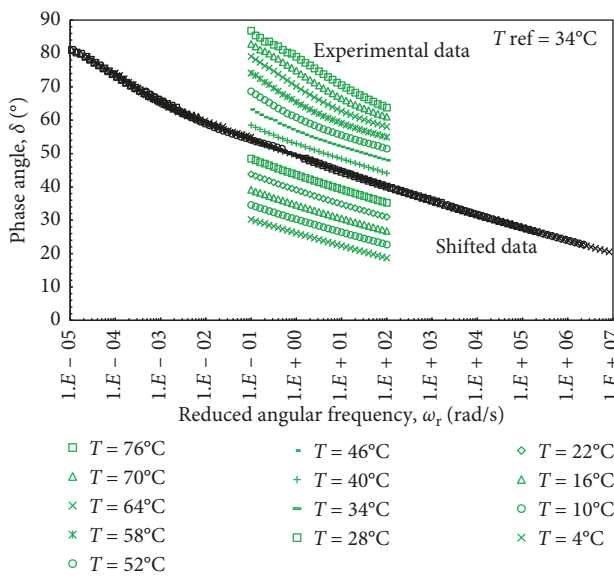


FIGURE 14: Phase angle master curve ( $\delta$  vs.  $\omega_r$ )—35/50 pen.

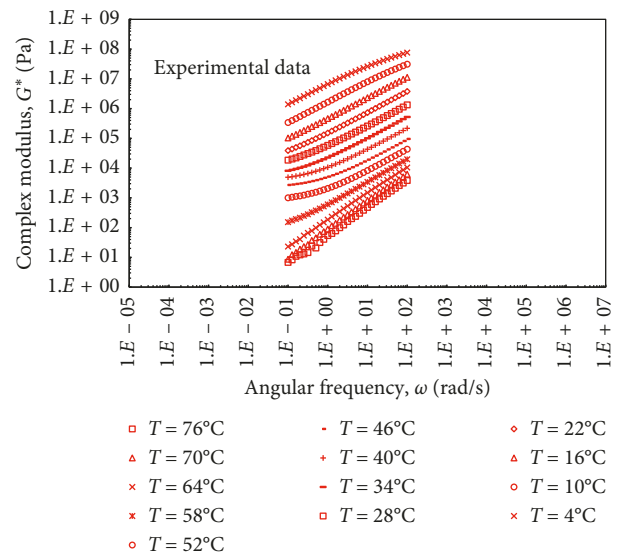


FIGURE 16: Experimental results of complex shear modulus ( $G^*$  vs.  $\omega$ )—CSR.

compounds reasonably conferred distinct properties to the synthetic binder. Moreover, it is interesting to note the unconventional “bell-shape” of the data series measured at temperatures up to 58°C for which  $\delta$  initially increased with  $G^*$  (opposite trend with respect to that of traditional bitumens) and then started to decrease. In this sense, the overall distribution of the measured LVE characteristics seemed to indicate the existence of three distinct regions, as discussed in detail below.

Figure 16 plots CSR complex modulus experimental data showing that  $G^*$  increased with increasing test frequencies and decreasing test temperatures, according to a typical viscous thermoplastic behaviour of bituminous binders. However, at the lowest and the highest investigated temperatures, CSR exhibited conventional quasilinear trends (similar to those of traditional bituminous binders), whereas

at intermediate temperatures (approximately between 22 and 58°C),  $G^*$  revealed unusual s-shaped curves, flattened in the proximity of the lowest experimental  $\omega$ .

As far as the phase angle  $\delta$  is concerned (Figure 17), a nonconventional behaviour (i.e., different from that of bitumens) was observed in the tested range of temperatures and frequencies, distinguishing the three abovementioned different trends which can be broadly schematized as (i) from 4 to 16°C, phase angles decreased as the frequency increased; (ii) from 16 to 58°C, a transition towards the opposite tendency can be detected ( $\delta$  increasing with frequency); and (iii) from 58 to 76°C, a further clear change of behaviour occurred towards a trend similar to that observed for the lowest temperatures ( $\delta$  decreasing as the frequency increases).

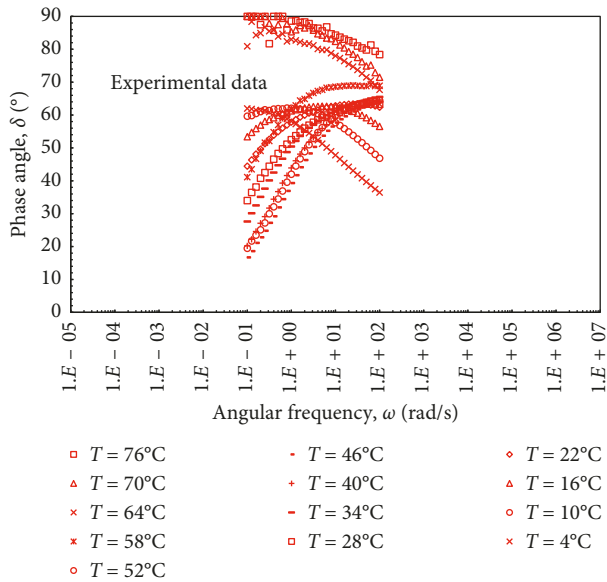


FIGURE 17: Experimental results of phase angle ( $\delta$  vs.  $\omega$ )—CSR.

The comparison of the linear viscoelastic properties of the tested binders is reported in the following, based on the trend of the measured experimental data  $G^*$  and  $\delta$  (Figures 18 and 19). Overall, the resin showed significantly lower stiffness than the traditional bitumen at a given temperature within the investigated frequency domain (Figure 18). As an example, complex modulus of the bitumen at 52°C was comparable with  $G^*$  at 28°C of the resin at a given test frequency.

Moreover, CSR exhibited noticeably higher  $\delta$  at both low ( $4 \div 22^\circ\text{C}$ ) and high ( $64 \div 76^\circ\text{C}$ ) test temperatures (even approaching  $90^\circ$  corresponding to a pure viscous behaviour) than the 35/50 pen bitumen, thus denoting a more viscous behaviour in that domain (Figure 19). On the other hand, given the observed properties of CSR discussed above, a direct comparison between the two binders at intermediate temperatures ( $22 \div 58^\circ\text{C}$ ) is not straightforward. However, with the aim of finding a correlation between these data and the empirical findings related to the elastic recovery of the materials measured at  $25^\circ\text{C}$  (Table 1), phase angle values at  $22 \div 28^\circ\text{C}$  and low frequencies can be compared. In this sense, a certain correlation could be observed since CSR seemed to exhibit lower phase angles at these test conditions than the traditional bitumen, thus denoting higher elasticity. Specific considerations related to fatigue resistance at intermediate temperatures and rutting potential at high-temperatures are given in the following, based on the corresponding specific rheological tests carried out.

The fatigue resistance of CSR and reference 35/50 pen bitumen assessed by LAS tests is summarized in Table 4 and Figure 20, which report the main LAS outcomes and the corresponding predicted fatigue lines, respectively.

First of all, the soundness of the obtained results seems to be confirmed by the fact that they are in accordance with those of previous studies on traditional bitumens [30]. The derived fatigue curves (Figure 20) indicated a significant

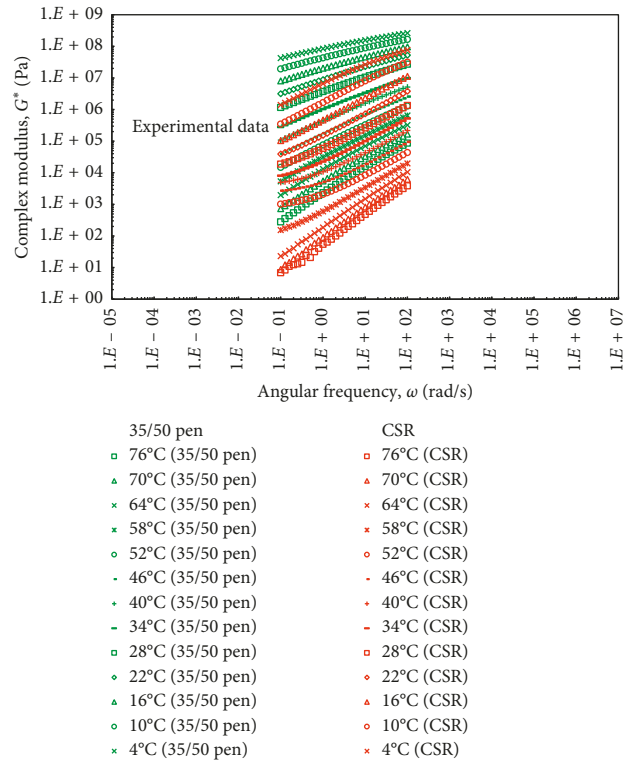


FIGURE 18: Experimental results of stiffness ( $G^*$  vs.  $\omega$ )—35/50 pen vs. CSR.

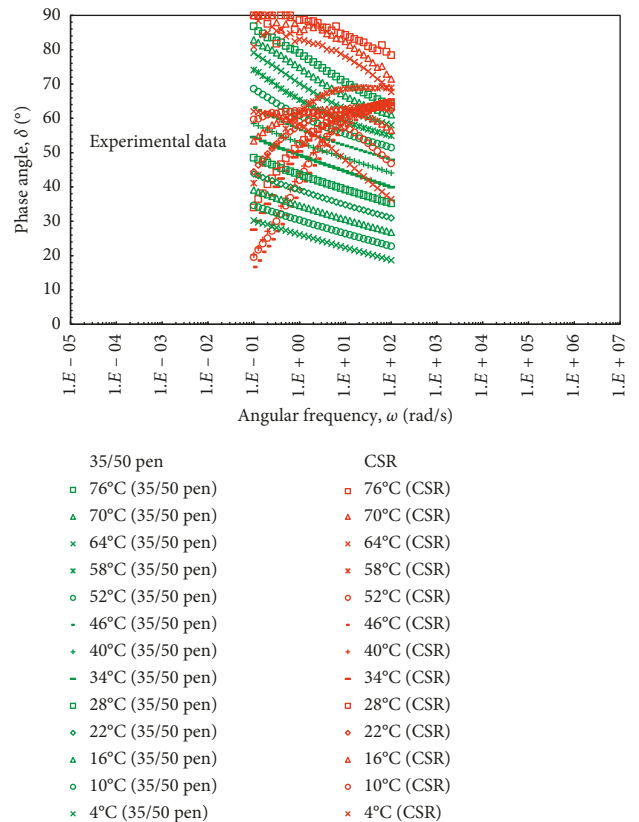


FIGURE 19: Experimental results of phase angle ( $\delta$  vs.  $\omega$ )—35/50 pen vs. CSR.

TABLE 4: Linear amplitude sweep parameters.

Material	LAS parameter						
	$M$	$\alpha$	$C_1$	$C_2$	$D_f$	$A$	$B$
35/50 pen	0.6749	1.4817	0.0872	0.5624	14.5167	7970.07	2.963
CSR	0.7681	1.3019	0.0365	0.6264	45.4842	60419.17	2.604

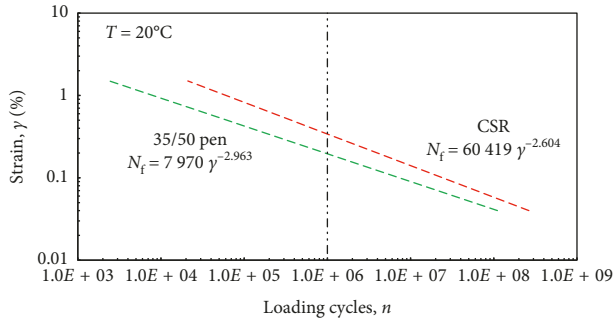


FIGURE 20: LAS test results ( $\gamma$  vs.  $n$ )—35/50 pen vs. CSR predicted fatigue lines.

improvement of the fatigue resistance in the case of CSR binder. In this respect, Figure 21 details the increase of number of cycles to failure for CSR at some representative strain levels (0.1, 0.5, and 1.0%) based on the above-mentioned fatigue lines. These findings seem to agree with the main linear viscoelastic rheological properties discussed in the previous sections where it was highlighted a reduced stiffness of CSR at the intermediate temperatures (LAS tests were carried out at 20°C), which should lead to a higher ductility of such a synthetic binder and thus to reduced cracking phenomenon. In this case, the lower stiffness of CSR (at 20°C) led to lower shear stress at fixed strain levels (Figure 22) up to  $\tau$  peak value of the 35/50 pen bitumen, which corresponds to the sample failure, as well as to a noticeably higher damage at failure  $D_f$  achieved by CSR (Table 4). Thus, faster  $G^*$  reduction and greater damage accumulation for 35/50 pen were reasonably possible.

As far as permanent deformation resistance is concerned, MSCR test results are presented in Figure 23 where the experimental data collected for both the tested binders are reported in terms of strain evolution over time. First, a strong temperature dependency could be clearly evinced in the case of CSR resin since the measured strains exhibited a very fast increase as the test temperature increased thus confirming the LVE properties presented above. In particular, CSR and 35/50 pen showed a comparable behaviour at 52°C and 58°C (CSR permanent deformation resistance at 52°C seemed even higher than that of the traditional bitumen) whereas sensibly higher strains were measured for CSR samples at the higher analysed temperatures (64, 70 and 76°C).

$J_{nr}/J_{TOT}$  and  $J_{nr}$  values calculated based on the experimental readings depicted in Figure 23 are summarized in Table 5 and represented in Figure 24, respectively. First, the results of Table 5 and Figure 24 clearly highlight the different stress and temperature dependency of the two

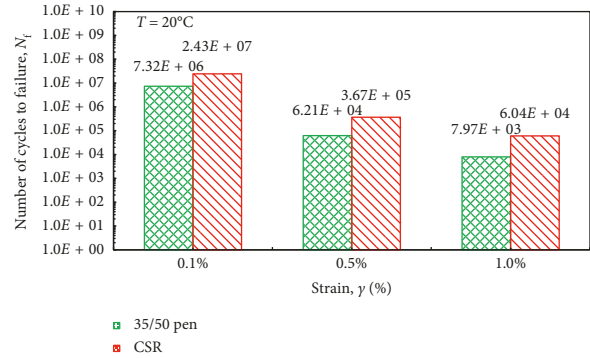


FIGURE 21: LAS test results ( $N_f$  vs.  $\gamma$ )—35/50 pen vs. CSR loading cycles at failure.

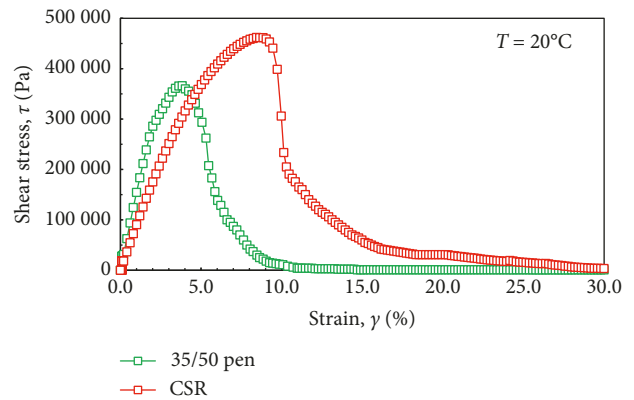


FIGURE 22: LAS test results ( $\tau$  vs.  $\gamma$ )—35/50 pen vs. CSR shear stress evolution.

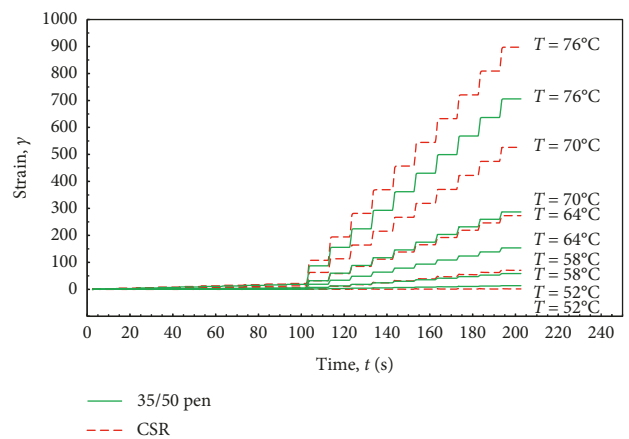


FIGURE 23: MSCR test results ( $\gamma$  vs.  $t$ )—35/50 pen vs. CSR strain evolution.

TABLE 5: MSCR test results— $J_{nr}/J_{TOT}$  ratios.

Temperature (°C)	$J_{nr}/J_{TOT}$ ratio			
	35/50 pen		CSR	
	$\tau = 0.1$ kPa	$\tau = 3.2$ kPa	$\tau = 0.1$ kPa	$\tau = 3.2$ kPa
52	0.88	0.91	0.02	0.08
58	0.95	0.98	0.12	0.77
64	0.98	1.00	0.87	0.99
70	0.99	1.00	0.94	1.00
76	0.99	1.00	0.98	1.00

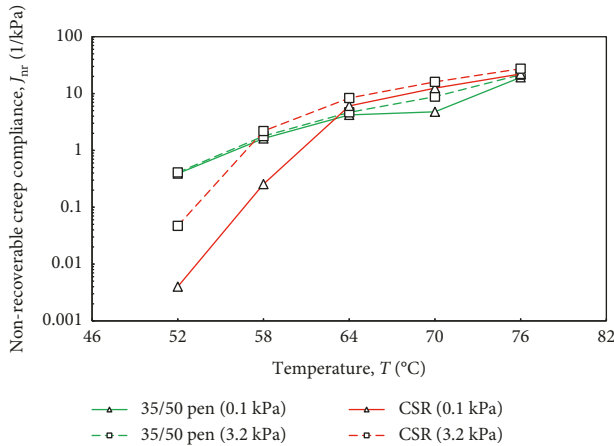


FIGURE 24: MSCR test results ( $J_{nr}$  vs.  $T$ )—35/50 pen vs. CSR nonrecoverable creep compliance.

materials up to 64°C. In particular, such results clearly show the noticeable elastic recovery aptitude of CSR, especially for temperatures up to 58°C. On the other hand, some issues occurred for CSR at the higher temperatures in terms of nonrecoverable creep compliance  $J_{nr}$ , which takes into account the permanent deformation at the end of the creep phase in relation with the corresponding applied stress level. This finding seems in accordance with the frequency sweeps results reported in the Black space of Figure 15, which denoted this specific temperature dependency (a clear change in behaviour was observed moving from 58 to 64°C).

However, it is worth highlighting that, at given environmental conditions (air temperature, solar radiation, humidity, wind, etc.), clear mixtures will achieve distinctly lower in-service temperatures than traditional “black” materials due to their chromatic and thermal properties [34]. Thus, a proper comparison between the two tested binders regarding their rutting resistance at high-temperatures should be carried out taking into account the different temperatures that clear and traditional materials would achieve in the field. As an example, Figures 25 and 26 represent a plausible scenario demonstrating that, if a surface course prepared with CSR will achieve in the field a temperature 6°C lower than that of a corresponding reference bituminous mixture (thanks to its chromatic and thermal properties), it will be able to guarantee distinctly higher performance in terms of permanent deformation resistance than that of traditional materials, thus demonstrating promising applicability.

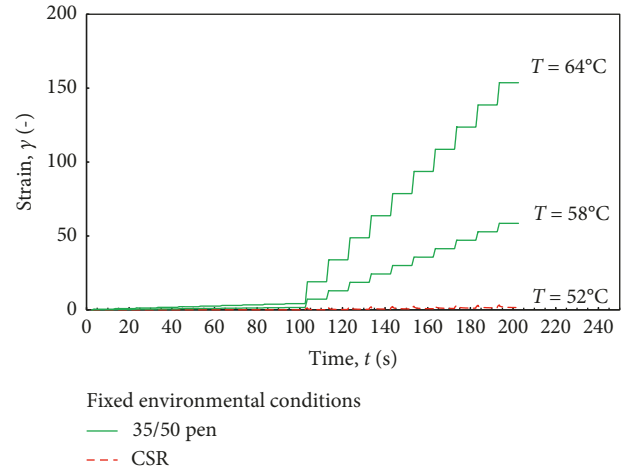


FIGURE 25: Hypothesis scenario ( $\gamma$  vs.  $t$ )—35/50 pen vs. CSR strain evolutions at different temperatures.

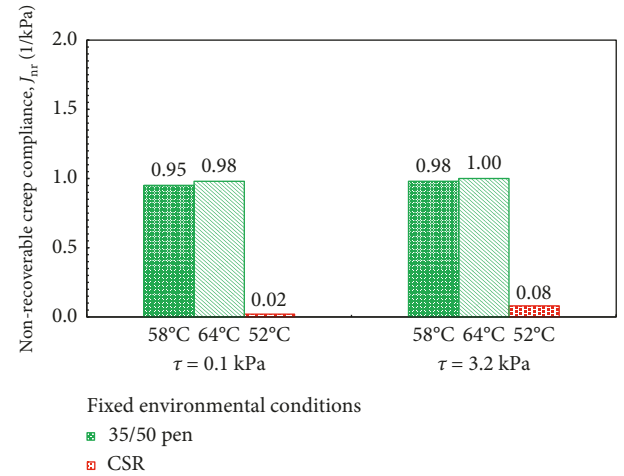


FIGURE 26: Hypothesis scenario ( $J_{nr}$ )—35/50 pen vs. CSR  $J_{nr}$  at different temperatures.

### 4. Conclusions

The present paper deals with an experimental study aimed at assessing aesthetic and rheological properties of a synthetic transparent resin (CSR) for clear road pavement surface courses. The observed performance was also related with that of a conventional 35/50 penetration grade bitumen (35/50 pen) selected as a reference binder for comparison purposes.

The chromatic analysis was performed to determine objective parameters describing the visual appearance of the resin and to investigate the aging effects on such chromatic characteristics, also in view of subsequent analysis aimed at quantifying correlation between colour and thermal properties. The chromatic characteristics of the tested materials were evaluated through hue, saturation, and lightness model. The experimental findings mainly revealed that

- (i) hue (i.e., tonality) of CSR did not seem to be significantly affected by aging

- (ii) saturation (i.e., light emission power) and lightness (i.e., colour brightness) showed higher variations due to aging (mainly related to the short-term aging)

Thus, a good chromatic durability of mixtures prepared with CSR could be supposed (once paved, binder colour should be affected by weathering and oxidizing to a limited extent). Indeed, a chromatic assessment at mixture scale is strongly suggested in order to both consider the possible in-service issues related to the pavement dirtying (vehicle tire actions, spillages, and atmospheric agents) and to determine the influence of aggregate colour in the final tonality of the mix (i.e., the transparency of the resin should exalt the chromaticity of the lithic matrix).

A comprehensive rheological characterization was also carried out to determine the main linear viscoelastic characteristics, the fatigue resistance, and the rutting potential of the investigated binder. In this sense, the obtained results mainly suggested that the clear synthetic resin

- (i) cannot be considered a thermorheologically simple material (time-temperature superposition principle not valid)
- (ii) seemed to be less temperature-dependent than the reference bitumen, especially at the midservice temperatures (20–50°C)
- (iii) presented three distinct behaviours depending on the temperature range; in fact, CSR showed a similar behaviour with respect to the reference bitumen below 16°C and above 58°C, whereas in the central temperature region, it revealed an opposite tendency (i.e., the increase of the test frequency enhanced the viscous component)
- (iv) exhibited an overall lower stiffness with respect to the reference 35/50 pen bitumen
- (v) was characterized by a higher fatigue resistance at 20°C than the reference bitumen
- (vi) seemed prone to accumulate higher permanent deformations than the reference bitumen at a given high in-service temperatures; however, it should be taken into account that given their particular chromatic characteristic, the clear mixtures will achieve lower temperatures in the field with respect to traditional black surfaces for a given environmental condition; thus, reduced rutting phenomena should be reasonably supposed for CSR-based mixes

Given this summary, it can be concluded that the studied resin demonstrated promising applicability as an innovative binder for road pavement wearing courses, even if a significantly lower structural contribution should be hypothesized, due to its reduced stiffness. Further research could concern the study of the low-temperature behaviour, as well as the analysis of such a product at mixture scale (e.g., a thermal monitoring should be able to quantify the possible temperature mitigation due to the use of clear mixture made with CSR).

## Data Availability

Data are available by means of Google Drive system. Files can be downloaded at the link [https://drive.google.com/file/d/1OBytdtnyrtIcEQGf-60\\_8FzCA0rK81JV/view?usp=sharing](https://drive.google.com/file/d/1OBytdtnyrtIcEQGf-60_8FzCA0rK81JV/view?usp=sharing) (the password can be obtained from the corresponding author).

## Disclosure

Test results and opinions are those of the authors and do not necessarily reflect those of the sponsoring company.

## Conflicts of Interest

The authors declare that there are no conflicts of interest regarding the publication of this paper.

## Acknowledgments

This study presents a part of the outcomes of a research project funded by the Department of Civil, Environmental and Architectural Engineering (ICEA) of the University of Padua (project no. BIRD168998). This study was also sponsored by Iterchimica Srl (Italy) that gave both financial and technical supports for the research project.

## References

- [1] H. Higashiyama, M. Sano, F. Nakanishi, O. Takahashi, and S. Tsukuma, "Field measurements of road surface temperature of several asphalt pavements with temperature rise reducing function," *Case Studies in Construction Materials*, vol. 4, pp. 73–80, 2016.
- [2] M. Bocci, A. Grilli, F. Cardone, and A. Virgili, "Clear asphalt mixture for wearing course in tunnels: experimental application in the province of bolzano," *Procedia-Social and Behavioral Sciences*, vol. 53, pp. 115–124, 2012.
- [3] N. Piérard, J. De Visscher, S. Vansteenkiste, and A. Vanelstraete, "Coloured asphalt pavements: mix design and laboratory performance testing," in *Proceedings of the 8th RILEM International Symposium on Testing and Characterization of Sustainable and Innovative Bituminous Materials*, vol. 11, *RILEM Bookseries*, pp. 283–294, Springer, Ancona, Italy, October 2016.
- [4] S. Babić, A. Deluka-Tibljaš, M. Cuculić, and S. Šurdonja, "Analysis of pavement surface heating in urban areas," *Gradevinar*, vol. 64, no. 2, pp. 125–132, 2012.
- [5] V. Di Maria, M. Rahman, P. Collins, G. Dondi, and C. Sangiorgi, "Urban heat island effect: thermal response from different types of exposed paved surfaces," *International Journal of Pavement Research and Technology*, vol. 6, no. 4, pp. 414–422, 2013.
- [6] Y. Qin, "A review on the development of cool pavements to mitigate urban heat island effect," *Renewable and Sustainable Energy Reviews*, vol. 52, pp. 445–459, 2015.
- [7] M. Santamouris, N. Gaitani, A. Spanou, M. Saliari, and K. Vassilakopoulou, "Using cool paving materials to improve microclimate of urban areas—design realization and results of the flisvos project," *Building and Environment*, vol. 53, pp. 128–136, 2012.
- [8] P. Weihs, S. Hasel, E. Mursch-Radlgruber et al., "Investigation of the effect of sealed surfaces on local climate in urban areas,"

- in *Proceedings of the 9th International Conference on Urban Climate Jointly with 12th Symposium on the Urban Environment*, pp. 1–6, Toulouse, France, July 2015.
- [9] K. K. Guan, “Surface and ambient air temperatures associated with different ground material: a case study at the University of California,” *Surface and Air Temperatures of Ground Material*, vol. 2011, 2011.
- [10] A. Synnefa, T. Karlessi, N. Gaitani et al., “Experimental testing of cool colored thin layer asphalt and estimation of its potential to improve the urban microclimate,” *Building and Environment*, vol. 46, no. 6, pp. 38–44, 2011.
- [11] F. J. Navarro, P. Partal, F. Martínez-Boza, and C. Gallegos, “Effect of composition and processing on the linear viscoelasticity of synthetic binders,” *European Polymer Journal*, vol. 41, no. 6, pp. 1429–1438, 2005.
- [12] G. D. Airey, M. H. Mohammed, and C. Fichter, “Rheological characteristics of synthetic road binders,” *Fuel*, vol. 87, no. 10–11, pp. 1763–1775, 2008.
- [13] F. Merusi and F. Giuliani, “Chromatic and rheological characteristics of clear road binders,” *Transportation Research Record: Journal of the Transportation Research Board*, vol. 2293, no. 1, pp. 114–122, 2012.
- [14] G. D. Airey and M. H. Mohammed, “Rheological properties of polyacrylates used as synthetic road binders,” *Rheologica Acta*, vol. 47, no. 7, pp. 751–763, 2008.
- [15] D. Lesueur, “The colloidal structure of bitumen: consequences on the rheology and on the mechanisms of bitumen modification,” *Advances in Colloid and Interface Science*, vol. 145, no. 1–2, pp. 42–82, 2009.
- [16] C. Efthymiou, M. Santamouris, D. Kolokotsa, and A. Koras, “Development and testing of photovoltaic pavement for heat island mitigation,” *Solar Energy*, vol. 130, pp. 148–160, 2016.
- [17] J. Yang, Z.-H. Wang, K. E. Kaloush, and H. Dylla, “Effect of pavement thermal properties on mitigating urban heat islands: a multi-scale modeling case study in Phoenix,” *Building and Environment*, vol. 108, pp. 110–121, 2016.
- [18] J. Chen, H. Wang, and H. Zhu, “Analytical approach for evaluating temperature field of thermal modified asphalt pavement and urban heat island effect,” *Applied Thermal Engineering*, vol. 113, pp. 739–748, 2017.
- [19] T. Berk, A. Kaufman, and L. Brownston, “A human factors study of color notation systems for computer graphics,” *Communications of the ACM*, vol. 25, no. 8, pp. 547–550, 1982.
- [20] M. W. Schwarz, W. B. Cowan, and J. C. Beatty, “An experimental comparison of RGB, YIQ, LAB, HSV, and opponent color models,” *ACM Transactions on Graphics*, vol. 6, no. 2, pp. 123–158, 1987.
- [21] A. R. Smith, “Color gamut transform pairs,” *ACM SIGGRAPH Computer Graphics*, vol. 12, no. 3, pp. 12–19, 1978.
- [22] D. A. Anderson, D. W. Christensen, B. U. Bahia et al., “Binder characterization, vol. 3: physical properties,” SHARP-A-369, p. 475, National Research Council, Washington, DC, USA, 1994.
- [23] M. O. Marasteanu and D. A. Anderson, “Establishing linear viscoelastic conditions for asphalt binders,” *Transportation Research Record: Journal of the Transportation Research Board*, vol. 1728, no. 1, pp. 1–6, 2000.
- [24] M. L. Williams, R. F. Landel, and J. D. Ferry, “The temperature dependence of relaxation mechanisms in amorphous polymers and other glass-forming liquids,” *Journal of the American Chemical Society*, vol. 77, no. 14, pp. 3701–3707, 1955.
- [25] C. Hintz, R. Velasquez, C. Johnson, and H. Bahia, “Modification and validation of linear amplitude sweep test for binder fatigue specification,” *Transportation Research Record: Journal of the Transportation Research Board*, vol. 2207, no. 1, pp. 99–106, 2011.
- [26] R. Botella, F. E. Pérez-Jiménez, and R. Miró, “Application of a strain sweep test to assess fatigue behavior of asphalt binders,” *Construction and Building Materials*, vol. 36, pp. 906–912, 2012.
- [27] M. C. Liao, J. S. Chen, and K. W. Tsou, “Fatigue characteristics of bitumen-filler mastics and asphalt mixtures,” *Journal of Materials in Civil Engineering*, vol. 24, no. 7, pp. 916–923, 2011.
- [28] A. Al-Haddad, “Fatigue evaluation of Iraqi asphalt binders based on the dissipated energy and viscoelastic continuum damage (VECD) approaches,” *Journal of Civil Engineering and Construction Technology*, vol. 6, no. 3, pp. 27–50, 2015.
- [29] Y. Kim, H. J. Lee, D. N. Little, and Y. R. Kim, “A simple testing method to evaluate fatigue fracture and damage performance of asphalt mixtures,” *Journal of Association of Asphalt Paving Technologists*, vol. 75, pp. 755–788, 2006.
- [30] A. Pereira, R. Micaelo, L. Quaresma, and M. T. Cidade, “Evaluation of different methods for the estimation of the bitumen fatigue life with DSR testing,” in *RILEM Bookseries*, vol. 11, pp. 1017–1028, Springer, Berlin, Germany, 2016.
- [31] C. M. Johnson, *Estimating asphalt binder fatigue resistance using an accelerated test method*, Ph.D. thesis, University of Wisconsin, Madison, WI, USA, 2010.
- [32] G. D. Airey, B. Rahimzadh, and A. C. Collop, “Linear viscoelastic limits of bituminous binders,” *Association of Asphalt Paving Technologists*, vol. 71, pp. 89–115, 2003.
- [33] J. P. Planche, D. Lesueur, and M. Hines, “Evaluation of elastomer modified bitumens using SHRP binder specifications,” in *Proceedings of the 1st Eurasphalt and Eurobitume Conference*, pp. 1–17, Strasbourg, France, May 1996.
- [34] M. Pasetto, E. Pasquini, G. Giacomello, and A. Baliello, “Innovative pavement surfaces as urban heat islands mitigation strategy: chromatic, thermal and mechanical characterisation of clear/coloured mixtures,” *Road Materials and Pavement Design*, vol. 20, no. 1, pp. S533–S555, 2019.

## Research Article

# 2S2P1D Model Calibration Error from User Panel for One Bitumen and One Bituminous Mixture

S. Mangiafico , C. Sauzéat, and H. Di Benedetto

Université de Lyon, École Nationale des Travaux Publics de l'État, LTDS (CNRS UMR 5513) Rue Maurice Audin, 69518 Vaulx-en-Velin, France

Correspondence should be addressed to S. Mangiafico; [salvatore.mangiafico@entpe.fr](mailto:salvatore.mangiafico@entpe.fr)

Received 8 February 2019; Revised 4 April 2019; Accepted 18 April 2019; Published 26 May 2019

Guest Editor: Jose Norambuena-Contreras

Copyright © 2019 S. Mangiafico et al. This is an open access article distributed under the Creative Commons Attribution License, which permits unrestricted use, distribution, and reproduction in any medium, provided the original work is properly cited.

The objective of this study is to analyse the differences between experimental LVE properties of both a straight-run bitumen and a bituminous mixture and simulations with analogical 2S2P1D (2 Springs, 2 Parabolic elements, and 1 Dashpot) model fitted by 14 different users. Data for the bitumen consisted of isotherms of  $|G^*|$  and  $\varphi$  obtained from DSR complex modulus tests at 12 different temperatures ranging from  $-29.9^\circ\text{C}$  to  $60.0^\circ\text{C}$  and frequencies ranging from 6.3 to 40 Hz, for a total of 60 data points. Data for the bituminous mixture consisted of isotherms of  $|E^*|$  and  $\varphi$  obtained from strain-controlled traction/compression complex modulus tests at 8 different temperatures ranging from  $-29.7^\circ\text{C}$  to  $38.8^\circ\text{C}$  and frequencies ranging from 0.01 to 10 Hz, for a total of 55 data points. All users worked independently and for the same time duration of one hour to fit the 2S2P1D model on both sets of data. Successful simulations of experimental data of both bitumen and mixture were generally obtained by all the users over the whole range of frequencies and temperatures, regardless of their familiarity and experience with the model. The accuracy of the model to fit experimental data is all the more evident if the great spans of complex modulus ( $|G^*|$  of the bitumen between  $10^{-2}$  and  $10^3$  MPa,  $|E^*|$  of the mixture between 10 and 40000 MPa) are considered. The obtained results highlight the convenience of 2S2P1D model to perform multiscale modelling of LVE behaviour of bituminous materials, from bitumens to mixtures.

## 1. Introduction

Modelling is an essential step in science. Several model-fitting methods, as well as sensitivity analysis methods, have been developed and are used in various scientific and engineering domains ([1–6], among others). The cited references offer a limited and nonexhaustive list of examples of existing methods, such as genetic algorithms, finite difference methods, direct differentiation methods, adjoint variable methods, etc.

In the domain of civil engineering, a wide range of models are available to simulate the various types of mechanical behaviour of construction materials. The 2S2P1D (2 Springs, 2 Parabolic creep elements, and 1 Dashpot) is a linear viscoelastic (LVE) analogical model developed at the University of Lyon/ENTPE to simulate the behaviour of all types of bituminous materials (bitumens, mastics, and bituminous mixtures) [7]. More details on the model are given in Section 2.

This model has gained attention in the scientific and technical community of the domain. The development of an

accurate algorithm to automatically fit the model on a given set of experimental data by optimizing model constants is under way. Some studies are found in the literature where the model is calibrated by applying least square method to minimize the gap between experimental and simulated values of a specific LVE property (as an example, norm of complex modulus of binders was considered in [8]). However, its calibration is still generally performed manually by individual users. The model is fitted on experimental data by adapting the values of its constants through a trial and error procedure, until satisfactory simulations are obtained and visually judged [9].

To the extent of the knowledge of the authors, no study has been published yet on the variability of 2S2P1D simulations of the same materials obtained by different users.

The objective of this study was precisely to perform an analysis of the differences between experimental LVE properties of both a straight-run bitumen and a bituminous mixture (respectively,  $G^*$  and  $E^*$ ) and 2S2P1D simulations

obtained by various users with different levels of expertise of the model.

## 2. 2S2P1D Analogical Model

As indicated by the acronym, the analogical 2S2P1D model (Figure 1) is a partial derivative model consisting of an assembly of two linear elastic springs, two parabolic creep elements, and one Newtonian dashpot. For a given material with a LVE behaviour, the model can be used to simulate its complex modulus  $E^*$  according to equation (1), where the variables are as follows:  $\omega$  is the pulsation, related to frequency  $f$  as  $\omega = 2\pi f$ ;  $E_{00}$  is the asymptotic static modulus, for  $\omega \rightarrow 0$ ;  $E_0$  is the asymptotic glassy modulus, for  $\omega \rightarrow \infty$ ;  $\delta$ ,  $k$ , and  $h$  are dimensionless constants related to the two parabolic creep element, with  $k < h$ ;  $\beta$  is a dimensionless constant related to the Newtonian dashpot as shown in equation (2); and  $\tau$  is a characteristic time and the only constant of the model depending on temperature  $T$ .

If the time-temperature superposition principle (TTSP) is respected, temperature shift factors  $a_T$  at any temperature  $T$  can be obtained as in equation (3), where  $\tau_0$  is the value of  $\tau$  at the reference temperature  $T_{\text{ref}}$ . Shift factors  $a_T$  can be fitted with the Williams-Landel-Ferry equation (4), as a function of constants  $C_1$  and  $C_2$  and reference temperature  $T_{\text{ref}}$ .

$$E^* = E_{00} + \frac{E_0 - E_{00}}{1 + \delta(i\omega\tau)^{-k} + (i\omega\tau)^{-h} + (i\omega\beta\tau)^{-1}}, \quad (1)$$

$$\eta = (E_0 - E_{00})\beta\tau, \quad (2)$$

$$a_T = \frac{\tau}{\tau_0}, \quad (3)$$

$$\log a_T = \frac{-C_1(T - T_{\text{ref}})}{C_2 + T - T_{\text{ref}}}. \quad (4)$$

The model can be used to simulate complex shear modulus  $G^*$  of the same material, by replacing constants  $E_{00}$  and  $E_0$  with the corresponding constants  $G_{00}$  and  $G_0$  (Figure 1), respectively, equal to the static and glassy shear complex modulus, as in the following equation:

$$G^* = G_{00} + \frac{G_0 - G_{00}}{1 + \delta(i\omega\tau)^{-k} + (i\omega\tau)^{-h} + (i\omega\beta\tau)^{-1}}. \quad (5)$$

Complex modulus  $E^*$  can be decomposed into its norm ( $|E^*|$ ) and phase angle ( $\varphi$ ), as well as its real ( $E_1$ ) and imaginary ( $E_2$ ) parts, as in equations (6) and (7). The same can be done for complex shear modulus  $G^*$ , as in equations (8) and (9).

$$E^* = E_1 + iE_2 = |E^*| \cos \varphi + i|E^*| \sin \varphi = |E^*| e^{i\varphi}, \quad (6)$$

$$|E^*| = \sqrt{E_1^2 + E_2^2}, \quad (7)$$

$$\varphi = \arctan \frac{E_2}{E_1},$$

$$G^* = G_1 + iG_2 = |G^*| \cos \varphi + i|G^*| \sin \varphi = |G^*| e^{i\varphi}, \quad (8)$$

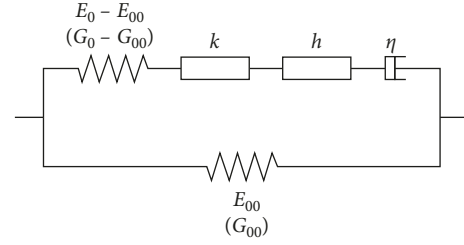


FIGURE 1: Analogical scheme of 2S2P1D model.

$$|G^*| = \sqrt{G_1^2 + G_2^2}, \quad (9)$$

$$\varphi = \arctan \frac{G_2}{G_1}.$$

In this paper, complex shear modulus  $G^*$  was used to simulate the LVE behaviour of a bitumen, while complex modulus  $E^*$  was used for a bituminous mixture. An extension of the model has been proposed to take into account the tridimensional linear viscoelastic behaviour of materials through their complex Poisson's ratio [10, 11]. In this paper, only the unidimensional formulation of the model has been studied.

## 3. Description of Input Experimental Data and Calibration Panel

The LVE behaviour of a straight-run unaged bitumen and of a bituminous mixture was simulated using the 2S2P1D model. The model was fitted on experimental data available for these two materials.

Data for the bitumen consisted of isotherms of  $|G^*|$  and  $\varphi$  obtained from DSR complex modulus tests at 12 different temperatures ranging from  $-29.90^\circ\text{C}$  to  $60.00^\circ\text{C}$  and frequencies ranging from 6.3 to 40 Hz, for a total of 60 data points (Figure 2). Data for the bituminous mixture consisted of isotherms of  $|E^*|$  and  $\varphi$  obtained from complex modulus tests (strain-controlled traction/compression sinusoidal loading on cylindrical specimens with a 75 mm diameter and 150 mm length) at 8 different temperatures ranging from  $-29.65^\circ\text{C}$  to  $38.83^\circ\text{C}$  and frequencies ranging from 0.01 to 10 Hz, for a total of 55 data points (Figure 3).

Data for the two materials were given to a calibration panel, composed of 14 users (including master and PhD students, postdoctoral fellows, senior academic researchers, and professionals in private companies) with different levels of knowledge, familiarity, and experience of the 2S2P1D model, from beginners (having learnt the theory of the model and practicing with it for less than one week) to experienced users (with more than 10 years of knowledge and extensive practice of the model). All users were given one hour to perform the calibration of the model for both materials (bitumen and mixture). All users worked independently, without any communication with the other components of the panel.

Before fitting the 2S2P1D model on each material, every user had to shift the isotherms and obtain master curves of norm and phase angle of complex modulus ( $G^*$  and  $E^*$  for

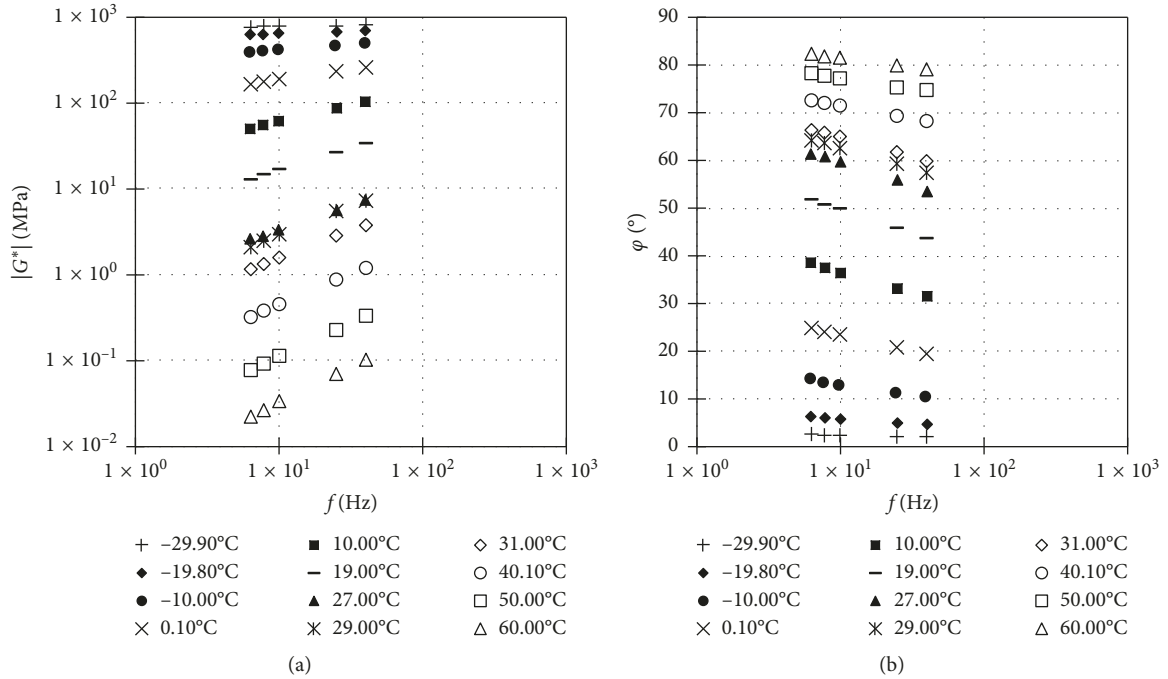


FIGURE 2: Experimental data of the bitumen given to calibration panel: isotherms of norm (a) and phase angle (b) of complex shear modulus  $G^*$ .

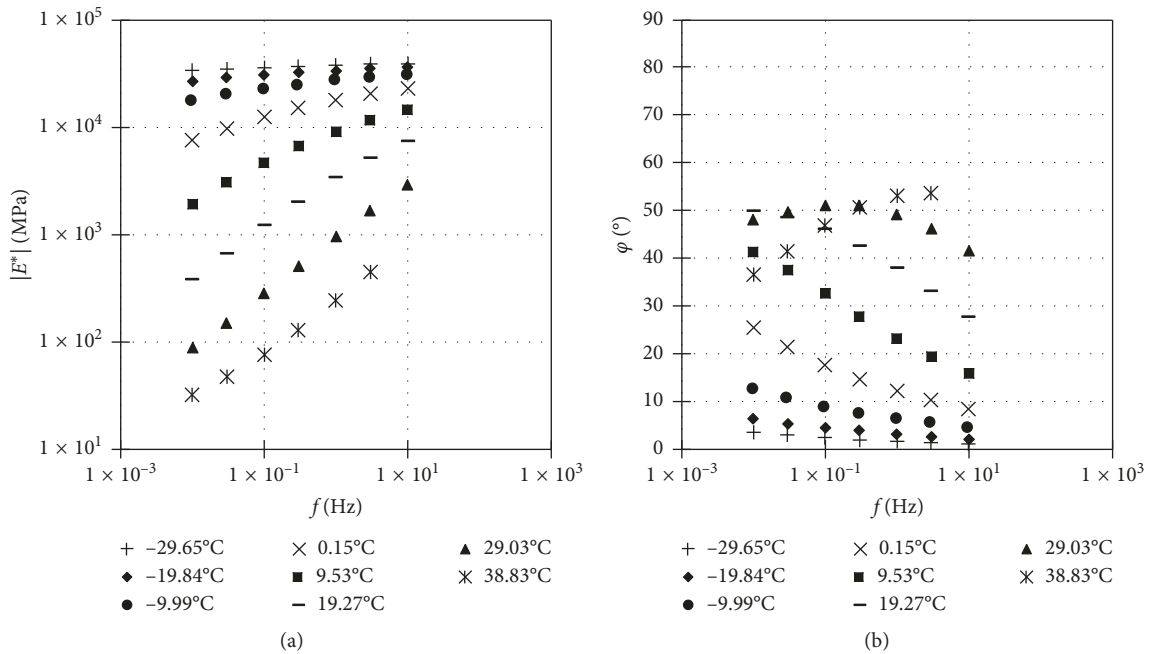


FIGURE 3: Experimental data of the bituminous mixture given to calibration panel: isotherms of norm (a) and phase angle (b) of complex modulus  $E^*$ .

the bitumen and the mixture, respectively). The reference temperatures of 10.00°C for the bitumen and 9.53°C for the mixture were imposed. For each  $i$ -th user, values of temperature shift factors  $a_{T_i}$  at all temperatures were first obtained by manually shifting isotherms and visually evaluating the goodness of the overlap. The WLF equation

was then fitted on all values of  $a_{T_i}$  obtained for each material, therefore obtaining the values of  $C_1$  and  $C_2$  at the imposed reference temperature. For this reason, for the same material, every user obtained a different set of WLF constants and, therefore, slightly different master curves. The fitting of the 2S2P1D was performed on master curves

obtained using shift factors calculated with the WLF equation.

At the end of the imposed time (one hour), each user was asked to give his/her values of the seven 2S2P1D constants ( $G_{00}$  or  $E_{00}$ ,  $G_0$  or  $E_0$ ,  $\delta$ ,  $k$ ,  $h$ ,  $\beta$ , and  $\tau$ ) and the two WLF constants ( $C_1$  and  $C_2$ ;  $T_{\text{ref}}$  was imposed) for each material.

The same Microsoft Excel® workbook, specifically designed to perform the fit, was given to all users. Several spreadsheets allow users to input data and compare experimental data points and simulated curves (WLF equation, Cole-Cole, Black and master curves).

#### 4. Analysis of Results from 2S2P1D Calibration Panel

In this section, experimental data points and 2S2P1D simulations of all users are compared, for both materials. A quantitative estimation of the relative (for  $|G^*|$  and  $|E^*|$ ) and absolute (for  $\varphi$ ) differences between data points and simulations is performed.

**4.1. 2S2P1D Fitting for a Bitumen.** Table 1 reports values of WLF and 2S2P1D constants obtained by all users of the calibration panel for the bitumen. Figure 4 shows a comparison of the simulations of the LVE behaviour of the bitumen obtained by all the users and the experimental data points. In particular, Figures 4(a) and 4(b) show, respectively, Black and Cole-Cole spaces, Figures 4(c) and 4(d) show master curves of, respectively,  $|G^*|$  and  $\varphi$ , and Figure 4(e) shows the various WLF curves obtained by the users, together with the average WLF curve, according to the constants shown in Table 1. Experimental points shown in master curves of Figures 4(c) and 4(d) are shifted using shift factors calculated with the mentioned average WLF curve, with the only purpose of having a graphical representation.

Apart from  $G_{00}$ , imposed equal to zero by all user, the constant with the lowest coefficient of variation (COV, defined as the ratio between standard deviation and mean) is  $G_0$  (1.62%), followed by the two constants  $k$  and  $h$  associated with the parabolic elements (lower than 7%). Although a high COV is observed for the characteristic time  $\tau$ , the variability of this constant is more rigorously evaluated by considering its logarithm  $\log \tau$  (whose COV is lower than 6% in absolute value), as it can be easily understood by taking into account its relationship with temperature and viscosity (equations (2) and (3)).

Generally satisfactory approximations of experimental points are obtained with 2S2P1D simulations of all users. At low frequency/high temperature, slight underestimation of  $|G^*|$  and overestimation of  $\varphi$  are observed for all users. However, these differences between the model and the experimental points are negligible in absolute value (less than 100 kPa for  $|G^*|$ ).

In order to have a quantitative estimation of the differences between the 2S2P1D simulation obtained by each  $i$ -th user and experimental points, relative errors  $\delta_{G_i}$ ,  $\delta_{G_{2i}}$  and  $\delta_{|G^*|_i}$  (respectively for  $G_1$ ,  $G_2$  and  $|G^*|$ ) and absolute error  $\delta_{\varphi_i}$

(for  $\varphi$ ) were calculated for each equivalent frequency  $a_{T_i}\omega$  (60 data points) according to the following equations:

$$\delta_{G_i}(a_{T_i}\omega) = \frac{G_{1,\text{exp}}(a_{T_i}\omega) - G_{1,2S2P1D_i}(a_{T_i}\omega)}{G_{1,\text{exp}}(a_{T_i}\omega)}, \quad (10)$$

$$\delta_{G_{2i}}(a_{T_i}\omega) = \frac{G_{2,\text{exp}}(a_{T_i}\omega) - G_{2,2S2P1D_i}(a_{T_i}\omega)}{G_{2,\text{exp}}(a_{T_i}\omega)}, \quad (11)$$

$$\delta_{|G^*|_i}(a_{T_i}\omega) = \frac{|G_{\text{exp}}^*(a_{T_i}\omega) - |G_{2S2P1D_i}^*(a_{T_i}\omega)|}{|G_{\text{exp}}^*(a_{T_i}\omega)|}, \quad (12)$$

$$\delta_{\varphi_i}(a_{T_i}\omega) = \varphi_{\text{exp}}(a_{T_i}\omega) - \varphi_{2S2P1D_i}(a_{T_i}\omega), \quad (13)$$

where  $G_{1,\text{exp}}(a_{T_i}\omega)$ ,  $G_{2,\text{exp}}(a_{T_i}\omega)$ ,  $|G_{\text{exp}}^*(a_{T_i}\omega)|$ , and  $\varphi_{\text{exp}}(a_{T_i}\omega)$  are experimental values of, respectively,  $G_1$ ,  $G_2$ ,  $|G^*|$ , and  $\varphi$  at the equivalent frequency  $a_{T_i}\omega$ .  $G_{1,2S2P1D_i}(a_{T_i}\omega)$ ,  $G_{2,2S2P1D_i}(a_{T_i}\omega)$ ,  $|G_{2S2P1D_i}^*(a_{T_i}\omega)|$ , and  $\varphi_{2S2P1D_i}(a_{T_i}\omega)$  are values of, respectively,  $G_1$ ,  $G_2$ ,  $|G^*|$ , and  $\varphi$  at the equivalent frequency  $a_{T_i}\omega$ , calculated with the 2S2P1D according to the constants of the  $i$ -th user reported in Table 1.

Master curves of  $\delta_{G_i}$ ,  $\delta_{G_{2i}}$ ,  $\delta_{|G^*|_i}$ , and  $\delta_{\varphi_i}$  are shown in Figure 5. Bold lines represent 10% and 5% limits for, respectively, relative and absolute errors. In order to avoid confusion, it is very important to highlight that errors  $\delta_{G_i}$ ,  $\delta_{G_{2i}}$ ,  $\delta_{|G^*|_i}$ , and  $\delta_{\varphi_i}$  were calculated for each  $i$ -th user at equivalent frequencies obtained with shift factors  $a_{T_i}$  calculated according to his/her WLF constants shown in Table 1. For this reason, the total range of equivalent frequencies is slightly different for each user. The results confirm the qualitative judgement made from Figure 4. The relative errors observed for equivalent frequencies lower than approximately  $10^1$  Hz are negligible because of the low values of  $G_1$ ,  $G_2$ , and  $|G^*|$  at these frequencies (lower than 100 kPa). The error for phase angle  $\varphi$  is generally lower than  $5^\circ$ , apart from some exceptions for some users.

The accuracy of the model to fit experimental data is all the more evident if the great spans of equivalent frequencies (between  $10^{-6}$  and  $10^{10}$  Hz at the reference temperature of  $10^\circ\text{C}$ ) and  $|G^*|$  (between  $10^{-2}$  and  $10^3$  MPa) are taken into consideration. The three most experienced users (2, 5, and 12) of the panel obtained particularly accurate approximations of experimental data, as shown by their corresponding master curves (at  $10^\circ\text{C}$ ) of relative errors for  $|G^*|$  and absolute errors for  $\varphi$  in Figure 6. This observation confirms the ability of the model to accurately simulate LVE behaviour of bitumens.

For each user, global error parameters over the whole range of frequencies were calculated for each of the considered relative and absolute errors. Equations (14)–(17) were used to calculate average values ( $\overline{\delta_{G_i}}$ ,  $\overline{\delta_{G_{2i}}}$ ,  $\overline{\delta_{|G^*|_i}}$ , and  $\overline{\delta_{\varphi_i}}$ ) and standard deviations ( $\mu_{G_i}$ ,  $\mu_{G_{2i}}$ ,  $\mu_{|G^*|_i}$ , and  $\mu_{\varphi_i}$ ) of relative and absolute errors of each user at the  $N$  considered equivalent frequencies  $a_{T_i}$  ( $N=60$ ), plotted in histograms of Figure 7. Error bars are plotted according to standard deviation values.

TABLE 1: WLF and 2S2P1D constants obtained for the bitumen by all the users of the calibration panel ( $T_{ref} = 10.00^\circ\text{C}$ ).

	$C_1$ (-)	$C_2$ ( $^\circ\text{C}$ )	$G_{00}$ (MPa)	$G_0$ (MPa)	$\delta$ (-)	$k$ (-)	$h$ (-)	$\beta$ (-)	$\tau$ (s)	$\log \tau$ (-)
User 1	22.98	165.49	0	877	2.38	0.223	0.560	115	$4.10 \times 10^{-4}$	-3.39
User 2	16.89	120.95	0	900	1.90	0.195	0.500	200	$1.50 \times 10^{-4}$	-3.82
User 3	22.56	169.33	0	900	1.79	0.195	0.510	250	$1.90 \times 10^{-4}$	-3.72
User 4	24.16	178.59	0	888	1.95	0.205	0.515	230	$2.00 \times 10^{-4}$	-3.70
User 5	19.05	141.39	0	900	2.10	0.204	0.550	200	$2.70 \times 10^{-4}$	-3.57
User 6	18.30	137.00	0	870	2.60	0.230	0.600	100	$5.50 \times 10^{-4}$	-3.26
User 7	28.83	200.18	0	880	2.30	0.217	0.560	140	$3.00 \times 10^{-4}$	-3.52
User 8	30.86	196.09	0	900	2.20	0.210	0.550	200	$3.40 \times 10^{-4}$	-3.47
User 9	32.31	235.19	0	900	1.88	0.200	0.500	300	$1.80 \times 10^{-4}$	-3.74
User 10	32.17	223.30	0	893	2.00	0.204	0.550	220	$2.50 \times 10^{-4}$	-3.60
User 11	18.03	124.75	0	862	2.70	0.235	0.608	80	$6.00 \times 10^{-4}$	-3.22
User 12	25.37	179.43	0	870	2.53	0.226	0.580	115	$4.80 \times 10^{-4}$	-3.32
User 13	23.15	170.33	0	870	2.60	0.230	0.580	120	$5.00 \times 10^{-4}$	-3.30
User 14	26.05	203.21	0	900	1.85	0.197	0.505	400	$2.00 \times 10^{-4}$	-3.70
Mean	24.34	174.66	0	886	2.20	0.212	0.548	191	$3.30 \times 10^{-4}$	-3.52
St. dev.	5.25	35.11	0	14	0.32	0.014	0.037	88	$1.52 \times 10^{-4}$	0.20
COV	21.56%	20.10%	—	1.62%	14.48%	6.72%	6.73%	46.32%	45.91%	-5.68%

Note. Coefficient of variation (COV): standard deviation/mean.

$$\overline{\delta_{G_{1i}}} = \frac{\sum_{a_{T_i}\omega} \delta_{G_{1i}}(a_{T_i}\omega)}{N},$$

$$\mu_{G_{1i}} = \sqrt{\frac{\sum_{a_{T_i}\omega} [\delta_{G_{1i}}(a_{T_i}\omega) - \overline{\delta_{G_{1i}}}]^2}{N}}, \quad (14)$$

$$\overline{\Delta_{G_{1i}}} = \frac{\sum_{a_{T_i}\omega} |\delta_{G_{1i}}(a_{T_i}\omega)|}{N},$$

$$M_{G_{1i}} = \sqrt{\frac{\sum_{a_{T_i}\omega} [|\delta_{G_{1i}}(a_{T_i}\omega)| - \overline{\Delta_{G_{1i}}}]^2}{N}}, \quad (18)$$

$$\overline{\delta_{G_{2i}}} = \frac{\sum_{a_{T_i}\omega} \delta_{G_{2i}}(a_{T_i}\omega)}{N},$$

$$\mu_{G_{2i}} = \sqrt{\frac{\sum_{a_{T_i}\omega} [\delta_{G_{2i}}(a_{T_i}\omega) - \overline{\delta_{G_{2i}}}]^2}{N}}, \quad (15)$$

$$\overline{\Delta_{G_{2i}}} = \frac{\sum_{a_{T_i}\omega} |\delta_{G_{2i}}(a_{T_i}\omega)|}{N},$$

$$M_{G_{2i}} = \sqrt{\frac{\sum_{a_{T_i}\omega} [|\delta_{G_{2i}}(a_{T_i}\omega)| - \overline{\Delta_{G_{2i}}}]^2}{N}}, \quad (19)$$

$$\overline{\delta_{|G^*|_i}} = \frac{\sum_{a_{T_i}\omega} \delta_{|G^*|_i}(a_{T_i}\omega)}{N},$$

$$\mu_{|G^*|_i} = \sqrt{\frac{\sum_{a_{T_i}\omega} [\delta_{|G^*|_i}(a_{T_i}\omega) - \overline{\delta_{|G^*|_i}}]^2}{N}}, \quad (16)$$

$$\overline{\Delta_{|G^*|_i}} = \frac{\sum_{a_{T_i}\omega} |\delta_{|G^*|_i}(a_{T_i}\omega)|}{N},$$

$$M_{|G^*|_i} = \sqrt{\frac{\sum_{a_{T_i}\omega} [|\delta_{|G^*|_i}(a_{T_i}\omega)| - \overline{\Delta_{|G^*|_i}}]^2}{N}}, \quad (20)$$

$$\overline{\delta_{\varphi_i}} = \frac{\sum_{a_{T_i}\omega} \delta_{\varphi_i}(a_{T_i}\omega)}{N},$$

$$\mu_{\varphi_i} = \sqrt{\frac{\sum_{a_{T_i}\omega} [\delta_{\varphi_i}(a_{T_i}\omega) - \overline{\delta_{\varphi_i}}]^2}{N}}, \quad (17)$$

$$\overline{\Delta_{\varphi_i}} = \frac{\sum_{a_{T_i}\omega} |\delta_{\varphi_i}(a_{T_i}\omega)|}{N},$$

$$M_{\varphi_i} = \sqrt{\frac{\sum_{a_{T_i}\omega} [|\delta_{\varphi_i}(a_{T_i}\omega)| - \overline{\Delta_{\varphi_i}}]^2}{N}}, \quad (21)$$

A further error estimation was performed by considering absolute values of errors  $\delta_{G_{1i}}$ ,  $\delta_{G_{2i}}$ ,  $\delta_{|G^*|_i}$ , and  $\delta_{\varphi_i}$ . Therefore, equations (18)–(21) were used to calculate average values ( $\overline{\Delta_{G_{1i}}}$ ,  $\overline{\Delta_{G_{2i}}}$ ,  $\overline{\Delta_{|G^*|_i}}$ , and  $\overline{\Delta_{\varphi_i}}$ ) and standard deviations ( $M_{G_{1i}}$ ,  $M_{G_{2i}}$ ,  $M_{|G^*|_i}$ , and  $M_{\varphi_i}$ ) of absolute values of relative and absolute errors of each user at the  $N$  considered equivalent frequencies  $a_{T_i}$  ( $N = 60$ ), plotted in histograms of Figure 8. As in Figure 7, error bars are plotted according to standard deviation values.

Apart from some exceptions regarding few users, global error parameters for phase angle are generally lower than  $5^\circ$  even considering the corresponding standard deviations. Higher error parameters are found for  $G_1$ ,  $G_2$ , and  $|G^*|$ , especially when absolute values of errors are considered. However, these parameters were calculated by arithmetically averaging all the 60 data points over the whole frequency range available. For this reason,

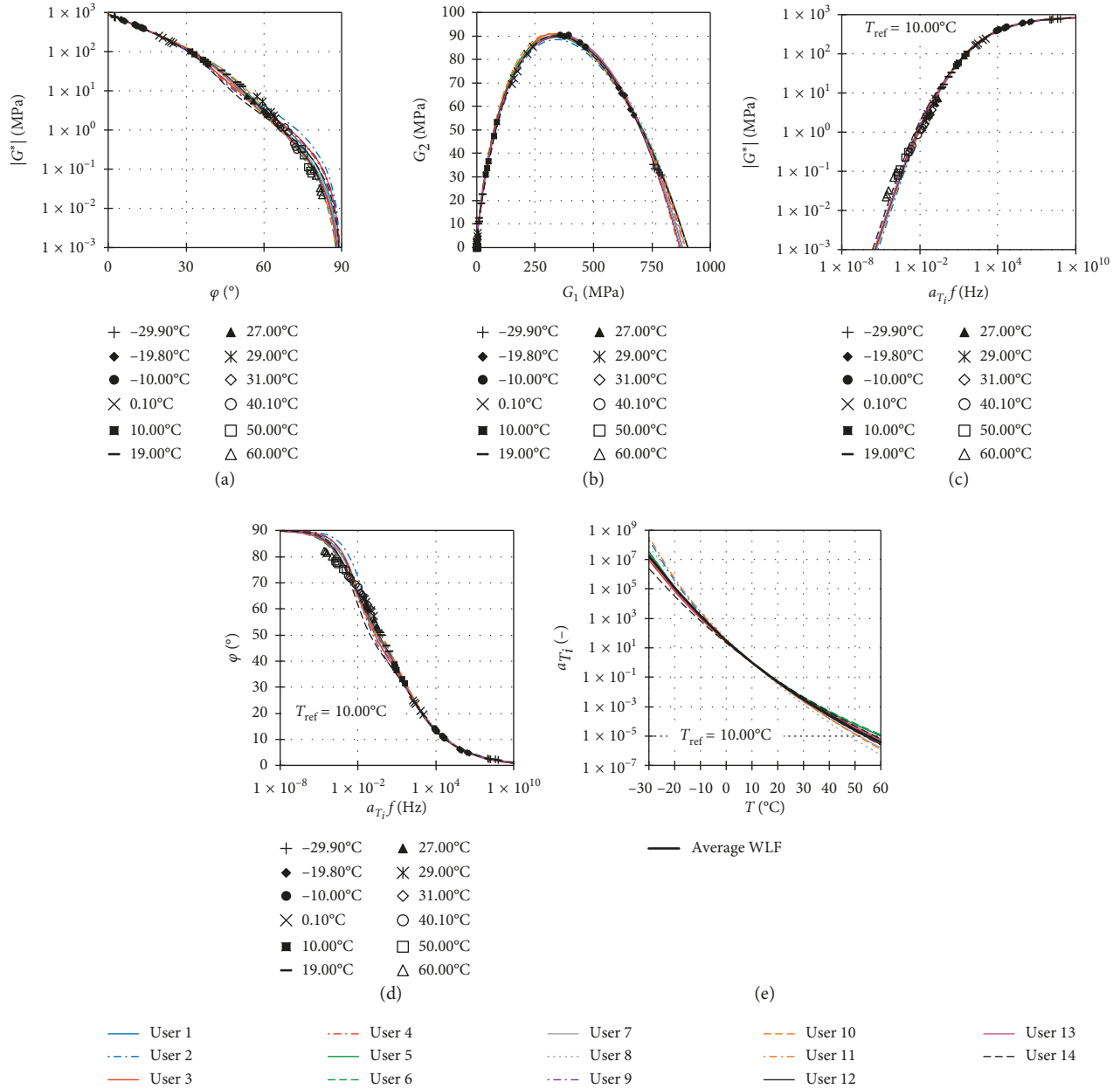


FIGURE 4: Results of 2S2P1D calibration panel for the bitumen: (a) Black space; (b) Cole-Cole plan; (c) master curves of  $|G^*|$  at  $10.00^\circ\text{C}$ ; (d) master curves of  $\varphi$  at  $10.00^\circ\text{C}$ ; (e) WLF equation used by users to obtain master curves in (c and d) and average WLF curve.

the global error parameters are affected by the high relative errors found at low frequency/high temperature. As already discussed, in this part of the frequency spectrum, the relative errors are not particularly important, given the low values of  $G_1$ ,  $G_2$ , and  $|G^*|$  (lower than 100 kPa).

Finally, overall error parameters were calculated for the whole calibration panel by averaging errors obtained for the 14 users, according to equations (22)–(29). The obtained parameters ( $\widehat{\delta}_{G_1}$ ,  $\widehat{\delta}_{G_2}$ ,  $\widehat{\delta}_{|G^*|}$  and  $\widehat{\delta}_\varphi$ ;  $\widehat{\Delta}_{G_1}$ ,  $\widehat{\Delta}_{G_2}$ ,  $\widehat{\Delta}_{|G^*|}$ , and  $\widehat{\Delta}_\varphi$  for absolute values of errors) and corresponding standard deviations ( $\widehat{\mu}_{G_1}$ ,  $\widehat{\mu}_{G_2}$ ,  $\widehat{\mu}_{|G^*|}$ , and  $\widehat{\mu}_\varphi$ ;  $\widehat{M}_{G_1}$ ,  $\widehat{M}_{G_2}$ ,  $\widehat{M}_{|G^*|}$ , and  $\widehat{M}_\varphi$  for absolute values of errors) are reported in Table 2.

$$\widehat{\delta}_{G_1} = \frac{\sum_i \sum_{a_{T_i} \omega} \delta_{G_{1i}}(a_{T_i} \omega)}{14N},$$

$$\widehat{\mu}_{G_1} = \sqrt{\frac{\sum_i \sum_{a_{T_i} \omega} [\delta_{G_{1i}}(a_{T_i} \omega) - \widehat{\delta}_{G_{1i}}]^2}{14N}}, \quad (22)$$

$$\widehat{\delta}_{G_2} = \frac{\sum_i \sum_{a_{T_i} \omega} \delta_{G_{2i}}(a_{T_i} \omega)}{14N},$$

$$\widehat{\mu}_{G_2} = \sqrt{\frac{\sum_i \sum_{a_{T_i} \omega} [\delta_{G_{2i}}(a_{T_i} \omega) - \widehat{\delta}_{G_{2i}}]^2}{14N}}, \quad (23)$$

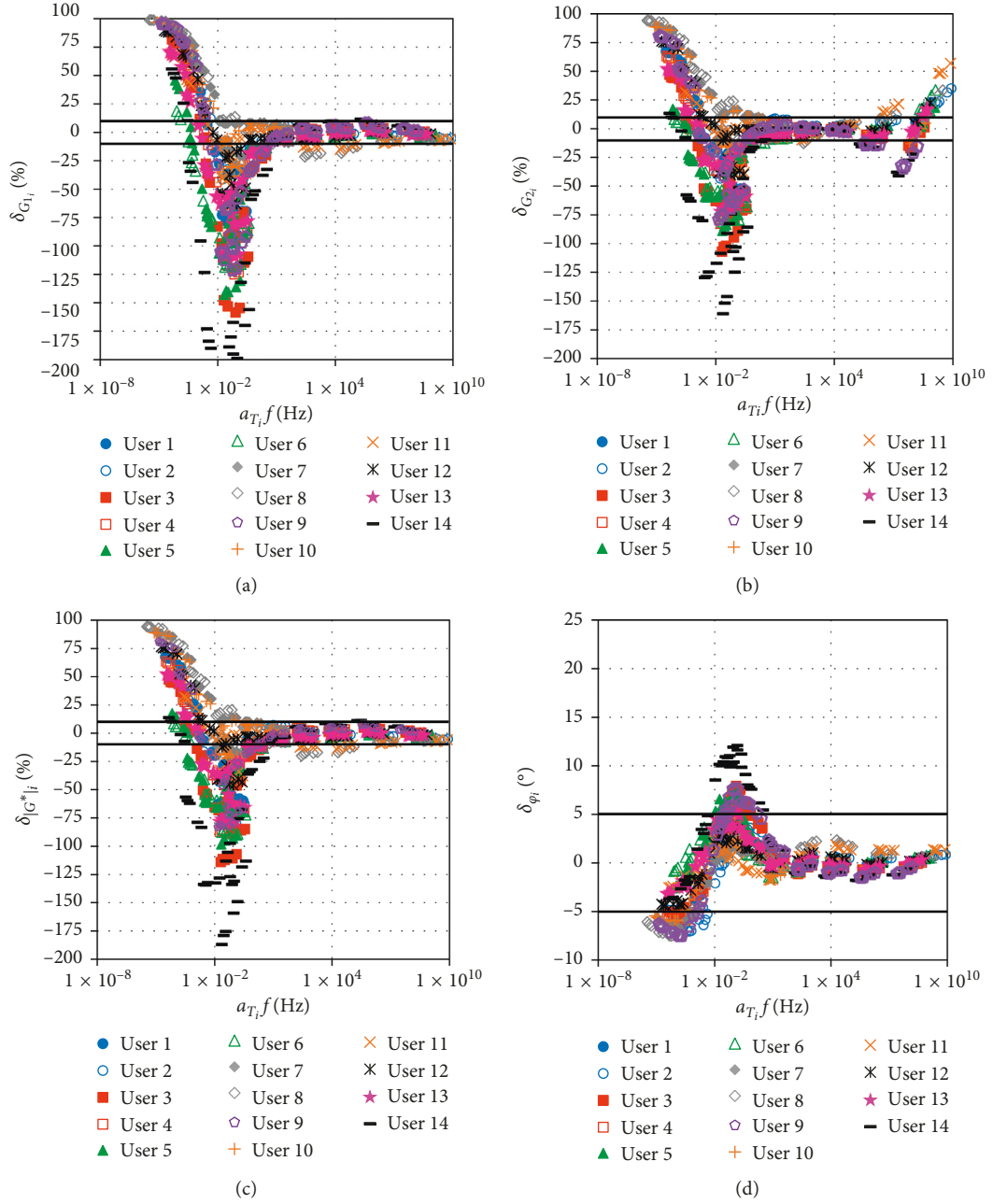


FIGURE 5: Errors between 2S2P1D simulations of all users and experimental data for the bitumen ( $T_{ref} = 10.00^\circ\text{C}$ ): relative errors for  $G_1$  (a),  $G_2$  (b), and  $|G^*|$  (c) and absolute error for  $\varphi$  (d). Bold lines represent 10% and  $5^\circ$  limits for, respectively, relative and absolute errors.

$$\widehat{\delta}_{|G^*|} = \frac{\sum_i \sum_{a_{T_i} \omega} \delta_{|G^*|_i}(a_{T_i} \omega)}{14N},$$

$$\widehat{\mu}_{|G^*|} = \sqrt{\frac{\sum_i \sum_{a_{T_i} \omega} [\delta_{|G^*|_i}(a_{T_i} \omega) - \widehat{\delta}_{|G^*|}]^2}{14N}}, \quad (24)$$

$$\widehat{\delta}_\varphi = \frac{\sum_i \sum_{a_{T_i} \omega} \delta_{\varphi_i}(a_{T_i} \omega)}{14N},$$

$$\widehat{\mu}_\varphi = \sqrt{\frac{\sum_i \sum_{a_{T_i} \omega} [\delta_{\varphi_i}(a_{T_i} \omega) - \widehat{\delta}_\varphi]^2}{14N}}, \quad (25)$$

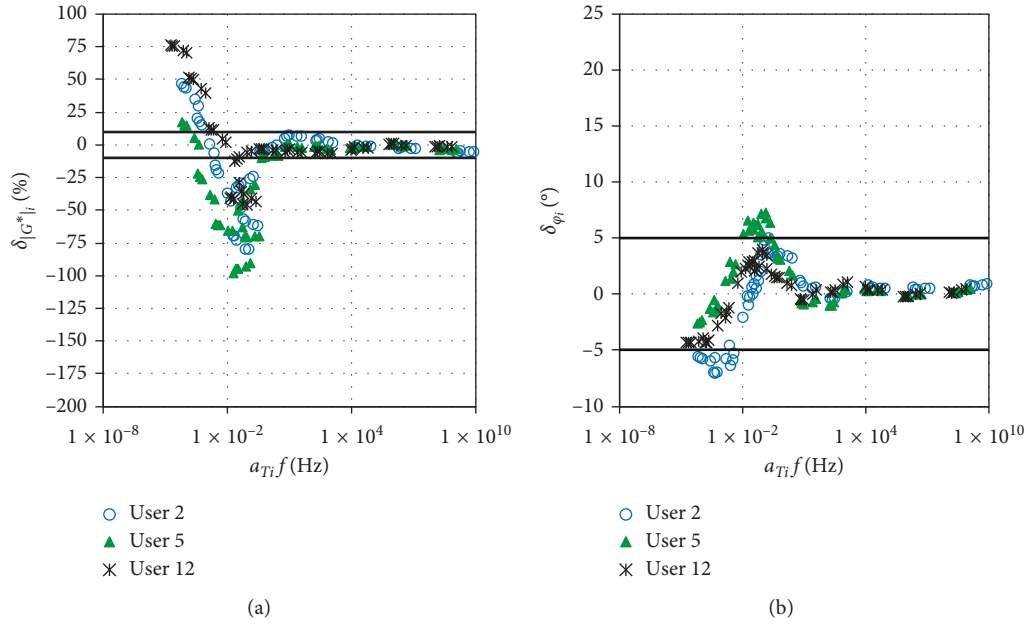


FIGURE 6: Errors between 2S2P1D simulations of the three most experienced users of the panel and experimental data for the bitumen ( $T_{ref} = 10.00^{\circ}\text{C}$ ): relative error  $|G^*|$  (a) and absolute errors for  $\varphi$  (b). Bold lines represent 10% and  $5^{\circ}$  limits for, respectively, relative and absolute errors.

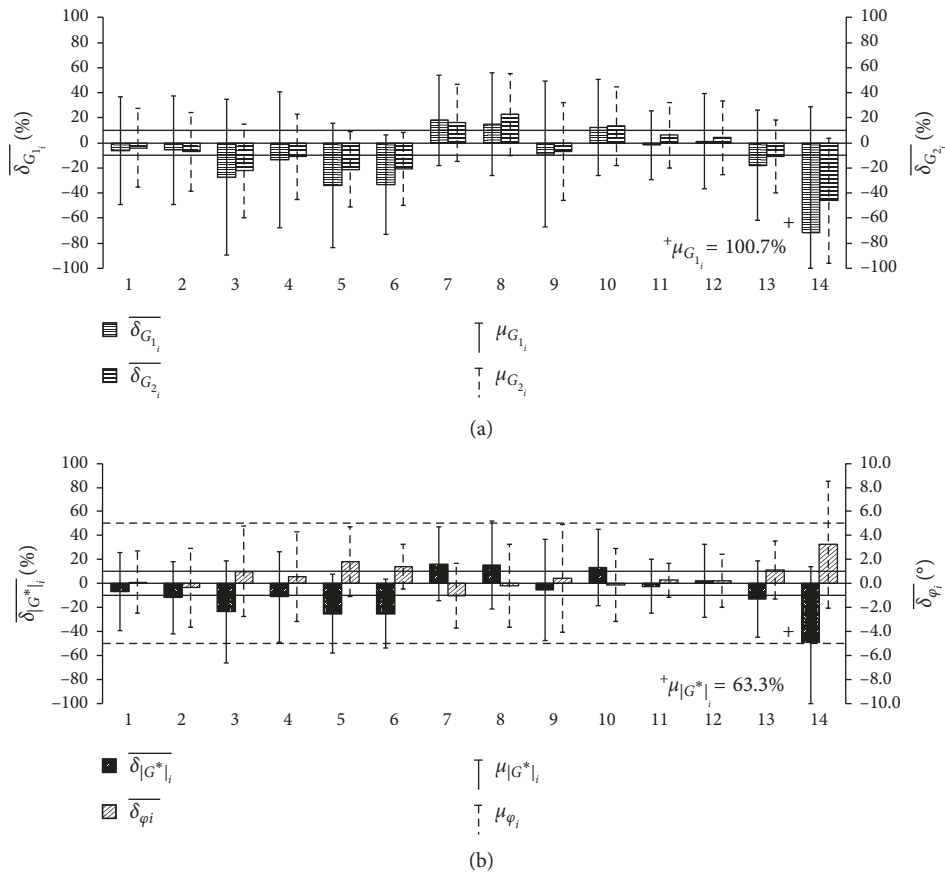


FIGURE 7: Histograms of global errors of 2S2P1D model fitting of all users for the bitumen (Figure 4), calculated according to equations (14)–(17): (a) relative errors for  $G_1$  and  $G_2$  ( $\overline{\delta_{G_{1i}}}$  and  $\overline{\delta_{G_{2i}}}$ , respectively); (b) relative error for  $|G^*|$  ( $\overline{\delta_{|G^*||_i}}$ ) and absolute error for  $\varphi$  ( $\overline{\delta_{\varphi_i}}$ ). Error bars are plotted according to standard deviations  $\mu_{G_{1i}}$ ,  $\mu_{G_{2i}}$ ,  $\mu_{|G^*||_i}$ , and  $\mu_{\varphi_i}$ .

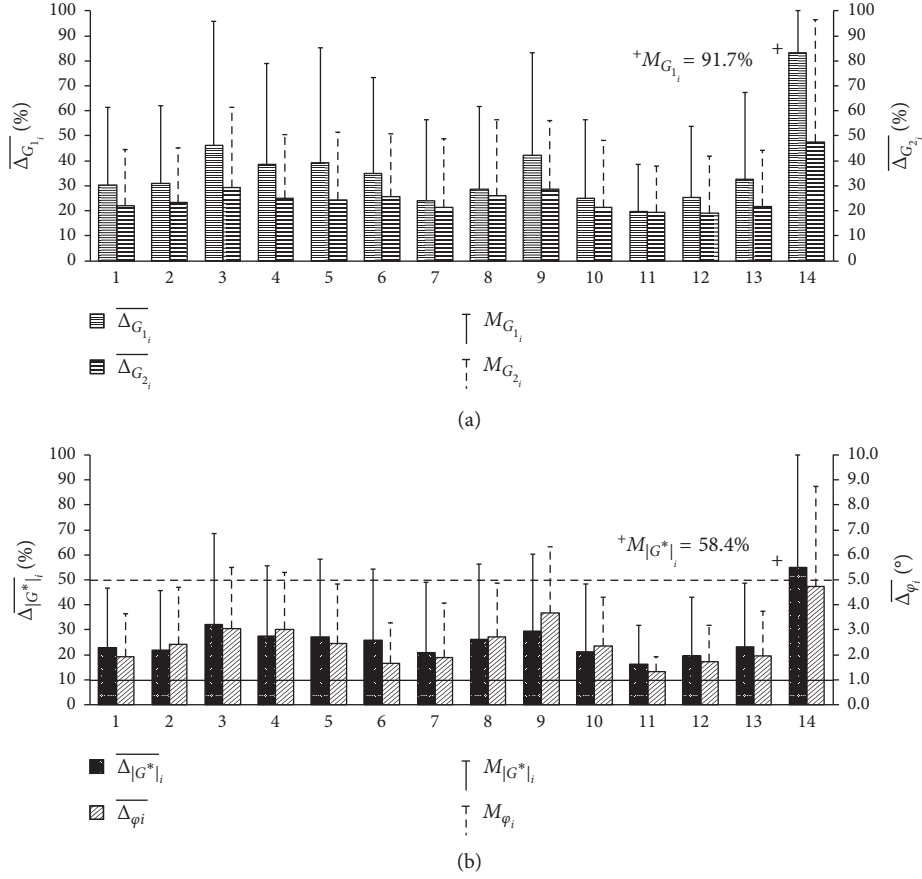


FIGURE 8: Histograms of global errors of 2S2P1D model fitting of all users for the bitumen (Figure 4), calculated according to equations (18)–(21): (a) relative errors for  $G_1$  and  $G_2$  ( $\overline{\Delta}_{G_1}$  and  $\overline{\Delta}_{G_2}$ , respectively); (b) relative error for  $|G^*|$  ( $\overline{\Delta}_{|G^*|}$ ) and absolute error for  $\varphi$  ( $\overline{\Delta}_{\varphi}$ ). Error bars are plotted according to standard deviations  $M_{G_1}$ ,  $M_{G_2}$ ,  $M_{|G^*|}$ , and  $M_{\varphi}$ .

TABLE 2: Overall global errors of 2S2P1D model fitting for a bitumen, calculated for the whole calibration panel according to equations (22)–(29).

$\widehat{\delta}_{G_1}$	$\widehat{\mu}_{G_1}$	$\widehat{\delta}_{G_2}$	$\widehat{\mu}_{G_2}$	$\widehat{\delta}_{ G^* }$	$\widehat{\mu}_{ G^* }$	$\widehat{\delta}_{\varphi}$	$\widehat{\mu}_{\varphi}$	$\widehat{\Delta}_{G_1}$	$\widehat{M}_{G_1}$	$\widehat{\Delta}_{G_2}$	$\widehat{M}_{G_2}$	$\widehat{\Delta}_{ G^* }$	$\widehat{M}_{ G^* }$	$\widehat{\Delta}_{\varphi}$	$\widehat{M}_{\varphi}$
-12.46%	56.13%	-6.27%	37.86%	-9.05%	40.49%	0.60°	3.40°	35.80%	44.99%	25.36%	28.80%	26.39%	32.02%	2.49°	2.39°

$$\widehat{\Delta}_{G_1} = \frac{\sum_i \sum_{a_{T_i} \omega} |\delta_{G_1}(a_{T_i} \omega)|}{14N},$$

$$\widehat{M}_{G_1} = \sqrt{\frac{\sum_i \sum_{a_{T_i} \omega} [|\delta_{G_1}(a_{T_i} \omega)| - \widehat{\Delta}_{G_1}]^2}{14N}}, \quad (26)$$

$$\widehat{\Delta}_{G_2} = \frac{\sum_i \sum_{a_{T_i} \omega} |\delta_{G_2}(a_{T_i} \omega)|}{14N},$$

$$\widehat{M}_{G_2} = \sqrt{\frac{\sum_i \sum_{a_{T_i} \omega} [|\delta_{G_2}(a_{T_i} \omega)| - \widehat{\Delta}_{G_2}]^2}{14N}}, \quad (27)$$

$$\widehat{\Delta}_{|G^*|} = \frac{\sum_i \sum_{a_{T_i} \omega} |\delta_{|G^*|}(a_{T_i} \omega)|}{14N},$$

$$\widehat{M}_{|G^*|} = \sqrt{\frac{\sum_i \sum_{a_{T_i} \omega} [|\delta_{|G^*|}(a_{T_i} \omega)| - \widehat{\Delta}_{|G^*|}]^2}{14N}}, \quad (28)$$

$$\widehat{\Delta}_{\varphi} = \frac{\sum_i \sum_{a_{T_i} \omega} |\delta_{\varphi}(a_{T_i} \omega)|}{14N},$$

$$\widehat{M}_{\varphi} = \sqrt{\frac{\sum_i \sum_{a_{T_i} \omega} [|\delta_{\varphi}(a_{T_i} \omega)| - \widehat{\Delta}_{\varphi}]^2}{14N}}. \quad (29)$$

TABLE 3: WLF and 2S2P1D constants obtained for the bituminous mixture by all the users of the calibration panel ( $T_{\text{ref}} = 9.53^\circ\text{C}$ ).

	$C_1$ (-)	$C_2$ ( $^\circ\text{C}$ )	$E_{00}$ (MPa)	$E_0$ (MPa)	$\delta$ (-)	$k$ (-)	$h$ (-)	$\beta$ (-)	$\tau$ (s)	$\log \tau$ (-)
User 1	23.42	154.38	26	40700	2.26	0.189	0.593	180	$2.10 \times 10^{-1}$	-0.68
User 2	26.20	170.02	20	40900	2.00	0.185	0.545	400	$1.00 \times 10^{-1}$	-1.00
User 3	30.63	203.51	20	41300	1.95	0.178	0.563	200	$9.00 \times 10^{-2}$	-1.05
User 4	23.93	158.02	20	40850	2.13	0.185	0.565	230	$1.00 \times 10^{-1}$	-1.00
User 5	22.75	156.29	13	40500	2.30	0.195	0.600	800	$1.50 \times 10^{-1}$	-0.82
User 6	19.80	135.00	25	40500	2.10	0.190	0.550	180	$9.50 \times 10^{-2}$	-1.02
User 7	31.07	199.78	18	40800	2.15	0.188	0.560	230	$9.00 \times 10^{-2}$	-1.05
User 8	30.86	196.09	14	41000	2.10	0.179	0.610	200	$1.40 \times 10^{-1}$	-0.85
User 9	35.17	238.76	23	41000	2.00	0.180	0.550	180	$9.00 \times 10^{-2}$	-1.05
User 10	37.95	238.01	23	41000	2.15	0.185	0.580	230	$2.50 \times 10^{-1}$	-0.60
User 11	25.41	170.77	18	40850	2.15	0.189	0.595	250	$1.40 \times 10^{-1}$	-0.85
User 12	25.67	172.20	19	40500	2.30	0.193	0.593	240	$1.30 \times 10^{-1}$	-0.89
User 13	20.28	134.42	15	40700	2.30	0.190	0.620	1000000	$1.70 \times 10^{-1}$	-0.77
User 14	27.89	189.50	16	41000	2.28	0.188	0.595	320	$1.10 \times 10^{-1}$	-0.96
Mean	27.22	179.77	19	40829	2.16	0.187	0.580	71689 <sup>a</sup>	$1.33 \times 10^{-1}$	-0.90
St. dev.	5.36	33.00	4	233	0.12	0.005	0.024	267186 <sup>b</sup>	$4.89 \times 10^{-2}$	0.14
COV	19.70%	18.36%	20.68%	0.57%	5.56%	2.71%	4.18%	372.7% <sup>c</sup>	36.70%	-15.96%

Note. Coefficient of variation (COV): standard deviation/mean. <sup>a</sup>280, if the unusually high value of  $\beta$  of user 13 is ignored. <sup>b</sup>168, if the unusually high value of  $\beta$  of user 13 is ignored. <sup>c</sup>60.0%, if the unusually high value of  $\beta$  of user 13 is ignored.

4.2. *2S2P1D Fitting for a Bituminous Mixture.* Table 3 reports values of WLF and 2S2P1D constants obtained by all users of the calibration panel for the bituminous mixture. Figure 9 shows a comparison of the simulations of the LVE behaviour of the mixture obtained by all the users and the experimental data points. In particular, Figures 9(a) and 9(b) show, respectively, Black and Cole-Cole spaces, Figures 9(c) and 9(d) show master curves of, respectively,  $|E^*|$  and  $\varphi$ , and Figure 9(e) shows the various WLF curves obtained by the users, together with the average WLF curve, according to the constants shown in Table 3. As for bitumen in Section 4.1, experimental points shown in master curves of Figures 9(c) and 9(d) are shifted using shift factors calculated with the mentioned average WLF curve, in order to have a graphical representation.

A very low value (0.57%) is found for the COV of  $E_{00}$ . Also, similarly to what was found for the bitumen, COV of constants  $k$  and  $h$  is quite low (lower than 5%). If the unusually high value of  $\beta$  chosen by user 13 is neglected, the COV for this constant is equal to 60.0%, of the same order of magnitude of the COV for the same constant found for the bitumen. Concerning this point, it should be highlighted that the value of  $\beta$  is directly related to the viscosity of the linear dashpot of the analogical model. For this reason, its variations should be considered in logarithmic scale; that is, a variation of this constant from 100 to 200 has a more important effect on the LVE simulation than a variation from 900 to 1000. In the case of the 2S2P1D fitting carried out by user 13, it can be easily verified that a relatively small variation occurs to the corresponding simulation if the value of  $\beta$  is fixed to 1000 instead of 1000000.

Overall, one important conclusion that can be drawn from the results of the calibration panel is that the variability (expressed by the COV) of constants  $G_{00}$  (for the bitumen),  $E_{00}$  and  $E_0$  (for the mixture),  $\delta$ ,  $k$ ,  $h$ , and  $\log \tau$  (for both) is approximately equal or lower than 20%.

2S2P1D simulations of all users satisfactorily approximate experimental points. At very low frequency/high temperature (less than  $10^{-3}$  Hz), a negligible underestimation of  $|E^*|$  and  $\varphi$  is observed for all users. However, these differences are negligible in absolute value (less than 20 MPa for  $|E^*|$ ) and concern only very few experimental points of the isotherms obtained at  $38.83^\circ\text{C}$ . As in the case of the bitumen, satisfactory fitting of experimental data is observed over the whole spans of equivalent frequencies (between  $10^{-6}$  and  $10^{10}$  Hz at the reference temperature of  $9.5^\circ\text{C}$ ) and  $|E^*|$  (between 10 and 40000 MPa).

Similarly to what was done for the bitumen, relative errors  $\delta_{E_{1i}}$ ,  $\delta_{E_{2i}}$ , and  $\delta_{|E^*|_i}$  (respectively, for  $E_1$ ,  $E_2$ , and  $|E^*|$ ) and absolute error  $\delta_{\varphi_i}$  (for  $\varphi$ ) were calculated for each equivalent frequency  $a_{T_i}\omega$  (55 data points) according to the following equations:

$$\delta_{E_{1i}}(a_{T_i}\omega) = \frac{E_{1,\text{exp}}(a_{T_i}\omega) - E_{1,2S2P1D_i}(a_{T_i}\omega)}{E_{1,\text{exp}}(a_{T_i}\omega)}, \quad (30)$$

$$\delta_{E_{2i}}(a_{T_i}\omega) = \frac{E_{2,\text{exp}}(a_{T_i}\omega) - E_{2,2S2P1D_i}(a_{T_i}\omega)}{E_{2,\text{exp}}(a_{T_i}\omega)}, \quad (31)$$

$$\delta_{|E^*|_i}(a_{T_i}\omega) = \frac{|E_{\text{exp}}^*(a_{T_i}\omega) - |E_{2S2P1D_i}^*(a_{T_i}\omega)|}{|E_{\text{exp}}^*(a_{T_i}\omega)|}, \quad (32)$$

$$\delta_{\varphi_i}(a_{T_i}\omega) = \varphi_{\text{exp}}(a_{T_i}\omega) - \varphi_{2S2P1D_i}(a_{T_i}\omega), \quad (33)$$

where the variables are listed as follows:  $E_{1,\text{exp}}(a_{T_i}\omega)$ ,  $E_{2,\text{exp}}(a_{T_i}\omega)$ ,  $|E_{\text{exp}}^*(a_{T_i}\omega)|$ , and  $\varphi_{\text{exp}}(a_{T_i}\omega)$  are experimental values of, respectively,  $E_1$ ,  $E_2$ ,  $|E^*|$ , and  $\varphi$  at the equivalent frequency  $a_{T_i}\omega$ ;  $E_{1,2S2P1D_i}(a_{T_i}\omega)$ ,  $E_{2,2S2P1D_i}(a_{T_i}\omega)$ ,  $|E_{2S2P1D_i}^*(a_{T_i}\omega)|$ , and  $\varphi_{2S2P1D_i}(a_{T_i}\omega)$  are values of, respectively,  $E_1$ ,  $E_2$ ,  $|E^*|$ , and  $\varphi$  at the equivalent frequency  $a_{T_i}\omega$ , calculated with the 2S2P1D according to the constants of the  $i$ -th user reported in Table 1.

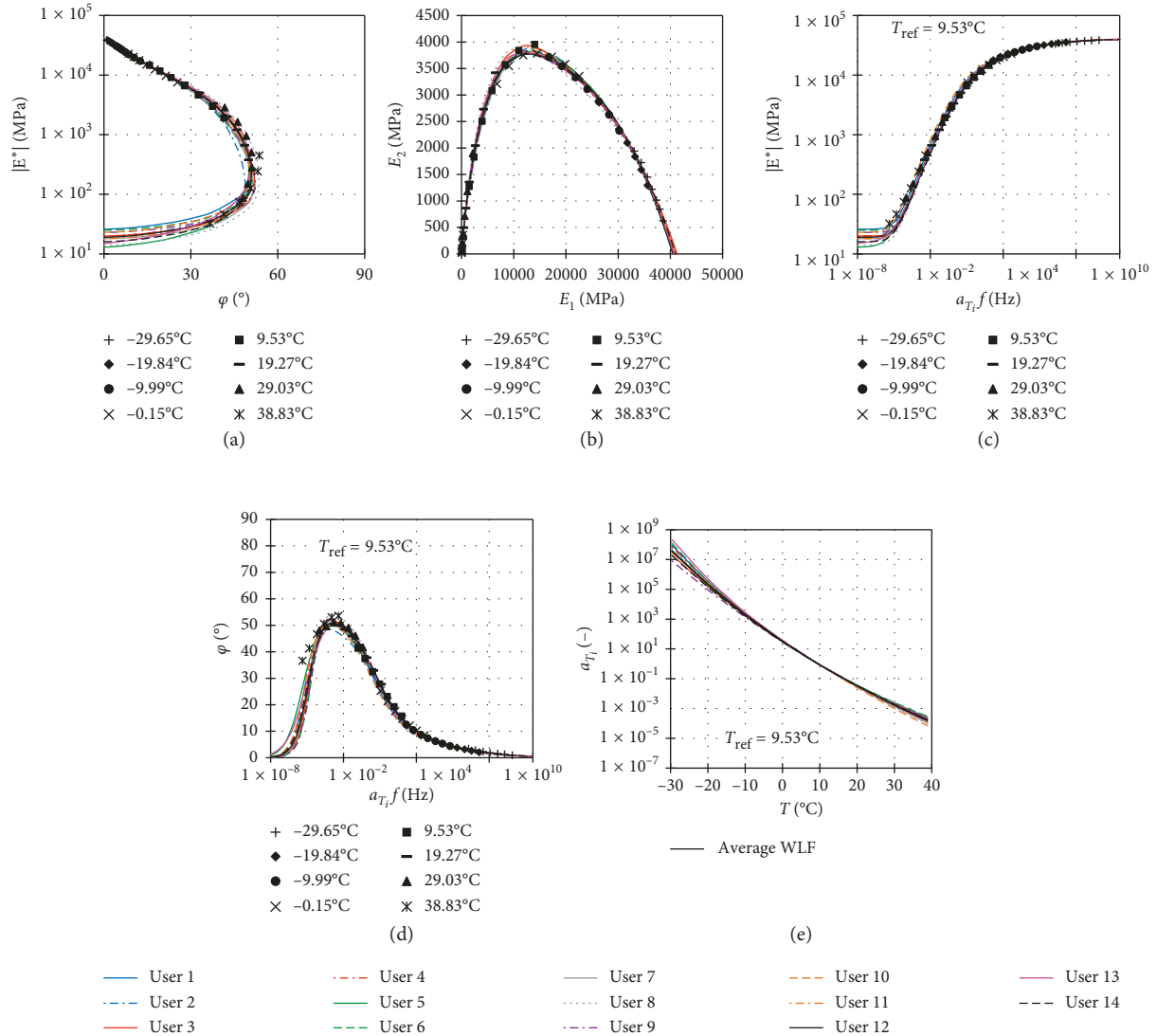


FIGURE 9: Results of 2S2P1D calibration panel for a mixture: (a) Cole-Cole plan; (b) Black space; (c) master curves of  $|G^*|$  at  $9.53^\circ\text{C}$ ; (d) master curves of  $\varphi$  at  $9.53^\circ\text{C}$ ; (e) WLF equation used by users to obtain master curves in (c) and (d) and average WLF curve.

Master curves of  $\delta_{E_{1i}}$ ,  $\delta_{E_{2i}}$ ,  $\delta_{|E^*|_i}$ , and  $\delta_{\varphi_i}$  are shown in Figure 10 (10% and  $5^\circ$  limits for, respectively, relative and absolute errors are represented by bold lines). As in the case of the bitumen, errors  $\delta_{E_{1i}}$ ,  $\delta_{E_{2i}}$ ,  $\delta_{|E^*|_i}$ , and  $\delta_{\varphi_i}$  were calculated for each  $i$ -th user at equivalent frequencies obtained with shift factors  $a_{T_i}$  calculated according to his/her WLF constants shown in Table 3. Hence, master curves corresponding to different users have slightly different total ranges of equivalent frequencies. Differences greater than  $5^\circ$  between experimental and simulated  $\varphi$  (parameter  $\delta_{\varphi_i}$  in Figure 10(d)) are observed only for the last two points of the isotherm at  $38.83^\circ\text{C}$ . Concerning errors in the simulation of  $E_1$ ,  $E_2$ , and  $|E^*|$ , for the majority of users, values greater than 10% of parameters  $\delta_{E_{1i}}$ ,  $\delta_{E_{2i}}$ , and  $\delta_{|E^*|_i}$  are observed only for equivalent frequencies lower than approximately  $10^{-2}$  Hz. Only for two users, values of 2S2P1D model simulations are significantly higher than experimental data for frequencies between  $10^{-3}$

and  $10^2$  Hz. The important relative errors observed for  $E_2$  at frequencies higher than  $10^5$  Hz can be neglected because of the very low values of  $E_2$  in this frequency range (lower than 2000 MPa) with respect to  $|E^*|$  (higher than 30000 MPa). Similarly to what was done for the bitumen (Section 4.1), the master curves (at  $9.5^\circ\text{C}$ ) of  $\delta_{|E^*|_i}$  and  $\delta_{\varphi_i}$  obtained for the mixture by the three most experienced users (2, 5, and 12) are plotted in Figure 11. Excellent correspondences between simulations and experimental data are observed, confirming the ability of the model to simulate LVE behaviour of mixtures.

Average values ( $\overline{\delta_{E_{1i}}}$ ,  $\overline{\delta_{E_{2i}}}$ ,  $\overline{\delta_{|E^*|_i}}$ , and  $\overline{\delta_{\varphi_i}}$ ) and standard deviations ( $\mu_{E_{1i}}$ ,  $\mu_{E_{2i}}$ ,  $\mu_{|E^*|_i}$ , and  $\mu_{\varphi_i}$ ) of relative and absolute errors  $\delta_{E_{1i}}$ ,  $\delta_{E_{2i}}$ ,  $\delta_{|E^*|_i}$ , and  $\delta_{\varphi_i}$  of each user at the  $N$  considered equivalent frequencies  $a_{T_i}$  ( $N = 55$ ) were calculated according to equations (34)–(37) and plotted in histograms of Figure 12. Error bars are plotted according to standard deviation values.

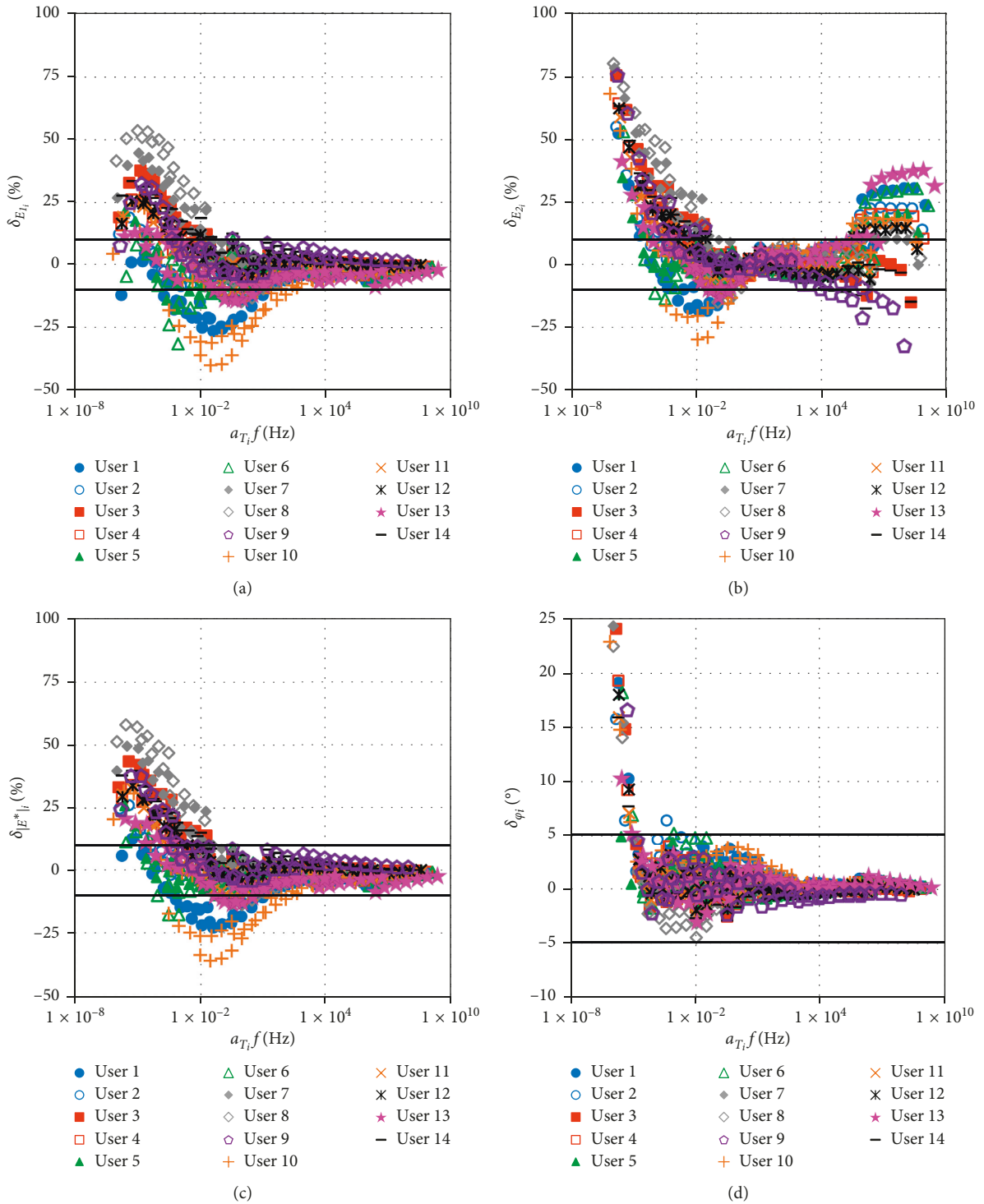


FIGURE 10: Errors between 2S2PID simulations of all users and experimental data for the bituminous mixture ( $T_{ref} = 9.53^{\circ}\text{C}$ ): relative errors for  $E_1$  (a),  $E_2$  (b), and  $|E^*|$  (c) and absolute error for  $\varphi$  (d). Bold lines represent 10% and  $5^{\circ}$  limits for, respectively, relative and absolute errors.

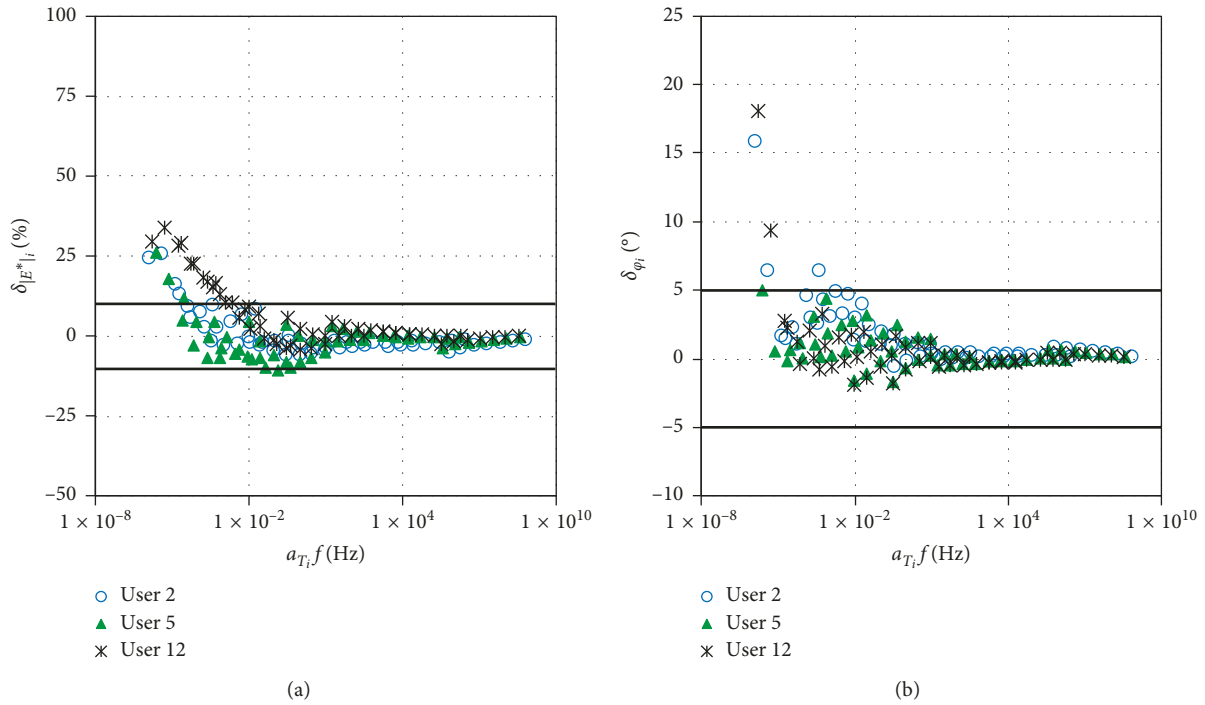


FIGURE 11: Errors between 2S2P1D simulations of the three most experienced users of the panel and experimental data for the bituminous mixture ( $T_{ref} = 9.53^{\circ}C$ ): relative error for  $|E^*|$  (a) and absolute error for  $\varphi$  (b). Bold lines represent 10% and  $5^{\circ}$  limits for, respectively, relative and absolute errors.

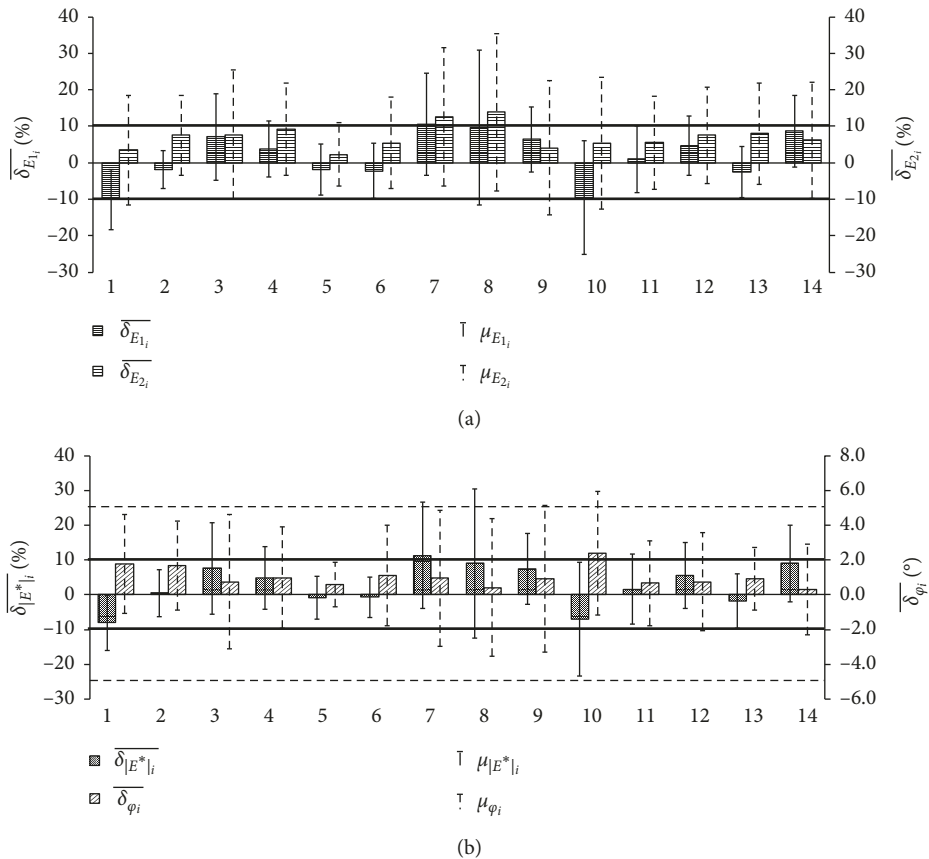


FIGURE 12: Histograms of global errors of 2S2P1D model fitting of all users for the bituminous mixture (Figure 9), calculated according to equations (34)–(37): (a) relative errors for  $E_1$  and  $E_2$  ( $\overline{\delta_{E_{1i}}}$  and  $\overline{\delta_{E_{2i}}}$ , respectively); (b) relative error for  $|E^*|$  ( $\overline{\delta_{|E^*|_i}}$ ) and absolute error for  $\varphi$  ( $\overline{\delta_{\varphi_i}}$ ). Error bars are plotted according to standard deviations  $\mu_{E_{1i}}$ ,  $\mu_{E_{2i}}$ ,  $\mu_{|E^*|_i}$ , and  $\mu_{\varphi_i}$ .

$$\begin{aligned}\overline{\delta_{E_{1i}}} &= \frac{\sum_{a_{T_i}\omega} \delta_{E_{1i}}(a_{T_i}\omega)}{N}, \\ \mu_{E_{1i}} &= \sqrt{\frac{\sum_{a_{T_i}\omega} [\delta_{E_{1i}}(a_{T_i}\omega) - \overline{\delta_{E_{1i}}}]^2}{N}},\end{aligned}\quad (34)$$

$$\begin{aligned}\overline{\delta_{E_{2i}}} &= \frac{\sum_{a_{T_i}\omega} \delta_{E_{2i}}(a_{T_i}\omega)}{N}, \\ \mu_{E_{2i}} &= \sqrt{\frac{\sum_{a_{T_i}\omega} [\delta_{E_{2i}}(a_{T_i}\omega) - \overline{\delta_{E_{2i}}}]^2}{N}},\end{aligned}\quad (35)$$

$$\begin{aligned}\overline{\delta_{|E^*|_i}} &= \frac{\sum_{a_{T_i}\omega} \delta_{|E^*|_i}(a_{T_i}\omega)}{N}, \\ \mu_{|E^*|_i} &= \sqrt{\frac{\sum_{a_{T_i}\omega} [\delta_{|E^*|_i}(a_{T_i}\omega) - \overline{\delta_{|E^*|_i}}]^2}{N}},\end{aligned}\quad (36)$$

$$\begin{aligned}\overline{\delta_{\varphi_i}} &= \frac{\sum_{a_{T_i}\omega} \delta_{\varphi_i}(a_{T_i}\omega)}{N}, \\ \mu_{\varphi_i} &= \sqrt{\frac{\sum_{a_{T_i}\omega} [\delta_{\varphi_i}(a_{T_i}\omega) - \overline{\delta_{\varphi_i}}]^2}{N}}.\end{aligned}\quad (37)$$

Equations (38)–(41) were used to calculate average values ( $\overline{\Delta_{E_{1i}}}$ ,  $\overline{\Delta_{E_{2i}}}$ ,  $\overline{\Delta_{|E^*|_i}}$ , and  $\overline{\Delta_{\varphi_i}}$ ) and standard deviations ( $M_{E_{1i}}$ ,  $M_{E_{2i}}$ ,  $M_{|E^*|_i}$ , and  $M_{\varphi_i}$ ) of absolute values of relative and absolute errors  $\delta_{E_{1i}}$ ,  $\delta_{E_{2i}}$ ,  $\delta_{|E^*|_i}$ , and  $\delta_{\varphi_i}$  of each user at the  $N$  considered equivalent frequencies  $a_{T_i}$  ( $N=55$ ), plotted in histograms of Figure 13. As shown in Figure 12, error bars are plotted according to standard deviation values.

$$\begin{aligned}\overline{\Delta_{E_{1i}}} &= \frac{\sum_{a_{T_i}\omega} |\delta_{E_{1i}}(a_{T_i}\omega)|}{N}, \\ M_{E_{1i}} &= \sqrt{\frac{\sum_{a_{T_i}\omega} [|\delta_{E_{1i}}(a_{T_i}\omega)| - \overline{\Delta_{E_{1i}}}]^2}{N}},\end{aligned}\quad (38)$$

$$\begin{aligned}\overline{\Delta_{E_{2i}}} &= \frac{\sum_{a_{T_i}\omega} |\delta_{E_{2i}}(a_{T_i}\omega)|}{N}, \\ M_{E_{2i}} &= \sqrt{\frac{\sum_{a_{T_i}\omega} [|\delta_{E_{2i}}(a_{T_i}\omega)| - \overline{\Delta_{E_{2i}}}]^2}{N}},\end{aligned}\quad (39)$$

$$\begin{aligned}\overline{\Delta_{|E^*|_i}} &= \frac{\sum_{a_{T_i}\omega} |\delta_{|E^*|_i}(a_{T_i}\omega)|}{N}, \\ M_{|E^*|_i} &= \sqrt{\frac{\sum_{a_{T_i}\omega} [|\delta_{|E^*|_i}(a_{T_i}\omega)| - \overline{\Delta_{|E^*|_i}}]^2}{N}},\end{aligned}\quad (40)$$

$$\begin{aligned}\overline{\Delta_{\varphi_i}} &= \frac{\sum_{a_{T_i}\omega} |\delta_{\varphi_i}(a_{T_i}\omega)|}{N}, \\ M_{\varphi_i} &= \sqrt{\frac{\sum_{a_{T_i}\omega} [|\delta_{\varphi_i}(a_{T_i}\omega)| - \overline{\Delta_{\varphi_i}}]^2}{N}}.\end{aligned}\quad (41)$$

Global error parameters  $\overline{\delta_{|E^*|_i}}$  and  $\overline{\Delta_{|E^*|_i}}$  (for  $|E^*|$ ) are generally lower than 10% and parameters  $\overline{\delta_{\varphi_i}}$  and  $\overline{\Delta_{\varphi_i}}$  (for  $\varphi$ ) are generally lower than 5° (even considering the corresponding standard deviations), except for the same few users. These estimates show that very satisfactory simulations were obtained by the vast majority of the users. This observation is all the more relevant because the error parameters were calculated by arithmetically averaging all the 55 data points over the whole frequency range available.

Overall error parameters were calculated for the whole calibration panel by averaging errors obtained for the 14 users, according to equations (42)–(49). The obtained parameters ( $\widehat{\delta_{E_1}}$ ,  $\widehat{\delta_{E_2}}$ ,  $\widehat{\delta_{|E^*|}}$ , and  $\widehat{\delta_{\varphi}}$ ;  $\widehat{\Delta_{E_1}}$ ,  $\widehat{\Delta_{E_2}}$ ,  $\widehat{\Delta_{|E^*|}}$ , and  $\widehat{\Delta_{\varphi}}$  for absolute values of errors) and corresponding standard deviations ( $\widehat{\mu_{E_1}}$ ,  $\widehat{\mu_{E_2}}$ ,  $\widehat{\mu_{|E^*|}}$ , and  $\widehat{\mu_{\varphi}}$ ;  $\widehat{M_{E_1}}$ ,  $\widehat{M_{E_2}}$ ,  $\widehat{M_{|E^*|}}$ , and  $\widehat{M_{\varphi}}$  for absolute values of errors) are reported in Table 4.

$$\begin{aligned}\widehat{\delta_{E_1}} &= \frac{\sum_i \sum_{a_{T_i}\omega} \delta_{E_{1i}}(a_{T_i}\omega)}{14N}, \\ \widehat{\mu_{E_1}} &= \sqrt{\frac{\sum_i \sum_{a_{T_i}\omega} [\delta_{E_{1i}}(a_{T_i}\omega) - \widehat{\delta_{E_1}}]^2}{14N}},\end{aligned}\quad (42)$$

$$\begin{aligned}\widehat{\delta_{E_2}} &= \frac{\sum_i \sum_{a_{T_i}\omega} \delta_{E_{2i}}(a_{T_i}\omega)}{14N}, \\ \widehat{\mu_{E_2}} &= \sqrt{\frac{\sum_i \sum_{a_{T_i}\omega} [\delta_{E_{2i}}(a_{T_i}\omega) - \widehat{\delta_{E_2}}]^2}{14N}},\end{aligned}\quad (43)$$

$$\begin{aligned}\widehat{\delta_{|E^*|}} &= \frac{\sum_i \sum_{a_{T_i}\omega} \delta_{|E^*|_i}(a_{T_i}\omega)}{14N}, \\ \widehat{\mu_{|E^*|}} &= \sqrt{\frac{\sum_i \sum_{a_{T_i}\omega} [\delta_{|E^*|_i}(a_{T_i}\omega) - \widehat{\delta_{|E^*|}}]^2}{14N}},\end{aligned}\quad (44)$$

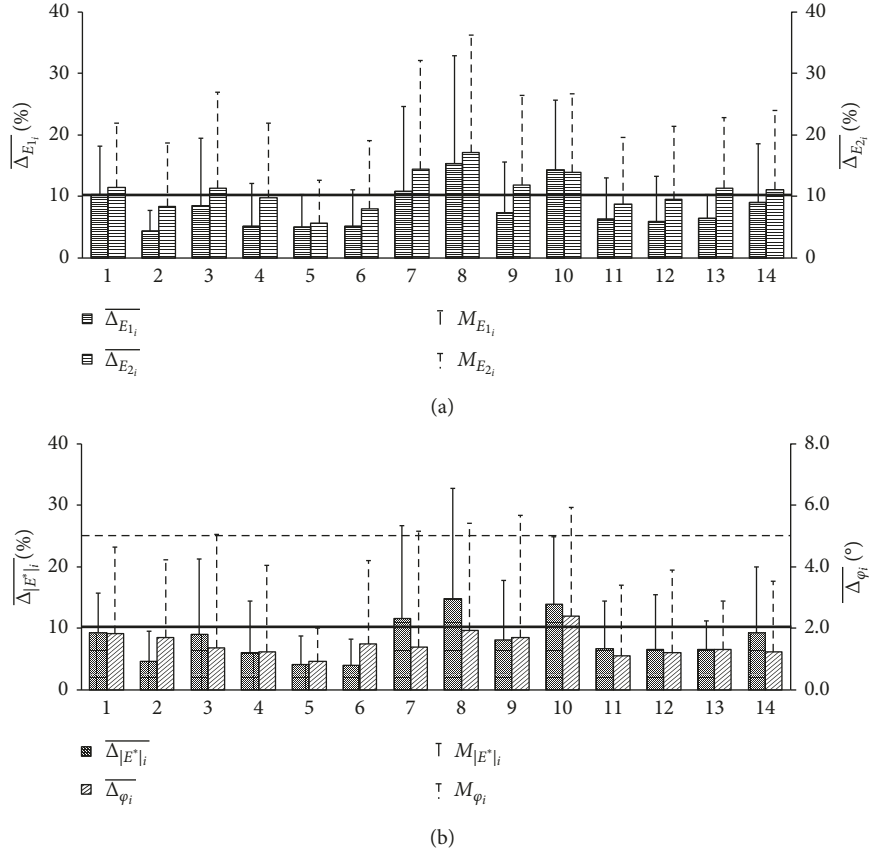


FIGURE 13: Histograms of global errors of 2S2P1D model fitting of all users for the bituminous mixture (Figure 9), calculated according to equations (38)–(41): (a) relative errors for  $E_1$  and  $E_2$  ( $\overline{\Delta_{E_{1i}}}$  and  $\overline{\Delta_{E_{2i}}}$ , respectively); (b) relative error for  $|E^*|$  ( $\overline{\Delta_{|E^*|_i}}$ ) and absolute error for  $\varphi$  ( $\overline{\Delta_{\varphi_i}}$ ). Error bars are plotted according to standard deviations  $M_{E_{1i}}$ ,  $M_{E_{2i}}$ ,  $M_{|E^*|_i}$ , and  $M_{\varphi_i}$ .

TABLE 4: Global errors of 2S2P1D model fitting for a bituminous mixture, calculated for the whole calibration panel according to equations (42)–(49).

$\widehat{\delta}_{E_1}$	$\widehat{\mu}_{E_1}$	$\widehat{\delta}_{E_2}$	$\widehat{\mu}_{E_2}$	$\widehat{\delta}_{ E^* }$	$\widehat{\mu}_{ E^* }$	$\widehat{\delta}_{\varphi}$	$\widehat{\mu}_{\varphi}$	$\widehat{\Delta}_{E_1}$	$\widehat{M}_{E_1}$	$\widehat{\Delta}_{E_2}$	$\widehat{M}_{E_2}$	$\widehat{\Delta}_{ E^* }$	$\widehat{M}_{ E^* }$	$\widehat{\Delta}_{\varphi}$	$\widehat{M}_{\varphi}$
1.70%	12.65%	7.06%	15.71%	2.77%	12.94%	1.02°	3.14°	8.10%	9.86%	10.86%	13.38%	8.15%	10.42%	1.48°	2.95°

$$\widehat{\delta}_{\varphi} = \frac{\sum_i \sum_{a_{T_i} \omega} \delta_{\varphi_i}(a_{T_i} \omega)}{14N},$$

$$\widehat{\mu}_{\varphi} = \sqrt{\frac{\sum_i \sum_{a_{T_i} \omega} [\delta_{\varphi_i}(a_{T_i} \omega) - \widehat{\delta}_{\varphi_i}]^2}{14N}}, \quad (45)$$

$$\widehat{\Delta}_{E_1} = \frac{\sum_i \sum_{a_{T_i} \omega} |\delta_{E_{1i}}(a_{T_i} \omega)|}{14N},$$

$$\widehat{M}_{E_1} = \sqrt{\frac{\sum_i \sum_{a_{T_i} \omega} [|\delta_{E_{1i}}(a_{T_i} \omega)| - \widehat{\Delta}_{E_{1i}}]^2}{14N}}, \quad (46)$$

$$\widehat{\Delta}_{E_2} = \frac{\sum_i \sum_{a_{T_i} \omega} |\delta_{E_{2i}}(a_{T_i} \omega)|}{14N},$$

$$\widehat{M}_{E_2} = \sqrt{\frac{\sum_i \sum_{a_{T_i} \omega} [|\delta_{E_{2i}}(a_{T_i} \omega)| - \widehat{\Delta}_{E_{2i}}]^2}{14N}}, \quad (47)$$

$$\widehat{\Delta}_{|E^*|} = \frac{\sum_i \sum_{a_{T_i} \omega} |\delta_{|E^*|_i}(a_{T_i} \omega)|}{14N},$$

$$\widehat{M}_{|E^*|} = \sqrt{\frac{\sum_i \sum_{a_{T_i} \omega} [|\delta_{|E^*|_i}(a_{T_i} \omega)| - \widehat{\Delta}_{|E^*|_i}]^2}{14N}}, \quad (48)$$

$$\widehat{\Delta}_{\varphi} = \frac{\sum_i \sum_{a_{T_i}, \omega} |\delta_{\varphi_i}(a_{T_i}, \omega)|}{14N},$$

$$\widehat{M}_{\varphi} = \sqrt{\frac{\sum_i \sum_{a_{T_i}, \omega} [|\delta_{\varphi_i}(a_{T_i}, \omega)| - \widehat{\Delta}_{\varphi_i}]^2}{14N}}. \quad (49)$$

## 5. Conclusions

Complex modulus test results obtained for a straight-run bitumen and a bituminous mixture (respectively,  $G^*$  and  $E^*$ ) were simulated using 2S2P1D model by 14 users with different levels of expertise of the model. All users worked independently and for the same time duration of one hour to fit the model on both sets of data, providing their own values for all the model constants (including WLF constants at the imposed reference temperatures, 10°C for the bitumen and 9.5°C for the mixture). The following conclusions can be drawn from the analysis of relative and absolute differences between experimental data of the LVE behaviour of both materials and 2S2P1D simulations obtained by all the users:

- (i) 2S2P1D simulations of LVE behaviour of both the bitumen and the bituminous mixture obtained by the users of the calibration panel satisfactorily approximate experimental data of complex modulus ( $G^*$  for the bitumen and  $E^*$  for the mixture) over the whole range of frequencies and temperatures. The accuracy of the model to fit experimental data is all the more evident if the great spans of equivalent frequencies (between  $10^{-6}$  and  $10^{10}$  Hz at the reference temperatures of 10°C for the bitumen and 9.5°C for the mixture) and complex modulus ( $|G^*|$  of the bitumen comprised between  $10^{-2}$  and  $10^3$  MPa;  $|E^*|$  of the mixture comprised between 10 and 40000 MPa) are taken into consideration.
- (ii) Very low values of COV were found for glassy moduli  $G_0$  (1.62%) and  $E_0$  (0.57%), for the bitumen and the mixture, respectively. Generally, the variability (expressed by the COV) of constants  $E_{00}$  (for the mixture),  $\delta$ ,  $k$ ,  $h$ , and  $\log \tau$  (for both bitumen and mixture) is approximately equal or lower than 20%.
- (iii) Acceptable errors were generally observed over the whole range of frequencies and temperatures for the simulations obtained for both bitumen and mixture by all the users of the panel, regardless of their familiarity and experience with the model. The three most experienced users of the panel obtained particularly accurate approximations of experimental data, confirming the ability of the model to simulate LVE behaviour of both bitumens and mixtures.

## Data Availability

The data used to support the findings of this study are included within the article.

## Conflicts of Interest

The authors declare that they have no conflicts of interest.

## Acknowledgments

The authors express their profound gratitude to all the other participants of the calibration panel: Thomas Attia, Lucas Babadopulos, Jean-Claude Carret, Philippe Gaborit, Pierre Gayte, Minh Duc Nguyen, Alvaro Pedraza, Cong Viet Phan, Simon Pouget, Diego Ramirez Cardona, and Nouffou Tapsoba.

## References

- [1] A. R. Tenpe and A. Patel, "Application of genetic expression programming and artificial neural network for prediction of CBR," *Road Materials and Pavement Design*, pp. 1–18, 2018.
- [2] Z. Ding, L. Li, G. Zou, and J. Kong, "Design sensitivity analysis for transient response of non-viscously damped systems based on direct differentiate method," *Mechanical Systems and Signal Processing*, vol. 121, pp. 322–342, 2019.
- [3] Q. Liu, J. Liu, F. Guan, X. Han, L. Cao, and K. Shan, "Identification of the visco-hyperelastic properties of brain white matter based on the combination of inverse method and experiment," *Medical & Biological Engineering & Computing*, vol. 57, no. 5, pp. 1109–1120, 2019.
- [4] I. M. Sobol', "Sensitivity estimates for nonlinear mathematical models," *MMCE*, vol. 1, pp. 407–414, 1993.
- [5] I. M. Sobol', "Global sensitivity indices for nonlinear mathematical models and their Monte Carlo estimates," *Mathematics and Computers in Simulation*, vol. 55, no. 1–3, pp. 271–280, 2001.
- [6] J. S. Marshall, "Modeling and sensitivity analysis of particle impact with a wall with integrated damping mechanisms," *Powder Technology*, vol. 339, pp. 17–24, 2018.
- [7] F. Olard and H. Di Benedetto, "General "2S2P1D" model and relation between the linear viscoelastic behaviours of bituminous binders and mixes," *Road Materials and Pavement Design*, vol. 4, no. 2, pp. 185–224, 2003.
- [8] C. Riccardi, A. C. Falchetto, D. Wang, and M. P. Wistuba, "Effect of cooling medium on low-temperature properties of asphalt binder," *Road Materials and Pavement Design*, vol. 18, no. S4, pp. 234–255, 2017.
- [9] N. I. M. Yusoff, D. Mounier, G. Marc-Stéphane, M. Rosli Hainin, G. D. Airey, and H. Di Benedetto, "Modelling the rheological properties of bituminous binders using the 2S2P1D model," *Construction and Building Materials*, vol. 38, pp. 395–406, 2013.
- [10] H. Di Benedetto, B. Delaporte, and C. Sauzéat, "Three-dimensional linear behavior of bituminous materials: experiments and modeling," *International Journal of Geomechanics*, vol. 7, no. 2, pp. 149–157, 2007.
- [11] S. Pouget, C. Sauzéat, H. Di Benedetto, and F. Olard, "From the behavior of constituent materials to the calculation and design of orthotropic bridge structures," *Road Materials and Pavement Design*, vol. 11, no. S1, pp. 111–144, 2010.

## Research Article

# Reuse of Zeolite By-Products Derived from Petroleum Refining for Sustainable Roads

M. Sol-Sánchez,<sup>1</sup> F. Moreno-Navarro ,<sup>1</sup> M. C. Rubio-Gómez ,<sup>1</sup> V. Pérez-Mena,<sup>2</sup> and P. Cabanillas<sup>2</sup>

<sup>1</sup>Laboratory of Construction Engineering, University of Granada, C/Severo Ochoa s/n, 18071 Granada, Spain

<sup>2</sup>Cepsa Comercial Petróleo, Carretera de Daganzo Km 5.5 Alcalá de Henares, Madrid, Spain

Correspondence should be addressed to F. Moreno-Navarro; [fmoreno@ugr.es](mailto:fmoreno@ugr.es)

Received 14 December 2018; Revised 13 February 2019; Accepted 4 March 2019; Published 2 May 2019

Guest Editor: Jose Norambuena-Contreras

Copyright © 2019 M. Sol-Sánchez et al. This is an open access article distributed under the Creative Commons Attribution License, which permits unrestricted use, distribution, and reproduction in any medium, provided the original work is properly cited.

The reduction in consumption of natural resources (fuel, gas, etc.) and contaminant emissions (CO<sub>2</sub>, CO, NO<sub>x</sub>, etc.) during the production of asphalt mixtures has become one of the main challenges in road engineering. Warm mix asphalts (WMAs) have been developed in order to achieve this objective while ensuring the mechanical performance and durability of traditional hot mix asphalts (HMAs). However, these materials are commonly manufactured using additives or products whose production could reduce both their environmental benefits and cost effectiveness. This paper presents a research study that aims to analyse the reuse of zeolite wastes derived from petroleum refining in the production of warm mix asphalts. For this purpose, two different types of zeolite wastes were analysed as additives for the manufacture of two warm mix asphalts, whose mechanical performance was compared with conventional WMA and hot mix asphalt. The results indicate that zeolite wastes with a lower particles size presented higher capacity to absorb water, while its dosage at 0.3% allows for producing warm mix asphalts at temperatures around 145°C, with comparable workability and densification to conventional HMA at 165°C without reducing its bearing capacity, fatigue life, and resistance to water action and plastic deformation.

## 1. Introduction

Asphalt mixtures are widely used in pavement for roads all around the world. To illustrate, the majority of European roads are composed of this type of pavement [1] due to its constructive benefits and other technical advantages (lower noise levels, flexibility to absorb distresses, etc.). However, the manufacturing of such materials includes a process of heating the components to temperatures higher than 150–160°C in order to reduce the viscosity of the binder. This generates harmful fumes during manufacturing in plant and during the transportation and spread process, whilst the significant consumption of energy is also required, leading to negative effects from both economic and environmental standpoints [2].

To reduce such negative effects, it has been shown that decreasing the manufacturing temperature of asphalt mixtures leads to a significant reduction in fuel consumption

and emissions of CO<sub>2</sub> and volatile organic compounds, amongst other benefits [3]. In addition, decreasing the binder temperature leads to lower loss of volatiles and oxidation of the bitumen (associated with material ageing) during the manufacturing process, resulting in a more viscous material that is less susceptible to brittle failure [4]. In this context, warm mix asphalt (WMA) allows for a reduction in manufacturing temperature of around 20–40°C in comparison with conventional hot mix asphalt (HMA), which reduces its negative environmental impacts without compromising its resistance to the main failure modes that occur in bituminous pavements in roads (rutting, stripping, fatigue, etc.) [5, 6].

Depending on the technique applied, WMA can be qualified into 3 different categories: incorporation of organic additives (Fischer-Tropsch wax, Montan Wax, etc.) [7, 8] chemical additives (emulsification agents, surfactants, etc.) [9]; and water to produce the foaming of the bitumen

[10, 11]. The latter can be conducted by directly injecting water into the bitumen or including particles such as zeolites or hydrophilic fillers that contain water, which is released during the manufacturing process at temperatures usually higher than 120°C. Nonetheless, all of these technologies also present some limitations that are mainly associated with cost and the consumption of raw materials [12]. Thus, solutions and materials are required that are able to improve the efficiency and potential benefits of these manufacturing technologies.

In this regard, this study analyses the viability of reusing the zeolites as a catalyst during the petroleum refining process (which are wastes), as an industrial by-product in the manufacture of WMA, and then, aiming to reduce costs and consumption of raw materials in the production of WMA. Zeolites are commonly used in the fluid catalytic cracking (FCC) step during the refining process to accelerate the disintegration of heavy molecules of petroleum, thanks to their crystal structure providing channels and chambers to facilitate the interaction of molecules. Nonetheless, after a number of refining processes of petroleum, the zeolites are discarded due to its degradation, and then, size of its pores changes. However, they still conserve the capacity to retain and release water under changing temperature conditions [13–15].

Therefore, zeolite by-products could be appropriate for use in the manufacture of WMA by indirect bitumen foaming, resulting in economic and environmental savings whilst reusing waste materials for the improvement of asphalt mixtures to be used in roads [16]. In the present study, two different types of waste zeolites were firstly characterized according to their requirements for use as additives containing water for WMA manufacture. Following this, the design and performance of two WMAs including both types of subproduct zeolite was compared with conventional WMAs and hot mix asphalt (HMA).

## 2. Methodology

**2.1. Materials.** For this study, three types of zeolites were studied: two zeolite by-products (referred to in this paper as Zeolite 1 and Zeolite 2) and a commercial zeolite (referred to as Reference Zeolite, and widely used to manufacture WMA). The conventional zeolite consisted of synthetic zeolites, 20% of whose mass is composed of crystallized water that is released during contact with bitumen at a temperature ranging 85–180°C [17]. Regarding the subproduct zeolite, both were obtained from the refining process of petroleum as end-of-life materials that were used as a catalyser with different properties.

Table 1 shows the main physical properties of the zeolite used in this study while, Table 2 represents the composition of the subproduct zeolites, the Reference Zeolite being a sodium-aluminum-silicate hydrothermal crystal. It can be seen that both subproduct zeolites (Zeolite 1 and Zeolite 2) present lower particle size and higher density than the Reference Zeolite, whilst the hygroscopic humidity of this latter material is the highest, followed by Zeolite 1 and Zeolite 2.

TABLE 1: Main physical properties of zeolites.

Properties	Zeolite 1	Zeolite 2	Reference Zeolite
Granulometry	Size (mm)	% passing	% passing
	0.5	100	100
	0.25	100	100
	0.125	100	92
Bulk density (mg/m <sup>3</sup> )	0.063	100	26
		0.67	0.81
Maximum density (mg/m <sup>3</sup> )	2.642	2.697	2.449
Hygroscopic humidity (%)	0.67	0.26	3.2

TABLE 2: Composition of subproduct zeolites.

Component	Zeolite 1	Zeolite 2
P <sub>2</sub> O <sub>5</sub> (%)	1.38	1.63
Oxides (%)	1.63	1.64
Calcium (mg/kg)	83	47
Copper (mg/kg)	17	<10
Iron (mg/kg)	3.057	2.635
Magnesium (mg/kg)	164	132
Nickel (mg/kg)	1.048	1.350
Sodium (mg/kg)	2.159	1.809
Vanadium (mg/kg)	502	701

To analyse the viability of using subproduct zeolite for the manufacture of asphalt mixtures, a conventional asphalt mixture type AC-22 S (EN 13108-1) was employed since it is commonly utilized in the construction of pavement for roads and during maintenance and rehabilitation operations. The mineral skeleton was composed of limestone aggregates for the different fractions (0/6, 6/12, 12/18, and 18/25) from filler to particles with a maximum size of 22 mm, while the bitumen was a conventional B35/50 (whose penetration was equal to 44 dmm according to EN 1426, with a softening point of approximately 52°C-EN 1427) with a dosage equal to 4.03% over the total weight of the mixture. Table 3 summarises the main characteristics of the design of the mixture used as a control (the conventional HMA), which was used to assess the effect of reducing the manufacturing temperature, along with the effectiveness of the zeolites.

Considering this conventional mixture as a reference, the effect of zeolite by-products in WMA manufacturing was analysed by using different types and dosages of zeolites to reduce production temperature to 145°C and 120°C. Thus, for this study, the following mixtures were considered: three asphalt mixtures (WMA-Z1, manufactured with Zeolite 1; WMA-Z2, manufactured with Zeolite 2; and WMA-RZ, manufactured with the Reference Zeolite) manufactured at low temperatures (145°C and 120°C), and different dosages of the three types of zeolite were analysed (0.1%, 0.3%, and 0.5% over the total weight of the asphalt mixture); and a conventional asphalt mixture (without using zeolites) that was manufactured at the routine temperature of HMA (165°C, used as a control) and at low temperatures (145°C and 120°C) to assess the influence of zeolites (these latter mixtures are referred to in this paper as WMA-R).

TABLE 3: Main physical and mechanical characteristics of the HMA used as a control.

Properties	AC 22 35/50 S
Optimal bitumen content (% over mix weight)	4.03
Bulk density ( $\text{mg}/\text{m}^3$ ), EN 12697-6	2.477
Air void content (%), EN 12697-8	4.1
Aggregates void content (%), EN 12697-8	13.7
Filler/bitumen ratio	1.0
Marshall stability (kN), EN 12697-34	17.79
Marshall deformation (mm), EN 12697-34	4.1

The designing factors of WMA were defined in base to the common use of conventional zeolites (as that used as a reference in this study) and following previous studies focused on using zeolites for WMA as indicated in a literature revision done by Wozuk and Franus [16].

**2.2. Testing Plan.** The testing plan was divided into three different stages: (i) characterization of the various types of zeolite for their application in WMA; (ii) study of the main design factors for WMA including the zeolite by-products as the bitumen foaming agent; (iii) and analysis of the mechanical performance of the WMA manufactured with the zeolite by-products, in comparison with the conventional HMA. Table 4 summarises the testing plan used in the present study.

In the first stage, the characterization process of the zeolite by-products consisted of analysing their capacity for water absorption and release under different temperatures and periods of time, comparing the results of the two types of zeolite by-products (Zeolite 1 and Zeolite 2) with that recorded for the commercial zeolite used as a control. This test consisted of storing three 30-gram samples of each type of zeolite (previously dehydrated) in a climatic chamber under controlled temperature ( $23 \pm 1^\circ\text{C}$ ) and humidity ( $98 \pm 1\%$ ), measuring water absorption after 1, 2, 3, 5, 72, 98, 120, 240, and 408 hours. Later, these same samples (partially moistened) were stored in an oven at different temperatures ( $120^\circ\text{C}$ ,  $130^\circ\text{C}$ , and  $145^\circ\text{C}$ , which correspond to WMA manufacturing temperature) to measure the capacity of each material to release its water content during different periods of time.

In the second stage, various asphalt mixtures (all type AC-22 S) were tested including a different quantity of each zeolite (0% in the cases of HMA and WMA-R, and 0.1%, 0.3%, and 0.5% in the cases of WMA-Z1, WMA-2, and WMA-RZ) under various manufacturing temperatures ( $145^\circ\text{C}$  and  $120^\circ\text{C}$ , as well as  $165^\circ\text{C}$  for the conventional HMA without zeolites), with the aim of defining the optimal design of the WMA produced by bitumen foaming through the use of zeolite by-products. To analyse the effect of these parameters, firstly, the workability and compactibility (these properties are essential in asphalt mixtures at low temperatures) of each mixture were evaluated by using a gyratory compactor (up to 210 gyros), which has been proven to be effective to measure the influence of additives in mixture manufacturing [12]. Following this, the indirect tensile strength (EN 12697-23) and bearing capacity (through the

stiffness modulus test, EN 12697-26 annex C) were measured at  $20^\circ\text{C}$  for the specimens (4 for each mixture) obtained from the gyratory compactor, with the objective of determining the cohesiveness and coating of each mixture. Based on the results obtained in these tests, the optimal manufacturing temperature and amount of zeolite by-products (Zeolite 1 and Zeolite 2) were selected for each mixture.

In the third stage of this study, the mechanical behaviour (in both short and long terms) of WMA manufactured with the optimal design for each zeolite by-product was compared with that recorded for conventional HMA in order to assess the viability of using such WMA in the construction of pavements for roads. For this purpose, the tests conducted were the water sensitivity test (EN 12697-12), wheel tracking test (EN 12697-22), and triaxial test (EN 12697-25 method B) at  $60^\circ\text{C}$ , stiffness modulus at different temperatures ( $5^\circ$ ,  $20^\circ$ , and  $40^\circ\text{C}$ ) (EN 12697-26 annex C), and UGR-FACT [18], which is an appropriate test for measuring the resistance of asphalt to fatigue cracking. This latter test was also conducted at  $10^\circ\text{C}$ ,  $20^\circ\text{C}$ , and  $30^\circ\text{C}$  since temperature plays an essential role in the performance of bituminous materials [19, 20]. This test was also carried out under stress-controlled conditions (cyclic loading with a stress amplitude of 0.8 MPa and a frequency of 5 Hz) in order to simulate the real conditions usually endured by the pavement, along with the effects of high-speed traffic.

### 3. Results and Discussion

**3.1. Stage 1. Characterization of Zeolite for Its Use in WMA.** Figure 1 displays the increase in the percentage of humidity (water absorption capacity) as a function of storage time in a climatic chamber (at 98% of humidity) of the zeolites studied. The results show that, at short time periods (less than 10 hours), all types of zeolite present a similar capacity to absorb water, showing values of humidity around 3-4% with a coefficient of variation around 20%. However, for longer time periods, the zeolite of reference absorbed close to 10% and 20% of water at 100 h and 400 h, respectively, while the by-products (Zeolite 1 and Zeolite 2) presented values around 7-8% and 12-13% for the same periods. This indicates that the zeolite wastes recorded lower percentages of humidity, particularly from a time of 100 hours, this effect being more pronounced for Zeolite 2, which generally presented values near 1-2% lower than the Zeolite 1. This therefore suggests that Zeolite 1, which presents lower particle size and then higher specific surface, could be more effective for bitumen foaming than Zeolite 2 since higher water content could be provided during the mixing process.

Figure 2 displays the development of humidity content of each zeolite under different temperatures in order to evaluate its capacity to release water molecules. It is clear that temperature plays an essential role in the phenomenon of water release (which directly affects the foaming process). All types of zeolite released most of its water content during the first 30 minutes at  $145^\circ\text{C}$ , passing from values of humidity close to 40% for the zeolite reference and 30% for the by-products, to percentages near 10 (regardless the type of

TABLE 4: Testing plan.

Study step	Mixtures	Zeolites	Manufacturing temperature (°C)	Tests
Zeolite characterization	—	Zeolite 1 Zeolite 2 Reference Zeolite	—	(i) Water absorption (ii) Water release
Design of WMA	HMA	—	165	(i) Workability (ii) Stiffness modulus at 20°C (iii) Indirect tensile strength (20°C)
	WMA-R	—	145–120	
	WMA-Z1	0.1–0.3–0.5% Zeolite 1	145–120	
	WMA-Z2	0.1–0.3–0.5% Zeolite 2	145–120	
Performance of WMA	HMA	—	165	(i) Water sensitivity (ii) Stiffness modulus at 5–20°C–40°C (iii) Wheel tracking (iv) Triaxial (v) UGR-FACT
	WMA-Z1	Optimal % Zeolite 1	Optimal	
	WMA-Z2	Optimal % Zeolite 2	Optimal	

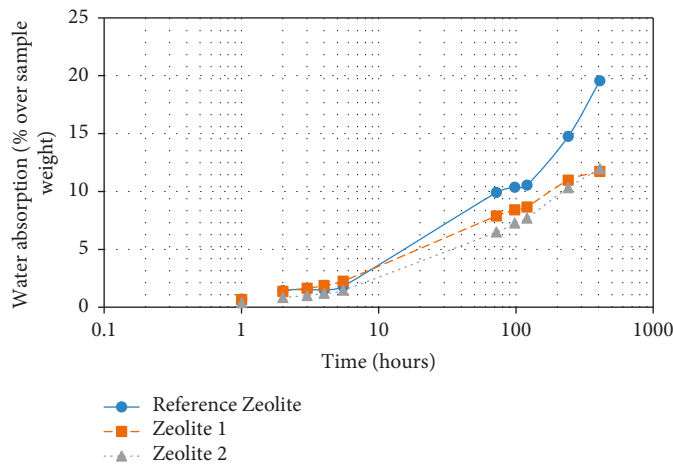


FIGURE 1: Evolution of water absorption capacity of zeolites.

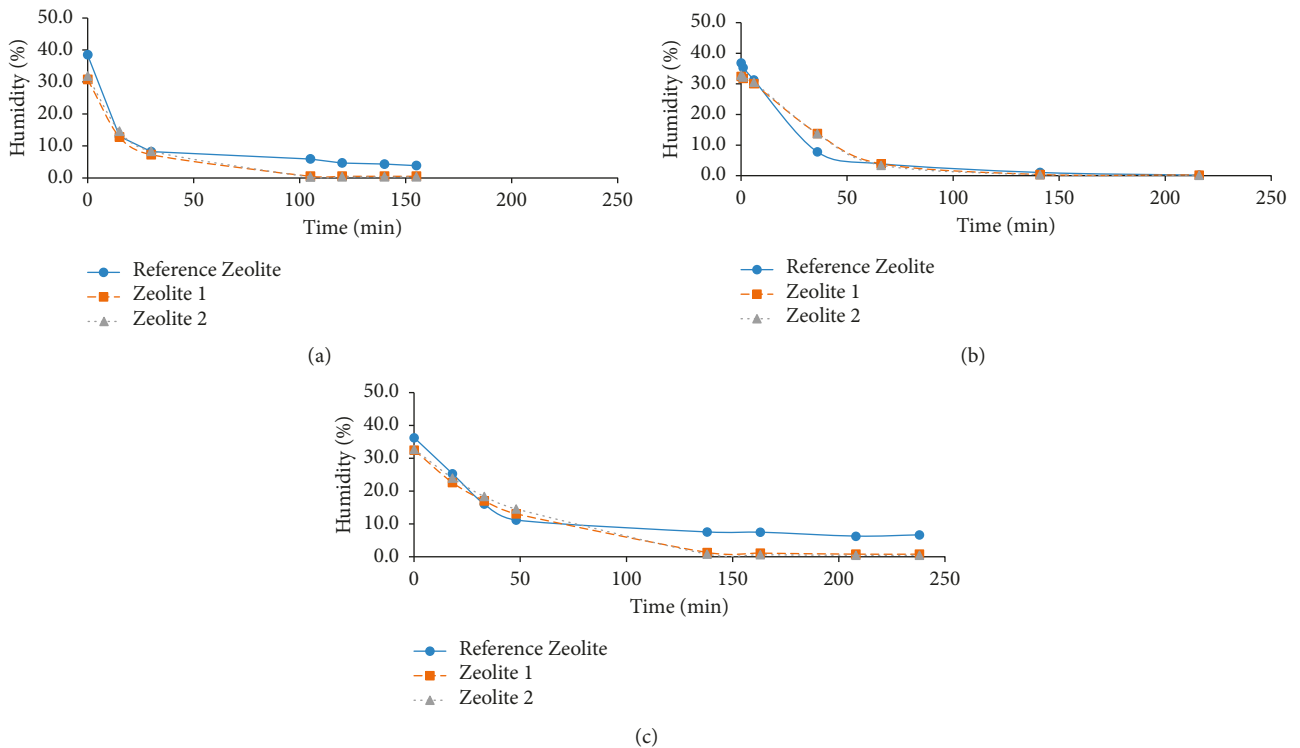


FIGURE 2: Evolution of the capacity of zeolites to release water at different temperatures: (a) 145°C; (b) 130°C; (c) 120°C.

material) with a coefficient of variation lower than 15%. However, to obtain such reduction in humidity content (water release) at a temperature of 120°C, the required time exceeded 50 minutes (coefficient of variations lower than 15%), which indicates that, at higher temperatures, the foaming process will proceed more rapidly than at lower temperatures. These results are in accord with those of previous studies suggesting that the release of zeolite water is not a sudden process, but a long-term phenomenon that decreases gradually the binder viscosity and improves the workability during mix asphalt production, placement, and compaction [21].

Regarding the influence of the type of zeolite, the Reference Zeolite showed higher values of humidity at long term, particularly at 120°C where this material presented values around 7% after 150 minutes while the by-products recorded percentages lower than 1. This could lead to a more prolonged foaming phenomenon than in the case of the zeolite by-products (both showing similar behaviour). Nonetheless, it is seen that all zeolites present comparable behaviour (for the different temperatures analysed) over a short time interval (around 50–100 minutes) when most of the water is released during mixture production and placement, which allows for the improvement of workability and compaction.

*3.2. Stage 2. Design of WMA including Zeolite By-Products for Indirect Bitumen Foaming.* Figure 3 displays the final air void content (including error bars with deviation values) recorded in the workability study for the different mixtures in order to select the most appropriate design parameters for WMA (zeolite dosage and manufacturing temperature), according to the densification capacity of the WMA. These results suggest that the decrease in manufacturing temperature leads to a significant reduction in mixture densification, passing from content in air void around 3.1% for the HMA (deviations lower than 0.4%) to values higher than 5.1% for the WMA at 120°C without additives (WMA-Reference). This demonstrates the remarkable influence of this factor in the production of these mixes.

However, the use of zeolite (regardless of the type) generally allows for increasing the workability of the material at low temperatures and facilitates its compaction, obtaining in most of the cases lower percentage of voids than the reference mixture at low temperatures (generally, lower than 4.5% for the WMA at 145°C and lower than 5.1% when the manufacturing temperature was close to 120°C). Also, results showed that the use of zeolites led to values close to those from the conventional HMA, particularly for the mixtures at 145°C. This, which is in agreement with other authors [16, 22, 23] who have demonstrated the improvement in WMA workability with zeolites, could lead to economic and environmental benefits associated with lower energy consumption during manufacturing of WMA, lower emissions, and longer transportation distances, without significant reduction in mixture compaction.

Regarding the influence of the dosage of zeolite, the results indicate that (for all types of zeolite) the increase in

percentage from 0.1% to 0.3% generally translates to lower void content (which could be associated with a more effective foaming process, and then, higher densification of the material), obtaining quite similar effect in the mixtures with the zeolite by-products to that recorded for the case with Reference Zeolite (WMA-RZ). However, it was seen that the use of a dosage of 0.5% zeolite leads to a decrease in compatibility in most of the mixtures (particularly at 120°C), which could be related to excessive use of these materials as indicated by other authors [12, 24, 25]. Therefore, it appears that 0.3% of zeolite generally leads to the highest values of density (lowest air void content) regardless of the manufacturing temperature, with zeolite by-products (WMA-Z1 and WMA-Z2) yielding broadly comparable values to WMA-RZ and particularly at a mixing temperature of 145°C.

Taken together, these findings suggest the viability of using these subproducts to manufacture WMA with appropriate workability properties, without important differences between the types of zeolite used as indicated by other authors [12] who indicated that the compaction temperature and additive dosage have greater effect than the type of zeolite in the densification of the material.

Figure 4 represents the stiffness modulus measured at 20°C for the specimens that were obtained from the workability analysis for all the mixtures. Results showed values near 7,000 MPa (deviations lower than 350 MPa) for the conventional HMA while the reduction in temperature led to modulus around 5,800 MPa and 4,000 MPa for the mixture without zeolites at 145°C and 120°C (deviations near 400 MPa for both cases), respectively. However, the use of zeolites, generally led to higher values for such manufacturing temperatures (obtaining even results near the conventional HMA for the WMA at 145°C), presenting limited differences between the cases with zeolite wastes and the reference.

Therefore, the results again indicate that the behaviour of conventional asphalt mixtures is somewhat susceptible to manufacturing temperature while the use of zeolite generally allows for reducing the negative effect of reducing manufacturing temperature on mixture performance, which is in consonance with other studies [12]. This trend is particularly marked in the case of a dosage of 0.3% zeolite (except in the case of WMA-RZ), which generally appears to be more effective. Also, it was seen that the improvement in the performance of the mixtures with zeolite by-products was comparable to the cases with Reference Zeolite (WMA-RZ), mainly for the Zeolite 1, which could be considered as more appropriate to increase the bearing capacity of WMA, primarily at 145°C.

Nonetheless, it must be taken into account that the majority of these mixtures recorded lower values of stiffness modulus than the conventional HMA, particularly in the case of WMA manufactured at 120°C that presented the lowest values of bearing capacity. This fact could be linked to the slight increase in void content in comparison to HMA, but also to the lower ageing and oxidation of bitumen when reducing mixing temperature [26], resulting in more viscous and less rigid materials. This phenomenon—in spite of the

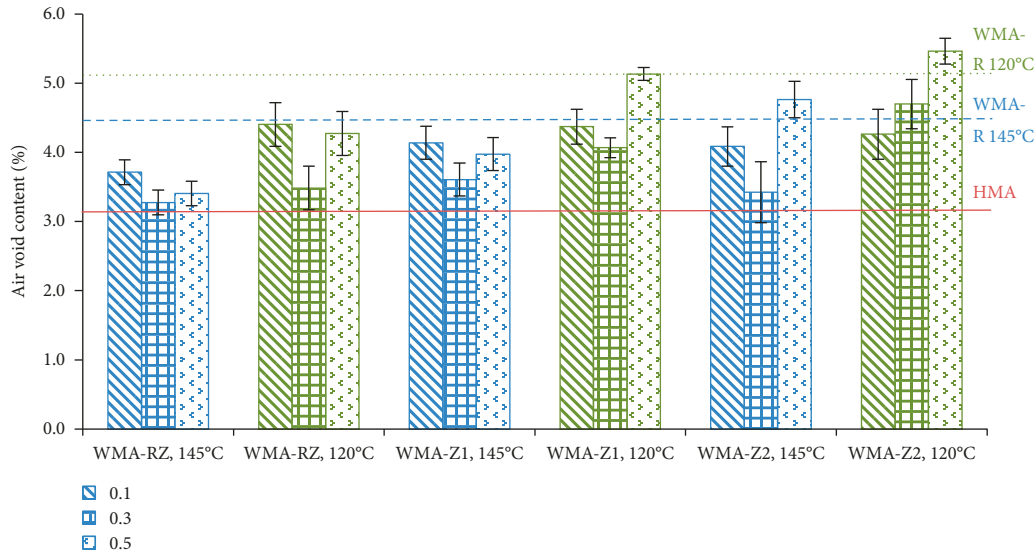


FIGURE 3: Influence of zeolite dosage and type on WMA workability and compactibility.

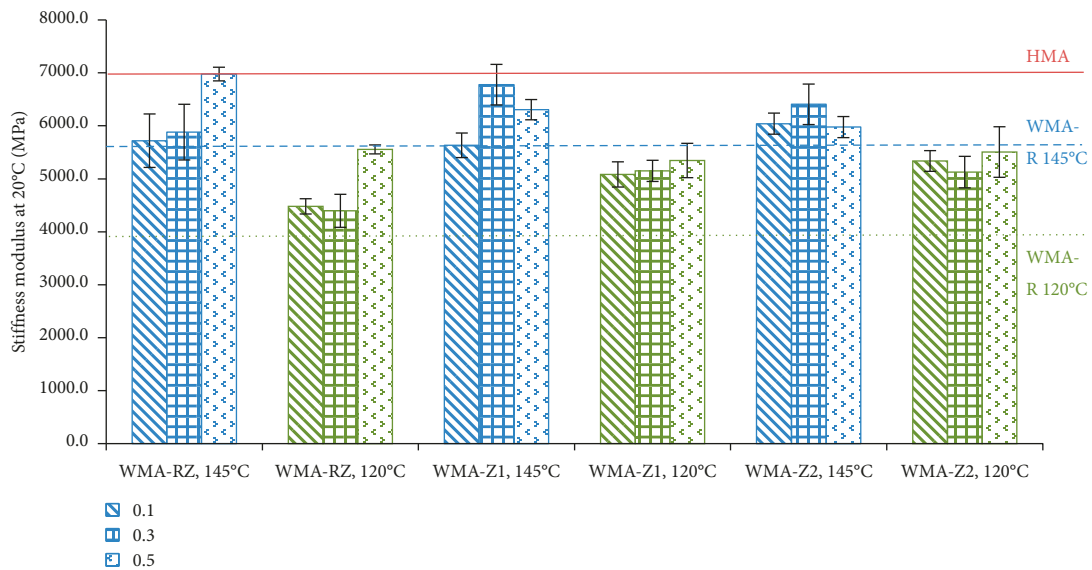


FIGURE 4: Results of the stiffness modulus from the specimens obtained in the workability study.

slight decrease in the stiffness modulus—could lead to longer service life of the material and higher resistance to cracking since it has been shown that less aged bitumen allows for a higher capacity to absorb distresses that occur in road pavements [4].

To understand the effect of zeolite on cohesiveness and coating of WMA, values of indirect tensile strength are shown in Figure 5. As observed previously, results demonstrate that the use of zeolites allows for values of ITS (indirect tensile strength) even higher than 1,600 kPa (which was the result for the HMA, with deviations lower than 70 kPa).

Regarding the effect of the type of zeolite by-products, results indicate that WMA with both subproducts recorded values quite similar to those measured for the WMA with the Reference Zeolite. Nonetheless, in agreement with other

authors [23], it must be considered that while reducing the mixing temperature lower than 140–145°C, a significant reduction in ITS can take place, particularly for high dosages of zeolite (higher than 0.5%). The negative effect of using high quantities of zeolite on ITS values (particularly with zeolite by-product) could be related to the lower cementing power of these materials while other studies [12, 24] have also shown that an excessive amount of water could lead to a loss of adhesion between aggregates and binder.

Therefore, these results confirm that the use of both types of zeolite by-products could lead to the adequate coating of aggregates by bitumen (probably due to the improvement in workability of the WMA when zeolite by-products are used), particularly when using a dosage of 0.3% at 145°C which allowed for comparable results to those with Reference Zeolite.

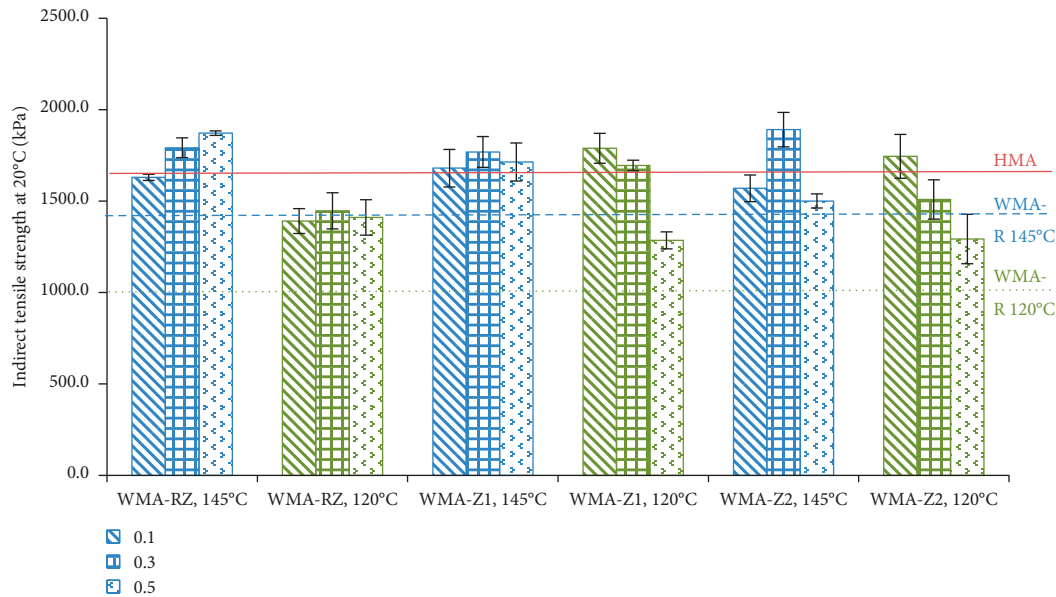


FIGURE 5: Effect of zeolite type and dosage on indirect tensile strength of WMA.

**3.3. Stage 3. Mechanical Performance of WMA with Zeolite By-Products.** In this stage, the mechanical performance of WMA manufactured at 145°C with 0.3% of each type of zeolite by-product is compared with that measured for conventional HMA produced at 165°C. These design parameters for the WMA were selected according to the results obtained in the previous stages (Table 5 lists the mean results of workability and their deviation for such WMA with zeolite wastes in comparison with the HMA), which show that it is possible to obtain comparable values of density, bearing capacity, and indirect tensile strength.

Figure 6 displays the results obtained on the water sensitivity test for the different mixtures, showing the indirect tensile strength for both dry and wet set of specimens, as well as the ratio of restrained strength (ITSR: indirect tensile strength ratio). Based on results, it is proven that the WMA with zeolites presented lower values of ITSR index (84.9% for the case with Zeolite 1 and 78.0% for Zeolite 2) than the traditional HMA 87.3%. This is in consonance with other studies [12, 16, 23] that have found that WMA with zeolites presents a reduction in ITSR around 5–8%. This could be associated with lower cohesiveness and adhesion between aggregates and bitumen due to the decrease in manufacturing temperature but also to lower interaction between the binder and the zeolites included during the mixing process.

Nonetheless, results indicate that WMA with Zeolite 1 (WMA-Z1) led to values of tensile strength comparable to those for HMA, for both wet and dry conditions, and then, this mixture presented only slight reduction in resistance to water action. However, Zeolite 2 (WMA-Z2) did lead to a higher reduction in mixture strength, particularly for the specimens in contact with water, which reflects lower values of retained strength, and thus higher susceptibility to water action. Therefore, Zeolite 1 could be more effective during the bitumen foaming process (probably associated with its higher capacity to absorb water because of the smaller

particles) used to produce WMA with lower susceptibility to water action.

Figure 7 shows the influence of in-service temperature on the bearing capacity of the WMA with both subproduct zeolites and the HMA. It can be seen that the reduction in the stiffness modulus when increasing the temperature is broadly similar for all the mixtures studied, which indicates comparable susceptibility of its bearing capacity to climatic gradients. Nonetheless, the results show that the WMA with Zeolite 2 presented values near those for HMA, while the Zeolite 1 (WMA-Z1) presented even higher stiffness values, which could be associated with the improvement in workability due to the foaming process induced by the use of this type of zeolite. These results are in accord with those found in previous studies on the effect of zeolites on the dynamic modulus of WMA compared with HMA [27].

To analyse the resistance of the mixture to permanent deformations, Figure 8(a) displays the results obtained in the wheel tracking test (depth of rut and slope of the curve of plastic deformations), while Figure 8(b) represents the results of the triaxial test: final permanent deformation (as a percentage of strain in reference to the initial height of the specimen) and slope of creep deformation and creep modulus.

In all cases, the results show that WMA with Zeolite 1 (WMA-Z1) presents quite similar values of final deformation at the end of the tests to those measured for the conventional HMA, while also showing a reduced tendency towards long-term rutting. This can be taken to indicate that this asphalt mixture offers resistance to permanent deformations comparable to HMA, which is in consonance with some authors [22] who state that WMA with zeolite reduce susceptibility to rutting, making it suitable for application in road pavements. However, also in agreement with other studies [28] where other types of zeolites are used, the application of the other kinds of zeolite by-product (Zeolite 2, WMA-Z2) results in a WMA with lower

TABLE 5: Comparative summary of results from the workability study.

Property	HMA		WMA-0.3% Z1, 145°C		WMA-0.3% Z2, 145°C	
	Mean	Deviation	Mean	Deviation	Mean	Deviation
Air void (%)	3.4	0.45	3.6	0.72	3.4	0.75
Stiffness at 20°C	6,956.0	329.1	6,778.4	382.9	6,407.1	382.3
ITS at 20°C	1,610.2	66.5	1,769.0	84.2	1,891.8	94.1

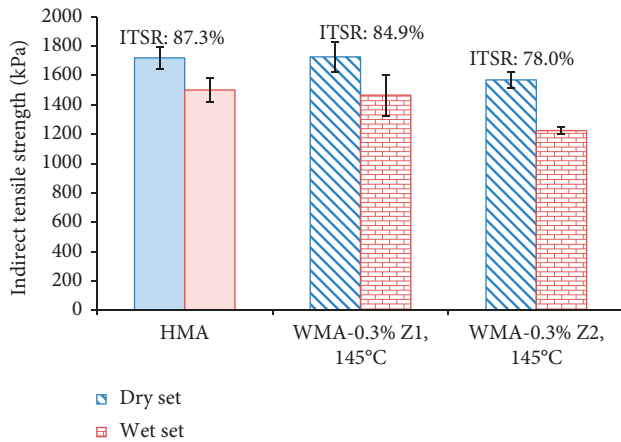


FIGURE 6: Results of the water sensitivity test for HMA and WMA with subproduct zeolite.

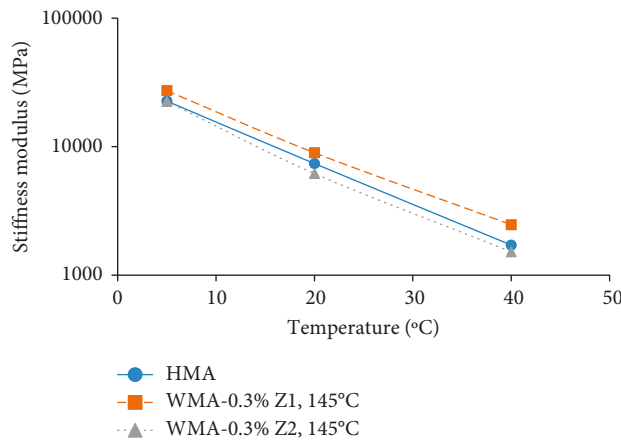
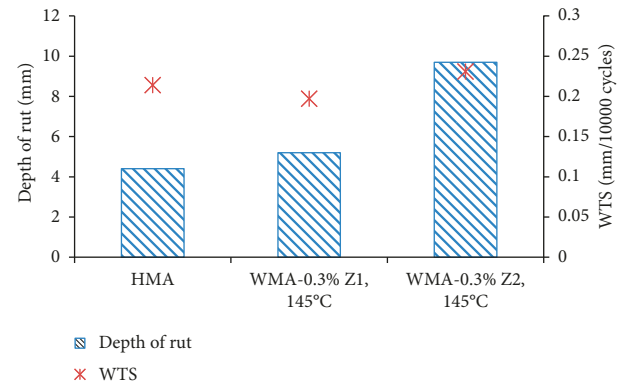


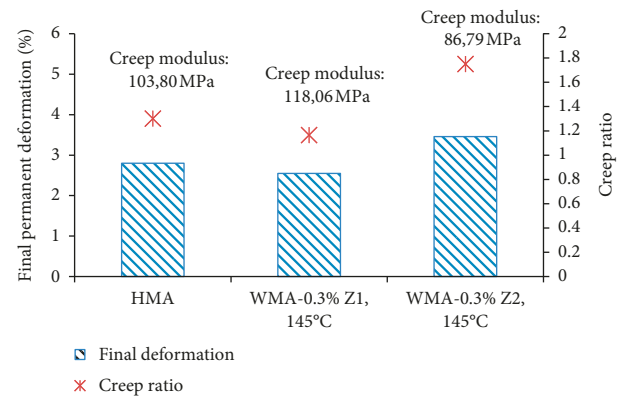
FIGURE 7: Stiffness modulus at different temperatures for both HMA and WMA with zeolites.

resistance to creep (lower modulus and ratio of creep) and thus a higher susceptibility to form rut deformations during its application in road pavements. This fact could be related to the higher size of particles in Zeolite 2 and their lower capacity to absorb water (and then, lower effectiveness for the foaming process) as seen in the characterization study of these materials.

Therefore, it can be said that the type of zeolite can lead to different behaviour under permanent deformations, where, in this study, Zeolite 1 could be the preferable option for obtaining WMA with higher resistance to rutting, showing comparable performance to HMA.



(a)



(b)

FIGURE 8: Resistance to plastic deformations measured by the wheel tracking test (a) and the triaxial test (b).

With the aim of evaluating the WMA in terms of resistance to cracking and fatigue life in comparison with conventional HMA, Figure 9 represents the values of mean damage parameter for the different mixtures under various testing temperatures. This parameter is used to quantify the susceptibility of mixtures to fatigue as an average of the energy dissipated per cycle due to the damage induced in the material [29], and therefore, the higher the parameter, the higher the damage in the material, reducing its fatigue life.

These results confirm that WMA-Z1 again presents comparable mechanical performance to conventional HMA, with higher resistance to cracking fatigue than the WMA-Z2, which shows higher values of damage than the other two mixtures analysed, and thus lower number of cycles are required to cause material failure. The results also show that the WMA presented similar thermal susceptibility to HMA, which implies that the warm mixtures and HMA would show comparable performance under different climate

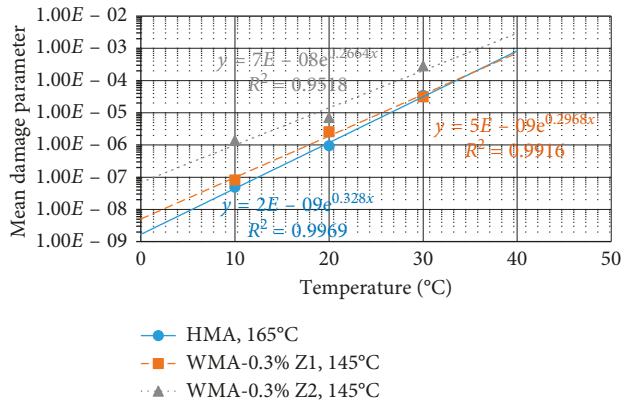


FIGURE 9: Mean damage parameter for the different mixtures under various testing temperatures.

conditions that can occur during the service life of the pavement.

#### 4. Conclusions

This study aims to examine the viability of using industrial zeolite by-products (obtained from the petroleum refining process) in the manufacturing of WMA by the technique of indirect bitumen foaming. For this purpose, these by-products were characterized according to their application, while the design and evaluation of the mechanical performance of WMA that included these by-products was compared with that of traditional hot mix asphalts (HMAs). From the results obtained in this study, the following conclusions can be drawn:

- (i) Zeolite by-products (particularly Zeolite 2) showed a slightly lower capacity to absorb water than the commercial by-product, which should be taken into account during the design and manufacturing stages of WMA. Nonetheless, the speed at which the various zeolites release the majority of the water content was comparable across a range of temperatures tests, if it is considered that water release is slower at lower temperatures. This means that zeolite by-products can be applied in a similar way to the conventional zeolites that are widely used in WMA.
- (ii) The use of 0.3% of zeolite by-products allowed obtaining mixtures with similar workability and mechanical performance to that measured for the WMA with Reference Zeolite at 120°C and 145°C, particularly in the case of the last manufacturing temperature when obtaining even comparable results to those recorded for the conventional HMA.
- (iii) WMA manufactured with Type 1 Zeolite by-products (Zeolite 1) presented quite similar performance to HMA in terms of water action, while WMA with Zeolite 2 showed a slight increase in water sensitivity, which could be associated with lower adhesiveness and cohesion when this additive is used.

(iv) The WMA manufactured with Zeolite 1 also recorded similar bearing capacity and resistance to plastic deformations to those measured for the conventional HMA whilst the WMA manufactured with Zeolite 2 showed lower mechanical performance, which could be associated with the lower effectiveness of this type of zeolite in producing bitumen foaming.

(v) Similarly, WMA manufactured with Zeolite 2 presented, across a range of test temperatures, lower resistance to fatigue cracking than that recorded for the WMA produced with Zeolite 1, which showed comparable performance to HMA.

Based on these results, it can be said that Zeolite 1 (which is the by-product with the lower particle size and the higher capacity to absorb water) could be suitable for application in the manufacturing of warm mix asphalts using the technology of indirect bitumen foaming. Use of this technology could bring important economic and environmental benefits to the field of road pavement construction without compromising mechanical performance.

#### Data Availability

The data used to support the findings of this study are available from the corresponding author upon request.

#### Conflicts of Interest

The authors declare that they have no conflicts of interest.

#### Acknowledgments

The present study has been conducted within the framework of the research project entitled “Soluciones de Pavimentación Ecológicamente Sostenibles: Ecoasfaltos” funded by the Ministry of Economy and Knowledge of Andalusia and the Ministry of Economy and Competitiveness of Spain in the framework of CTA (Corporación Tecnológica de Andalucía).

#### References

- [1] EAPA—European Asphalt Pavements Association, *Asphalt in Figures*, EAPA, Brussels, Belgium, 2015.
- [2] A. Almeida-Costa and A. Benta, “Economic and environmental impact study of warm mix asphalt compared to hot mix asphalt,” *Journal of Cleaner Production*, vol. 112, pp. 2308–2317, 2016.
- [3] M. Hassan, “Evaluation of the environmental and economic impacts of warm-mix asphalt using life-cycle assessment,” *International Journal of Construction Education and Research*, vol. 6, no. 3, pp. 238–250, 2010.
- [4] F. Moreno-Navarro, M. Sol-Sánchez, G. García-Travé, and M. C. Rubio-Gámez, “Understanding the effects of ageing and temperature on the fatigue cracking resistance of bituminous mixtures,” in *RILEM Bookseries*, vol. 13, Springer, Dordrecht, Netherlands, 2016.
- [5] T. Blankendaal, P. Schuur, and H. Voordijk, “Reducing the environmental impact of concrete and asphalt: a scenario

- approach," *Journal of Cleaner Production*, vol. 66, pp. 27–36, 2014.
- [6] L. P. Thives and E. Ghisi, "Asphalt mixtures emission and energy consumption: a review," *Renewable and Sustainable Energy Reviews*, vol. 72, pp. 473–484, 2017.
  - [7] M. Pérez-Martínez, F. Moreno-Navarro, J. Martín-Marín, C. Ríos-Losada, and M. C. Rubio-Gámez, "Analysis of cleaner technologies based on waxes and surfactant additives in road construction," *Journal of Cleaner Production*, vol. 65, pp. 374–379, 2014.
  - [8] J. Zhang, F. Yang, J. Pei, S. Xu, and F. An, "Viscosity-temperature characteristics of warm mix asphalt binder with Sasobit®," *Construction and Building Materials*, vol. 78, pp. 34–39, 2015.
  - [9] M. Sol-Sánchez, F. Moreno-Navarro, G. García-Travé, and M. C. Rubio-Gámez, "Analysing industrial manufacturing in-plant and in-service performance of asphalt mixtures cleaner technologies," *Journal of Cleaner Production*, vol. 121, pp. 56–63, 2016.
  - [10] A. Chimicz-Kowalska, W. Gardziejczyk, and M. Iwański, "Moisture resistance and compactibility of asphalt concrete produced in half-warm mix asphalt technology with foamed bitumen," *Construction and Building Materials*, vol. 126, pp. 108–118, 2016.
  - [11] A. Sharma and B. K. Lee, "Energy savings and reduction of CO<sub>2</sub> emission using Ca(OH)<sub>2</sub> incorporated zeolites as an additive for warm and hot mix asphalt production," *Energy*, vol. 136, pp. 142–150, 2017.
  - [12] A. Wozzuk and W. Franus, "Properties of the warm mix asphalt involving clinoptilolite and Na-P1 zeolite additives," *Construction and Building Materials*, vol. 114, pp. 556–563, 2016.
  - [13] S. Chałupnik, W. Franus, M. Wysocka, and G. Gzyl, "Application of zeolites for radium removal from mine water," *Environmental Science and Pollution Research*, vol. 20, no. 11, pp. 7900–7906, 2013.
  - [14] W. Franus, "Characterization of X-type zeolite prepared from coal fly ash," *Polish Journal of Environmental Studies*, vol. 21, no. 2, pp. 337–343, 2012.
  - [15] M. Wdowin, W. Franus, and R. Panek, "Preliminary results of usage possibilities of carbonate and zeolitic sorbents in CO<sub>2</sub> capture," *Fresenius Environmental Bulletin*, vol. 21, no. 12, pp. 3726–3734, 2012.
  - [16] A. Wozzuk and W. Franus, "A review of the application of zeolite materials in warm mix asphalt technologies," *Applied Sciences*, vol. 7, no. 3, p. 293, 2017.
  - [17] F. Xiao, P. E. Wenbin Zhao, and S. N. Amirkhanian, "Fatigue behavior of rubberized asphalt concrete mixtures containing warm asphalt additives," *Construction and Building Materials*, vol. 23, no. 10, pp. 3144–3151, 2009.
  - [18] F. Moreno-Navarro and M. C. Rubio-Gámez, "UGR-FACT test for the study of fatigue cracking in bituminous mixes," *Construction and Building Materials*, vol. 43, pp. 184–190, 2013.
  - [19] M. Sol-Sánchez, F. Moreno-Navarro, G. García-Travé, and M. C. Rubio-Gámez, "Laboratory study of the long-term climatic deterioration of asphalt mixtures," *Construction and Building Materials*, vol. 88, pp. 32–40, 2015.
  - [20] M. R. Taha, S. Hardwiyono, N. I. M. Yusoff, M. R. Hainin, J. Wu, and K. A. M. Nayan, "Study of the effect of temperature changes on the elastic modulus of flexible pavement layers," *Research Journal of Applied Sciences, Engineering and Technology*, vol. 5, no. 5, pp. 1661–1667, 2013.
  - [21] J. D'Angelo, E. Harm, J. Bartoszek et al., "Warm-mix asphalt: European practice," Report No. FHWA-PL-08-007, Federal Highway Administration, Alexandria, VA, USA, 2008.
  - [22] J. De Visscher, F. Vervaecke, A. Vanelstraete, H. Soenen, T. Tanghe, and P. Redelius, "Asphalt production at reduced temperatures using zeolites and the impact on asphalt performance," *Road Materials and Pavement Design*, vol. 11, no. 1, pp. 65–81, 2010.
  - [23] E. Sanchez-Alonso, A. Vega-Zamanillo, D. Castro-Fresno, and M. DelRio-Prat, "Evaluation of compactability and mechanical properties of bituminous mixes with warm additives," *Construction and Building Materials*, vol. 25, no. 5, pp. 2304–2311, 2011.
  - [24] O. R. Larsen, O. Moen, C. Robertus, and B. G. Koenders, "WAM-foam asphalt production at lower operating temperatures as an environmental friendly alternative to HMA," in *Proceedings of the 3rd Eurasphalt & Eurobitume Congress*, Vienna, Austria, May 2004.
  - [25] R. Vaiana, T. Iuele, and V. Gallelli, "Warm mix asphalt with synthetic zeolite: a laboratory study on mixes workability," *International Journal of Pavement Research and Technology*, vol. 6, no. 5, pp. 562–569, 2013.
  - [26] S. W. Goh and Z. You, "Evaluation of warm mix asphalt produced at various temperatures through dynamic modulus testing and four point beam fatigue testing," in *Proceedings of the GeoHunan international Conference—Pavements and Materials: Recent Advances in Design, Testing, and Construction*, Hunan, China, May 2011.
  - [27] A. S. M. A. Rahman and R. A. Tarefder, "Dynamic modulus and phase angle of warm-mix versus hot-mix asphalt concrete," *Construction and Building Materials*, vol. 126, pp. 434–441, 2016.
  - [28] E. Sanchez-Alonso, A. Vega-Zamanillo, M. A. Calzada-Perez, and D. Castro-Fresno, "Effect of warm additives on rutting and fatigue behaviour of asphalt mixtures," *Construction and Building Materials*, vol. 47, pp. 240–244, 2013.
  - [29] F. Moreno-Navarro and M. C. Rubio-Gámez, "Mean damage parameter for the characterization of fatigue cracking behavior in bituminous mixes," *Materials & Design (1980–2015)*, vol. 54, pp. 748–754, 2014.

## Research Article

# Induction Heating and Healing Behaviors of Asphalt Concretes Doped with Different Conductive Additives

Hechuan Li,<sup>1</sup> Jianying Yu,<sup>1</sup> Quantao Liu ,<sup>1</sup> Yuanyuan Li,<sup>1</sup> Yaqi Wu,<sup>2</sup> and Haiqin Xu<sup>1</sup>

<sup>1</sup>State Key Laboratory of Silicate Materials for Architectures, Wuhan University of Technology, Wuhan 430070, China

<sup>2</sup>China University of Geosciences (Wuhan), Wuhan 430074, China

Correspondence should be addressed to Quantao Liu; [liuqt@whut.edu.cn](mailto:liuqt@whut.edu.cn)

Received 30 November 2018; Revised 25 February 2019; Accepted 7 March 2019; Published 15 April 2019

Academic Editor: Pramod Koshy

Copyright © 2019 Hechuan Li et al. This is an open access article distributed under the Creative Commons Attribution License, which permits unrestricted use, distribution, and reproduction in any medium, provided the original work is properly cited.

It is consensual that the self-healing property of asphalt concrete can repair the damage inside it during high temperature and rest period. In order to not affect the traffic, the rest period of asphalt pavement is very short and uncontrollable; so, it is necessary to obtain enough high temperature in a limited time to achieve higher healing efficiency of asphalt concrete. The purpose of this paper is to study the induction heating efficiency and healing behaviors of asphalt concretes doped with different conductive additives. Steel fiber, steel grit, and steel slag were added to asphalt mixtures as conductive additives to prepare induction healing asphalt concretes. The steel grit and steel slag were added to replace the aggregates of corresponding particle size by equal volume to ensure the consistency of asphalt concrete volume, which can avoid degrading the performance of asphalt concrete due to the change of porosity. The induction heating efficiency and healing rate of asphalt concrete were quantified by infrared camera and three-point bending-healing experiment, respectively. The results showed that the thermal properties of asphalt concrete changed with the addition of different conductive additives. The asphalt concrete with steel fiber had the best induction heating property. While steel slag had extremely weak induction heating speed, the better thermal insulation property of the asphalt concrete with steel slag resulted in a higher induction healing rate. It was suggested to add steel slag to induction healing asphalt concrete to improve the healing rate.

## 1. Introduction

Asphalt concrete pavement has attracted more and more attention because of its excellent service performance [1–5]. However, due to environmental and human factors, such as temperature [6], moisture [7], ultraviolet rays [8], and heavy load [9], it is often difficult for the service life of the asphalt concrete pavement to reach the design life. Macroscopic distresses, such as potholes, cracks, and ruts, are often caused by microdamage inside asphalt concrete [10, 11]. Induction heating is a new maintenance technology to repair microcracks in asphalt concrete to avoid macroscopic distresses [12–14]. Similar to other self-healing materials, asphalt concrete can repair the damage autonomously. Asphalt concrete has a potential to restore its stiffness and strength during rest periods. However, this internal restoration is

very slow; so, this process needs to be speeded up in some way. Liu et al. first published the work on self-healing asphalt concrete with steel fiber in 2011 [15], and after that, more and more research has been carried out in this direction. Among most of those previous works, temperature is widely considered as a key factor for induction heating efficiency of asphalt concrete, and a higher induction healing rate is expected to be obtained during the road rest period. But at the moment, the most common way is to add conductive additives to asphalt binder [16, 17]. A major advantage of this method is that the energy is generated from the asphalt mortar and does not directly act on the aggregate, with the coarse aggregate being not subjected to excessive temperature stress due to excessive temperature change. However, it will take longer time to transfer the temperature from the asphalt binder to the whole asphalt concrete, thus

prolonging the induction heating time. Since asphalt concrete has about 95% aggregate, if conductive additives can be used to replace some aggregates without affecting the service performance of asphalt concrete, it may obtain better induction heating efficiency.

Steel slag is one of the industrial wastes, which makes up a portion of more than 10% of raw steel output [18, 19], and a large amount of steel slag will be produced in the steel-making process. The mineral composition of steel slag includes calcium silicate ( $C_2S$ ), calcium ferrite ( $C_4AF$ ,  $C_2F$ ), and calcium aluminate ( $C_3A$ ,  $C_{12}A_7$ ) [20]. Steel slag has been applied in many fields, such as the production of cement and concrete [18, 20], purification engineering [21, 22], and road construction [23]. However, little research has been done on the application of steel slag in induction heating asphalt concrete. On the one hand, steel slag has excellent thermal insulation; on the other hand, the energy generated by induction heating needs to be long standingly preserved in order to achieve an adequate repair of asphalt concrete. Therefore, the application of steel slag in induction heating asphalt concrete can not only better induce healing performance but also save resources.

Induction heating asphalt concrete has been paid more and more attention because of its great potential, such as prolonging the pavement service life [12, 13, 15, 16] and the application in melting snow and ice [24]. It is one of the research directions of the new generation smart pavement in the world at present. Steel slag, as a kind of solid waste, has been paid equal attention to its recycling and reuse. Its excellent performance has made it possible to use as pavement building material. At the same time, the excellent thermal properties of steel slag make it perfectly fit for induction heating asphalt concrete. The combination of them can not only improve the performance of induction heating asphalt concrete but also provide a new idea for the reuse of steel slag.

This study aims to explore the induction heating efficiency and healing rate of asphalt concrete by using conductive additives, especially steel slag and steel grit, to partially replace aggregates of certain sizes. The study investigated the induction heating and healing behaviors of asphalt concretes doped with different conductive additives by an infrared camera and universal testing machine. The thermal property of different asphalt concretes was evaluated by the thermal constants analyzer (TPS 2500S, Hot Disk, Sweden). The chemical elements and oxide of steel slag were analyzed by X-ray fluorescence. In order to avoid the change of voids, the improved method (equal volume substitution method) was used to add steel grit and steel slag into asphalt concrete.

## 2. Materials and Experiments

**2.1. Materials.** Base asphalt graded 70 (penetration grade) obtained from Hubei Guochuang Hi-tech Material Co., Ltd of China was used in this paper. Steel wool fiber provided by Jiangsu Golden Torch Metal products Co., Ltd and steel grit provided by Ningbo Hongyang cleaning equipment Co., Ltd were used as the induction heating units for asphalt

concrete, as shown in Figure 1. The properties of asphalt, steel wool fiber, and steel grit are shown in Table 1, while the impurity element composition of two conductive additives is shown in Table 2. During electromagnetic induction, the elements that can be heated are Fe, Co, and Ni [12]. The optimal content of fiber is 6% by the volume of asphalt according to the previous research [4]. Asphalt mixture with 6% steel wool fiber has best mechanical properties (highest strength and particle loss resistance) and quite high induction heating speed. The particle size of steel grit was 0.6–1.18 mm, which replaced the fine aggregate of corresponding size by equal volume to avoid changing the void of asphalt concrete. The basalt aggregate, steel slag aggregate, and limestone filler were used in this study. Specifically, two sizes of steel slag (4.75–9.5 mm and 9.5–13.2 mm) were used to replace basalt to study the induction heating characteristics and healing behavior of steel slag induction heating asphalt concrete. According to [25], the properties of steel slag were evaluated, as shown in Table 3. All properties meet the requirements of the code for steel slag aggregate for asphalt pavement. Although the water absorption rate was on the high side, it did not exceed the technical requirements too much.

### 2.2. Specimen Preparation

**2.2.1. Asphalt Concrete.** In order to study the induction heating efficiency and healing behaviors, six kinds of asphalt concretes were designed. Firstly, AC-13 basalt asphalt concrete was designed according to the Marshall design method, and the asphalt-aggregate ratio was 4.7%. The aggregate gradations and grading curves of asphalt concrete are shown in Figure 2. This kind of asphalt concrete was named BA. Secondly, the asphalt concrete was doped with 6% steel wool fiber by the volume of asphalt in BA, which was named FA. Thirdly, on the basis of FA, two sizes of steel slag aggregates (4.75–9.5 mm and 9.5–13.2 mm) were used to replace basalt aggregates to generate new asphalt concrete, which was named FSA. Fourthly, also on the basis of FA, steel grit (0.6–1.18 mm) was used to replace basalt aggregates to design a new asphalt concrete named FGA. Fifthly, the above steel grit and steel slag simultaneously replaced basalt aggregates to obtain GSA. Finally, FGSA was obtained by adding steel fiber into BA and replacing basalt aggregate with steel grit and steel slag. The list of different asphalt concretes ingredients is given in Table 4. It should be pointed out that steel slag and steel grit replaced basalt aggregates by the same volume, which avoids changing air void content of asphalt concrete for the future researches. In the three-point bending test and induction heating test, the specimens were rectangular beam with a notch cut by rutting board in a size of 85 mm × 50 mm × 10 mm, as shown in Figure 3.

**2.3. Thermal Property Test.** The thermal conductivity of steel fiber, steel grit, and steel slag is very good, which is different from that of aggregate, asphalt, and filler in asphalt concrete; so, it is necessary to study their influence on the thermal constants of asphalt concrete as a whole. The thermal

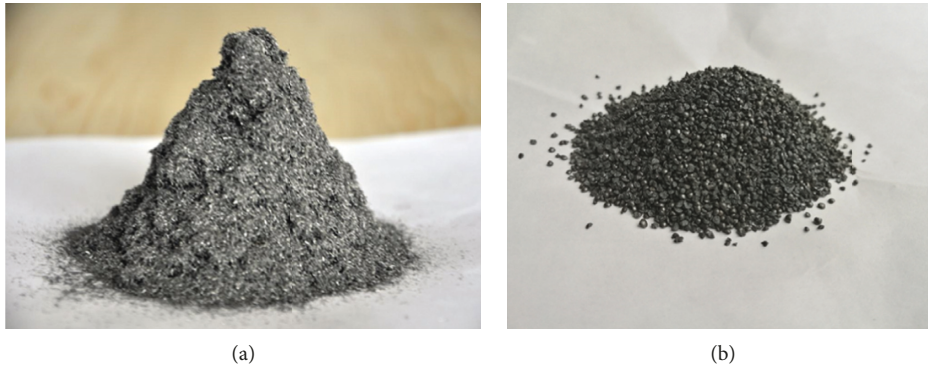


FIGURE 1: Steel wool fiber (a) and steel grit (b).

TABLE 1: The properties of asphalt, steel wool fiber, and steel grit.

Materials	Properties	Values	Specifications
Asphalt	Penetration (25°C, 100 g, 5 s, 0.1 mm)	68	60–80
	Ductility (15°C, cm)	>100	100
	Softening point (°C)	47.5	47
	Density (g/cm <sup>3</sup> )	1.034	—
Steel wool fiber	Average length (mm)	4.2	—
	Equivalent diameter (μm)	70–130	—
	Gravity (g/cm <sup>3</sup> )	7.8	—
Steel grit	Gravity (g/cm <sup>3</sup> )	7.4	—
	Hardness (HRC)	42–50	—

TABLE 2: The impurity element content of steel wool fiber and steel grit.

Materials	Chemical element				
	C (%)	Mn (%)	P (%)	S (%)	Si (%)
Steel wool fiber	0.06–0.12	0.8–1.2	≤0.05	≤0.05	≤0.07
Steel grit	≤0.12	≤2.00	≤0.035	≤0.03	≤1.00

TABLE 3: Steel slag properties.

Test	Size (mm)	Unit	Result	Technical requirement
Apparent relative density	9.5–13.2	—	3.386	≥2.9
	4.75–9.5	—	3.426	
Water absorption	9.5–13.2	%	2.651	≤3
	4.75–9.5	%	3.473	
Crushing value		%	18.9	≤22
Los Angeles wear value		%	20.8	≤22
Needle flake content		%	4.2	≤12
Adhesion grade		Level	5	≥4
Soft stone content		%	0.4	≤3

constants of different asphalt concretes were measured using cylindrical samples with the size of  $\Phi 101.6 \text{ mm} \times 30 \text{ mm}$ . Different types of asphalt concrete Marshall specimens were prepared and cut to be tested at room temperature, as shown in Figure 4.

In the testing process, the particle size of the aggregate may be larger than the diameter of the Hot Disk probe, which leads to the difference of the test results. Therefore, in addition to increasing the parallel test data, the test deviation was reduced by changing the test area for the same test. The

test areas of thermal constants are shown in Figure 5. The straight diameter of the sample is 101.6 mm. The thermal constants were measured in 4 regions of the center, and the mean value was taken for 3 times for each part, that is, 12 times for each kind of asphalt concrete.

**2.4. Induction Heating.** Induction heating test, as shown in Figure 6, was divided into two parts: induction temperature and induction healing, where the distance from the surface

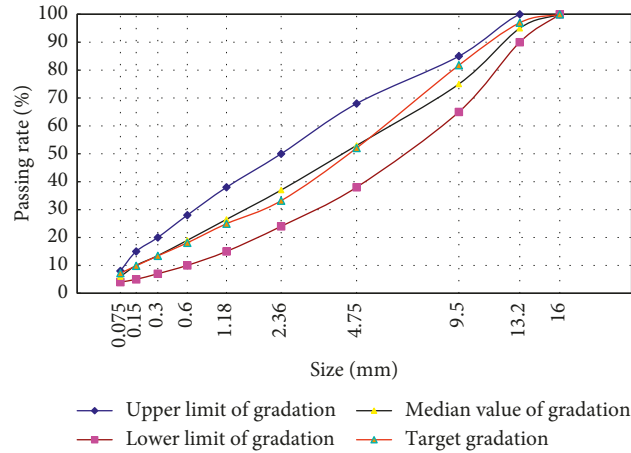


FIGURE 2: Grading curve of AC-13 basalt asphalt mixture.

TABLE 4: Composition of different kinds of asphalt concrete.

AC-13	Component	
	Common	Particular
BA	Basalt, asphalt, limestone fillers, and air void	—
FA		Steel fiber
FSA		Steel fiber and steel slag
FGA		Steel fiber and steel grit
GSA		Steel grit and steel slag
FGSA		Steel fiber, steel grit, and steel slag



FIGURE 3: Asphalt concrete beams.



FIGURE 4: Thermal constant test samples.

frequency of the induction heating apparatus is always 123 kHz. For the induction temperature test, the output power was 7.6 kW, while the power was 8.4 kW for the induction heating test. In order to obtain the best healing performance, the temperature of the induction heating test was set at 85°C, which was verified in the previous research [26]. After each induction heating test, the samples had enough time to recover to ambient temperature. In this study, for Marshall samples, the temperature was the average temperature on the upper surface, while for other samples, the temperature was the average temperature of the sample as a whole.

**2.5. Fracture and Healing Test.** In this study, the three-point bending test was used to evaluate the induction healing performance of asphalt concrete. To avoid creeping, the experimental temperature was below -20°C, as shown in Figure 7 [27]. The load was applied at a rate of 5 mm/min, and the tests were stopped when the discharge curve did not change anymore. The average of ten parallel samples for each type of asphalt concrete was recorded.

The healing rate of asphalt concrete was defined as the relationship between the ultimate force ( $F_0$ ) of the beam during a three-point bending test and the ultimate force ( $F_t$ ) measured in the beam after some time healing, as shown in the following equation:

$$H_i = \frac{F_t}{F_0} \times 100\%. \tag{1}$$

of the sample to the coil was kept constantly at 10 mm [4]. The induction temperatures of both tests were monitored by an infrared camera with a resolution of 320 × 240 pixels. The

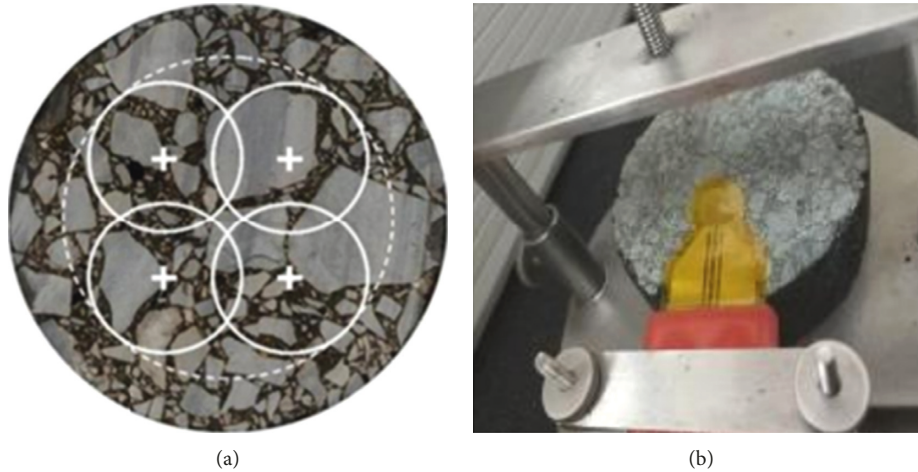


FIGURE 5: Thermal constant test region.

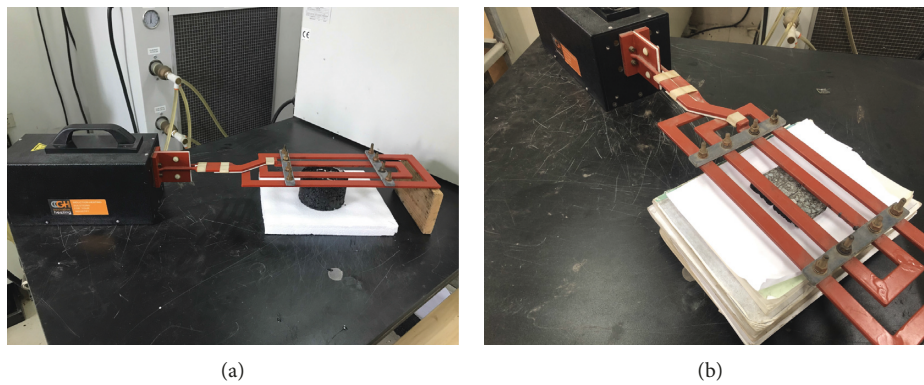


FIGURE 6: Experiment on (a) induction heating temperature and (b) induction healing.



FIGURE 7: Three-point bending test.

### 3. Results and Discussion

**3.1. Thermal Property Analysis.** The difference of thermal conductivity will cause the difference of heat transfer in asphalt concrete. Therefore, the thermal conductivity of asphalt concrete is the factor that needs to be considered in the process of electromagnetic induction healing. The thermal conductivity of different materials varies greatly, among which metals are prominent. The larger the thermal conductivity, the faster the temperature transfers, and the

more uniform the temperature distribution of the pavement is, which is more helpful to avoid the pavement distresses caused by the temperature change. But at the same time, the lower the rate of heat exchange between asphalt concrete and external environment, the more the beneficial to the healing of internal damage of asphalt concrete, because this can make asphalt concrete in the favorable healing temperature range for a longer time. So, our goal was to get an asphalt concrete that had a faster heat transfer rate inside and a slower heat exchange with the outside, which were evaluated by thermal diffusivity and specific heat.

Figure 8 shows the thermal diffusivity and specific heat of different asphalt concretes. From left to right, it was analyzed in turn how the thermal constants of asphalt concrete changed with the addition of steel fiber, steel grit, and steel slag. With the addition of steel fiber, asphalt concrete got higher thermal conductivity and smaller specific heat capacity, which was conducive to the rapid diffusion of internal temperature, but not conducive to the overall thermal insulation of asphalt concrete. Since the thermal conductivity of the metal was much greater than that of the other components of BA, and the specific heat was the opposite, it was easy to understand the change. The addition of steel grit also led to these changes, but the rate of change seemed to be greater, perhaps because steel grit

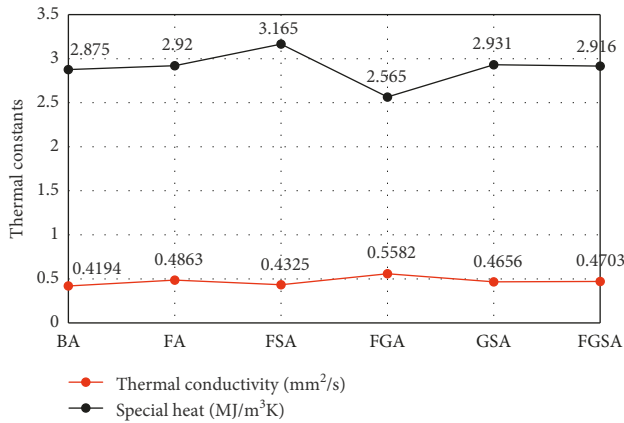


FIGURE 8: Thermal constants of different asphalt concretes.

replaced aggregates, rather than being wrapped in asphalt binders like steel fiber. Although steel slag could not be heated quickly by induction, which would be analyzed in the next section, the addition of steel slag seemed to increase the specific heat of asphalt concrete. For example, FSA reached to 3.165 MJ/m<sup>3</sup>K, which was more conducive to the insulation of asphalt concrete for better induction healing rate. This could be explained by the physicochemical characteristics of steel slag confirmed in the research by Chen et al. [1]. Although the limited metallic components and porous structure led slower induction heating rate of steel slag, its thermal insulation effect was better, and the purpose of using energy more reasonably was achieved. To sum up, although steel slag could not be effectively heated by induction, the asphalt concrete replaced traditional aggregates by steel slag can improve the efficiency of induction energy utilization, which helps to increase the induction healing rate.

**3.2. Induction Heating Temperature Analysis.** Figure 9 shows induction heating ability of steel fiber, steel grit, and steel slag after 5 s when the output power of the induction heating instrument is 8.3 kW. It can be seen that the induction heating abilities of the three materials were in the order of steel fiber > steel grit > steel slag, where steel slag had extremely weak ability for induction heating. Through Wan et al. research [28], only iron and Fe<sub>3</sub>O<sub>4</sub> can be heated by induction. The content of chemical elements and main oxides of steel slag were measured by XRF (PANalytical Axios, RIGAKU ZSX Priums), as shown in Table 5. From the table, it was found that all iron elements exist in the form of Fe<sub>2</sub>O<sub>3</sub>, which did not help much with induction heating.

Figure 10 shows average surface temperature of different kinds of asphalt concretes after induction heating for 60 s, 120 s, and 180 s, and the 120 s infrared image is shown in Figure 11. In the light of the above study, the difference between the induction heating properties of the three materials was very clear. Because the induction heating ability of the steel fiber was better than that of the steel grit, it was observed that the induction heating ability of FSA was better than that of GSA. Therefore, the induction heating ability of conductive additives is paramount for induction heating

asphalt concrete. FGA had the highest induction temperature, reaching 122.5°C after 180 s. Comparing SA with FSA, also FGA with FGSA, it was found that, even though the internal inductive ability of asphalt concretes was the same, the temperature of asphalt concretes added with steel slag was lower than that of basalt after same induction time. This phenomenon verified the conclusion of the previous section. Although the energy generated by induction was the same, the specific heat capacity of asphalt concrete increased after adding steel slag, which resulted in slower temperature rising speed. It was also found that, because of the different induction heating efficiencies of above three materials, the temperature difference of different asphalt concretes became more obvious with time increasing. Higher specific heat can result in slower energy exchange and lower temperature loss, which improve the induction healing rate of asphalt concrete. Therefore, it is harmful to pursue the exorbitant induction heating efficiency, and the heat storage performance of asphalt concrete should also be considered, because too low thermal storage performance and too high induction heating efficiency will cause asphalt concrete to experience more serious thermal expansion. It is more scientific to study the induction heating ability of asphalt concrete on the premise of considering its temperature storage ability.

**3.3. Fracture Resistances.** Figure 12 shows the variation tendency of  $F_0$  of different asphalt concretes. From BA to FA and GSA to FGSA,  $F_0$  increased obviously, resulting from toughening effect of steel fiber. The strength of asphalt concrete with steel fiber is composed of the cohesion of asphalt, the intercalation force between aggregate and aggregate, the tensile stress of fiber, and the adsorption force between fiber and asphalt. The overall strength of asphalt concrete depends on the performance of asphalt, properties of aggregates, and steel fiber. As shown in Figure 13, when ordinary asphalt concrete is subjected to tensile stress, the strength is mainly borne by the cohesion between asphalt. Because asphalt has poor effect of resisting external force, the tensile strength of ordinary asphalt concrete is low. A sudden brittle failure occurs when the ultimate tensile stress is reached. After the addition of steel fiber, the tensile stress is supported by the cohesion of asphalt and the force between asphalt and steel fiber. When asphalt concrete is subjected to force, the cohesion of asphalt first disappears and then relies on the adhesion between asphalt and steel fiber. The tensile stress is transferred to the contact surface of the asphalt and steel fibers, and the tensile strength of the asphalt concrete increases with the addition of fiber because of the enhanced bond between the asphalt and the fiber. From FA to FSA and other asphalt concretes with steel slag,  $F_0$  dropped dramatically. This is contrary to our previous study [4]. Steel slag shows weak alkalinity due to the presence of metal oxides, which is more conducive to the adhesion to asphalt. This should lead to higher fracture strength. In the previous study, after the steel slag replacing the traditional aggregate, the bitumen-aggregate ratio increased, because the porous structure of the steel slag would need more asphalt binders. Therefore, sufficient asphalt can be combined with steel slag

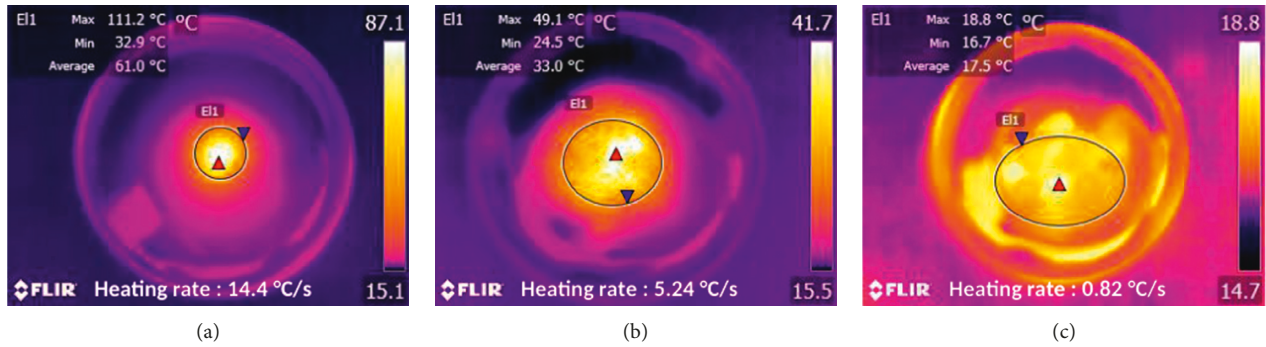


FIGURE 9: Infrared images of steel fiber (a), steel grit (b), and steel slag (c).

TABLE 5: Main chemical elements and oxides of steel slag.

Element (Wt.%)	Si	Fe	Al	Ca	Mg	Na	Ti	K	Px	Mn
	16.85	11.11	5.76	7.75	5.17	1.69	0.858	0.442	0.164	0.202
Oxide (Wt.%)	SiO <sub>2</sub>	Fe <sub>2</sub> O <sub>3</sub>	Al <sub>2</sub> O <sub>3</sub>	CaO	MgO	Na <sub>2</sub> O	TiO <sub>2</sub>	K <sub>2</sub> O	P <sub>2</sub> O <sub>5</sub>	MnO
	36.04	15.89	10.89	10.84	8.58	2.28	1.43	0.532	0.376	0.260

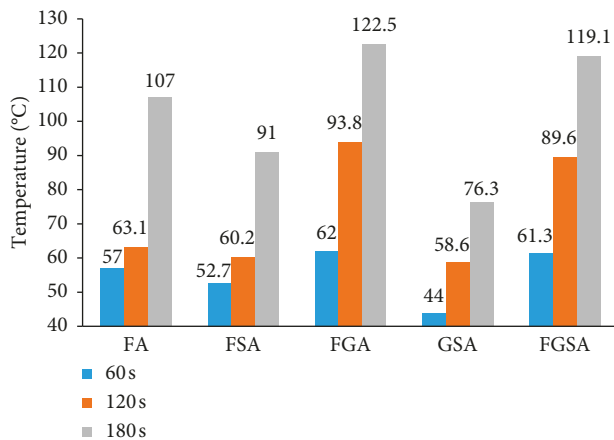


FIGURE 10: Induction heating temperature of asphalt concretes after different induction heating times.

to provide adhesion force. Unfortunately, in this study, in order to control the influencing factors, the bitumen-aggregate ratio was the same for each kind of asphalt concrete, so the asphalt binder of asphalt concrete with steel slag was insufficient, and the fracture strength was affected. Nevertheless, after a reasonable design of the bitumen-aggregate ratio of steel slag asphalt concrete, the steel slag still has a good application prospect in induction heating asphalt concrete because of promoting effect on improving healing rate. Overall, the addition of steel grit had a negative effect on the strength of asphalt concretes. This may be due to the shape and surface properties of the steel grit, which was not conducive to become stronger adhesion with asphalt, and the smooth surface also had a negative effect compared to steel fiber. As shown in Figure 14, the surface of the steel fiber was not a completely smooth structure after magnifying the steel fiber 50 times taken by optical microscope (BXF-150). It could be seen that there were more textures on the surface of steel fiber, and the existence of the

texture enhanced the adhesion between the asphalt and the steel fiber. Thus, the shear stress was increased at the interface. When the stress acting on the interface was greater than the shear strength between the two interfaces, the fiber was gradually pulled out and destroyed, which did not happen on steel grit.

**3.4. Induction Heating Rate.** Figure 15 shows the healing rates of asphalt concretes doped with different conductive additives. Firstly, although the fracture resistances of the samples with steel slag were relatively low, when they were heated to 85°C, the healing rates were high, of which FSA was the highest. The defective bitumen-aggregate ratio led to the decrease of fracture resistance, but the better heat preservation property of steel slag led to a better healing rate of asphalt concretes. In this study, the excellent performance of steel slag was firstly combined with electromagnetic induction heating, which may provide a new direction for the utilization of steel slag. In addition, the steel fiber not only gave the asphalt concrete better healing rate but also improved its fracture resistance. However, the performance of steel grit was unsatisfactory.

#### 4. Conclusions

In this research, the induction heating and healing behaviors of asphalt concretes doped with different conductive additives were investigated. Based on the results discussed above, the following conclusions could be drawn:

- (1) The addition of steel fiber and steel grit made asphalt concretes obtain better thermal conductivity, and the addition of steel slag improved the heat storage performance of asphalt concretes, which was beneficial to induction healing.
- (2) Steel fiber had the best induction heating properties, and its induction heating temperature was 93.8°C

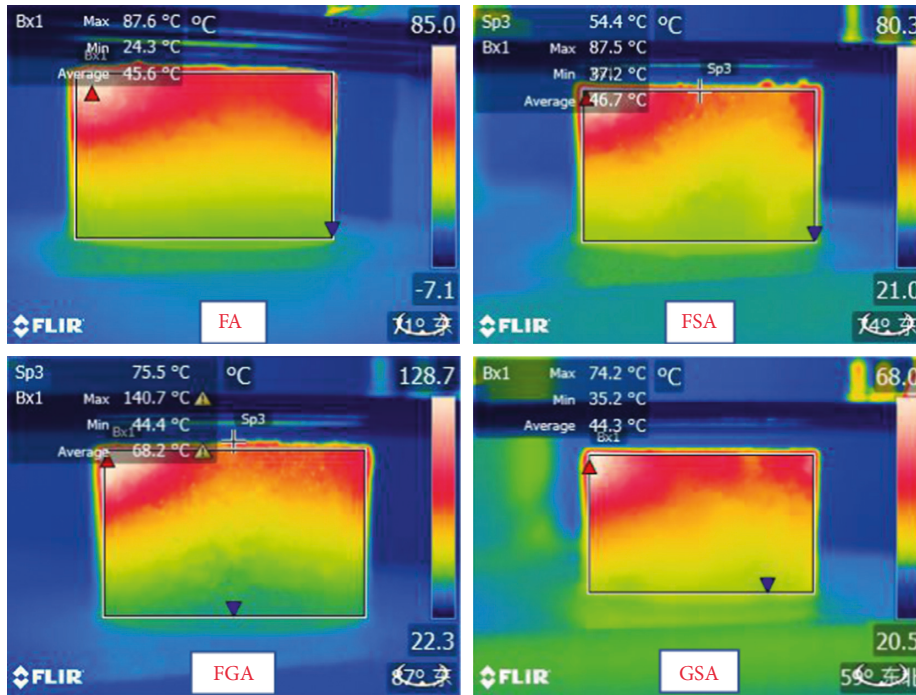


FIGURE 11: Induction heating infrared images of different asphalt concretes after 120 s.

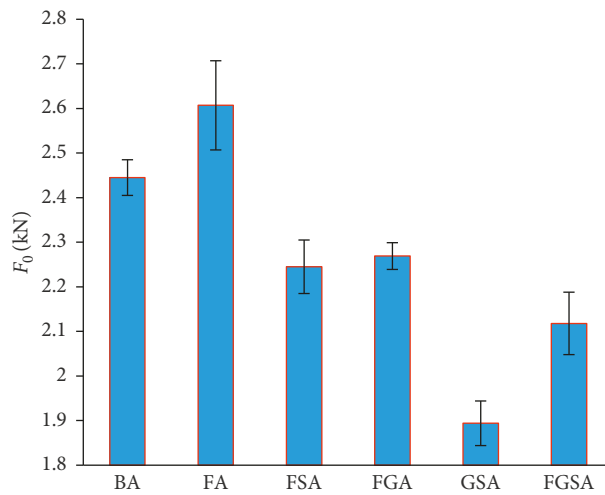


FIGURE 12: Fracture resistance of different asphalt concretes.

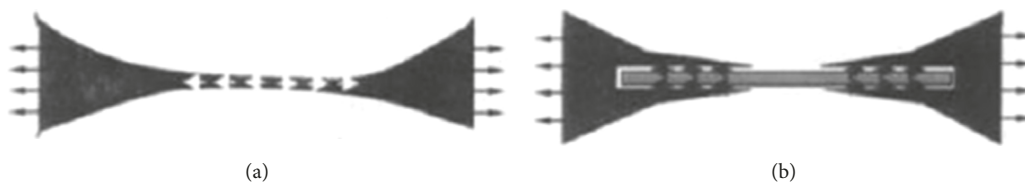


FIGURE 13: Failure mechanism of asphalt concrete: without steel fiber (a) and with steel fiber (b).

after 120 s, the idea of replacing aggregate with steel grit in order to achieve better induction heating efficiency was not very successful, and steel slag had

extremely weak induction heating ability due to the lack of elements or oxides that can be induction heating.

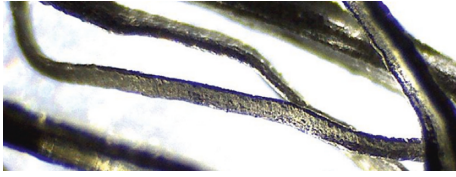


FIGURE 14: Surface texture of steel fiber.

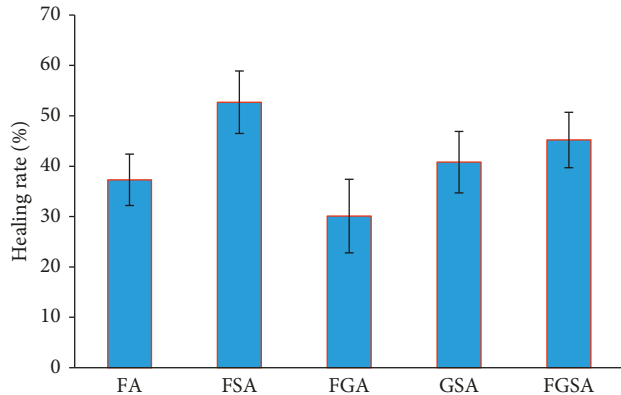


FIGURE 15: Healing rate of different asphalt concretes.

- (3) Although the insufficient bitumen content lowered the mechanical strength of asphalt concretes with steel slag, its better thermal insulation property resulted in higher induction healing rate.
- (4) It was suggested to adding steel slag to induction healing asphalt concrete.

## 5. Future Researches

The pavement performance of asphalt concretes needs to be evaluated and tested, such as high temperature rutting performance test, low temperature cracking performance test, fatigue performance test, water damage performance test, and freeze-thaw cycle test. More types of steel slag need to be evaluated to determine a new index on the application of steel slag in induction healing asphalt concrete.

## Data Availability

The data used to support the findings of this study are available from the corresponding author upon request.

## Conflicts of Interest

The authors declare that they have no conflicts of interest.

## Acknowledgments

This research was funded by National Key R&D Program of China (no. 2017YFE0111600) and National Natural Science Foundation of China (nos. 51778515 and 51508433).

## References

- [1] Z. Chen, S. Wu, Y. Xiao, W. Zeng, M. Yi, and J. Wan, "Effect of hydration and silicone resin on Basic Oxygen Furnace slag and its asphalt mixture," *Journal of Cleaner Production*, vol. 112, pp. 392–400, 2016.
- [2] P. Pan, S. Wu, Y. Xiao, and G. Liu, "A review on hydronic asphalt pavement for energy harvesting and snow melting," *Renewable and Sustainable Energy Reviews*, vol. 48, pp. 624–634, 2015.
- [3] P. Q. Cui, S. P. Wu, Y. Xiao, M. Wan, and P. D. Cui, "Inhibiting effect of layered double hydroxides on the emissions of volatile organic compounds from bituminous materials," *Journal of Cleaner Production*, vol. 108, pp. 987–991, 2015.
- [4] Q. Liu, C. Chen, B. Li et al., "Heating characteristics and induced healing efficiencies of asphalt mixture via induction and microwave heating," *Materials*, vol. 11, no. 6, 2018.
- [5] H. Li, J. Yu, S. Wu, L. Pang, Y. Li, and Y. Wu, "Property of anti-ultraviolet aging of LDHs modified asphalt," *Journal of Wuhan University of Technology-Mater. Sci. Ed.*, vol. 33, no. 3, pp. 634–638, 2018.
- [6] W. Zeng, S. Wu, J. Wen, and Z. Chen, "The temperature effects in aging index of asphalt during UV aging process," *Construction and Building Materials*, vol. 93, pp. 1125–1131, 2015.
- [7] A. Chen, K. Şamlioglu, S. Tayfur, and H. Özen, "Effects of various additives on the moisture damage sensitivity of asphalt mixtures," *Construction and Building Materials*, vol. 19, no. 1, pp. 11–18, 2005.
- [8] Y. Özen, S. Wu, Y. Dai et al., "Investigation of sodium stearate organically modified LDHs effect on the anti aging properties of asphalt binder," *Construction and Building Materials*, vol. 172, pp. 509–518, 2018.
- [9] F. F. Chen and X. M. Huang, "Analysis of the mechanical response of rigid base asphalt pavement under heavy load," *Journal of Highway & Transportation Research & Development*, vol. 6, 2007.
- [10] T. Li, "Study on influence of mineral aggregate gradations and spatial distribution on performance of asphalt mixture," *Advanced Materials Research*, vol. 586, pp. 191–198, 2012.
- [11] T. You, R. K. A. Al-Rub, E. A. Masad et al., "Three-dimensional microstructural modeling framework for dense-graded asphalt concrete using a coupled viscoelastic, viscoplastic, and viscodamage model," *Journal of Materials in Civil Engineering*, vol. 26, no. 4, pp. 607–621, 2013.
- [12] Á. García, E. Schlangen, M. van de Ven, and Q. Liu, "A simple model to define induction heating in asphalt mastic," *Construction and Building Materials*, vol. 31, pp. 38–46, 2012.
- [13] A. García, M. Bueno, J. Norambuena-Contreras, and M. N. Partl, "Induction healing of dense asphalt concrete," *Construction and Building Materials*, vol. 49, pp. 1–7, 2013.
- [14] D. Partl, B. Li, F. Ye et al., "Fatigue behavior of microcapsule-induced self-healing asphalt concrete," *Journal of Cleaner Production*, vol. 188, pp. 466–476, 2018.
- [15] Q. Liu, Á. García, E. Schlangen, and M. v. d. Ven, "Induction healing of asphalt mastic and porous asphalt concrete," *Construction and Building Materials*, vol. 25, no. 9, pp. 3746–3752, 2011.
- [16] Q. Ven, W. Yu, E. Schlangen, and G. van Bochove, "Unravelling porous asphalt concrete with induction heating," *Construction and Building Materials*, vol. 71, no. 71, pp. 152–157, 2014.

- [17] A. van Bochove, A. Garcia, M. N. Partl, G. Tebaldi, and P. Schuetz, "Induction healing of fatigue damage in asphalt test samples," *Construction and Building Materials*, vol. 74, pp. 162–168, 2015.
- [18] A. S. Reddy, R. K. Pradhan, and S. Chandra, "Utilization of Basic Oxygen Furnace (BOF) slag in the production of a hydraulic cement binder," *International Journal of Mineral Processing*, vol. 79, no. 2, pp. 98–105, 2006.
- [19] G. Wang, Y. Wang, and Z. Gao, "Use of steel slag as a granular material: volume expansion prediction and usability criteria," *Journal of Hazardous Materials*, vol. 184, no. 1–3, pp. 555–560, 2010.
- [20] H. Alanyali, L. M., M. Çöl, and Ş. Karagöz, "Concrete produced by steel-making slag (basic oxygen furnace) addition in portland cement," *International Journal of Applied Ceramic Technology*, vol. 6, no. 6, pp. 736–748, 2009.
- [21] Y. Karagöz, H. Hou, and S. Zhu, "Characteristics and mechanisms of phosphate adsorption onto basic oxygen furnace slag," *Journal of Hazardous Materials*, vol. 162, no. 2–3, pp. 973–980, 2009.
- [22] Y. Xue, H. Hou, and S. Zhu, "Competitive adsorption of copper(II), cadmium(II), lead(II) and zinc(II) onto basic oxygen furnace slag," *Journal of Hazardous Materials*, vol. 162, no. 1, pp. 391–401, 2009.
- [23] P. Ahmedzade and B. Sengoz, "Evaluation of steel slag coarse aggregate in hot mix asphalt concrete," *Journal of Hazardous Materials*, vol. 165, no. 1–3, pp. 300–305, 2009.
- [24] Y. Sun, S. Wu, Q. Liu, J. Hu, Y. Yuan, and Q. Ye, "Snow and ice melting properties of self-healing asphalt mixtures with induction heating and microwave heating," *Applied Thermal Engineering*, vol. 129, pp. 871–883, 2018.
- [25] Highway Science Research Institute, *Ministry of Communications, Road Engineering Aggregate Test Code*, China Communication Press, Beijing, China, 1994.
- [26] Q. Liu, E. Schlangen, M. van de Ven, G. van Bochove, and J. van Montfort, "Evaluation of the induction healing effect of porous asphalt concrete through four point bending fatigue test," *Construction and Building Materials*, vol. 29, pp. 403–409, 2012.
- [27] Á. García, "Self-healing of open cracks in asphalt mastic," *Fuel*, vol. 93, no. 1, pp. 264–272, 2011.
- [28] J. Wan, S. Wu, Y. Xiao, Z. Chen, and D. Zhang, "Study on the effective composition of steel slag for asphalt mixture induction heating purpose," *Construction and Building Materials*, vol. 178, pp. 542–550, 2018.

## Research Article

# Assessment Model and Virtual Simulation for Fatigue Damage Evolution of Asphalt Mortar and Mixture

Danhua Wang,<sup>1</sup> Xunhao Ding<sup>1</sup>,,<sup>2</sup> Linhao Gu,<sup>2</sup> and Tao Ma<sup>2</sup>

<sup>1</sup>School of Computer Engineering, Nanjing Institute of Technology, 1 Hongjin Road, Nanjing, Jiangsu 211167, China

<sup>2</sup>School of Transportation, Southeast University, 2 Sipailou, Nanjing, Jiangsu 210096, China

Correspondence should be addressed to Tao Ma; [matao@seu.edu.cn](mailto:matao@seu.edu.cn)

Received 26 October 2018; Accepted 22 November 2018; Published 9 December 2018

Guest Editor: Quantao Liu

Copyright © 2018 Danhua Wang et al. This is an open access article distributed under the Creative Commons Attribution License, which permits unrestricted use, distribution, and reproduction in any medium, provided the original work is properly cited.

Focused on the fatigue performance of the asphalt mortar, this study proposed an assessment model for fatigue damage evolution based on the continuum mechanics. From the perspective of the material scale rather than the macrostructure, the proposed damage model was set by concentrating on the stress-strain state of a tiny point which could characterize the material performance accurately. By the mechanical formula derivation and based on the four-point bending fatigue tests, the damage evolution law was determined and then the proposed model was verified. Based on the finite element method (FEM), a commercial software named ABAQUS was utilized to develop the random mixtures consisting of coarse aggregates, mortar, and voids. Eventually, combined with the damage model and virtual simulation of bending tests, the factors influencing the fatigue resistance of the whole asphalt mixtures were analyzed further.

## 1. Introduction

Asphalt mixture is a three-phase structure consisting of aggregate, void, and mortar [1–3]. The asphalt mortar, acting as a bonding layer between adjacent particles, has been highlighted by many researchers to play an important role in the performance of the whole mixtures [4, 5]. Different from the mixtures, the asphalt mortar consists of the binder, mineral powder, and the fine aggregates only.

Tests conducted by Tan et al. [6] have pointed out that the fine aggregate properties play an important role in the viscoelastic performance of the asphalt mortar. To obtain better viscous properties and low-temperature performance, abundant angular fine aggregates are necessary. Hasan et al. [7] designed and carried out the creep tests of the asphalt mortar. In their tests, four kinds of binder were used including one base binder and three modified ones. It is found that the test environmental temperature along with the binder types all affected the occurrence of the mortar creep in porous asphalt. Permeability loss was more significant when the base binder was used. Wang et al. [8] utilized the rolling thin film oven to reveal the influence of mineral powder on the aging characters of asphalt mortar.

The results showed that when the mass ratio of mineral powder to mortar was less than 1.5, the mineral powder contents had a positive effect on asphalt aging; when the mass ratio of mineral powder to mortar was more than 1.5, increasing the contents of mineral powder could only accelerate asphalt aging. Thus, it is necessary to determine the best ratio of mineral powder during pavement construction. Similar findings have been put forward by many others showing the mortar effects in the whole mixtures [9–11].

Apart from the research studies based on the laboratory tests, many numerical methods such as discrete element method (DEM) and finite element method (FEM) were introduced to illustrate the mechanical behavior of the asphalt mortar. These computational techniques accelerate the related studies and reveal the materials' mechanism from a new perspective [12–15]. Based on these numerical methods, many researchers have done virtual tests to evaluate the performance of the asphalt mortar and concluded some meaningful findings [16–18].

In the road engineering, the main concern is about how to evaluate the fatigue properties of the materials and establish the corresponding mathematical model to predict the

long-term performance of the pavement structure. These fatigue damage evolution models were necessary guarantees for the precise simulations. Only by importing the model into numerical simulation firstly, the outputs from the numerical software can be convinced and valuable. To reveal the long-term behavior of pavements under cyclic vehicle load, many researchers proposed their own damage models [19–23]. However, most of the proposed damage evolution models were developed from the macrostructure scale and could only predict the behavior of the designed composition and structures. The methods characterizing the damage evolution from the material scale still need to be further studied, especially for the asphalt mortar in the road field.

## 2. Objective and Scope

The objective of this study is to establish the fatigue damage evolution model for the asphalt mortar. It is for the mortar material rather than the test structures. To achieve this, the four-point bending fatigue tests and the FEM simulation were utilized together. Prior to processing, several assumptions were made as follows:

- (1) The macrofracture of the aggregate, mortar, and mixtures was not included here, and only the damage evolution was taken into considerations. The damage and fracture are two different stages for the materials [24]. This helps to determine the study scope of this paper, and the damage evolution of the materials was concentrated on only here.
- (2) The damage of the asphalt mortar dominated within the whole mixtures while the coarse aggregates were regarded as the variation of the boundary conditions. It is believed that the damage mainly occurs within the asphalt mortar rather than the aggregates. Because the properties of aggregates are not changed mostly under the cyclic loading, few of the particles will break. Oppositely, the interfaces between aggregates and mortar and the inner area of the mortar tend to generate microcracks more easily which leads to a performance decline. And this is the main cause of the fatigue damage. So, the damage of the asphalt mortar rather than the mixtures was studied here.
- (3) Due to the low temperature of the designed tests, the viscoelastic characteristics of asphalt mixtures could be neglected temporary, and the mixtures were regarded as elastic materials [25]. Thus, the fatigue damage evolution models of the asphalt mortar could be derived based on the linear elastic theory.

The rest of this paper is organized as follows. Section 3 mainly introduces the materials, apparatus, simulation methods, and the derivation of the fatigue damage evolution formulas. In Section 4, the damage evolution law and the major factors on the damage process are analyzed based on the laboratory tests. Moreover, the validation of the proposed model is verified and is applied

within the FEM simulation to predict structure performance further. Finally, some research findings are summarized in Section 5.

## 3. Methodology and Experimental

**3.1. Materials.** The asphalt binder, mineral powder, and aggregates were prepared for this study. Prior to laboratory tests, the base properties of materials were measured firstly to meet the requirements of the Chinese Technical Specification for Construction of Highway Asphalt Pavement [26]. The summaries of the material properties are shown in Tables 1–3. Two types of the specimens are needed in the following process: (a) asphalt mixtures consisting of asphalt binder, mineral powder, and aggregates and (b) asphalt mortar consisting of asphalt binder, mineral powder, and the fine part of aggregates. The testing gradation of the asphalt mixture is shown in Figure 1(a) meeting the requirements of Chinese standard [26]. Since the aggregates smaller than 2.36 mm are regarded as part of asphalt mortar, the specific content of the fine aggregates within mortar can be determined based on the mixture gradation as shown in Figure 1(b). This recalculation of the mortar gradation is necessary to keep the other compositions same as the prepared mixtures. Only the coarse aggregates should be extracted.

**3.2. Laboratory Test.** According to the Chinese specification named Standard Test Methods of Bitumen and Bituminous Mixtures for Highway Engineering (T0739-2011) [27], the four-point bending beam fatigue tests based on the universal testing machine (UTM) were selected to evaluate the fatigue performance of the asphalt mortar and asphalt mixture. The fatigue tests of asphalt mortar were used to obtain model parameters and to study the influencing factors of fatigue performance. Three major factors were taken into consideration and varied during the test process, including the test temperature (5°C and 10°C), loading strain (700  $\mu\epsilon$  and 1000  $\mu\epsilon$ ), and the asphalt content of mortar (4.3%, 4.8%, and 5.5%). Hereafter, in this study, the asphalt content of 4.3%, 4.8%, and 5.5% was referred to as low, moderate, and high contents, respectively. One fatigue test of asphalt mixture under the condition of 5°C, 700  $\mu\epsilon$  and moderate asphalt content was conducted. The test data were used to verify the FE model of asphalt mixture. The tests were conducted strictly according to the Chinese standard [27], and the bending stiffness modulus was calculated as shown in equations (1)–(3). A load with haversine amplitude is applied to simulate the strain-control loading condition (10 Hz). The fatigue life was defined as the load cycles when the bending stiffness modulus decreased to 50% compared to the initial one:

$$\sigma_t = \frac{(L \times P)}{(w \times h^2)}, \quad (1)$$

where  $\sigma_t$  is the maximum tensile stress of the centre bottom of the test beam, Pa;  $L$  is the length of the test beam, m;  $P$  is

TABLE 1: Base properties of asphalt binder.

Index	Results	Requirements
Penetration (25°C, 100 g, 5s)/0.1 mm	71	60–80
Ductility (10°C)/cm	31.3	≥20
Softening point (°C)	48.2	≥46
Flash point (°C)	287	260
Density (g/cm <sup>3</sup> )	1.031	—

TABLE 2: Base properties of mineral powder.

Index	Results	Requirements
	<0.6 mm	100
Granularity (%)	<0.15 mm	96.5
	<0.075 mm	85.3
		100
		90–100
		75–100

peak load during test,  $N$ ;  $w$  is the width of the test beam, m; and  $h$  is the height of the test beam, m.

$$\varepsilon_t = \frac{(12 \times \delta \times h)}{(3 \times L^2 - 4 \times a^2)}, \quad (2)$$

where  $\varepsilon_t$  is the maximum tensile strain of the centre bottom of the test beam, m/m;  $\delta$  is the maximum deflection of the beam centre, m; and  $a$  is the spacing distance between two adjacent chucks.

The bending stiffness modulus was defined as follows:

$$S = \frac{\sigma_t}{\varepsilon_t}, \quad (3)$$

where  $S$  is the bending stiffness modulus, Pa;  $\sigma_t$  is the maximum tensile stress of the centre bottom of the test beam, Pa; and  $\varepsilon_t$  is the maximum tensile strain of the centre bottom of the test beam, m/m.

The damage of the centre bottom of the test beam at the  $N$ th load cycle was calculated as follows:

$$D_N = 1 - \frac{S_N}{S_0}, \quad (4)$$

where  $D_N$  is the damage at the  $N$ th load cycle;  $S_N$  is the bending stiffness modulus at the  $N$ th load cycle, Pa; and  $S_0$  is the initial bending stiffness modulus, which is the bending stiffness modulus at the 50th load cycle according to the Chinese specification [27].

### 3.3. Fatigue Damage Model Development for Asphalt Mortar.

As a design index according to the Chinese standard [26], the requirement of the tensile strain in the layer bottom is much more significant to ensure fatigue resistance. Thus, only focused on the tensile damage, which dominated within the pavement structure under the cyclic load, the tensile damage evolution model was proposed to characterize the mixture performance. Since the bending stiffness modulus ( $S$ ) obtained from the tests can only represent the structure performance, it is a macroindex characterizing the whole beam rather than materials. Thus, the fatigue damage model was developed further. Based on the principle of the continuum mechanics, when all the external load, boundary conditions, and structure size are

determined, the stress-strain state of point C can be obtained obviously. By establishing the mathematic relation of damage between the beam structure and centre bottom point, the damage evolution model of a tiny point can be obtained. And this point damage model is regarded as the micromaterial properties under the cyclic load regardless of the macrostructures. The details of the fatigue damage model are shown in Figure 2.

$D_c$ ,  $\varepsilon_c$ , and  $\sigma_c$  are defined as the damage, strain, and stress of point C after  $N$  times cyclic load, while the  $D$ ,  $\varepsilon$ , and  $\sigma$  are the damage, strain, and stress of random points in the cross section of the beam after  $N$  times cyclic load. The constitutive model and fatigue damage evolution model are developed as an initial form as shown in equations (5) and (6).

The constitutive model:

$$\sigma = (1 - D)E\varepsilon. \quad (5)$$

The fatigue damage evolution model:

$$\frac{dD}{dN} = A[\varepsilon(1 - D)]^p, \quad (6)$$

where  $E$  is the elastic modulus and  $A$  and  $p$  are the coefficients to be determined, related to the material properties.

When derived the evolution formulas for mortar, the mortar was assumed as an isotropic continuum medium. So the four-point bending fatigue test for mortar could be regarded as a plane stress problem. The stress and strain vertical to the cross section were selected for formula derivation then. For random points in the cross section of the beam, equilibrium condition should be reached at any time, and then equations (8) and (9) can be obtained as follows:

$$\int_0^1 \sigma wh d\lambda = 0, \quad (7)$$

$$\int_0^1 \sigma wh^2 \lambda d\lambda = M, \quad (8)$$

$$\lambda = \frac{y}{h}, \quad (9)$$

where  $\lambda$  is the relative position of random points along the Y-coordinates direction;  $y$  is the Y-coordinates of the random points;  $M$  is the bending moment of the cross section of the beam, N·m; and the other parameters are the same as the formers.

Since the cyclic load, more microcracks and microholes will appear during the process especially in the centre bottom area of the beam. This causes damage and will make the neutral axis move upwards gradually. Thus,  $\lambda_N$  is proposed and defined as the new position of the neutral axis after  $N$  times cyclic load as follows:

$$\lambda_n = \frac{y_n}{h}, \quad (10)$$

where  $\lambda_n$  is the relative position of neutral axis along the Y-coordinates direction after  $N$  times cyclic load;  $y_n$  is the

TABLE 3: Base properties of aggregates.

Coarse part						
Size (mm)	16-13.2	13.2-9.5	9.5-4.75	4.75-2.36		
Density (g/cm <sup>3</sup> )	2.771	2.791	2.688	2.735		
Fine part						
Size (mm)	2.36-1.18	1.18-0.6	0.6-0.3	0.3-0.15	0.15-0.075	<0.075
Density (g/cm <sup>3</sup> )	2.715	2.718	2.716	2.717	2.720	2.752

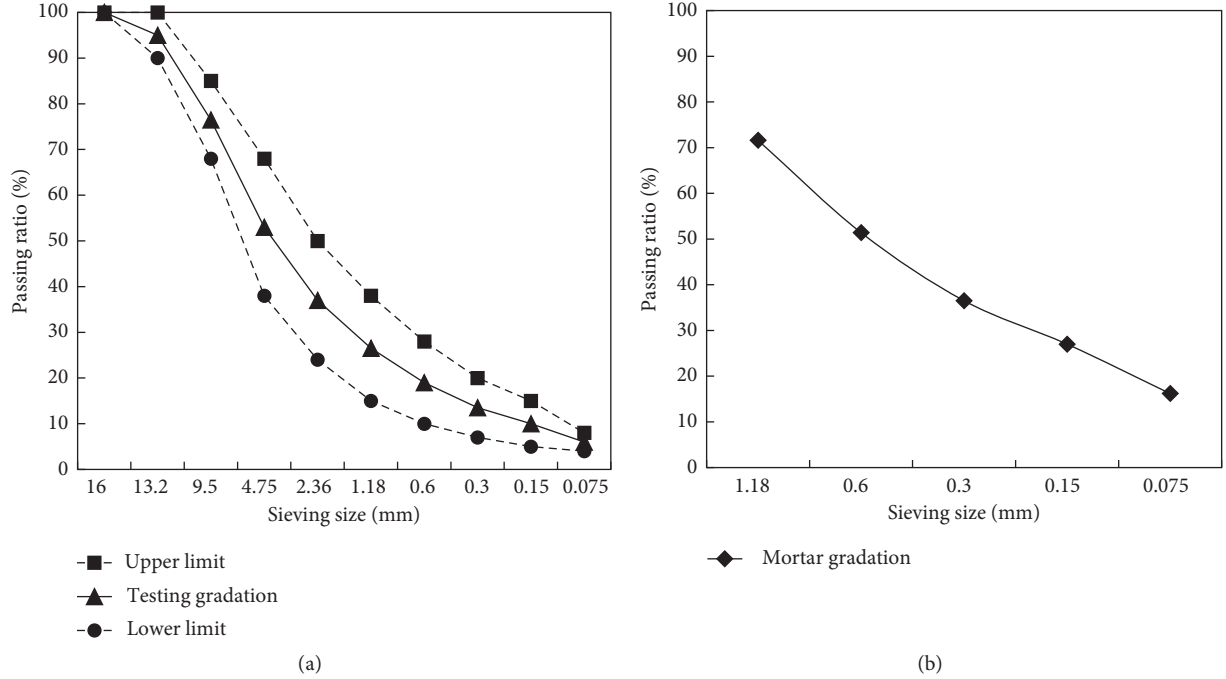


FIGURE 1: Testing gradations: (a) gradations for the asphalt mixtures; (b) gradations for the asphalt mortar.

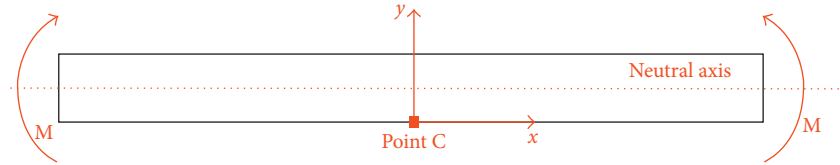


FIGURE 2: Fatigue damage of the point C.

Y- coordinates of the neutral axis after  $N$  times cyclic load,  $m$ ; and the other parameters are the same as the formers.

Substituting equation (5) into equations (8) and (9), we obtain

$$\int_0^{\lambda_n} whE(1-D)\varepsilon d\lambda + \int_{\lambda_n}^1 whE\varepsilon d\lambda = 0, \quad (11)$$

$$\int_0^{\lambda_n} wh^2E(1-D)\varepsilon\lambda d\lambda + \int_{\lambda_n}^1 wh^2E\varepsilon\lambda d\lambda = M,$$

where the parameters are the same as the formers.

In the strain control mode, the strain of the centre bottom of the beam remains the same; thus, we obtain

$$\varepsilon = \frac{y}{\rho}, \quad (12)$$

where  $\rho$  is the curvature of the beam.

Defining  $\eta = (\lambda_n - \lambda)/\lambda_n$  and substituting it into equation (12), the strain of random points can be obtained as follows:

$$\varepsilon = \varepsilon_c \eta, \quad (13)$$

$$d\lambda = -\lambda_n d\eta. \quad (14)$$

Substituting equations (13) and (14) into (9), we obtain

$$\int_0^1 \eta D d\eta = \frac{1}{\lambda_n} - \frac{1}{2\lambda_n^2}, \quad (15)$$

$$\int_0^1 \eta \left[ \int_0^N \left( \frac{dD}{dN} \right) dN \right] d\eta = \frac{1}{\lambda_n} - \frac{1}{2\lambda_n^2}. \quad (16)$$

Taking equation (6) into (16), we obtain

$$\int_0^N A[\varepsilon(1-D)]^p dN = 2\left(\frac{1}{\lambda_n} - \frac{1}{2\lambda_n^2}\right). \quad (17)$$

To the point C,  $\lambda = 0$ , combined with the equation (6), we obtain

$$\int_0^N A[\varepsilon_c(1-D_c)]^p dN = D_c. \quad (18)$$

The damage of the point C can be determined through equations (17) and (18) as follows:

$$D_c = 2\left(\frac{1}{\lambda_n} - \frac{1}{2\lambda_n^2}\right). \quad (19)$$

The unknown parameter  $\lambda_n$  can be solved through equation (19) as follows:

$$\lambda_n = \frac{1}{1 + \sqrt{1 - D_c}}. \quad (20)$$

Apply the integral operation on both sides of equation (6), the fatigue damage evolution model for each point can be developed as shown in equation (21), and the Point C is shown in equation (22):

$$D = 1 - [1 - (-p + 1)A\varepsilon^p N]^{1/(-p+1)}, \quad (21)$$

$$D_c = 1 - [1 - (-p + 1)A\varepsilon_c^p N]^{1/(-p+1)}. \quad (22)$$

**3.4. FEM Modelling of Asphalt Mixture.** Virtual models were developed based on the FEM software named ABAQUS. Two model forms were taken into consideration. One is the virtual asphalt mortar and another is the asphalt mixtures. The virtual four-point bending fatigue tests for mortar were carried out to verify the FEM implementation of the proposed fatigue damage model. After that, the precise damage model of the mortar was imported into the virtual mixtures, and the virtual four-point bending fatigue tests for mixture were conducted. The simulation results were compared with the laboratory results of asphalt mixture to verify the mesostructure FE model. More simulations were conducted to analyze the effect of air void on damage evolution.

The coarse aggregates were regarded as pure elastomer without any damage evolution. When conducted the virtual tests, Young's modulus and Poisson's ratio of the coarse aggregates were set as 5.55 GPa and 0.15, respectively. The virtual specimens were developed with a 377 mm length and 50 mm height in two dimensions, which were identical to the realistic. The final virtual specimens for asphalt mixture are shown in Figure 3(a). Free meshing algorithm with quad-dominated element shape was used. And the type is CPS8R (an 8-node biquadratic plane stress quadrilateral, reduced integration). The green, white, and red areas represent aggregates, asphalt mortar, and air voids, respectively. Asphalt mortar was considered as an isotropic material, and its FE model is shown in Figure 3(b). Structured meshing

algorithm with quad element shape was used. And the element type is also CPS8R.

As shown in Figure 3(c), the position of four virtual clamps was the same as the real test. Clamp C was fixed in all degrees of freedom. A vertical displacement boundary condition with haversine amplitude was applied to clamp A to simulate the strain-control loading condition (10 Hz, 700  $\mu\epsilon$ , and 1000  $\mu\epsilon$ ). The horizontal displacement and rotation of clamp A were constrained. The clamps were connected to the sample using surface-to-surface contact with geometric properties. The clamps were considered as pure elastomer with Young's modulus far greater than that of the sample.

The virtual mixtures including the asphalt mortar, irregular shape voids, and coarse aggregates were also developed in ABAQUS. Prior to FEM modelling, pre-processing for the random composition generations was completed based on Matlab. A user-defined routine was coded in Matlab to help develop the irregular shapes of particles and finally form the total mixtures as shown in Figures 4 and 5. As shown in Figure 4, polar coordinates were utilized in the irregular shapes plotting. Several groups of coordinate values were determined randomly within a designed range firstly and then a circumscribing polygon was plotted to form the final shapes. When developed the mixtures, particles of different grades were generated in turns based on their sizes. As shown in Figure 5, the rectangle was plotted as a virtual container, and then particles of 16 mm size were plotted firstly followed by 13.2 mm, 9.5 mm, 4.75 mm, etc. After the particle generations were completed, the voids were plotted in the same way. As shown, three kinds of mixtures were developed randomly. The blue lines represented the coarse aggregates while the red ones are the voids. The percent air voids in bituminous mixtures (VV) were 0%, 4%, and 8%, and the percent voids in mineral aggregate in bituminous mixtures (VCA) were 32.3%, 32.1%, and 30.7%, respectively. It should be noted that when plotted the irregular shapes of particles and voids, a judgment routine was conducted in Matlab to avoid the shape overlaps. If there existed a particle or void already, the next particle or void generation would not be permitted here until another available location was found. After the mixture images were generated successfully finally, they were imported to ABAQUS for structure and mesh generations as shown in Figure 6.

### 3.5. Model Parameter Determination of the Asphalt Mortar.

Since the damage evolution of the asphalt mortar dominates within the whole mixtures, its model should be further specified by determining the related parameters. As illustrated in equation (22), the fatigue damage variable is related to two material parameters ( $A$  and  $p$ ). A nonlinear minimization algorithm using differential evolution method is performed on the target error function  $F$  as

$$\min F(A, p) = \frac{1}{N} \sqrt{\sum_{i=1}^N \left(1 - \frac{D_{c,i}}{D_{t,i}}\right)^2}, \quad (23)$$

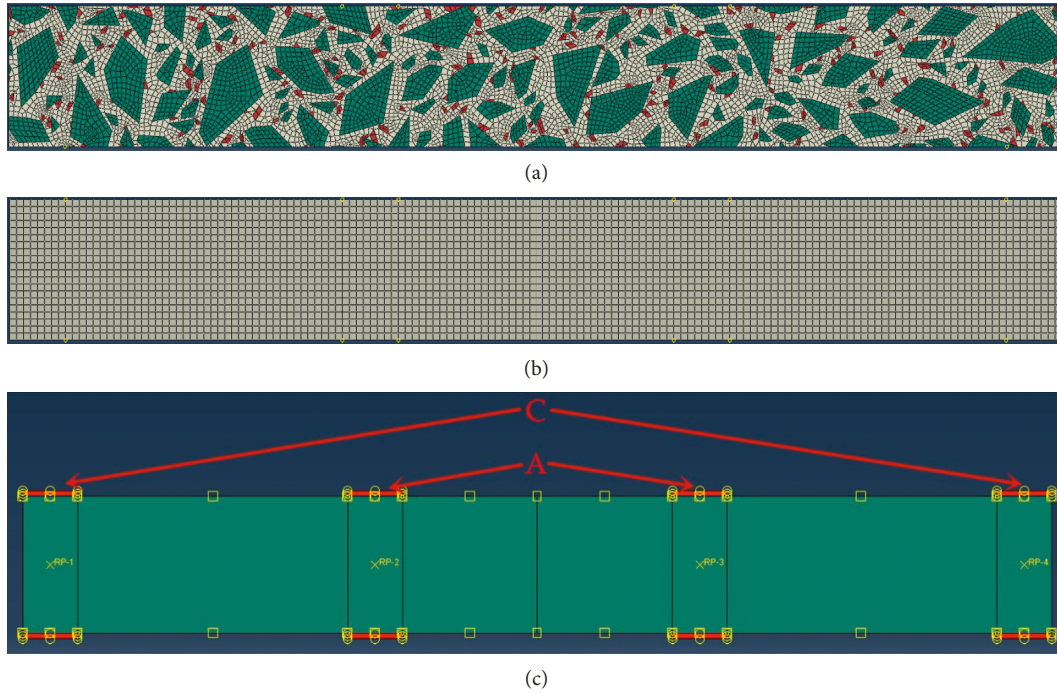


FIGURE 3: FEM modelling: (a) asphalt mixture sample; (b) asphalt mortar; (c) clamps.

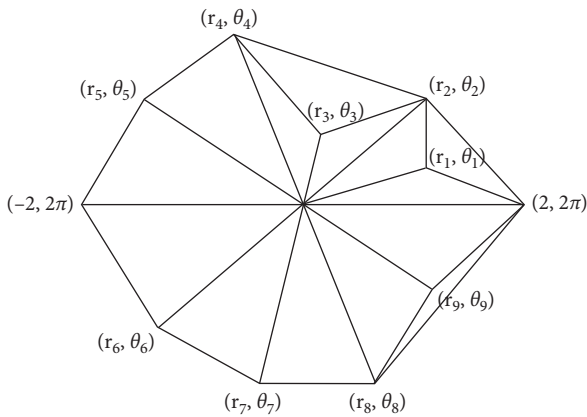


FIGURE 4: Irregular shape modelling for particles.

where  $D_{c,i}$  is the calculated damage and  $D_{t,i}$  is the damage obtained from laboratory results using equation (4).

By fitting the laboratory results, these undetermined parameters could be confirmed. Figures 7 and 8 are the fitting results of the proposed fatigue damage evolution models. Different conditions including the temperature, loading strain, and asphalt content were taken into considerations. The values of  $A$  and  $p$  applied for these conditions are all calibrated and summarized in Table 4. As shown in Figures 7 and 8, it is concluded that the proposed damage model could well characterize the fatigue performance of the asphalt mortar in the first two stages. In the third stage, the damage evolved rapidly converting the inner microcracks into macrofracture. In this stage, the macrocracks dominated, and therefore the modulus of the structure decreased sharply. Thus, focusing on the damage

evolution only without the macrofracture mechanism, the fitting lines could only characterize the first two stages. And it has been verified in Figures 7 and 8 that the proposed damage evolution models could well predict the performance of asphalt mortar before fracture.

## 4. Results and Discussion

**4.1. Analysis of the Laboratory Fatigue Tests.** The results of the four-point bending fatigue tests in laboratory are summarized in Figures 9 and 10. Figure 9 illustrates the influences of the temperatures and strain levels on the fatigue performance of asphalt mortar. As shown in Figure 9, when compared the curves of  $5^{\circ}\text{C}$ ,  $700\ \mu\epsilon$  with the  $5^{\circ}\text{C}$ ,  $1000\ \mu\epsilon$  in Figures 9(a)–9(c), it is concluded that the strain level has a negative effect on the changes of the bending stiffness modulus ( $S$ ). When comes to the curves of  $5^{\circ}\text{C}$ ,  $1000\ \mu\epsilon$  and  $10^{\circ}\text{C}$ ,  $1000\ \mu\epsilon$ , it is found that as the temperature increases, the asphalt mortar will have better fatigue resistances. Moreover, the strain level plays a much more important role than temperature in affecting the fatigue performance of asphalt mortar which can be obviously summarized from Figure 9. The fatigue lives of  $5^{\circ}\text{C}$ ,  $700\ \mu\epsilon$  are much more than the  $10^{\circ}\text{C}$ ,  $1000\ \mu\epsilon$  despite the asphalt content. It is believed that the load strain decreased by  $300\ \mu\epsilon$  has a more positive effect than increasing the temperature by  $5^{\circ}\text{C}$ . Thus, avoiding the heavy traffic is significant to maintain the pavement permanent performance. As for Figure 9(c), different trends could be also found that the bending stiffness modulus ( $S$ ) of the  $5^{\circ}\text{C}$ ,  $1000\ \mu\epsilon$  was a litter larger than the other two at high asphalt contents. This is because of the lowest temperature and largest strain level which are the worst conditions for the mortar. When the asphalt content is high, the lower

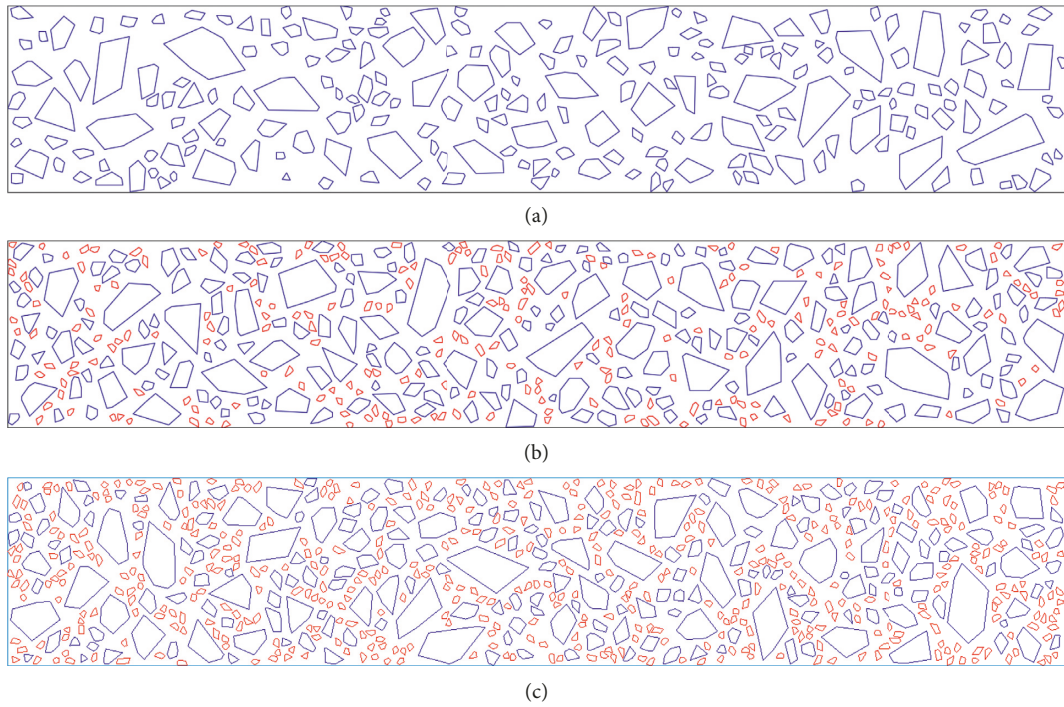


FIGURE 5: Irregular shape modelling for mixtures: (a) VCA = 32.3%, VV = 0%; (b) VCA = 32.1%, VV = 4%; (c) VCA = 30.7%, VV = 8%.

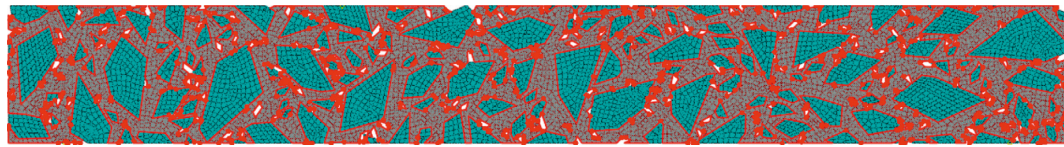


FIGURE 6: Final FEM modelling for the asphalt mixtures.

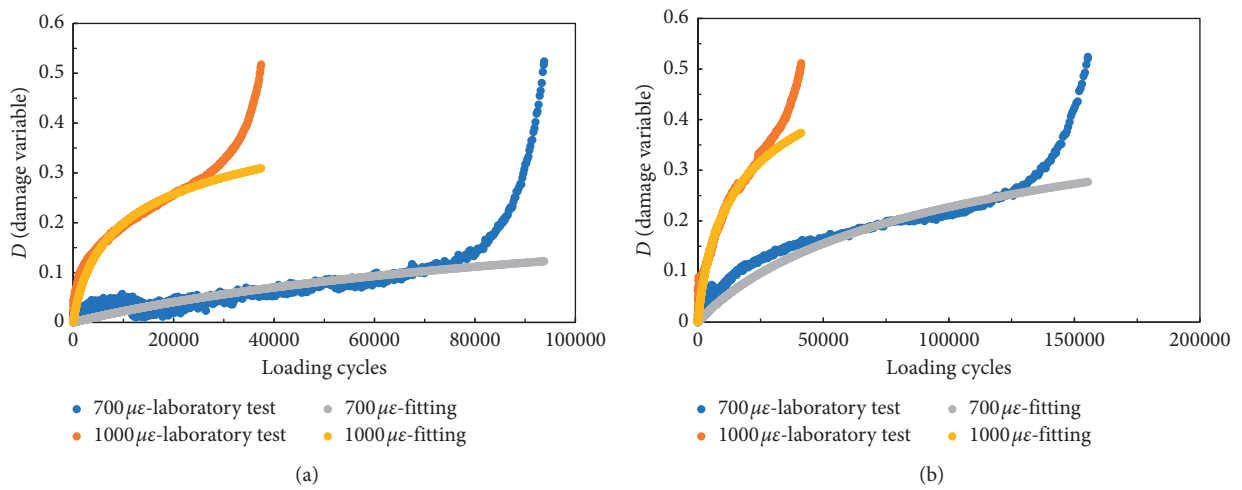


FIGURE 7: Continued.

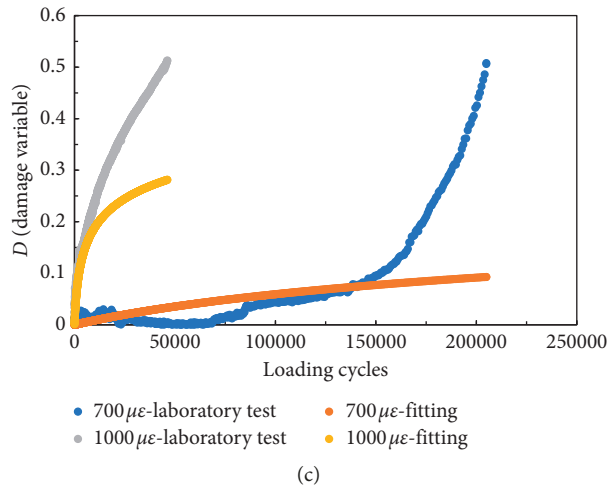


FIGURE 7: Fatigue performance prediction of the asphalt mortar at 5°C: (a) low asphalt content; (b) moderate asphalt content; (c) high asphalt content.

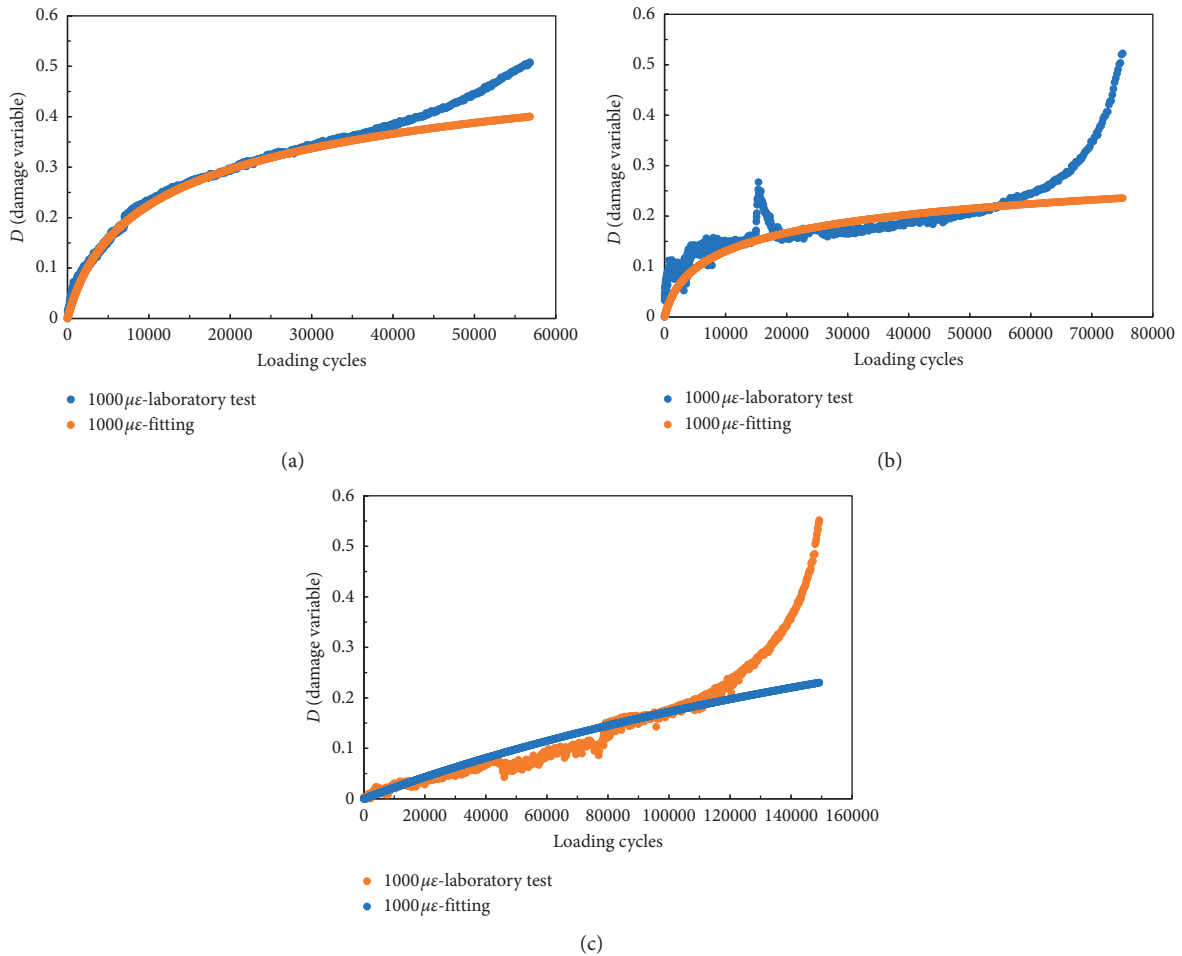


FIGURE 8: Fatigue performance prediction of the asphalt mortar at 10°C: (a) low asphalt content; (b) moderate asphalt content; (c) high asphalt content.

temperature means the beam structure is more similar to the elastic solid. So, the performance of the mortar at the high asphalt content was slightly different from the low and

moderate ones. With the worst conditions (highest asphalt content at the lowest temperature), the mortar would become stiffer than others. So, the bending stiffness

TABLE 4: Fitting parameters of the proposed damage evolution model under different conditions.

Asphalt content (%)	Temperature (°C)	Loading strain ( $\mu\epsilon$ )	$A$	$p$
Low	5	700	$6.1e - 5$	9
	5	1000	$6.1e - 5$	9
	10	1000	$6e - 5$	7
Moderate	5	700	$4.7e - 5$	6.1
	5	1000	$4.7e - 5$	6.1
	10	1000	$4.6e - 5$	15.7
High	5	700	$9.3e - 5$	13
	5	1000	$9.3e - 5$	13
	10	1000	$2.3e - 6$	3

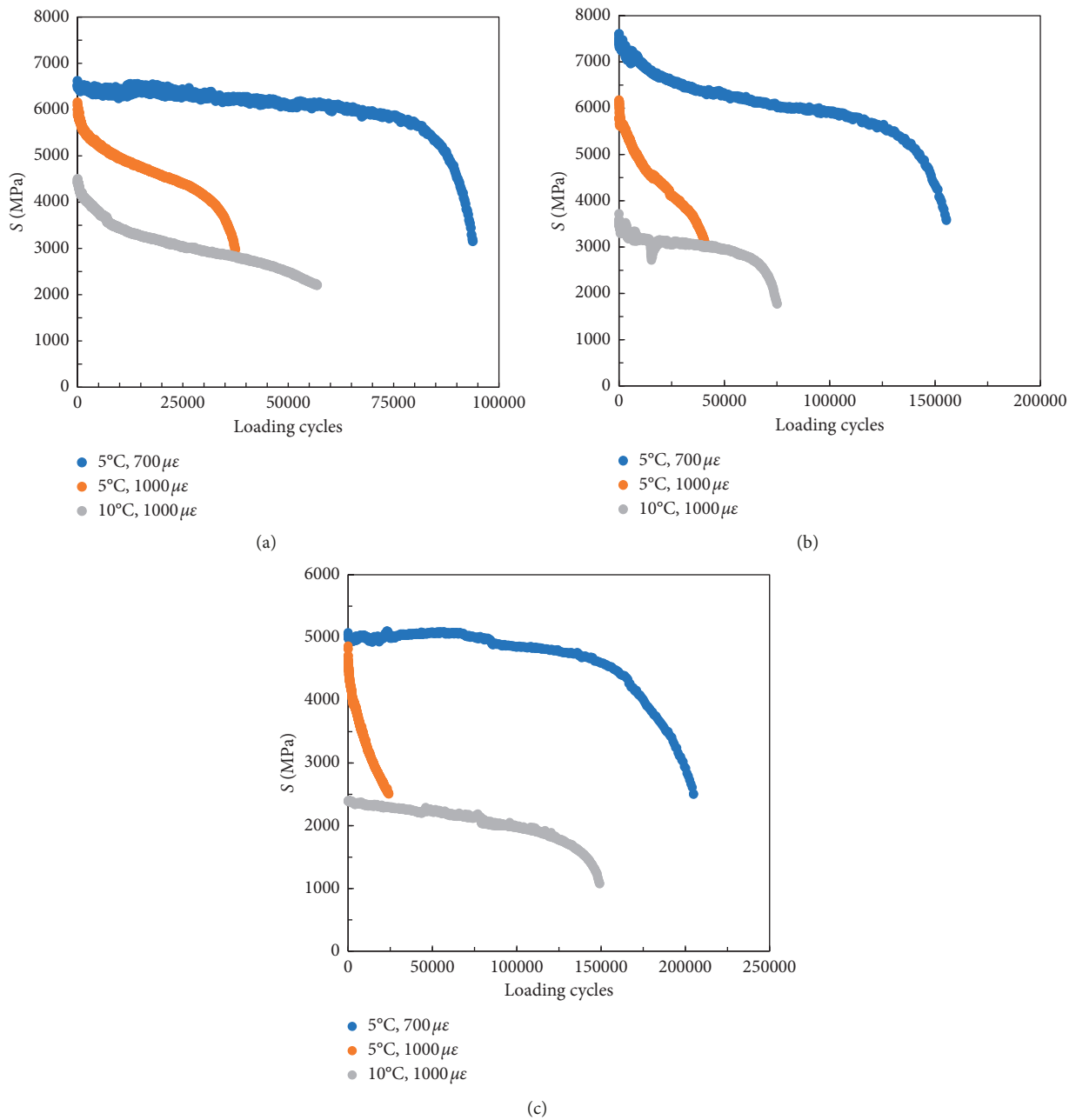


FIGURE 9: Influences of the temperatures and strain levels on the fatigue performance of asphalt mortar: (a) low asphalt content; (b) moderate asphalt content; (c) high asphalt content.

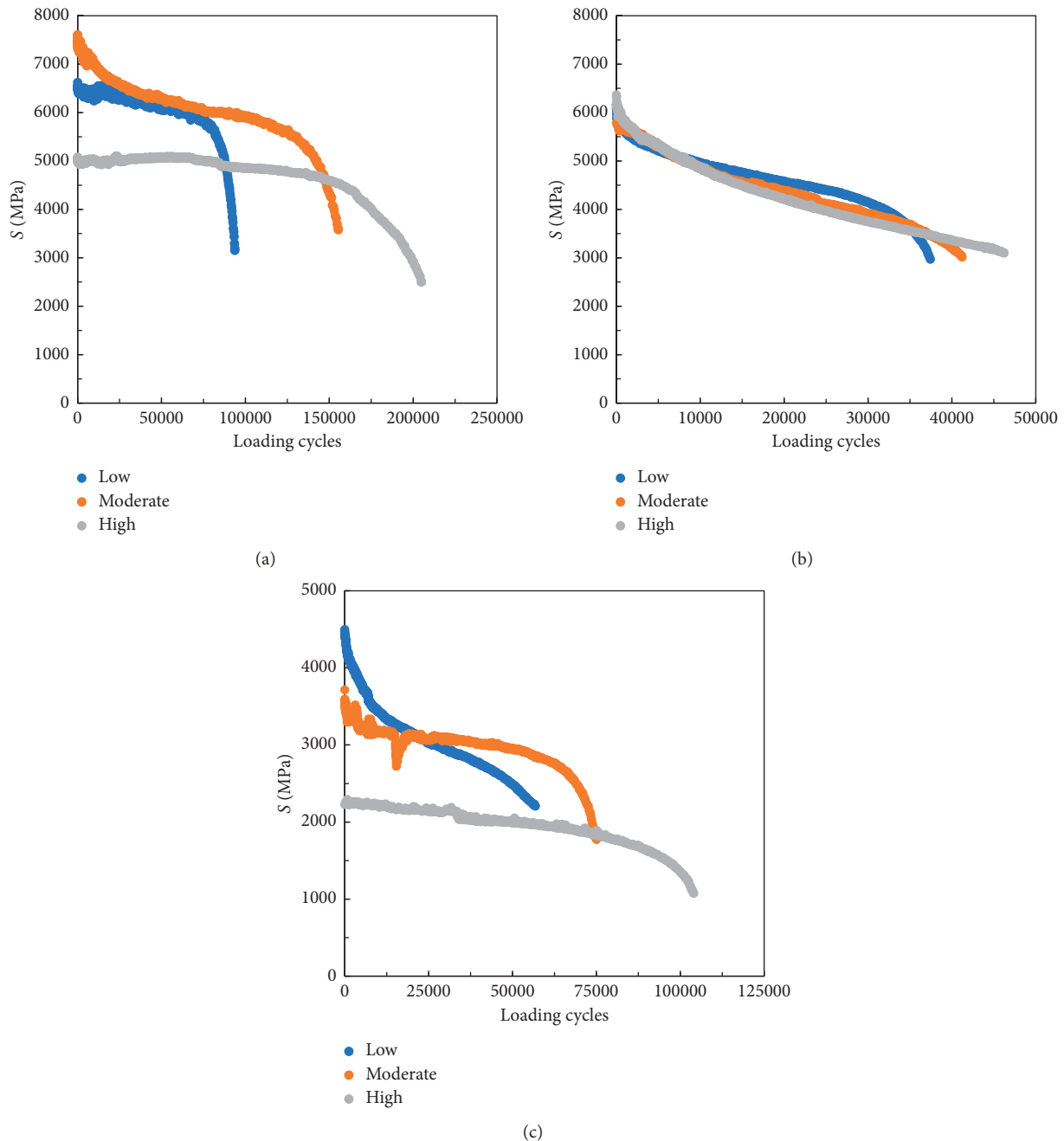


FIGURE 10: Influences of the asphalt content on the fatigue performance of asphalt mortar: (a) 5°C, 700  $\mu\epsilon$ ; (b) 5°C, 1000  $\mu\epsilon$ ; (c) 10°C, 1000  $\mu\epsilon$ .

modulus ( $S$ ) of the 5°C, 1000  $\mu\epsilon$  was a little larger than the other two at the beginning. Under the largest strain level of 1000  $\mu\epsilon$ , it would decline sharply at the fastest speed which could be seen in Figure 9(c).

Figure 10 shows the influences of the asphalt content on the fatigue performance of asphalt mortar. As shown, the asphalt content has a positive effect on the fatigue performance of the asphalt mortar despite the loading conditions. Compared to the asphalt mixtures, although there is no coarse aggregate skeleton, the curve trends of the mortar also go through three stages known as starting stage, stable stage, and unstable stage. It is a rough verification of the

assumption that the damage evolution mainly processed within the mortar and the aggregates only form the skeleton in mixtures. From the perspective of mechanical calculation, these coarse aggregates can be regarded as boundary conditions directly.

*4.2. Verification of the FEM Implementation of the Fatigue Damage Model.* The proposed fatigue damage model was implemented into the ABAQUS software via UMAT user subroutine. The FE model of the asphalt mortar was constructed as described in Section 3.4. In the real test,

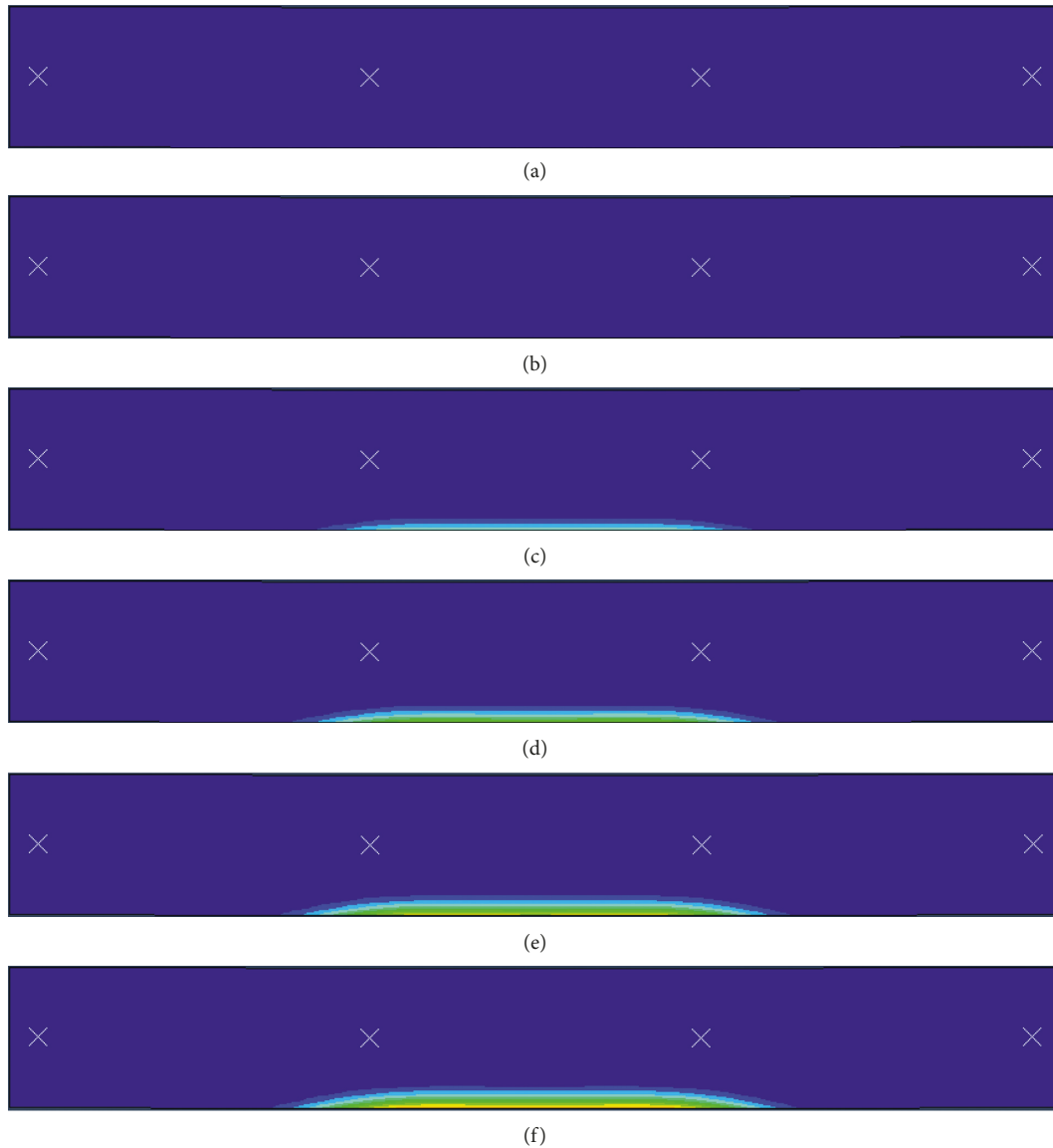


FIGURE 11: Damage evolution of asphalt mortar with load cycles. (a) Load cycles  $N = 200$ ,  $D_{\max} = 2.041e - 4$ ; (b) load cycles  $N = 2000$ ,  $D_{\max} = 5.492e - 3$ ; (c) load cycles  $N = 20000$ ,  $D_{\max} = 5.278e - 2$ ; (c) load cycles  $N = 40000$ ,  $D_{\max} = 8.840e - 2$ ; (e) load cycles  $N = 60000$ ,  $D_{\max} = 1.137e - 1$ ; (f) load cycles  $N = 77600$ ,  $D_{\max} = 1.422e - 1$ .

maximum deflection and peak load of each cycle were recorded. Correspondingly, vertical displacement of the beam centre and the contact force between clamp A and the sample were recorded in the simulations. Additionally, the damage variable in the UMAT subroutine was also outputted.

The four-point bending beam fatigue tests of the asphalt mortar specimens with different asphalt contents, different temperatures, and different loading strains as described previously were simulated. The simulation results of the sample with moderate asphalt content under test condition of  $5^{\circ}\text{C}$  and  $700\mu\epsilon$  are shown in Figure 11.

It can be seen from Figure 11 that in the whole fatigue evolution process of the asphalt mortar sample, the damaged area slightly increased, showing an upward expansion trend. The main damage area was concentrated between clamp A

on the bottom of the sample, and the damage variables were substantially the same at the same height. This is because the middle part of the sample was in a purely bending state and the tensile strain of the sample was the same at the same height. In other parts of the sample, the specimen was subjected to compressive stress, or the tensile strain generated was very small, which was negligible compared with the area where the damage had occurred. The damage area was relatively small, which accounted for about 1/30 of the area of the sample.

The load cycles of the simulations were recorded, and the calculated damage variables at the end of simulations were compared with those of the tests. The results are summarized in Table 5. It indicated that the FE implementation can accurately characterize the mechanical behavior of the proposed fatigue model.

TABLE 5: Comparison between simulated damage variable and measured damage variable under different test conditions.

Asphalt content (%)	Temperature (°C)	Loading strain ( $\mu\epsilon$ )	Simulated damage	Measured damage
4.3	5	700	0.13	0.132
	5	1000	0.31	0.307
	10	1000	0.42	0.39
4.8	5	700	0.23	0.282
	5	1000	0.38	0.357
	10	1000	0.23	0.24
5.5	5	700	0.09	0.098
	5	1000	0.18	0.173
	10	1000	0.27	0.22

**4.3. Fatigue Performance Predictions of the Asphalt Mixture.** The fatigue damage evolution of the asphalt mixtures was analyzed further based on the verified FE implementation of the proposed fatigue model.

A four-point bending fatigue test for asphalt mixture was conducted under the condition of 5°C, 700  $\mu\epsilon$  and moderate asphalt content. The void ratio of the sample is 4%. A virtual test with the same void ratio was constructed using random packing method described in Section 3.4. A fatigue test was simulated under the same test condition. The peak load and maximum deflection were outputted, and the bending stiffness modulus was calculated using equations (1)–(3). As shown in Figure 12, the proposed FE model can well characterize the fatigue performance of the asphalt mixture in the first two stages.

Three virtual mixture samples with 0% VV, 4% VV, and 8% VV were constructed. Fatigue test simulations were conducted. Figure 13 shows the details of the virtual simulations at the 100000th loading cycle. As shown, the voids content plays a negative role in the fatigue performance of the asphalt mixtures. The maximum damage variables are 0.2042, 0.2232, and 0.2755 for the 0% VV, 4% VV, and 8% VV, respectively. Since there are no voids in Figure 13(a), the maximum damage occurred in the particles' edge. Differently, when comes to Figure 13(b) and 13(c), it is found that the boundary of the voids tend to cause damage more easily. The maximum damage always arose from the void edges. Comparing the simulation results of Figures 13(a)–13(c), it is concluded that as the void content increased, the damage evolved more sharply and the damage tended to arise from the void edges due to a stress concentration.

The reduction of the bending stiffness modulus of three virtual fatigue tests is shown in Figure 14. It can be seen that as the void ratio increased, the decay rate of the stiffness modulus increased. The difference between curves of samples with 4% VV and 8% VV was much larger than that between curves of samples with 0% VV and 4% VV. It indicated that the damage accumulation increased nonlinearly when the void ratio increased linearly. The void ratio had a significant influence on the fatigue performance of asphalt mixture.

## 5. Conclusions

This paper proposed a fatigue damage evolution model of the asphalt mortar based on the four-point fatigue

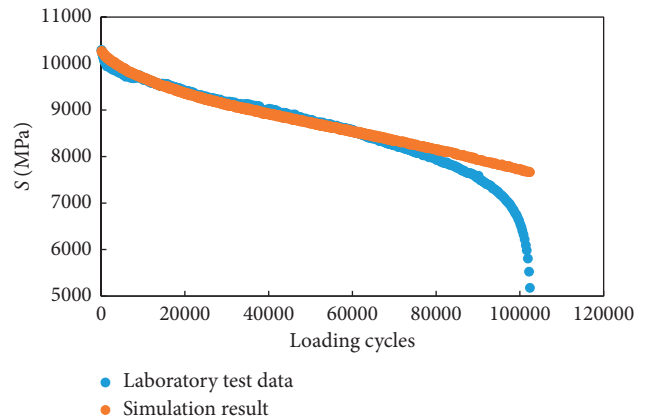


FIGURE 12: Comparison between simulated damage variable and measured damage variable of asphalt mixture.

bending tests. By fitting the laboratory results, the proposed model was verified, and the related parameters were determined under different loading conditions. By importing the damage model into FEM simulation, the major influences on the fatigue damage of the asphalt mixtures were analyzed further. The main conclusions drawn from the study are as follows.

The load strain has a negative effect on the bending stiffness modulus of asphalt mortar while the temperature and asphalt content have a positive one. When the asphalt content is fixed, decreasing the load strain is more effective than increasing the temperatures in improving the fatigue life of the mortar. Since the environmental temperature is uncontrollable during the pavement usage, avoiding the heavy traffic is an effective means to maintain the pavement permanent performance.

The proposed damage model was established based on the continuum mechanics. It characterized the performance of the tiny point within the whole structure which can represent the micromaterial property rather than the macrostructure. By fitting the model curves with the realistic, it has been validated that the proposed methods can well characterize the fatigue life of the asphalt mortar in the first two stages.

The damage evolution curves of the mortar are similar with the asphalt mixtures. It is a rough verification of the assumption that the damage evolution mainly processed within the mortar and the coarse aggregates only form the

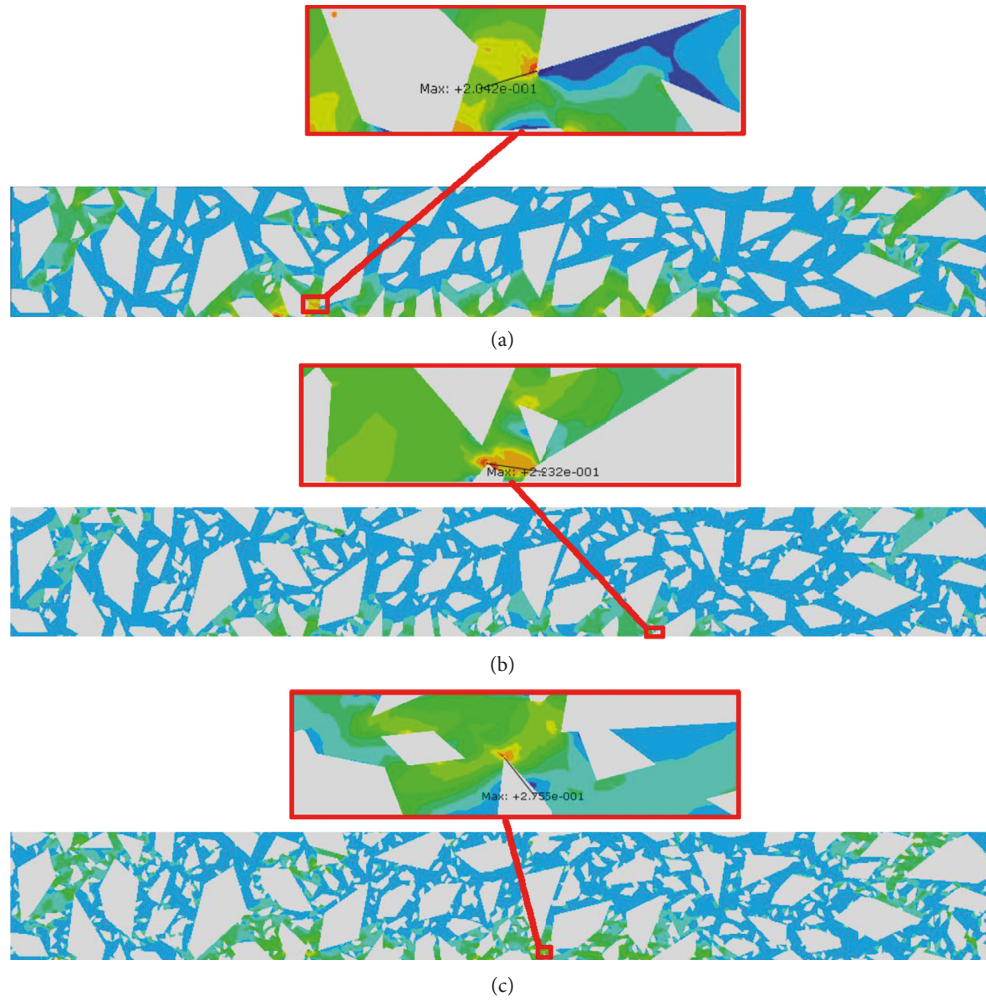


FIGURE 13: Influences of the voids on the fatigue damage of asphalt mixtures: (a) 0% VV; (b) 4% VV; (c) 8% VV.

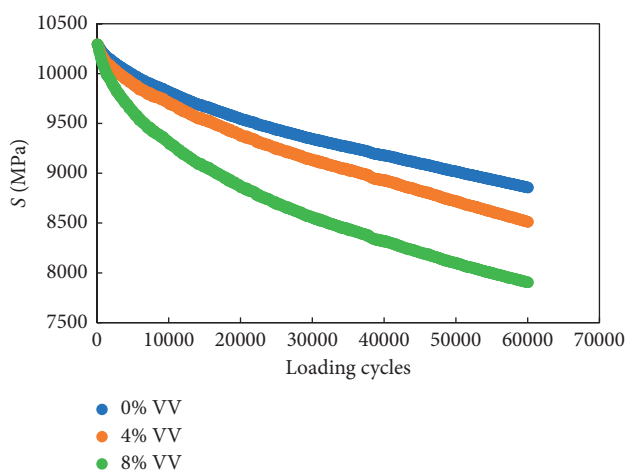


FIGURE 14: Bending stiffness modulus of virtual asphalt mixture samples with different air void ratios.

skeleton in mixtures serving as boundary conditions. Through the FEM simulation, it shows that the damage always arose from the void edges firstly, and as the void

contents increased, the damage grew more sharply. By comparing the simulation results of virtual samples with different void ratios, it indicates that the damage accumulation increased nonlinearly when the void ratio increased linearly. The void ratio had a significant negative influence on the fatigue performance of asphalt mixture.

**Data Availability**

The FEM simulation data and laboratory test data used to support the findings of this study are available from the corresponding author upon request.

**Conflicts of Interest**

The authors declare that they have no conflicts of interest regarding the publication of this article.

**Acknowledgments**

The study was financially supported by the Science Foundations of Nanjing Institute of Technology (YKJ201423), National Natural Science Foundation of China (51878164),

Jiangsu Natural Science Foundation (BK20161421), Scientific Research Foundation of Graduate School of Southeast University (YBJJ 1843), and Graduate Innovation Project of Jiangsu Province (KYCX18\_0147).

## References

- [1] E. Gasthauer, M. Mazé, J. P. Marchand, and J. Amouroux, "Characterization of asphalt fume composition by GC/MS and effect of temperature," *Fuel*, vol. 87, no. 7, pp. 1428–1434, 2008.
- [2] W. Wang, P. Song, and Y. Miao, "Research summary of the composition characteristics and performance of mineral aggregate of asphalt mixture," *Municipal Engineering Technology*, vol. 26, no. 8, pp. 13–16, 2014.
- [3] T. Ma, Y. Zhong, T. Tang, and X. Huang, "Design and evaluation of heat-resistant asphalt mixture for permafrost regions," *International Journal of Civil Engineering*, vol. 14, no. 5, pp. 339–346, 2016.
- [4] G. D. Airey, A. C. Collop, S. E. Zoorob, and R. C. Elliott, "The influence of aggregate, filler and bitumen on asphalt mixture moisture damage," *Construction and Building Materials*, vol. 22, no. 9, pp. 2015–2024, 2008.
- [5] T. Ma, X. Ding, D. Zhang, X. Huang, and J. Chen, "Experimental study of recycled asphalt concrete modified by high-modulus agent," *Construction and Building Materials*, vol. 128, pp. 128–135, 2016.
- [6] Y. Tan, H. Zhang, H. Xu, Y. Wang, and X. Yao, "Effect of fine aggregate form, angularity and texture on the viscoelastic properties of asphalt mortar," *Asphalt Pavements*, vol. 1-2, no. 1, pp. 637–648, 2014.
- [7] M. R. M. Hasan, M. O. Hamzah, M. V. D. Ven, and J. Voskuilen, "Disruption of air voids continuity based on permeability loss due to mortar creep," *Construction and Building Materials*, vol. 116, pp. 347–354, 2016.
- [8] B. G. Wang, L. I. Ping, Z. Q. Zhang, and H. W. Sun, "Influence of mineral powder on aging properties of asphalt mortar," *Journal of Chang'an University (Natural Science Edition)*, vol. 4, pp. 6–9, 2007.
- [9] F. Wang, Z. Liu, and S. Hu, "Temperature stability of compressive strength of cement asphalt mortar," *ACI Materials Journal*, vol. 107, no. 1, pp. 27–30, 2010.
- [10] M. F. Woldekidan, M. Huurman, and A. C. Pronk, "Linear and nonlinear viscoelastic analysis of bituminous mortar," *Transportation Research Record: Journal of the Transportation Research Board*, vol. 2370, no. 1, pp. 53–62, 2013.
- [11] S. G. Hu, T. Wang, F. Z. Wang, Z. C. Liu, T. Gao, and J. Z. Zou, "Freezing and thawing resistance of cement asphalt mortar," *Key Engineering Materials*, vol. 400-402, pp. 163–167, 2009.
- [12] P. Cundall, "A computer model for simulating progressive large scale movement in block rock systems," in *Proceedings of International Symposium. Fracture, ISRM*, pp. 11–8, Nancy, France, September 1971.
- [13] S. Kobayashi, S. I. Oh, T. Altan, and A. Chaudhary, "Metal forming and the finite-element method," *Journal of Materials Shaping Technology*, vol. 8, no. 1, p. 65, 1990.
- [14] J. Zhang, J. Peng, J. Zhang, and Y. Yao, "Characterization of stress and moisture-dependent resilient behaviour for compacted clays in South China," *Road Materials and Pavement Design*, pp. 1–14, 2018.
- [15] J. H. Zhang, J. Li, Y. S. Yao, J. Zheng, and F. Gu, "Geometric anisotropy modeling and shear behavior evaluation of graded crushed rocks," *Construction and Building Materials*, vol. 183, pp. 346–355, 2018.
- [16] S. Y. Zhu, Q. Fu, C. B. Cai, and P. D. Spanos, "Damage evolution and dynamic response of cement asphalt mortar layer of slab track under vehicle dynamic load," *Science China Technological Sciences*, vol. 57, no. 10, pp. 1883–1894, 2014.
- [17] P. Wang, H. Xu, R. Chen, J. Xu, and X. Zeng, "Effect of cement asphalt mortar debonding on dynamic properties of CRTS II slab ballastless track," *Advances in Materials Science and Engineering*, vol. 2014, Article ID 769248, 6 pages, 2014.
- [18] X. Ding, T. Ma, and W. Gao, "Morphological characterization and mechanical analysis for coarse aggregate skeleton of asphalt mixture based on discrete-element modeling," *Construction and Building Materials*, vol. 154, pp. 1048–1061, 2017.
- [19] W. P. Sun, Y. R. Kim, and R. A. Schapery, "A viscoelastic continuum damage model and its application to uniaxial behavior of asphalt concrete," *Mechanics of Materials*, vol. 24, no. 4, pp. 241–255, 1996.
- [20] H. J. Lee and Y. R. Kim, "Viscoelastic continuum damage model of asphalt concrete with healing," *Journal of Engineering Mechanics*, vol. 124, no. 11, pp. 1224–1232, 1998.
- [21] J. L. Zheng and S. T. Lu, "Nonlinear fatigue damage model for asphalt mixtures," *China Journal of Highway and Transport*, vol. 22, no. 5, pp. 21–28, 2009.
- [22] Y. R. Kim, C. Baek, B. S. Underwood, V. Subramanian, M. N. Guddati, and K. Lee, "Application of viscoelastic continuum damage model based finite element analysis to predict the fatigue performance of asphalt pavements," *KSCE Journal of Civil Engineering*, vol. 12, no. 2, pp. 109–120, 2008.
- [23] B. Underwood, C. Baek, and Y. Kim, "Simplified viscoelastic continuum damage model as platform for asphalt concrete fatigue analysis," *Transportation Research Record Journal of the Transportation Research Board*, vol. 2296, no. 1, pp. 36–45, 2015.
- [24] T. Boukharouba, M. Elboujdaini, and G. Pluvinage, *Damage and Fracture Mechanics: Failure Analysis of Engineering Materials and Structures*, Springer Science + Business Media, Berlin, Germany, 2009.
- [25] J. E. Kliewer, H. Zeng, and T. S. Vinson, "Aging and low-temperature cracking of asphalt concrete mixture," *Journal of Cold Regions Engineering*, vol. 10, no. 3, pp. 134–148, 1996.
- [26] Ministry of Transport of the People's Republic of China, *Technical Specification for Construction of Highway Asphalt Pavements*, China Communications Press, Beijing, China, 2004.
- [27] Ministry of Transport of the People's Republic of China, *Standard Test Methods of Bitumen and Bituminous Mixtures for Highway Engineering*, China Communications Press, Beijing, China, 2011.